

DISCLAIMER

This contractor document was prepared for the U.S. Department of Energy (DOE), but has not undergone programmatic, policy, or publication review, and is provided for information only. The document provides preliminary information that may change based on new information or analysis, and represents a conservative treatment of parameters and assumptions to be used specifically for Total System Performance Assessment analyses. The document is a preliminary lower level contractor document and is not intended for publication or wide distribution.

Although this document has undergone technical reviews at the contractor organization, it has not undergone a DOE policy review. Therefore, the views and opinions of authors expressed may not state or reflect those of the DOE. However, in the interest of the rapid transfer of information, we are providing this document for your information per your request.

11/25/07

**OFFICE OF CIVILIAN RADIOACTIVE WASTE MANAGEMENT
ANALYSIS/MODEL COVER SHEET**
Complete Only Applicable Items

1. QA: QA

Page: 1 of 201

<p>2. <input checked="" type="checkbox"/> Analysis Check all that apply</p> <table border="1" style="width:100%; border-collapse: collapse;"> <tr> <td style="width:20%;">Type of Analysis</td> <td><input type="checkbox"/> Engineering</td> </tr> <tr> <td></td> <td><input type="checkbox"/> Performance Assessment</td> </tr> <tr> <td></td> <td><input checked="" type="checkbox"/> Scientific</td> </tr> </table> <table border="1" style="width:100%; border-collapse: collapse;"> <tr> <td style="width:20%;">Intended Use of Analysis</td> <td><input type="checkbox"/> Input to Calculation</td> </tr> <tr> <td></td> <td><input type="checkbox"/> Input to another Analysis or Model</td> </tr> <tr> <td></td> <td><input checked="" type="checkbox"/> Input to Technical Document</td> </tr> <tr> <td></td> <td><input type="checkbox"/> Input to other Technical Products</td> </tr> </table> <p>Describe use: The evaluation of property sets, discussed in this AMR, will be used by Performance Assessment, Waste Package Design, Repository Design as they assess TH behavior</p>	Type of Analysis	<input type="checkbox"/> Engineering		<input type="checkbox"/> Performance Assessment		<input checked="" type="checkbox"/> Scientific	Intended Use of Analysis	<input type="checkbox"/> Input to Calculation		<input type="checkbox"/> Input to another Analysis or Model		<input checked="" type="checkbox"/> Input to Technical Document		<input type="checkbox"/> Input to other Technical Products	<p>3. <input checked="" type="checkbox"/> Model Check all that apply</p> <table border="1" style="width:100%; border-collapse: collapse;"> <tr> <td style="width:20%;">Type of Model</td> <td><input checked="" type="checkbox"/> Conceptual Model</td> <td><input type="checkbox"/> Abstraction Model</td> </tr> <tr> <td></td> <td><input checked="" type="checkbox"/> Mathematical Model</td> <td><input type="checkbox"/> System Model</td> </tr> <tr> <td></td> <td><input checked="" type="checkbox"/> Process Model</td> <td></td> </tr> </table> <table border="1" style="width:100%; border-collapse: collapse;"> <tr> <td style="width:20%;">Intended Use of Model</td> <td><input type="checkbox"/> Input to Calculation</td> </tr> <tr> <td></td> <td><input type="checkbox"/> Input to another Model or Analysis</td> </tr> <tr> <td></td> <td><input checked="" type="checkbox"/> Input to Technical Document</td> </tr> <tr> <td></td> <td><input type="checkbox"/> Input to other Technical Products</td> </tr> </table> <p>Describe use: The evaluation of property sets, discussed in this AMR, will be used by Performance Assessment, Waste Package Design, and Repository Design as they assess TH behavior</p>	Type of Model	<input checked="" type="checkbox"/> Conceptual Model	<input type="checkbox"/> Abstraction Model		<input checked="" type="checkbox"/> Mathematical Model	<input type="checkbox"/> System Model		<input checked="" type="checkbox"/> Process Model		Intended Use of Model	<input type="checkbox"/> Input to Calculation		<input type="checkbox"/> Input to another Model or Analysis		<input checked="" type="checkbox"/> Input to Technical Document		<input type="checkbox"/> Input to other Technical Products
Type of Analysis	<input type="checkbox"/> Engineering																															
	<input type="checkbox"/> Performance Assessment																															
	<input checked="" type="checkbox"/> Scientific																															
Intended Use of Analysis	<input type="checkbox"/> Input to Calculation																															
	<input type="checkbox"/> Input to another Analysis or Model																															
	<input checked="" type="checkbox"/> Input to Technical Document																															
	<input type="checkbox"/> Input to other Technical Products																															
Type of Model	<input checked="" type="checkbox"/> Conceptual Model	<input type="checkbox"/> Abstraction Model																														
	<input checked="" type="checkbox"/> Mathematical Model	<input type="checkbox"/> System Model																														
	<input checked="" type="checkbox"/> Process Model																															
Intended Use of Model	<input type="checkbox"/> Input to Calculation																															
	<input type="checkbox"/> Input to another Model or Analysis																															
	<input checked="" type="checkbox"/> Input to Technical Document																															
	<input type="checkbox"/> Input to other Technical Products																															

4. Title:
Thermal Tests Thermal-Hydrological Analyses/Model Report

5. Document Identifier (including Rev. No. and Change No., if applicable):
ANL-NBS-TH-000001 REV 00

6. Total Attachments: wo	7. Attachment Numbers - No. of Pages in Each: Attachment I, 144; Attachment II, 94
-----------------------------	---

	Printed Name	Signature	Date
8. Originator	Ralph Wagner	Signature <i>Tim Vogt</i> for	Date 4/12/00
9. Checker	David Mohr	<i>David E. Mohr</i>	4/12/00
10. Lead/Supervisor	James Blink	<i>James Blink</i>	13 Apr 00
11. Responsible Manager	James Blink	<i>James Blink</i>	13 Apr 00

12. Remarks:

Additional technical contributors are cited below:
Ananda Wijesinghe, Kenrick Lee, Thomas Buschek, Ronald Shaffer, Sumit Mukhopadhyay, Yvonne Tsang, Nicholas Francis, Sanford Ballard, Tim Vogt, Jay Cho

The users of software are as follows:

- Nicholas Francis used software items 1 through 13 listed in Table 1.
- Sumit Mukhopadhyay and Yvonne Tsang used software items 14 through 40 listed in Table 1.
- Ananda Wijesinghe and Kenrick Lee used software items 41 through 47 listed in Table 1.

INFORMATION COPY
LAS VEGAS DOCUMENT CONTROL

OFFICE OF CIVILIAN RADIOACTIVE WASTE MANAGEMENT
ANALYSIS/MODEL REVISION RECORD

Complete Only Applicable Items

1. Page: 2 of 201

2. Analysis or Model Title:

Thermal Tests Thermal-Hydrological Analyses/Model Report

3. Document Identifier (including Rev. No. and Change No., if applicable):

ANL-NBS-TH-000001 REV 00

4. Revision/Change No.

5. Description of Revision/Change

00

Initial Issue

CONTENTS

	Page
ACRONYMS AND ABBREVIATIONS	12
1. PURPOSE.....	14
2. QUALITY ASSURANCE.....	15
3. COMPUTER SOFTWARE AND MODEL USAGE.....	15
4. INPUTS	22
4.1 DATA AND PARAMETERS.....	22
4.2 CRITERIA.....	28
4.3 CODES AND STANDARDS	28
5. ASSUMPTIONS	28
5.1 GENERAL ASSUMPTIONS	29
5.1.1 Test Configuration	29
5.1.2 Boundary and Initial Conditions.....	29
5.1.3 Heat Source.....	29
5.1.4 Material Properties and Behavior	29
5.2 SINGLE HEATER TEST ASSUMPTIONS.....	31
5.3 DRIFT SCALE TEST ASSUMPTIONS	32
5.3.1 TOUGH2 Simulations	32
5.3.2 NUFT Simulations.....	32
5.4 LARGE BLOCK TEST ASSUMPTIONS.....	33
6. ANALYSIS/MODEL.....	35
6.1 NUMERICAL ANALYSES	35
6.1.1 Single Heater Test.....	35
6.1.2 Drift Scale Test - TOUGH2 Simulations.....	38
6.1.3 Drift Scale Test - NUFT Simulations	41
6.1.4 Large Block Test.....	46
6.2 COMPARATIVE ANALYSES	49
6.2.1 Single Heater Test.....	49
6.2.2 Drift Scale Test - TOUGH2 Simulations.....	52
6.2.3 Drift Scale Test - NUFT Simulations	60
6.2.4 Large Block Test.....	69
6.3 SENSITIVITY STUDIES	72
6.3.1 Single Heater Test.....	72
6.3.2 Drift Scale Test - TOUGH2 Simulations.....	73
6.3.3 Drift Scale Test - NUFT Simulations	77
6.3.4 Large Block Test.....	79
6.4 SUMMARY OF ANALYSIS	82
6.4.1 Single Heater Test.....	82
6.4.2 Drift Scale Test - TOUGH2 Simulations.....	83

CONTENTS (Continued)

	Page
6.4.3 Drift Scale Test - NUFT Simulations	84
6.4.4 Large Block Test.....	86
6.5 THERMAL TEST MODEL VALIDATION	87
6.5.1 The Single Heater Test as Simulated by the TOUGH2 Model.....	87
6.5.2 The Drift Scale Test as Simulated by the TOUGH2 Model	89
6.5.3 The Drift Scale Test as Simulated by the NUFT Model.....	89
6.5.4 The Large Block Test as Simulated by the NUFT Model	91
6.5.5 Summary of Thermal Test Model Validation.....	92
7. CONCLUSIONS	189
8. INPUTS AND REFERENCES.....	191
8.1 DOCUMENTS CITED	191
8.2 CODES, STANDARDS, REGULATIONS, AND PROCEDURES	195
8.3 SOURCE DATA (LISTED BY DATA TRACKING NUMBERS).....	195
8.4 COMPUTER SOFTWARE AND ROUTINES	198

FIGURES

		Page
1.	Vertical Cross Section of DST (TOUGH2) Numerical Grid Intersecting the HD at $Y \approx 10$ m from the Bulkhead and Containing Hydrology Boreholes 57-61	93
2.	Detailed View of Vertical Cross Section of DST (TOUGH2) Numerical Grid through Plane Containing Hydrology Boreholes 57-61	94
3.	Detailed View of Vertical Cross Section of DST (TOUGH2) Numerical Grid through Plane Containing RTD Boreholes 137-144, Looking into the HD from the Bulkhead	95
4.	Plan View of the DST	96
5.	Cross Section (A-A') Parallel to the Heated Drift in the DST	97
6.	Cross Section (B-B') Orthogonal to the Heated Drift in the DST	98
7.	Idealized NUFT Computational Domain Used for Computing the TH Response of the DST	99
8.	Horizontal Cross Section Passing through the Axis of the HD of the Nested-Mesh Finite Difference Computational Grid Employed for the DST (NUFT) Calculations	100
9.	Vertical Cross Section Passing through the Mid-Point of the HD of the Nested-Mesh Finite Difference Computational Grid Employed for the DST (NUFT) Calculations	101
10.	Photograph of Large Block Test (LBT) Site	102
11.	LBT Heating Power History for Heater No. 3	103
12.	Schematic of the LBT Model Geometry (NUFT)	104
13.	Monthly Average Air Temperature During 1997 Measured at Site 8 in Fran Ridge	105
14.	Comparison of the TOUGH2 Simulation Using the Drift-Scale Property Set and the SHT Measured Temperatures at Thermocouple Location TMA-TC-1A-7 (22 cm horizontally away from the heater center)	106
15.	Comparison of the TOUGH2 Simulation Using the Drift-Scale Property Set and the SHT Measured Temperatures at Thermocouple Location TMA-TC-4A-6 (73 cm below the heater center)	106
16.	Comparison of the TOUGH2 Simulation Using the Drift-Scale Property Set and the SHT Measured Temperatures at Thermocouple Location TMA-TC-5A-7 (66 cm above the heater center)	107
17.	Comparison of the TOUGH2 Simulation Using the Drift-Scale Property Set and the SHT Measured Temperatures Radially Around Heater Mid-Length	107
18.	Statistical Measures for SHT Thermal Analyses	108
19.	Measured (top) and TOUGH2 Simulated (bottom) DST Temperatures as a Function of Distance of Sensor Locations from Borehole Collars in RTD Boreholes 137-144 after 3 Months of Heating. The DS/AFM-UZ99 Properties were used in the Simulation	109
20.	Measured (top) and TOUGH2 Simulated (bottom) DST Temperatures as a Function of Distance of Sensor Locations from Borehole Collars in RTD Boreholes 137-144 after 12 Months of Heating. The DS/AFM-UZ99 Properties were used in the Simulation	110

FIGURES (Continued)

Page

21.	Measured (top) and TOUGH2 Simulated (bottom) DST Temperatures as a Function of Distance of Sensor Locations from Borehole Collars in RTD Boreholes 137-144 after 18 Months of Heating. The DS/AFM-UZ99 Properties were used in the Simulation.....	111
22.	Measured (top) and TOUGH2 Simulated (bottom) DST Temperatures as a Function of Time at Selected Sensor Locations of Borehole 160 (Horizontal near the Wing Heaters). The DS/AFM-UZ99 Properties were used in the Simulation.	112
23.	Measured (top) and TOUGH2 Simulated (bottom) DST Temperatures as a Function of Time at All Sensor Locations of Borehole 59, above the Heated Region. The DS/AFM-UZ99 Properties were used in the Simulation.	113
24.	Measured (top) and TOUGH2 Simulated (bottom) DST Temperatures as a Function of Time at All Sensor Locations of Borehole 60, below the Heated Region. The DS/AFT-UZ99 Properties were used in the Simulation.	114
25.	Statistical Measures for DST TOUGH2 Thermal Analyses.....	115
26.	Schematic Representation of Thermal Hydrological Processes in an Unsaturated Fractured Geological Medium.....	116
27.	TOUGH2 Simulated Fracture Liquid Saturation in the Plane of Hydrology Boreholes 57-61 After 3 Months (top) and 6 Months (bottom) of DST Heating, Using the DS/AFM-UZ99 Properties	117
28.	TOUGH2 Simulated Fracture Liquid Saturation in the Plane of Hydrology Boreholes 57-61 After 12 Months (top) and 18 Months (bottom) of DST Heating, Using the DS/AFM-UZ99 Properties.....	118
29.	TOUGH2 Simulated Matrix Liquid Saturation in the Plane of Hydrology Boreholes 57-61 After 3 Months (top) and 6 Months (bottom) of DST Heating, Using the DS/AFM-UZ99 Properties	119
30.	TOUGH2 Simulated Matrix Liquid Saturation in the Plane of Hydrology Boreholes 57-61 at 12 Months (top) and 18 Months (bottom) of DST Heating, Using the DS/AFM-UZ99 Properties	120
31.	Changes in Air Permeability Values with Respect to Pre-Heat Values as Obtained Through Air-Injection Tests in DST Hydrology Boreholes 57-59 Above the Heated Drift.....	121
32.	Changes in Air Permeability Values with Respect to Pre-Heat Values as Obtained Through Air-Injection Tests in DST Hydrology Boreholes 60-61 Below the Heated Drift.....	122
33.	Tomogram Showing Saturation Change from Pre-Heat Ambient Values Derived from a Cross-Hole Radar Survey Taken in January of 1999 (~13 months of heating) in the Plane of DST Boreholes 64-68	123
34.	TOUGH2 Simulated Matrix Liquid Saturation in the Plane of DST Boreholes 64-68 After 12 Months of Heating, Using the DS/AFM-UZ99 Properties	124
35.	Distribution of the Simulated Temperature on a Horizontal Plane through the Wing Heater Arrays (Z=-0.5 m) at 365 Days for the DS DST NUFT Analyses.....	125
36.	Distribution of the Simulated Water Saturation on a Horizontal Plane through the Wing Heater Arrays (Z=-0.5 m) at 365 Days for the DS DST NUFT Analyses.....	126
37.	Distribution of the Simulated Temperature on a Vertical Slice through the Mid-Length of the DST at 365 Days for the DS DST NUFT Analyses.....	127

FIGURES (Continued)

		Page
38.	Distribution of the Simulated Water Saturation on a Vertical Slice through the Mid-Length of the DST at 365 Days for the DS DST NUFT Analyses	128
39.	Distribution of the Simulated Temperature on a Vertical Plane through the Longitudinal Axis of Heated Drift Array (X=0m) at 365 Days for the DS DST NUFT Analyses	129
40.	Distribution of the Simulated Water Saturation on a Vertical Plane through the Longitudinal Axis of Heated Drift Array (X=0m) at 365 Days for the DS DST NUFT Analyses	130
41.	Distribution of the Simulated Temperature on a Vertical Plane Normal to Wing Heater Array (X=-6.24 m) Near the Center of the Inner Wing Heater Array at 365 Days for the DS DST NUFT Analyses	131
42.	Distribution of the Simulated Water Saturation on a Vertical Plane Normal to Wing Heater Array (X=-6.24 m) Near the Center of the Inner Wing Heater Array at 365 Days for the DS DST NUFT Analyses	132
43.	Comparison of NUFT Simulated and Measured Temperatures from the DST, Along Borehole 137 (Vertical Upward) at (a) 12 Months and (b) 18 Months	133
44.	Comparison of NUFT Simulated and Measured Temperature Histories for Sensors No. 2, 5, 10, 40, and 67 Over the 18 Months in Borehole 158 (Vertical Up, top) and Borehole 162 (Vertical Down, bottom) for the DST, Using the DS Property Set.....	134
45.	Comparison of NUFT Simulated and Measured Temperature Histories for Sensors No. 2, 5, 10, 40, and 67 over 18 Months in Borehole 159 (45° Upward) for the DST, Using the DS Property Set	135
46.	Comparison of NUFT Simulated and Measured Temperature Histories for Sensors No. 2, 5, 10, 40, and 67 Over the 18 Months in Borehole 160 (Horizontal near the Wing Heaters) for the DST, Using the DS Property Set.....	136
47.	Comparison of NUFT Simulated and Measured Temperature Histories for Sensors No. 2, 5, 10, 40, and 67 Over the 18 Months in Borehole 161 (45° Downward) for the DST, Using the DS Property Set.....	137
48.	Comparison of NUFT Simulated and Measured Temperature Histories for Sensors No. 2, 16, 30, 44, and 60 Over the 18 Months in Borehole 80 (Parallel to the Drift Slightly Above and to the Side) for the DST, Using the DS Property Set.....	138
49.	Comparison of NUFT Simulated and Measured Temperature Along Borehole 160 (Horizontal Near the Wing Heaters) at 100, 182, and 365 Days of Heating for the DST	139
50.	Comparison of NUFT Simulated and Measured Temperature Along Borehole 80 (Parallel to the HD, Slightly Above and to the Side) at 100, 182, and 365 Days of Heating for the DST.....	140
51.	Statistical Measures for DST NUFT Thermal Analyses	141
52.	Two Cross-Sections Orthogonal to the HD Showing the Location of the ERT Boreholes Drilled from the OD and Selected Boreholes Drilled from the HD of the DST	142
53.	Comparison of Distributions of Measured and Simulated (NUFT) Water Saturation at 100 Days for the DST, Using the DS Property Set	143
54.	Comparison of Distributions of Measured and Simulated (NUFT) Water Saturation at 182 Days for the DST, Using the DS Property Set	144

FIGURES (Continued)

	Page
55. Comparison of Distributions of Measured and Simulated (NUFT) Water Saturation at 365 Days for the DST, Using the DS Property Set	145
56. Comparison of Distributions of Measured and Simulated (NUFT) Water Saturation at 547 Days for the DST, Using the DS Property Set	146
57. Fraction Volume of Water Content in DST Boreholes as Measured by Neutron Logging Boreholes 64 to 68 for Nominal Heating Duration of 3 Months.	147
58. Fraction Volume of Water Content in DST Boreholes as Measured by Neutron Logging Boreholes 64 to 68 for Nominal Heating Duration of 6 Months.	148
59. Fraction Volume of Water Content in DST Boreholes as Measured by Neutron Logging Boreholes 64 to 68 for Nominal Heating Duration of 12 Months	149
60. Fraction Volume of Water Content in DST Boreholes as Measured by Neutron Logging Boreholes 64 to 68 for Nominal Heating Duration of 18 Months	150
61. Fraction Volume of Water Content in DST Boreholes 79 and 80 as Measured by Neutron Logging for Nominal Heating Duration of 3 Months.....	151
62. Fraction Volume of Water Content in DST Boreholes 79 and 80 as Measured by Neutron Logging for Nominal Heating Duration of 6 Months.....	152
63. Fraction Volume of Water Content in DST Boreholes 79 and 80 as Measured by Neutron Logging for Nominal Heating Duration of 12 Months.....	153
64. Fraction Volume of Water Content in DST Boreholes 79 and 80 as Measured by Neutron Logging for Nominal Heating Duration of 18 Months.....	154
65. Simulated Versus Measured Temperature Profile for Borehole TT1 of LBT. The DS Property Set was Used in the Simulation. The Heaters were Active for 375 Days	155
66. Statistical Measures for LBT Thermal Analyses	156
67. Simulated Versus Measured Temperature Histories for Sensors TT1-14 and TT1-19 at Borehole TT1 of the LBT. The DS Property Set was Used in the Simulation.....	157
68. Liquid Saturation Profile Along Borehole TN3 for the LBT. The DS Property Set was Used in the Simulation	158
69. Comparison of ERT Measurements and Simulated (DS-LBT) Water Saturations	159
70. Image of Simulated Temperature and Liquid-Phase Saturation Distribution at 30 Days for the LBT, Using the DS Property Set.....	160
71. Image of Simulated Temperature and Liquid-Phase Saturation Distribution at 100 Days for the LBT, Using the DS Property Set.....	160
72. Image of Simulated Temperature and Liquid-Phase Saturation Distribution at 200 Days for the LBT, Using the DS Property Set.....	161
73. Image of Simulated Temperature and Liquid-Phase Saturation Distribution at 300 Days for the LBT, Using the DS Property Set.....	161
74. Image of Simulated Temperature and Liquid-Phase Saturation Distribution at 400 Days for the LBT, Using the DS Property Set.....	162
75. Image of Simulated Temperature and Liquid-Phase Saturation Distribution at 600 Days for the LBT, Using the DS Property Set.....	162
76. Simulated Temperature (top) and Liquid-Phase Saturation (bottom) Profiles along the LBT Block.....	163

FIGURES (Continued)

		Page
77.	Comparison of Three SHT TOUGH2 Simulations (Property Sets: DS, Median k_b , and TSPA-VA) and Measured SHT Temperatures at Thermocouple Location TMA-TC-1A-7.....	164
78.	Comparison of Three SHT TOUGH2 Simulations (Property Sets: DS, Median k_b , and TSPA-VA) and SHT Measured Temperatures at Thermocouple Location TMA-TC-4A-6.....	164
79.	Comparison of Three SHT TOUGH2 Simulations (Property Sets: DS, Median k_b , and TSPA-VA) and Measured SHT Temperatures at Thermocouple Location TMA-TC-5A-7.....	165
80.	Comparison of Three SHT TOUGH2 Simulations (Property Sets: DS, Median k_b , and TSPA-VA) and SHT Measured Temperatures Radially Around the Heater Mid-Length.....	166
81.	TOUGH2 Simulated Temperatures along RTD Boreholes 137-144 after 3 Months of DST Heating (Case: DKM-TT99).....	167
82.	TOUGH2 Simulated Temperatures along RTD Boreholes 137-144 after 12 Months of DST Heating (Case: DKM-TT99).....	168
83.	TOUGH2 Simulated Temperatures along RTD Boreholes 137-144 after 18 Months of DST Heating (Case: DKM-TT99).....	169
84.	TOUGH2 Simulated Temperature Histories of Selected DST Sensor Locations in RTD Borehole 160 (Horizontal Near the Wing Heaters) for DKM-TT99 Properties.....	170
85.	Contours of TOUGH2 Simulated Temperatures in the Plane of DST Hydrology Boreholes 57-61 after 6 Months of Heating (top: Case DS/AFM-UZ99; bottom: Case DKM-TT99).....	171
86.	Contours of TOUGH2 Simulated Temperatures in the Plane of DST Hydrology Boreholes 57-61 after 18 Months of Heating (top: Case DS/AFM-UZ99; bottom: Case DKM-TT99).....	172
87.	Contours of TOUGH2 Simulated Fracture Liquid Saturation after 18 Months of Heating in the Plane of DST Hydrology Boreholes 57-61 (top: Case DS/AFM-UZ99; bottom: Case DKM-TT99).....	173
88.	Contours of TOUGH2 Simulated Fracture Liquid Saturation after 18 Months of Heating in the Plane of DST Hydrology Boreholes 57-61 (top: Case DS/AFM-UZ99; bottom: Case DKM-TT99).....	174
89.	Capillary Pressure Characteristic Curves for Both Fractures and Matrix with the DS/AFM-UZ99 and DKM-TT99 Property Sets.....	175
90.	Liquid-Phase Relative Permeability Characteristic Curves for Both Fractures and Matrix with the DS/AFM-UZ99 and DKM-TT99 Property Sets.....	176
91.	Gas-Phase Relative Permeability Characteristic Curves for Both Fractures and Matrix with the DS/AFM-UZ99 and DKM-TT99 Property Sets.....	177
92.	Contours of DST TOUGH2 Simulated Matrix Liquid Saturation in the Plane of Hydrology Boreholes 57-61 after 6 Months of Heating (Case: DKM-TT99).....	178
93.	Contours of DST TOUGH2 Simulated Matrix Liquid Saturation in the Plane of DST Hydrology Boreholes 57-61 after 18 Months of Heating (Case: DKM-TT99).....	179
94.	Comparison of Simulated (NUFT) and Measured Temperature Histories for Sensor #10 in Borehole 158 (Vertical Upward) for All Property Sets in the DST.....	180

FIGURES (Continued)

	Page
95. Comparison of Simulated (NUFT) and Measured Temperature Histories for Sensor #10 in Borehole 159 (45° Upward) for All Property Sets in the DST	181
96. Comparison of Simulated (NUFT) and Measured Temperature Histories for Sensor #10 in Borehole 160 (Horizontal Near the Wing) for All Property Sets in the DST	182
97. Comparison of Simulated (NUFT) and Measured Temperature Histories for Sensor #10 in Borehole 161 (45° Upward) for All Property Sets in the DST	183
98. Comparison of Simulated (NUFT) and Measured Temperature Histories for Sensor #10 in Borehole 162 (Vertical Downward) for All Property Sets in the DST	184
99. Comparison of Simulated (NUFT) and Measured Temperature Histories for Sensor #30 in Borehole 80 (Parallel to the Drift, Slightly Above and to the Side) for All Property Sets in the DST	185
100. Simulated Temperature Profile Along Borehole TT1 in the LBT Computed Using the DS and MS Rock Property Data Set, Compared to Measured Data	186
101. Comparison of the Liquid Saturation Along Borehole TN3 in the LBT for the DS and MS Rock Property Data Set	187
102. Temperature Profiles along Borehole TT1 in the LBT at 200 Days for Field Measurements and NUFT Simulations	188

TABLES

	Page
1. Computer Software and Routines	16
2. Model Descriptions	21
3. Nomenclature of Various Property sets Used for the Model Studies.	22
4. Single Heater Test Model Inputs.....	23
5. Drift Scale Test Model Inputs (TOUGH2)	24
6. Drift Scale Test Model Inputs for tsw34 Unit (NUFT).....	25
7. Large Block Test Model Inputs (NUFT).....	26
8. Data Tracking Numbers of Source Data in Figures	27
9. Data Tracking Numbers of Input/Output from Analyses.....	28
10. Model Validation Results for the Single Heater Test TOUGH2 Model ^a	88
11. Model Validation Results for the Drift Scale Test TOUGH2 Model ^a	89
12. Model Validation Results for the Drift Scale Test NUFT Model ^a	90
13. Model Validation Results for the Large Block Test NUFT Model ^a	91

ACRONYMS AND ABBREVIATIONS

Acronyms

1-D	one-dimensional
2-D	two-dimensional
3-D	three-dimensional
AFM	active fracture model
AFM-UZ99	active fracture model – unsaturated zone flow and transport 1999
AMR	analysis/model report
CD	connecting drift
CON	conduction only [data]
DIRS	Document Input Reference System
DKM	dual-permeability model
DKM-TT99	dual-permeability model - thermal test 1999
DOE	U.S. Department of Energy
DS	drift scale thermal-hydrologic [property set]
DST	Drift Scale Test
DTN(s)	data tracking number(s)
ECM(s)	equivalent continuum model(s)
ERT	electrical resistivity tomography
ESF	Exploratory Studies Facility
GPR	ground penetrating radar
HD	heated drift
LBT	Large Block Test
MD	mean difference
Median k_b	median bulk permeability [property set]
MS	mountain scale thermal-hydrologic [property set]
MSFP	mountain scale with higher fracture permeability [property set]
MSLK	mountain scale with local thermal conductivity [property set]
NAMD	normalized absolute mean difference
NEU	neutron logging
OD	observation drift

ACRONYMS AND ABBREVIATIONS (Continued)

PA	performance assessment
RH	relative humidity
RMSD	root mean square difference
RTD	resistance temperature detector
SHT	Single Heater Test
STN	software tracking number
TBV	to be verified
TH	thermal-hydrological
TSPA	Total System Performance Assessment/Analyses
TSPA-SR	Total System Performance Assessment for the Site Recommendation
TSPA-VA	Total System Performance Assessment for the Viability Assessment
UZ	unsaturated zone
YMP	Yucca Mountain Site Characterization Project

Abbreviations

Ttptll	Tertiary Miocene (Age), Paintbrush (Group), Topopah Spring Tuff (Formation), Crystal Poor (Member), Lower Lithophysal (Zone)
Ttptmn	Tertiary Miocene (Age), Paintbrush (Group), Topopah Spring Tuff (Formation), Crystal-Poor (Member), Middle Nonlithophysal (Zone)

1. PURPOSE

The purpose of the Thermal Tests Thermal-hydrological (TH) Analysis/Model Report (AMR) is to evaluate the drift scale thermal-hydrologic (DS) property set derived from the unsaturated zone (UZ) flow and transport analyses for thermally perturbed conditions. Also, the secondary purpose is to conduct sensitivity studies of other TH property sets, including the mountain scale thermal-hydrologic (MS) property set, and to investigate modifications that would result in adequate agreement between simulated and measured TH data.

Heat and mass transfer models applicable to the Yucca Mountain Site Characterization Project (YMP) have been developed and documented in other reports. The TOUGH2 software package implements a set of these conceptual heat and mass transfer models, primarily in support of the Unsaturated Zone Flow and Transport Process Model Report. The NUFT software package implements another set of conceptual heat and mass transfer models (with a great deal of similarity to those implemented in TOUGH2), primarily in support of the Engineered Barrier System Degradation Process Model Report and the Total System Performance Assessment/Analyses (TSPA) TH abstractions. Validation of these models, (i.e., comparison with the actual behavior of the modeled system) is a key part of developing confidence in the U.S. Department of Energy's (DOE's) ability to meet regulatory requirements on repository performance with reasonable assurance. Application of the models to in situ thermal tests is one means of validation, although care must be taken to interpret the importance of the various physical processes at the smaller spatial scale and for the limited duration of the field tests.

This AMR has both Analysis and Model aspects. As an analysis, this report uses existing repository scale models to simulate smaller scale field tests, and compares the results to measured temperatures and saturations in the tests. The analysis supports existing AMRs describing the models implemented in TOUGH2 and NUFT. As a model report, this document describes the formulation of the tests, including the conceptual models, properties, and boundary conditions; these formulations have been constructed for the purpose of this AMR. The field test models have a strong overlap with the repository level models that the tests are designed to validate; therefore, the description of these field test models in this AMR will rely on references to the repository level model documents to a large extent.

The evaluation is based on TH measurements from the three in situ thermal tests in potential repository lithologic units at Yucca Mountain. The importance of this is to ensure that the hydrologic properties used by the ambient models can also be used by the Total System Performance Assessments for the Site Recommendation (TSPA-SR) models that incorporate the thermal perturbation caused by repository heating. The three in situ tests and the respective software codes used in the numerical simulations are: the Single Heater Test (SHT)/TOUGH2, the Drift Scale Test (DST)/TOUGH2 and NUFT, and the Large Block Test (LBT)/NUFT. For the purposes of this AMR, all three thermal tests are simulated employing the dual-permeability [conceptual] model (DKM) (Pruess 1991), including the active fracture model (AFM) (Liu et al. 1998) to represent fracture-matrix interactions. Simulated temperatures and saturations are compared to the measurements from the tests. These comparative analyses form the basis for the inferences and conclusions drawn in this AMR.

The technical development plan for this AMR, *Thermal Test Thermal – Hydrological Analysis and Models report*, DI# ANL-NBS-TH-000001 (CRWMS M&O 1999a) has been prepared and submitted to the Records Processing Center. Constraints and limitations of the numerical simulations are mostly discussed in Section 5 (Assumptions) and Section 6 (Analysis/Model).

The sensitivity cases considered in this study target only major changes as they relate to the property sets. Sensitivity studies of minor to moderate changes of input parameters were considered beyond the scope of this study.

The SHT, located in Alcove #5 of the Exploratory Studies Facility (ESF), is described in the *Single Heater Test Status Report* (CRWMS M&O 1997a) and *Single Heater Test Final Report* (CRWMS M&O 1999b). The heating phase of the SHT started in August 1996 and continued for 275 days until May 1997. Cooling continued until January 1998, at which time posttest characterization of the test block commenced. Tests in the laboratory, modeling, analyses and documentation were completed, and the final report was submitted to the DOE in May 1999.

The DST is described in the reports, *Drift Scale Test Design and Forecast Results* (CRWMS M&O 1997b) and *Drift Scale Test As-Built Report* (CRWMS M&O 1998a). The results of characterizing the test block are contained in the report, *Ambient Characterization of the Drift Scale Test Block* (CRWMS M&O 1997c). Early results of the DST are discussed in the *Drift Scale Test Progress Report No. 1* (CRWMS M&O 1998b). The heating phase of the DST started in December 1997 and is expected to last approximately four years until December 2001. Measurements made in the DST during the first eighteen months of heating (through May 31, 1999) are considered in this AMR.

The LBT, located in Fran Ridge, southeast of Yucca Mountain, is described in the report, *Large Block Test Status Report* (Wilder et al. 1997). The heating phase of the LBT, started in February 1997, continued until March 1998 at which time the heaters were turned off. Measurements at the LBT were made until September 1998. Posttest characterization of the block, which started in October 1998, has been completed, but results have not yet been reported.

2. QUALITY ASSURANCE

The activities documented in this AMR were evaluated in accordance with QAP-2-0, *Conduct of Activities*, and were determined to be subject to the requirements of the U.S. DOE Office of Civilian Radioactive Waste Management *Quality Assurance Requirements and Description* (DOE 2000). This evaluation is documented in *M&O Site Investigations* (CRWMS M&O 1999c) and Wemheuer (1999). This AMR has been prepared in accordance with procedure AP-3.10Q.

3. COMPUTER SOFTWARE AND MODEL USAGE

The conceptual model underlying the mathematical simulations performed for this AMR is the DKM (Pruess 1991) including the AFM (Liu et al. 1998) to represent fracture-matrix interactions. Both the TOUGH2 and NUFT codes are employed for the simulations.

The SHT is simulated by TOUGH2 Version 3.4.3, software tracking number (STN) 10146-3.4.3-00. The LBT and the DST are simulated by NUFT Version 3.0.1s, STN 10130-3.0.1s-00. The DST is also simulated by TOUGH2 V1.4, STN: 10007-1.4-01. TOUGH2 and NUFT software are appropriate for the implementation of the DKM/AFM model. All software is considered appropriate for its application and was used within the ranges of validation in accordance with AP-SI.1Q, *Software Management*, pending qualification of NUFT – version 3.0.1s and TOUGH2 – version 3.4.3. These versions of the software used for the modeling in this AMR are identical with the corresponding versions submitted to the Configuration Management System for baselining.

The software used in the simulations along with the subroutines and macros used for post processing and data reduction are listed in Table 1 below. For many software routines, software routine reports have been prepared and STNs are provided in Table 1. For the remaining software routines, descriptions are provided in Attachment 1 (SHT) and Attachment 2 (DST/LBT). All software routines are listed in Table 1. The computer platforms are also indicated in Table 1. The base case (DS) property set (DTN: LB990861233129.001) was derived by the UZ Flow and Transport Model (CRWMS 2000b and 2000c).. Table 2 lists the thermal test models documented in this AMR (Items 1-4) as well as conceptual models that support this AMR (Items 5-8). The quality-status of the computer software and routines is provided in the electronic Document Input Reference System (DIRS) database.

Table 1. Computer Software and Routines

Item No.	Software Name	Version	Software Tracking Number	Computer Platform, Operating System, Compiler	Simulation	Description
1	TOUGH2	3.4.3	10146-3.4.3-00	Sun, UNIX OS, Sun FORTRAN 77	SHT ^a by TOUGH2	Multiphase, multicomponent modeling code for numerical solutions of non-isothermal flow and transport in porous media
2	amb.f	1	Attachment I	Sun, UNIX OS, Sun FORTRAN 77	SHT by TOUGH2	Inserts ECM ^p boundary conditions into MESHMAKER file from TOUGH2 for initialization runs
3	bdryinselem.f	1	Attachment I	Sun, UNIX OS, Sun FORTRAN 77	SHT by TOUGH2	Inserts ECM boundary conditions into MESHMAKER file from TOUGH2 for heating runs
4	dkmmesha mb.f	1	Attachment I	Sun, UNIX OS, Sun FORTRAN 77	SHT by TOUGH2	Creates DKM ^d file from amb.f output file
5	dkmmesha mb_mod_1 D.f	1	Attachment I	Sun, UNIX OS, Sun FORTRAN 77	SHT by TOUGH2	Creates DKM/AFM ^e 1-D column file from TOUGH2 MESHMAKER file and bdryinselem.f output

Table 1. Computer Software and Routines (Continued)

Item No.	Software Name	Version	Software Tracking Number	Computer Platform, Operating System, Compiler	Simulation	Description
6	dkmmeshamb_mod.f	2	Attachment I	Sun, UNIX OS, Sun FORTRAN 77	SHT by TOUGH2	Uses the amb.f output and TOUGH2 output (from dkmmeshamb_mod_1D.f input) to produce full 3-D grid with initial conditions for initialization runs
7	icpredkm.f	1	Attachment I	Sun, UNIX OS, Sun FORTRAN 77	SHT by TOUGH2	Uses results of TOUGH2 run (with dkmmeshamb_mod.f or dkmmeshamb.f input) to produce full 3-D grid with initial conditions for heating runs
8	dkmmesh.f	1	Attachment I	Sun, UNIX OS, Sun FORTRAN 77	SHT by TOUGH2	Creates DKM file from bdryinselem.f output
9	dkmmesh_mod.f	2	Attachment I	Sun, UNIX OS, Sun FORTRAN 77	SHT by TOUGH2	Creates DKM/AFM file from bdryinselem.f and icpredkm.f output
10	Compare	1	Attachment I	PC, Windows	SHT by TOUGH2	Calculates Statistical Measures
11	read_temp_vs_time_models	1	Attachment I	PC, Windows	SHT by TOUGH2	Generates a Plot File
12	tough_extract_frac.f	1	Attachment I	Sun, UNIX OS, Sun FORTRAN 77	SHT by TOUGH2	Extract TOUGH2 fracture output for input to Items Blanks, Compare, and read_temp_vs_time_models
13	tough_extract_mtx.f	1	Attachment I	Sun, UNIX OS, Sun FORTRAN 77	SHT by TOUGH2	Extract TOUGH2 matrix output for input to Items Blanks, Compare, and read_temp_vs_time_models
14	mk_rect.f	1.0	10228-1.0-00	Sun SPARC, UNIX OS DEC ALPHA, UNIX OS	DST by TOUGH2	Rectangular mesh generation
15	mk_circ.f	1.0	10229-1.0-00	Sun SPARC, UNIX OS DEC ALPHA, UNIX OS	DST by TOUGH2	Radial mesh generation
16	merggrid.f	1.0	10230-1.0-00	Sun SPARC, UNIX OS DEC ALPHA, UNIX OS	DST by TOUGH2	Merges rectangular and radial meshes
17	mk_grav2d.f	1.0	10231-1.0-00	Sun SPARC, UNIX OS DEC ALPHA, UNIX OS	DST by TOUGH2	Creates a 2-D ⁹ vertical mesh from a horizontal 2-D mesh

Table 1. Computer Software and Routines (Continued)

Item No.	Software Name	Version	Software Tracking Number	Computer Platform, Operating System, Compiler	Simulation	Description
18	mk_3dsize.f	1.0	10232-1.0-00	Sun SPARC, UNIX OS DEC ALPHA, UNIX OS	DST by TOUGH2	3-D mesh from 2-D slices
19	mk_grav3d.f	1.0	10233-1.0-00	Sun SPARC, UNIX OS DEC ALPHA, UNIX OS	DST by TOUGH2	3-D ECM mesh for DST ^h
20	mk_gener.f	1.0	10234-1.0-00	Sun SPARC, UNIX OS DEC ALPHA, UNIX OS	DST by TOUGH2	Prepares GENER for TOUGH2
21	mk_observ.f	1.0	10235-1.0-00	Sun SPARC, UNIX OS DEC ALPHA, UNIX OS	DST by TOUGH2	Calculates observation elements for hydrology holes
22	mk_dual.f	1.0	10236-1.0-00	Sun SPARC, UNIX OS DEC ALPHA, UNIX OS	DST by TOUGH2	3-D dual permeability mesh generator from MESHMAKER output
23	mk_time*.f	1.0	10237-1.0-00	Sun SPARC, UNIX OS DEC ALPHA, UNIX OS	DST by TOUGH2	Processes time history of temperature data for a specified borehole
24	mk_obs3d.f	1.0	10238-1.0-00	Sun SPARC, UNIX OS DEC ALPHA, UNIX OS	DST by TOUGH2	Reads GASOBS.DAT file from TOUGH2 simulations and produces TECPLOT file for plotting
25	mk_tec*.f	1.0	10239-1.0-00	Sun SPARC, UNIX OS DEC ALPHA, UNIX OS	DST by TOUGH2	Processes temperature profile data for plotting
26	mk_cluster*.f	1.0	10240-1.0-00	Sun SPARC, UNIX OS DEC ALPHA, UNIX OS	DST by TOUGH2	Determines observation elements for a specified cluster of RTD ^h holes
27	mk_3dinter*.f	1.0	10241-1.0-00	Sun SPARC, UNIX OS DEC ALPHA, UNIX OS	DST by TOUGH2	Interpolates TOUGH2 simulated temperature data to all sensor locations of 26 RTD holes
28	mk_temp3d_all.f	1.0	10242-1.0-00	Sun SPARC, UNIX OS DEC ALPHA, UNIX OS	DST by TOUGH2	Prepares list of element name vs. temperature from TOUGH2 results

Table 1. Computer Software and Routines (Continued)

Item No.	Software Name	Version	Software Tracking Number	Computer Platform, Operating System, Compiler	Simulation	Description
29	mk_evaluate_*.f	1.0	10243-1.0-00	Sun SPARC, UNIX OS DEC ALPHA, UNIX OS	DST by TOUGH2	Computes statistical measures of goodness of temperature prediction by TOUGH2 simulations
30	2kgridv1.f	1.0	10244-1.0-00	Sun SPARC, UNIX OS DEC ALPHA, UNIX OS	DST by TOUGH2	Dual permeability mesh generator for AFM application
31	mk_ysw_element.f	1.0	10245-1.0-00	Sun SPARC, UNIX OS DEC ALPHA, UNIX OS	DST by TOUGH2	Modifies output from 2kgridv1.f
32	mk_ysw_connection.f	1.0	10246-1.0-00	Sun SPARC, UNIX OS DEC ALPHA, UNIX OS	DST by TOUGH2	Modifies output from 2kgridv1.f
33	mk_canister_power.f	1.0	10247-1.0-00	Sun SPARC, UNIX OS DEC ALPHA, UNIX OS	DST by TOUGH2	Computes the average of total canister heater power
34	mk_wing_power.f	1.0	10248-1.0-00	Sun SPARC, UNIX OS DEC ALPHA, UNIX OS	DST by TOUGH2	Computes the average of total wing heater power
35	mk_mesh_correct.f	1.0	10249-1.0-00	Sun SPARC, UNIX OS DEC ALPHA, UNIX OS	DST by TOUGH2	Removes duplicate connections from mesh files
36	mk_incon_3d_dual.f	1.0	10250-1.0-00	Sun SPARC, UNIX OS DEC ALPHA, UNIX OS	DST by TOUGH2	Creates INCON file for 3-D dual permeability applications
37	AMESH	1.0	10045-1.0-00	Sun SPARC, UNIX OS DEC ALPHA, UNIX OS	DST by TOUGH2	Mesh Generator
38	EXT	1.0	10047-1.0-00	Sun SPARC, UNIX OS DEC ALPHA, UNIX OS	DST by TOUGH2	Output Extraction
39	TOUGH2	1.4	10007-1.4-01	Sun SPARC, UNIX OS DEC ALPHA, UNIX OS	DST by TOUGH2	Multiphase, multicomponent modeling code for numerical solutions of non-isothermal flow and transport in porous media

Table 1. Computer Software and Routines (Continued)

Item No.	Software Name	Version	Software Tracking Number	Computer Platform, Operating System, Compiler	Simulation	Description
40	TOUGH2	1.3, Module EOS4 VI.0	10062-1.3MEOS4VI.0-00	Sun SPARC, UNIX OS DEC ALPHA, UNIX OS	DST (Sensitivity study) by TOUGH2	Multiphase, multicomponent modeling code for numerical solutions of non-isothermal flow and transport in porous media
41	NUFT	3.0.1s	10130-3.0.1s-00	Sun SPARC, UNIX OS	DST by NUFT LBT by NUFT	Multiphase, multicomponent modeling code for numerical solutions of non-isothermal flow and transport in porous media
42	RADPRO	3.22	10204-3.22-00	Sun SPARC, UNIX OS	DST by NUFT	Calculate radiation coefficients between grid blocks for a 2-D or 3-D grid
43	XTOOL	10.1	10208-10.1-00	Sun SPARC, UNIX OS	DST by NUFT LBT by NUFT	Graphical Display Routine for NUFT output
44	YMESH	1.53	10172-1.53-00	Sun SPARC, UNIX OS	DST by NUFT	NUFT mesh generator, assigns rock type and flow connectivity information to each mesh element using the stratigraphic database
45	MULTIDST	1.0	Attachment II	Sun SPARC UNIX OS	DST by NUFT	Software routine for computing error statistics for the DST TH ⁱ test
46	LBT_STATS	1.0	Attachment II	Sun SPARC UNIX OS	LBT by NUFT	Software routine for computing error statistics for LBT TH test
47	ROCK_SUN .m	1.0	Attachment II	Sun SPARC UNIX OS	DST by NUFT, LBT by NUFT	Matlab macro running under Matlab V5.3.0.10183 (R11) for converting measured material property sets (DTNs ^f LB990861233129.001 for drift scale and LB997141233129.001 for mountain scale) to NUFT Input Format

NOTE: ^a SHT (Single Heater Test) ^f 3-D (three-dimensional)
^b ECM (equivalent continuum model) ^g 2-D (two-dimensional)
^c Q (qualified) ^h DST (Drift Scale Test)
^d DKM (dual-permeability model) ⁱ RTD (resistance temperature detector)
^e AFM (active fracture model)

Table 2. Model Descriptions

Item	Thermal Test Models ^a	Acronym	Description	Dimension	Reference	Used in AMR Section
1	Single Heater Test – TOUGH2	SHT-TOUGH2	Heat and mass transfer in the SHT	3-D ^b	Sections 6.1.1 and 6.5.1 of this report	6.2.1, 6.3.1, 6.4.1
2	Drift Scale Test – TOUGH2	DST-TOUGH2	Heat and mass transfer in the DST	3-D	Sections 6.1.2 and 6.5.2 of this report	6.2.2, 6.3.2, 6.4.2
3	Drift Scale Test – NUFT	DST-NUFT	Heat and mass transfer in the DST	3-D	Sections 6.1.3 and 6.5.3 of this report	6.2.3, 6.3.3, 6.4.3
4	Large Block Test – NUFT	LBT-NUFT	Heat and mass transfer in the LBT	3-D	Sections 6.1.4 and 6.5.4 of this report	6.2.4, 6.3.4, 6.4.4
Item	Supporting Conceptual Models	Acronym	Description	Dimension	Reference	Used in AMR Section
5	Flow Model (Repository Scale)	FM	Mountain scale flow model basis used in TOUGH2 and NUFT. Supports Models 1-4 above	3-D	CRWMS 2000b, Table 1-1 and CRWMS 2000c	6
6	Drift Scale Test Thermal-Hydrological-Chemical Model	DST THCM	TOUGH2 model basis for thermal-hydrological calculations. Supports Model 1 and 2 above	2-D ^c in the reference although 3-D formulations support Models 1 and 2 above	CRWMS 2000b, Table 1-1 and CRWMS 2000d	6
7	Mountain-Scale Thermal-Hydrological Model	THM	TOUGH2 model basis for thermal-hydrological calculations. Supports Model 1 and 2 above	2-D and 3-D in the reference although 3-D formulations support Models 1 and 2 above	CRWMS 2000b, Table 1-1 and CRWMS 2000e	6
8	Multiscale Thermohydrologic Model	MSTHM	NUFT model basis for thermal-hydrological calculations. Supports Model 3 and 4 above	3-D	CRWMS 2000f	6

Note: ^a These models are implemented in software tracked by STNs (see Table 1). Input and output files of the models used directly in this AMR (items 1-4) are referenced by (see Table 9)

^b 3-D (three dimensional)

^c 2-D (two-dimensional)

4. INPUTS

4.1 DATA AND PARAMETERS

Table 3 presents the nomenclature of the property sets used for the simulations. Inputs for each of the four distinct numerical analyses (SHT [TOUGH2], DST [TOUGH2], DST [NUFT], LBT [NUFT]) are provided in Tables 4 through 9. Data tracking numbers (DTNs) are provided for both base case and sensitivity case TH properties.

Table 8 provides DTNs for all figures displaying data from the Technical Data Management System. Table 9 provides DTNs for input and output from the base case (DS) of each of the four analyses. The quality status for all input is documented in the DIRS database. The analyses of thermal testing reported in this AMR are not directly linked to a principal factor in the Repository Safety Strategy (CRWMS M&O 2000a) as per AP-3.15Q. The data and parameters used as input is considered appropriate because they are linked to laboratory and/or field measurements of TH behavior in the host rock unit for the three thermal tests.

Table 3. Nomenclature of Various Property Sets Used for the Model Studies

Case	Single Heater Test (TOUGH2)	Drift Scale Test (TOUGH2)	Drift Scale Test (NUFT)	Large Block Test (NUFT)
Base Case	Drift Scale Property Set (DS)	Drift Scale Property Set (DS/AFM-UZ99)	Drift Scale Property Set (DS)	Drift Scale Property Set (DS)
Sensitivity Cases	Total System Performance Assessment - Viability Assessment (TSPA-VA)	Alcove # 5 Property Set (DKM-TT99)	Mountain Scale Property Set (MS)	Mountain Scale Property Set (MS)
	Single Heater Test Median Bulk Permeability (Median kb)		Mountain Scale Local Thermal Conductivity (MSLK)	Mountain Scale Local Thermal Conductivity (MSLK)
			Conduction Only (CON) Data	Conduction Only (CON) Data
			N/A	Mountain Scale Higher Fracture Permeability (MSFP)

Table 4. Single Heater Test Model Inputs

Property	Base Case	Sensitivity Cases	
	DS ^{a,d}	TSPA -VA ^{b,e}	Median k_b ^{c,f}
Matrix permeability (m ²)	4.07 x 10 ⁻¹⁸	4.07 x 10 ⁻¹⁸	4.07 x 10 ⁻¹⁸
Bulk fracture permeability (m ²)	2.76 x 10 ⁻¹³	Vertical: 6.76 x 10 ⁻¹² Horizontal: 4.27 x 10 ⁻¹³	5.85 x 10 ⁻¹⁴
Matrix porosity	0.11	0.089	0.11
Fracture porosity	0.01	1.24 x 10 ⁻⁴	3.435 x 10 ⁻⁴
Matrix van Genuchten α_m (1/Pa)	3.86 x 10 ⁻⁶	1.02 x 10 ⁻⁶	6.4 x 10 ⁻⁷
Matrix van Genuchten β_m	0.291	0.322	0.3197
Matrix residual saturation	0.19	0.18	0.18
Fracture van Genuchten α_f (1/Pa)	5.16 x 10 ⁻⁴	8.36 x 10 ⁻⁴	3.139 x 10 ⁻⁴
Fracture van Genuchten β_f	0.608	0.492	0.667
Fracture residual saturation	0.01	0.01	0.03
Dry thermal conductivity W/(m·°C)	1.56	1.56	1.67
Wet thermal conductivity W/(m·°C)	2.33	2.33	2.1
Specific heat J/(kg·°C)	948	948	928
Grain density (kg/m ³)	2530	2530	2526
Tortuosity	0.7	0.7	0.7
Gamma parameter for the AFM (γ)	0.41	N/A	N/A
Fracture Frequency (m ⁻¹)	4.32	1.88	7.6
NOTES: ^a DTN:LB990861233129.001 ^b SNT05071897001.002, LB971212001254.001 ^c LB960500834244.001, CRWMS M&O 1999b ^d DS (drift scale thermal-hydrologic property set) ^e TSPA-VA (Total System Performance Assessment-Viability Assessment) ^f Median k_b (Single Heater Test median bulk permeability case)			
X_{fm} (Fracture-Matrix Interaction Parameter)	N/A	8 x 10 ⁻³	8 x 10 ⁻⁶
Initial liquid saturation (matrix) ^b	0.924	0.924	0.924
Initial liquid saturation (fracture) ^b	0.01435	0.114	0.196
Fracture to matrix connection area m ² /m ³	13.54	N/A	N/A
Top boundary temperature (°C)	25	25	25
Bottom boundary temperature (°C)	25.43	25.43	25.43
Bottom and top boundary gas-phase pressure, Pa (approximate)	8.7 x 10 ⁴	8.7 x 10 ⁴	8.7 x 10 ⁴
Heating duration (days) ¹	275	275	275
Heater length (m) ²	5	5	5
Heater stand-off (location into rock from the front face, m) ³	2	2	2
Average heater power for 275 days (watts) ⁴	3758	3841 ⁵	3841 ⁵

- NOTES: ¹ CRWMS M&O 1999b, p. 7-2.
² CRWMS M&O 1999b, p. 3-2.
³ CRWMS M&O 1999b, p. 3-3.
⁴ CRWMS M&O 1999b, p. 8-46.
⁵ CRWMS M&O 1997b, p. 3-2.

Table 5. Drift Scale Test Model Inputs (TOUGH2)

Property	Base Case ^{a,b}			Sensitivity Case ^b		
	DS/AFM-UZ99 ^c			DKM-TT99 ^d		
	Model Layer					
	tsw33	tsw34	tsw35	tsw33	tsw34	tsw35
Matrix permeability (m ²)	3.08 x 10 ⁻¹⁷	4.07 x 10 ⁻¹⁸	3.04 x 10 ⁻¹⁷	5.25 x 10 ⁻¹⁸	1.24 x 10 ⁻¹⁷	2.47 x 10 ⁻¹⁶
Bulk fracture permeability (m ²)	5.50 x 10 ⁻¹³	2.76 x 10 ⁻¹³	1.29 x 10 ⁻¹²	6.353 ₁₃ x 10 ⁻¹³	1.00 x 10 ⁻¹³	1.87 x 10 ⁻¹²
Matrix porosity	0.154	0.11	0.131	0.154	0.11	0.13
Fracture porosity	0.0066	0.0.10	0.011	0.000171	0.000263	0.000329
Matrix van Genuchten α_m (1/Pa)	2.13 x 10 ⁻⁵	3.86 x 10 ⁻⁶	6.44 x 10 ⁻⁶	1.06 x 10 ⁻⁵	2.25 x 10 ⁻⁶	2.82 x 10 ⁻⁶
Matrix van Genuchten β_m	0.298	0.291	0.236	0.243	0.247	0.207
Matrix residual saturation	0.12	0.19	0.12	0.06	0.18	0.13
Fracture van Genuchten α_f (1/Pa)	1.46 x 10 ⁻³	5.16 x 10 ⁻⁴	7.39 x 10 ⁻⁴	1.57 x 10 ⁻⁴	9.73 x 10 ⁻⁵	1.66 x 10 ⁻⁵
Fracture van Genuchten β_f	0.608	0.608	0.611	0.492	0.492	0.492
Fracture residual saturation	0.01	0.01	0.01	0.01	0.01	0.01
Dry thermal conduct W/(m ² ·C)	0.79	1.56	1.20	1.15	1.67	1.59
Wet thermal conduct W/(m ² ·C)	1.68	2.33	2.02	1.7	2.0	2.29
Specific heat (J/kg·C)	882	948	900	917	953	953
Grain density (kg/m ³)	2510	2530	2540	2510	2530	2540
Tortuosity	0.7	0.7	0.7	N/A	N/A	N/A
Gamma parameter for the active fracture model (γ)	0.41	0.41	0.41	N/A	N/A	N/A
Mean fracture frequency (m ⁻¹)	0.81	4.32	3.16	N/A	N/A	N/A
Fracture intensity (m/m ²) ^e	0.36	1.26	N/A	N/A	N/A	N/A
Aperture (m) ^e	2.3x10 ⁻⁴	9.8x10 ⁻⁵	1.5x10 ⁻⁴	N/A	N/A	N/A
Fracture-matrix interface area (m ² /m ³) ^e	4.44	13.54	9.68	N/A	N/A	N/A

NOTE: ^a The Base Case, DS/AFM-UZ99, tsw34 properties are the same as the DS property set for the SHT (Table 4).

^b DTN:LB990861233129.001

^c DS/AFM-UZ99 (drift scale thermal hydrological property set/active fracture model-unsaturated zone flow and transport 1999)

^d DKM-TT99 (dual-permeability model-thermal test 1999)

^e DTN: LB990501233129.001

Table 6. Drift Scale Test Model Inputs for tsw34 Unit (NUFT)

Property	Base Case ^{a,b}		Sensitivity Cases	
	DS ^e	MS ^{c,d,f}	MSLK ^{d,g}	CON ^{d,h}
Matrix permeability (m ²)	4.07 x 10 ⁻¹⁸	4.07 x 10 ⁻¹⁸	4.07 x 10 ⁻¹⁸	N/A
Bulk fracture permeability (m ²)	2.76 x 10 ⁻¹³	1.70 x 10 ⁻¹¹	1.70 x 10 ⁻¹¹	N/A
Matrix porosity	0.11	0.11	0.11	N/A
Fracture porosity	0.01	0.01	0.01	N/A
Matrix van Genuchten α_m (1/Pa)	3.86 x 10 ⁻⁶	3.86 x 10 ⁻⁶	3.86 x 10 ⁻⁶	N/A
Matrix van Genuchten β_m	0.291	0.291	0.291	N/A
Matrix residual saturation	0.19	0.19	0.19	N/A
Fracture van Genuchten α_f (1/Pa)	5.16 x 10 ⁻⁴	5.16 x 10 ⁻⁴	5.16 x 10 ⁻⁵	N/A
Fracture van Genuchten β_f	0.608	0.608	0.608	N/A
Fracture residual saturation	0.01	0.01	0.01	N/A
Dry thermal conductivity W/(m·°C)	1.56	1.56	1.67	2.33 for T < 100°C 1.56 for T ≥ 100°C
Wet thermal conductivity W/(m·°C)	2.33	2.33	2.00	N/A
Specific heat J/(kg·°C)	948	948	948	948 for T < 95°C or T ≥ 114°C, 4567.94 for 114 > T ≥ 95°C
Grain density (kg/m ³)	2530	2530	2530	2530
Tortuosity	0.7	0.7	N/A	N/A
Gamma parameter for the active fracture model (γ)	0.41	0.41	0.41	N/A
Fracture frequency (m ⁻¹)	4.32	4.32	N/A	N/A

NOTE: ^a The DS properties are the same as in the SHT (Table 4) and as the DS/AFM-UZ99 properties in the TOUGH2 analysis of the DST (Table 5).

^b DTN: LB990861233129.001

^c DTN: LB997141233129.001

^d DTN: LL000314404242.095

^e DS (drift scale thermal-hydrological property set)

^f MS (mountain scale thermal-hydrological property set)

^g MSLK (mountain scale with local thermal conductivity)

^h CON (conduction only)

Table 7. Large Block Test Model Inputs (NUFT)

Property	Base Case ^{a,b}	Sensitivity Cases			
	DS ^g	MS ^{c,d,l,h}	MSLK ^{d,i}	CON ^{d,j}	MSFP ^{d,k}
Matrix permeability (m ²)	4.07 × 10 ⁻¹⁸	4.07 × 10 ⁻¹⁸	4.07 × 10 ⁻¹⁸	N/A	4.07 × 10 ⁻¹⁸
Bulk fracture permeability (m ²)	2.76 × 10 ⁻¹³	1.70 × 10 ⁻¹¹	1.70 × 10 ⁻¹¹	N/A	1.70 × 10 ⁻¹¹
Matrix porosity	0.11	0.11	0.11	N/A	0.11
Fracture porosity	2.43 × 10 ⁻⁴	2.43 × 10 ⁻⁴	2.43 × 10 ⁻⁴	N/A	2.43 × 10 ⁻⁴
Matrix van Genuchten α _m (1/Pa)	3.86 × 10 ⁻⁶	3.86 × 10 ⁻⁶	3.86 × 10 ⁻⁶	N/A	3.86 × 10 ⁻⁶
Matrix van Genuchten β _m	0.291	0.291	0.291	N/A	0.291
Matrix residual saturation	0.19	0.19	0.19	N/A	0.19
Fracture van Genuchten α _f (1/Pa)	5.16 × 10 ⁻⁴	5.16 × 10 ⁻⁴	5.16 × 10 ⁻⁴	N/A	5.16 × 10 ⁻⁴
Fracture van Genuchten β _f	0.608	0.608	0.608	N/A	0.608
Fracture residual saturation	0.01	0.01	0.01	N/A	0.01
Dry thermal conductivity W/(m·°C)	1.56	1.56	1.67	1.67 x f(T)	1.56
Wet thermal conductivity W/(m·°C)	2.33	2.33	2.0	N/A	2.33
Specific heat J/(kg·°C)	948	948	948	948 x f(T)	948
Grain density (kg/m ³)	2530	2530	2530	2530	2530
Tortuosity	0.7	0.7	N/A	N/A	N/A
Gamma parameter for the actual fracture model (γ)	0.41	0.41	0.41	N/A	0.41
Fracture frequency (m ⁻¹)	4.32	4.32	N/A	N/A	N/A
Ultratemp thermal conductivity W/(m·°C)	0.095 ^e	0.095 ^d	0.095 ^d	N/A	0.095 ^d
Ultratemp specific heat J/(kg·°C)	1130 ^e	1130 ^d	1130 ^d	N/A	1130 ^d
Insulator thermal conductivity W/(m·°C) (after 125 days)	0.05 ^e	0.05 ^d	0.05 ^d	N/A	0.05 ^d
Initial liquid saturation ^f	75% ^e	75% ^d	75% ^d	N/A	75% ^d
Fracture to matrix interface area m ² /m ³	13.54 ^e	N/A	N/A	N/A	N/A

NOTE: ^a Except for fracture porosity, and initial saturation, the DS property set is the same as in the SHT (Table 4) and DST (NUFT, Table 6), and in the DS/AFM-UZ99 property set in the TOUGH2 analysis of the DST (Table 5).

^b DTN:LB990861233129.001

^c DTN:LB997141233129.001

^d DTN:LL000314304242.094

^e DTN:LL000321204242.092

^f Initial values are functions of infiltration rate and properties used in ambient calculations

^g DS (drift scale thermal-hydrological property set)

^h MS (mountain scale thermal-hydrological property set)

ⁱ MSLK (mountain scale with local thermal conductivity)

^j CON (conduction only)

^k MSFP (mountain scale with higher fracture permeability)

Table 8. Data Tracking Numbers of Source Data in Figures

Figure Number	DTN
2 through 6	MO0002ABBLSLDS.000
11	LL980918904244.074
13	TM000000000001.100 TM000000000001.104 TM000000000001.107 MO98METDATA110.000
14 through 17	SNF35110695001.008 SNF35110695001.009
19 through 24 44 through 50	MO9807DSTSET01.000 MO9810DSTSET02.000 MO9906DSTSET03.000
31 and 32	LB980120123142.004 LB980420123142.002 LB980715123142.002 LB981016123142.002 LB990630123142.001
33	LB990630123142.005 LB980120123142.006
52 through 56	LL990702704244.099
57 through 64	LL980409604244.059 LL990708904243.033
65, 67 and 68	LL970803004244.036
69	LL980913304244.072 LL980916704244.073
70 through 75	LL971204304244.047 LL970803004244.036
76	LL970803004244.036
77 through 80 and 94 through 99	LL970803004244.036
101	LL971204304244.047

Table 9. Data Tracking Numbers of Input/Output from Analyses

Test	Case	Data Tracking Number for Input and Output
Single Heater Test: (TOUGH2)	DS TSPA-VA Median K_b	SN0003T0872799.012 SN0003T0872799.010 SN0003T0872799.011
Drift Scale Test (TOUGH2)	DS/AFM-UZ99 DKM-TT99	LB000300123142.001 LB000300123142.001
Drift Scale Test (NUFT)	DS MS MSLK CON	LL000321704242.093 LL000314404242.095 LL000314404242.095 LL000314404242.095
Large Block Test (NUFT)	DS MS MSLK CON	LL000321204242.092 LL000314304242.094 LL000314304242.094 LL000314304242.094

4.2 CRITERIA

The Nuclear Regulatory Commission (NRC) has proposed regulatory standards (10 CFR 63 draft) for a potential repository at Yucca Mountain (see the Federal Register for February 22, 1999, 64 FR 8640). Until the final rulemaking for 10 CFR 63 is completed, the interim guidance provided by DOE (Dyer 1999) will be followed. The *Monitored Geologic Repository Requirements Document* (DOE 1999) (MGR-RD) will be revised to include any final regulatory standards. The standards in the *MGR-RD* then will be followed. The Environmental Protection Agency (EPA) has issued a draft of 40 CFR 197, *Environmental Radiation Protection Standards for Yucca Mountain, Nevada* (see the Federal Register for August 27, 1999, 64 FR 46976). Proposed standards in 40 CFR 197 will also be considered as directed by the Management and Operating Contractor management and DOE.

4.3 CODES AND STANDARDS

No specific formally established standards have been identified as applying to this analysis and modeling activity.

5. ASSUMPTIONS

The following assumptions are grouped into general and analyses-specific categories. The general assumptions apply to all four analyses discussed in Section 6, whereas the specific assumptions pertain to identified analyses in Section 6. Confirmation of the appropriateness of these assumptions is provided in Section 6 by comparing agreement between measured and simulated TH data. Based on the overall good agreement in these comparative analyses, it appears the following assumptions are valid.

5.1 GENERAL ASSUMPTIONS

5.1.1 Test Configuration

- A. Nominal dimensions and approximations are used throughout in developing the geometric model instead of exact dimensions of as-built configurations, such as the periphery of a drift.

Basis: The limited sensitivity of the models to slight variations from nominal dimensions does not merit the usage of exact dimensions. Note that modeling the heated drift (HD) cross-section as a square introduces some error in thermal simulations within about one meter of the drift periphery.

5.1.2 Boundary and Initial Conditions

- A. The initial conditions for the three-dimensional (3-D) computational domain for modeling each test were determined by first simulating groundwater infiltration into a one-dimensional (1-D) column having the required stratigraphy and allowing the column to equilibrate, while constraining the water saturation at a specified point in the column to a laboratory determined saturation.

Basis: Field measurements of the initial matrix water saturation distributions are not precise enough for the simulation. Equilibration to obtain initial conditions ensures that the simulation is driven by the added heat, rather than equilibration from an inappropriate initial condition.

5.1.3 Heat Source

- A. Spatial variation of heater power along the lengths of the individual heaters/heater arrays was not significant. DST wing heater arrays can be represented as two (inner and outer) smeared, spatially uniform, time-varying heat sources.

Basis: Only temperatures within one heater spacing of the wing heaters will be significantly misrepresented in the simulation due to this assumption, and the comparisons in this report do not focus on that small region of the test. Also, the total simulated power of electrical heat in the DST block is acceptably close to the actual power used. Axial variations are designed to be small.

5.1.4 Material Properties and Behavior

- A. If field measurements for rock mass properties are not available, then laboratory determined properties are used.

Basis: Best available properties were used in the absence of field measurements and are deemed to be adequate based on agreement between measured and simulated TH behavior discussed in Section 6.

B. The TH property sets used in this study are appropriate for simulating thermally-perturbed tests even though they were derived from ambient-thermal conditions.

Basis: Specific property data for elevated temperatures are not available. Ambient temperature properties are appropriate for much of the test block, where the temperature remains well below boiling. Also, many parameters in the TH property sets do not have significant temperature dependency. Temperature sensitivity to thermal and hydrological property variations is not thought to be strong. This assumption is considered adequate based on agreement between measured and simulated TH behavior discussed in Section 6.

C. Material property variations (due to the creation of a near-field damage zone adjacent to the HD wall), water drainage, and change in the water saturation distribution at the HD wall during construction are not significant for thermal performance.

Basis: Temperature comparisons include locations beyond the described region affected by construction and other factors cited. This assumption is considered adequate based on agreement between measured and simulated TH behavior discussed in Section 6.

D. Fracture-matrix interactions follow the AFM, (Liu et al. 1998, pp. 2635 to 2636).

Basis: If flow occurs through all the connected fractures and is uniformly distributed over the entire fracture area, the entire fracture area is available for coupling of flow between the matrix and fractures, implying relatively large fracture-matrix interactions (Bandurraga and Bodvarsson 1997). However, experimental evidence exists that fractures have limited interaction with the surrounding rock matrix at Yucca Mountain. Since the degree of fracture-matrix coupling can significantly affect flow and transport in the UZ, the reduction of fracture-matrix interaction from the full interface area must be considered in models describing flow and transport. Bandurraga and Bodvarsson (1997, p. 6-23) proposed a fracture-matrix interaction reduction factor to reduce the magnitude of fracture-matrix interaction flux. The three factor formulations considered were: (1) constant, (2) proportional to a power function of liquid saturation, and (3) equal to the liquid-phase relative permeability. Implementation of a constant fracture-matrix interaction reduction factor gives rise to acceptable matches between case-specific simulation results and the observed matrix water saturation and water-potential data. However, the active fracture parameter used is empirical and not rigorously derived.

Liu et al. (1998) proposed an AFM formulation for fracture-matrix interactions that is physically based. In this model, fracture-matrix interaction is based on the hypothesis that only a limited fraction of the connected fractures actively conduct water in the UZ of Yucca Mountain. Detailed discussions regarding how the "activity" of the fractures affects flow and transport at Yucca Mountain can be found in Liu et al (1998).

E. Liquid- and gas-phase flow in a partially saturated medium is governed by key hydrological parameters such as permeability, and by characteristic curves that relate the relative permeability and capillary suction pressure to the liquid saturation. Though

the characteristic curves may be fitted to various analytical expressions, additional relationships (Brooks and Corey 1966 and van Genuchten 1980) were selected for the work presented in this analysis report. For modeling the thermal tests, following the UZ Flow and Transport Model, the van Genuchten relations for the dependence of the capillary pressure and the liquid-phase relative permeability on liquid-phase saturations, in both the fracture and matrix continua, were adopted. The gas-phase relative permeability is assumed to follow the modified Brooks-Corey (van Genuchten 1980) relationships. Furthermore, the dependence of the capillary pressure and the liquid-phase relative permeability on liquid-phase saturations has been corrected to reflect flow in an active fracture continuum (Liu et al. 1998).

Basis: Widely employed in the literature. Consistent with ambient temperature UZ Flow and Transport Model (CRWMS M&O 2000b). This assumption is considered adequate based on agreement between measured and simulated TH behavior discussed in Section 6.

F. Simulation of complex, TH behavior is not warranted for the purposes of this study.

Basis: Simplification of complex, difficult-to-measure, TH behavior is typically done and is especially applicable in this study, which focuses on comparative differences between the TH property sets considered.

5.2 SINGLE HEATER TEST ASSUMPTIONS

A. An idealized SHT model domain described by Francis et al. (1997) is adequate to model the SHT.

Basis: The “adiabatic” boundaries are far enough from the heater that they may be treated as no heat flow boundaries during the duration of the test. The “tunnel condition” boundaries are locations of imposed temperatures.

B. The drifts around this SHT model domain are maintained at a constant temperature of 25°C and a relative humidity (RH) of 100 percent.

Basis: The temperature was imposed on the test. A film insulation prevented mass transfer to the tunnel air, providing a high humidity at the rock surface. Spatial fluctuations in the ambient temperature and RH are expected to be less than 10 percent in the simulated region of interest.

C. The temperature profile is symmetric to a vertical plane through the heater axis.

Basis: Boundary conditions are symmetric. Both sides of the plane are in the same stratigraphic unit. Measured temperatures on both sides of the heater can be compared to the simulation.

D. The SHT model domain is located in a region of the tsw34 that can be represented by a homogeneous layer of rock matrix and fractures having properties stated in Table 4.

Basis: The properties in Table 4 are the best available properties for homogeneous rock matrix and fractures. Nonhomogeneous rock properties are difficult to measure.

E. The DKM, with or without the AFM, can be applied in the SHT model analysis developed to represent heat and mass flow within and between the matrix and fracture continua in the SHT model domain. A constant area reduction factor between matrix and fracture is used in the dual permeability analysis of the viability assessment property set and the median bulk permeability (Median k_b) property set. The DKM/AFM is used in the DS analysis. Both are continuum flow models. Implied in this assumption is that the matrix blocks in the dual permeability representation are not further discretized. See discussion in Ho (1997) and Liu et al. (1998). Also, the statistical reduction of matrix and fracture interaction is sufficient without identification of discrete locations of reduced interaction.

Basis: The DKM simulates TH behavior better than alternate models including the effective continuum model.

5.3 DRIFT SCALE TEST ASSUMPTIONS

The following assumptions for the DST can be better understood by reviewing the configuration described in the design report (CRWMS M&O 1997b).

5.3.1 TOUGH2 Simulations

A. The model boundaries (excluding drift walls) are zero heat and mass transfer boundaries.

Basis: These conditions were imposed on the test.

5.3.2 NUFT Simulations

A. The conduction, convection, and radiation transport of heat from the floor heaters to the drift walls can be represented by an effective porous (conduction and convection only) medium.

Basis: This approximation is accurate in an average (over the drift walls) sense because radiant heat transfer that accounts for 80-90 percent of the total heat transfer is relatively uniform. However, it can result in significant errors near the apex of the drift because the heat transferred by natural convection of air becomes focused and confined to a few locations at high Rayleigh numbers (convective heat transfer coefficient). Consequently, at the apex of the drift the heat flux can be in error by as much as 35 percent under prevailing conditions. By selecting the effective thermal and hydraulic properties of the porous medium as dependent on the temperature difference between these surfaces, this error can be reduced when using the effective porous medium approximation. However, such a selection of the thermal properties of the pseudo-porous medium was not made. The calculated temperatures at the apex of the drift are artificially high partly because of this modeling assumption. While the calculated local temperatures are affected significantly by this assumption, the overall

temperature and saturation distributions in the rock will not be significantly affected because the average and total heat loads are accurately represented, and the rock conduction smoothes out temperature variations.

B. Vapor and gas transport along leaking wing heater boreholes is not significant.

Basis: Simulation of this mass transport cannot be justified in these analyses because it will not provide much additional accuracy in simulating the response in the bulk of the DST block.

C. The approximately circular HD geometry was represented in these simulations by a square HD equal in cross-sectional area to the circular drift.

Basis: This approximation will cause differences between the simulated and measured temperatures very near to the drift wall, but will not affect the overall temperature and saturation distributions in the DST due to conduction in the rock. A more refined calculation using an accurate stepped approximation to the circular geometry of the drift wall has been performed with greatly increased computational effort for repository performance assessment.

5.4 LARGE BLOCK TEST ASSUMPTIONS

The following assumptions for the DST can be better understood by reviewing the configuration described by Wilder et al. (1997).

A. A fully 3-D quarter-symmetry model can represent the entire large block.

Basis: The excavated block is nearly symmetric about the two vertical mid-planes and all of the block is within the same stratigraphic unit. Refer to Section 6.1.4.2 that presents a schematic of the block, highlighting the modeled section and showing the locations of the five heater boreholes. This assumption is considered adequate based on agreement between measured and simulated TH behavior discussed in Section 6.

B. Homogeneous fracture and matrix properties adequately represent the modeled block.

Basis: More refined data are not available and would be difficult to measure. Additional complexity in fracture and matrix properties is not warranted because non-homogeneous properties are not typically used and are not needed to evaluate the comparative differences in property sets.

C. The power history for each heater borehole in the model can be represented by the average history for the five boreholes. Heat is delivered uniformly along the length of each heater.

Basis: The five heater power histories measured in the block were almost identical, and each heater was designed to deliver heat uniformly along its length. The total heat is accurate, and thermal condition in the rock smoothes out variations between heaters.

D. The upper boundary variables are established based on an average barometric pressure of 8.87×10^4 Pa (DTNs: TM000000000001.100, TM000000000001.104, TM000000000001.107, MO98METDATA110.000) and a RH that yields an initial liquid-phase saturation of 0.75.

Basis: The initial liquid-phase saturation is based on neutron probe measurements along boreholes in the block (DTNs: LL971204304244.047, LL980919304244.075), which are considered representative parts of the entire LBT block (above ground level). The pressure was measured.

E. Monthly averaged ambient air temperatures at nearby Site 8 for 1997 (DTNs: TM000000000001.100, TM000000000001.104, TM000000000001.107, MO98METDATA110.000) can be used for time-varying temperatures of the atmosphere around the block. Air temperatures for times later than 1997 were assumed to be identical to the values for the corresponding month in 1997.

Basis: Site 8 is a Bureau of Land Management meteorology monitoring site at Fran Ridge, within Area 25 of the Nevada Test Site, located close to the LBT.

F. Impervious (to mass transfer) insulation at the sides of the block that permit some heat loss to the atmosphere through the sides represents the test. Heat and moisture losses are allowed through the top surface of the block.

Basis: These represent actual test conditions. Heat flow through the insulation is measured by temperature sensors. The top of the block had an imposed test temperature. Mass transfer from the top can be calculated from atmospheric conditions.

G. A 1-D initialization calculation can establish the initial liquid-phase saturation, temperature, and gas pressure profiles used for 3-D calculations.

Basis: The variations are small at this scale, and gravity is a key influence.

H. The upper boundary temperature for initialization is 16.3°C .

Basis: This was the mean atmospheric temperature measured at Site 8 in 1997.

I. The lower boundary, 370 m below the base of the block, is set at 25°C .

Basis: This gives a geothermal gradient of about $0.024^\circ\text{C}/\text{m}$, which is typical of the area.

J. Hydraulic and thermal properties of the subsurface tsw34 modeling layer (DTN: LB990861233129.001) can represent the LBT.

Basis: The hydrogeologic unit of the LBT block is in the tsw34 modeling layer of the site-scale UZ flow model.

6. ANALYSIS/MODEL

The four distinct sets of numerical analyses use either the TOUGH2 or NUFT codes because the respective mathematical models of TH behavior are similar and both codes have been used extensively in numerical simulations of thermal tests. The evaluation of the DS and other sensitivity sets of properties is discussed in the following subsections. Basically, the evaluation relies on the assessment of the agreement between measured and simulated TH data. The model used in this analysis simulates the TH behavior in thermally-perturbed rock. The rationale for the use of TH models is that TH behavior is an important coupled process in the three Yucca Mountain thermal tests considered in this analysis.

6.1 NUMERICAL ANALYSES

As presented in Section 1, the primary purpose of this study is to evaluate the DS thermal and hydrological property sets. This evaluation is carried out by comparing field measurements with numerical simulations of three thermal tests: SHT, DST, and LBT. The simulations use alternative property sets to facilitate selection of a set for design and performance assessment.

6.1.1 Single Heater Test

An analysis of SHT TH models and experimental measurements is performed for evaluating UZ drift scale hydrologic and thermal properties as well as calibration of the conceptual models. Property evaluation is necessary to assess the ability of a specified hydrologic property set, calibrated only for ambient conditions, such as borehole saturations, to reproduce the processes caused by a thermal perturbation. Specifically, the importance of this verification is to ensure that the hydrologic properties used by TSPA ambient models (e.g., flow field models) can also be used by the TSPA models that incorporate the thermal perturbation caused by repository heating.

The TSPA models that contain repository heating provide the in-drift thermodynamic environment (e.g., temperature and RH) and flow driven processes (e.g., rate of thermally enhanced fracture flow) in the host rock above the drift wall that influence the seepage into the emplacement drift. These are transient heat-driven flow processes and hence the properties (and conceptual flow models) used to estimate them should be compared to experimentally determined TH results at a variety of different scales. In this case, the SHT field test is considered a small to intermediate sized field test. Other scale tests will be considered in this AMR. With the measured temperature and liquid saturation data obtained from a known thermal perturbation (e.g., SHT results), it is possible to assess if the hydrologic properties developed for ambient conditions alone can also reproduce the extent of the transient flow processes driven by a thermal perturbation.

In addition to the properties utilized in a TH model, of equal importance is the conceptual model used to estimate how the trends of the processes initiated by a thermal perturbation occur. It has been found, in general, that the DKM better represents the trends of the processes occurring in the host rock during a thermal perturbation than do the equivalent continuum model(s) (ECM) using the same hydrologic properties (*Total System Performance Assessment-Viability Assessment (TSPA-VA) Analyses Technical Basis Document*, CRWMS M&O 1998c,

Figures 3-27 and 3-28). The trends resulting from heating include host rock temperature increases up to and above the boiling point, fast path movement of water away from the heat source as it is allowed to enter and drain through the fractures, and the rate of heat driven redistribution of water in the form of vapor to different regions in the model. In previous TH simulations of the SHT (CRWMS M&O 1999b, Section 8.8.2.1), the ECM model results are contrary to experimental measured results, and therefore it is not the appropriate flow model to use for the SHT analysis.

Considering these trends, alternate forms of the DKM can be used to make model comparisons to measured values. Previous versions of the DKM assumed that all connected fractures are hydraulically active with the entire geometric fracture-matrix connection area available for flow. To achieve preferential flow through fractures (or fingering), the interfacial area between matrix and fractures is reduced by an arbitrary factor less than one such that non-equilibrium liquid flows will tend to remain in the fractures only (Ho 1997, p. 403). It is through this reduction parameter that this conceptualized DKM results in only a fraction of the fractures being hydraulically active (e.g., preferential fracture surface wetting, flow channeling).

In the current analysis, the active fracture DKM is utilized for fracture-fracture, matrix-matrix, and fraction-matrix flow. In this conceptual flow model, not all connected fractures are hydraulically active. As in the DKM model with an area factor reduction, this model also presumes that water movement is gravity-dominated, non-equilibrium, preferential flow in the fracture domain. The conceptual measure of hydraulic activity is given by the gamma (γ) parameter in the AFM. This parameter along with the effective water saturation is used to determine the fracture-matrix interface reduction factor (Liu et al. 1998, p. 2638, Eq. 18). The classical DKM with no fracture-matrix interface reduction factor corresponds to a gamma value of zero in the AFM. (Ho 1997). A DKM that uses a non-zero fracture-matrix interface reduction factor corresponds to an AFM with non-zero gamma, but the AFM formulation has more physical basis than the more arbitrary fracture-matrix interface reduction factors used in some DKM formulations.

In the fracture continuum, the gamma parameter for the AFM operates on the characteristic curves of capillary pressure and relative permeability; a lower capillary pressure and higher liquid relative permeability result from gamma greater than zero. The gamma parameter for the AFM, much like the fracture van Genuchten alpha parameter, is calibrated to reproduce the ambient measured borehole saturations. Therefore, an assessment is required as to the ability of this parameter, derived for ambient conditions, to reproduce the processes inherent in a transient thermal perturbation.

Sections 6.2.1 and 6.3.1 provide the details of the hydrologic property sets (past and present), application of the conceptual flow model, model equilibration methods, SHT inputs, and other details used to make detailed temperature prediction comparisons to measured data from the SHT. The SHT model analysis is a two step process. First, the entire 3-D model domain is equilibrated to local ambient conditions. After the model domain has been equilibrated, heating is applied for 275 days to the model domain that contains appropriate initial and boundary conditions.

6.1.1.1 Ambient Conditions

Table 4 provides the hydrologic and thermal input values used in the equilibration process for the SHT model with the DS property set. A single 1-D column is extracted from the working 3-D SHT model domain to initiate the ambient equilibration process. In this initial step, the bottom most boundary element in the 1-D column is fixed at the initial fracture and matrix liquid saturations given in Table 4 as obtained from the site-scale model. The top boundary element is then supplied with a water infiltration input. Since the site-scale model uses the MS properties rather than the DS properties used in this analysis, the infiltration rate used in the site-scale model at the thermal test location (~ 0.6 mm/yr.) had to be greatly reduced in the 1-D equilibrium model to ensure that the matrix elements in the 1-D column did not saturate to values greater than 0.924.

Although the matrix elements are not allowed to saturate above the value given in Table 4, the fractures elsewhere in the column are allowed to increase above the value indicated in Table 4 (due to hydrologic property set differences). The input infiltration rate for this 1-D column model is 0.0022 mm/yr. With these boundary conditions, the 1-D column is equilibrated until the inflow at the top of the model is equal to outflow at the bottom (approximately 1×10^6 years). This initial step in the ambient equilibration provides the fracture and matrix saturation distribution in the 1-D column. The next step in the initialization process is to enforce the geothermal and pressure gradients on the 1-D column.

This step in the initialization process is done by fixing the top and bottom boundaries of the 1-D column with the liquid saturations in the fractures and matrix obtained from the previously described infiltration equilibration run. The temperature and gas-phase pressures at the top and bottom boundaries (refer to Table 4) are fixed based on a representative geothermal gradient and pneumo-static gas-phase pressure gradient (top pressure 8.68×10^4 Pa, which is the value obtained from the infiltration initialization run described above). With the infiltration rate removed, the 1-D column is re-equilibrated to include the geothermal gradient. This simulation is carried out to 1×10^6 years as in the infiltration rate equilibration run described above.

The 1-D ambient initialization process results in equilibrated values of the matrix and fracture liquid saturations, temperature, and gas-phase pressure for the 1-D column extracted from the 3-D model. This fixed (top and bottom) boundary information from the 1-D equilibration run is then applied in the 3-D model for a final ambient equilibration of the full 3-D model domain. This equilibration is also carried out to 1×10^6 years. This sequence of steps resulted in equilibrated initial conditions for the 3-D heating simulation used to make predictions against the measured data at selected thermocouple locations.

6.1.1.2 Heating Conditions

Table 4 also provides the input values used in the heating process for the SHT model analysis. The initial conditions for the liquid saturation, temperature, and gas-phase pressure developed in Section 6.1.1.1 are inputs to the heating simulation. As indicated in Section 5.2, at those locations far removed from the heater, the ambient conditions (temperature, liquid saturation, gas-phase pressure) remain unchanged as a result of heat input during the duration of the test. Specifically, the equilibrated values remain unchanged during the 275-day heating simulation.

The remaining step in the heating run is to include different material elements inclusive of appropriate bounding materials (e.g., insulation on the rock faces) and the heating elements. Consequently, the heating mesh file is slightly modified from the ambient mesh in that it is equipped with an insulation layer on the front and side faces, the ambient air elements that represent the access tunnels adjacent to the insulation layers, and the heater elements themselves. The effective heater power input to the SHT model domain is 3.758 kW. Since the SHT model includes a symmetry boundary at the heater vertical center plane, only one half of the total heater output is input directly to the model heater elements. To resolve the gradients in temperature and liquid saturation near the heater, a refined rectangular mesh (the same used for both ambient and heating conditions) occurs in the model domain at a 2 m radius from the heater element centerline. Since a majority of the heat flow occurs radially outward, radial symmetry is maintained within the refined region and beyond out to about 4 m radially. The mesh is gradually coarsened starting from the refined 2-m radial distance out to the boundaries of the model domain. The overall model domain contains 12,600 primary volume elements in each (fracture and matrix) continuum.

The results of a 275-day heating simulation (along with approximately one week of cooling) are shown in Section 6.2.1 for the DS property set case (e.g., the base case property set for the TH models used in TSPA-SR). A comparison of the DS property set case to the locally measured Median k_b and the base case hydrologic property set used in Total System Performance Assessment for the Viability Assessment (TSPA-VA) is shown in Section 6.3.1.

6.1.2 Drift Scale Test - TOUGH2 Simulations

Two separate analyses of the DST were conducted in which variations included software (TOUGH2 and NUFT) and conceptual models.

6.1.2.1 Test Geometry and 3-D Numerical Mesh

For the TOUGH2 simulation of the DST (Figure 4), a 3-D numerical grid is generated separately for the matrix and fracture continua. The 3-D matrix continuum numerical grid designed for the DST was developed to follow the as-built test configuration (DTN: MO0002ABBLSLDS.000), allowing for efficient simulation of the DST TH conditions. The origin of the 3-D coordinate system is located on the hot side of the bulkhead, in the center of the drift. The positive x-axis points horizontally, approximately towards the north (transverse to the HD away from the observation drift [OD]); the positive y-axis points horizontally along the HD, approximately towards the west; and the positive z-direction points vertically upward from the origin.

The symmetry of the DST heater configuration allows the construction of the 3-D numerical grid as a series of vertical xz sections orthogonal to the HD centerline. In each xz vertical section, the discretization is extremely refined around the HD and wing heaters, where the temperature gradient is expected to be large, whereas the local mesh refinement is gradually reduced farther away from the heaters. The complete 3-D DST grid was created by appropriately extending these vertical two-dimensional (2-D) planes into the third dimension and merging them together. The entire 3-D matrix continuum grid of the DST comprises 24 such 2-D vertical planes.

Figure 1 shows the 2-D vertical grid in a typical xz cross section intersecting the HD at $y \sim 10$ m from the bulkhead (i.e., approximately in the plane of hydrology boreholes 57 through 61). As described earlier in Section 5.3.1, the model layers corresponding to three geological units of the Topopah Spring unit, the Upper (tsw33/Ttpul) and Lower (tsw35/Ttpll) Lithophysal, and the Middle Nonlithophysal (tsw34/Ttpmn) unit, which hosts the DST. The grid was designed such that the assumed interfaces between layers are represented by gridblock interfaces (i.e., interfaces are maintained at $z = +14.0$ m and $z = -26.68$ m).

Figure 2 shows the same cross section in a detailed view of the rock areas adjacent to the HD and the wing heaters. The figure also depicts the as-built location of five hydrology boreholes 57 through 61, which are collared on the north wall of the OD. The solid symbols indicate the as-built location of temperature sensors (DTN: MO0002ABBLSLDS.000). Figure 3 presents a detailed view depicting the configuration of boreholes 137 through 144, which form a cluster oriented radially outward from the HD. This vertical plane intersects the long axis of the drift at $y \sim 12$ m. Temperature sensors are grouted in each of these boreholes at approximately 0.3 m spacing.

The HD, 47.5 m long in the y-direction, is discretized into ten drift elements along the y direction (i.e., one drift element for each of the ten 2-D vertical segments that make up the heated length of the drift). The concrete invert in the drift is also explicitly modeled. Since heat radiation is the heat-transfer mechanism from the floor heaters to the HD, and since less effective conduction is the heat-transfer mechanism in the concrete invert, the presence of the concrete invert tends to retard the temperature build-up in the rock below the HD. A comparison of the simulated temperature in the rock mass was made (Tsang et al. 1998, pp. 2-12 and 2-33) a few meters below the HD for the first few months of heating for test configurations with and without the concrete invert. This showed that the simulated temperature without the invert exceeded the measured temperature by about 10°C , while the match between the simulated and measured temperatures for the configuration including the concrete invert was within 1°C . Therefore, discrete elements are included in the lower parts of the HD to represent the concrete invert with a maximum thickness of 1.2 m. The concrete is assigned properties similar to the surrounding rock, with the exception of thermal conductivity. For thermal conductivity in the concrete, an average value of $1.7 \text{ W/m}^{\circ}\text{C}$ (Liley et al. 1984, p. 3-260) is used.

The wing heaters are represented by horizontal smeared-out heat sources on either side of the drift. In the vertical direction, the wing heater source is distributed over a thickness of 0.5 m, extending from $z = -0.5$ m to $z = 0.0$ m, thus fixing the center of the distributed heat source at the vertical center of the 9.6-cm-diameter wing heater boreholes at -0.25 m, conforming to as-built configurations. Each of the 50 wing heaters consists of two 4.44-m long heating elements. The first element in each wing heater starts about 1.67 m from the HD wall, whereas the second element ends at about 11.21 m from the drift wall. There is a gap of about 0.66 m between the two wing heater elements.

The fracture continuum grid to be superimposed on the matrix continuum numerical grid was generated much the same way as described above for the rock mass. No separate fracture continuum grids were needed for the HD and the OD. Implementation of the active fracture conceptual model also requires parameters governing the fracture geometry (for example,

fracture-matrix interface area, mean fracture frequency, and fracture porosity). These input parameters are given in DTN: LB990501233129.001 as shown in Table 5.

The 3-D numerical grid for TOUGH2 simulations of the DST has 91,579 elements and 348,437 connections among them.

6.1.2.2 Heating Power

Total heating power values in the numerical simulations presented herein reflect the average of the actual heating power from the start of heating on December 3, 1997, through May 31, 1999. The quality measurements of the total heating power are given in DTNs: MO9807DSTSET01.000, MO9810DSTSET02.000, and MO9906DSTSET03.000. The average total power of the floor heaters over the period mentioned above was 52.1 kW. The average total power of the wing heaters for the same time period was 132.1 kW. The ratio of the heating powers of the outer and inner wing heaters is taken as 1.32 as given in DTN: MO9912SEPDOIHP.000.

6.1.2.3 Initial and Boundary Conditions

Initial conditions for the DST model are developed from a vertical column simulation in 1-D, using the calibrated DS properties derived for the base-case infiltration scenario in the UZ flow and transport site scale model (DTN: LB990861233129.001). Simulation results obtained with this vertical column model (vertical profiles of initial liquid saturation, pressure, and temperature) are mapped to the 3-D DST numerical model grid. The top and bottom boundaries of the DST domain ($z = +99.39$ m and -156.76 m, respectively) are given boundary conditions such that the equilibrated values of pressure, saturation, and temperature from the 1-D column are kept constant throughout the simulation period. To correct for inaccuracies that might occur from mapping of 1-D equilibrated pressure, saturation and temperature values to the complex 3-D grid, initialization runs with the 3-D grid are performed for a long time before turning on heat, to ensure that an equilibrium condition is achieved. In summary, the matrix liquid saturations for regions near the HD are approximately 95 percent for the two property sets (DS/active fracture model-unsaturated zone flow and transport 1999 [AFM-UZ99] and dual-permeability model thermal test 1999 [DKM-TT99]) based on initialization and inverse modeling.

The OD, the Connecting Drift (CD), and the cool section of the HD are given constant pressure, temperature, and saturation boundary conditions. The nonheated section of the HD and the walls of the CD and OD nearer the HD are insulated, but allowing for moisture to escape from the test block in the form of both liquid water and vapor.

6.1.2.4 Thermal Bulkhead

Pressure readings from a gauge located inside the HD registered no pressure build up from heating. Barometric-pressure fluctuations were also tracked in the OD. This indicated that the fractures or the insulated bulkhead separating the heated and unheated section of the HD was acting as an open boundary for gas flow. The numerical model for DST utilized a bulkhead boundary condition that conformed to the actual test conditions. A connection is introduced between the grid blocks representing the hot side and the cool side of the HD, and the bulkhead

is given a boundary condition of constant pressure, temperature, and saturation, thus allowing vapor to leave the HD and heat transfer by convection. On the other hand, the bulkhead is given zero thermal conductivity preventing heat transfer at the bulkhead by conduction.

6.1.2.5 Heat Transfer in the Heated Drift

Heat transfer from the nine floor heaters in the HD to the drift wall takes place by radiation. In the TOUGH2 3-D numerical model, the heat radiation is not modeled explicitly; rather, the heat is directly applied at the drift wall. Prior to start of heating, predictive simulations were carried out for the DST. At that time, it was not known how effective the radiative heat exchange would be. Consequently, two bounding studies were performed. One implemented a thermal conductivity tangential to the drift wall that was several orders of magnitude higher than the rock thermal conductivity; the other assigned the rock thermal conductivity for both components, orthogonal and tangential to the HD wall. The former conceptual model implied 100 percent effective radiative heat exchange and gave rise to temperatures that were well equilibrated, both around and along the HD wall. The latter conceptual model produced simulated temperatures at the spring-line of the HD (the wing heater horizon) that was higher than that at the crown by over 25°C and a temperature difference of as much as 40°C between the middle and the end(s) of the HD (Birkholzer and Tsang 1997, pp. F-13 and F-14). Early-time temperature data of the rock surface in the HD had indicated limited temperature variation on the drift wall. Therefore, in the model, the heat-radiation scenario is adopted in which the temperature is well equilibrated both around and along the drift wall.

6.1.2.6 Rock Properties

The rock property set employed to numerically simulate the thermal-hydrology at the DST with DST has its origin in the UZ Drift Scale Flow/Transport model (see Table 5). This property set (DTN: LB990861233129.001) is derived from calibration runs for ambient conditions. In these calibration runs, the hydrological properties of the various stratigraphic layers of Yucca Mountain, from surface to water table, were used as calibration parameters to fit measured data from various surface-based boreholes. These measured data included temperature profiles, liquid-saturation profiles, matrix potential profiles, and air-permeability profiles (Bandurraga and Bodvarsson 1999). This UZ drift scale property set (DS) also implemented the AFM for the fracture-matrix interaction. Note that the dry and wet thermal conductivities for the fractures were determined by multiplying the fracture porosity by the respective dry and wet thermal conductivities for the matrix.

6.1.3 Drift Scale Test - NUFT Simulations

6.1.3.1 Model Geometry

The DST was performed in a drift excavated in the tsw34 modeling layer of the stratigraphic sequence beneath Yucca Mountain. The configuration of the DST, shown in Figures 4, 5 and 6, includes the following principal components:

- A heated section of the HD containing nine in-floor heaters
- An unheated section of the HD

- A thermal bulkhead separating the heated and unheated HD sections
- An outer wing heater array located in the outer part of 50 horizontal boreholes drilled normal to the axis of the HD
- An inner wing heater array located in the inner part of the 50 horizontal boreholes
- A CD intersecting normal to the unheated section of the HD
- An OD parallel to the HD and connected to the CD
- A plate-loading niche.

Previous NUFT calculations of the DST included the CD and OD (Buscheck et al. 1997). A sensitivity study of model geometry (Buscheck et al. 1997) showed that thermal behavior around the immediate DST area is insensitive to the influence of the CD and OD. For this reason, those two features are not included in the current TH model.

All of the TH-model calculations described here were performed in three spatial dimensions to capture the effects of spatial variations in test geometry, material properties of the rock, and in the placement and heat generation rates of the heating elements. In particular, the fully 3-D simulation was expected to accurately capture the end-effects at both ends of the HD. The idealized computational domain used for computing the TH response of the DST is shown in Figure 7.

The origin of the field coordinate frame (x,y,z) in the xz-plane is located at the center of the bulkhead that separates the heated and unheated sections of the HD. The Y-axis extends from its origin on the unheated side of the thermal bulkhead through the bulkhead towards the blind end of the HD. This coordinate origin is located 1052.86 m above sea level at an elevation that is 267.5 m below the ground surface, and 321.5 m above the water table. The computational mesh extends from x=-286.4m to +293.6m, y=-294.5m to + 316.5m, and z= -267.5.m to +321.5 m.

The NUFT code utilized a numerical mesh that extended from the tsw34 model layer, within which the drift was located, upwards to the ground surface and down to the groundwater table. In contrast, the TOUGH2 code utilized a numerical mesh that spanned only the tsw34 model layer and the adjoining tsw33 and tsw35 model layers. All NUFT code simulations were performed using a DKM model with an active fracture sub-model whereas the TOUGH2 simulations were carried out with DKM models with and without the active fracture sub-model. The NUFT and TOUGH2 codes utilized the same active fracture property set for the tsw34 model layer. Because the differences between the different property sets in the NUFT simulations are primarily in the properties of the tsw34 model layer, only the data for this layer are given in Table 6 for the NUFT model.

6.1.3.2 Measurement Systems

The DST boreholes contain a variety of instruments to record the thermal, hydrological, mechanical and chemical responses of the DST during eight years of heating and cooling. These boreholes are identified in the plan, elevation and in cross-sectional drawings of the DST in

Figures 4, 5, and 6, respectively. The simulated temperatures are compared to temperature measurements made using thermocouple and resistance temperature detector (RTD) sensors installed in boreholes. Water saturations are compared against water saturation ratios deduced from electrical resistivity and neutron logging (NEU) measurements in select boreholes.

6.1.3.3 Material Properties

The NUFT simulations were performed for the four distinct property sets identified in Table 6. The first of these cases, the DS property set or baseline case was considered to contain the primary property set for the numerical analyses presented in this Section. This property set represents the set of data developed using local property values for the DST horizon (tsw34) in the stratigraphic section at the site. Given that the DST is a short term test spanning only a few years, the test is expected to probe and be influenced by only the near field of the test. As such, the DS property set is viewed as the most realistic property set for simulating the response of the DST.

The MS utilizes property values that are derived from various levels in the stratigraphic column at the site, and is expected to represent in some sense the average behavior at the site. The main difference between the MS and DS property sets is that the fracture permeability of the rock at the DST horizon in the MS property set is about two orders of magnitude greater than the fracture permeability of the DS property set. The mountain scale with local thermal conductivity (MSLK) data set is a modified version of the MS property set with 20 percent greater thermal conductivity of rock at the DST horizon. In the conduction only (CON) property set, water and moisture flow are suppressed and heat conduction is the only allowed transport process. The only difference in the thermal data between the CON property set from those of the DS and MS property sets is that the thermal conductivity and specific heat in CON are varied with temperature to mimic the effects of liquid saturation change and boiling, similar to the practice of the design organization using the CON ANSYS code (Swanson 1995).

Given that the infiltration rate is very small, and the boundary conditions at the ground surface and the water table are adjusted to yield a specified fixed set of initial conditions (e.g., temperature, water saturation) at the DST horizon, the material properties, temperatures and water saturations of the other stratigraphic sections do not significantly affect the performance of the DST during the heating period. In the simulations presented here, the entirety of each property set was used. However, only the material properties for the DST horizon (tsw34 model layer) are presented because the results of the DST simulations can be interpreted almost entirely in terms of the differences between the property sets for only this layer of the stratigraphic column.

The thermal bulkhead was modeled as a porous material with high permeability properties. The floor of the HD (the invert) is made of concrete. However, in these simulations the invert was assumed to have the same material properties as the surrounding rock for simplicity.

6.1.3.4 Boundary Conditions and Computational Grid

The lateral boundaries of the models are adiabatic/no-mass-flow boundaries. The ground surface, which is 267.5 m above the coordinate origin, is a constant temperature (17.48°C),

constant-gas-phase-pressure, and constant-relative-humidity boundary. The water table, which is approximately 600 m below the ground surface, is a constant-temperature (29.5°C), constant liquid-phase-saturation (100 percent), constant dissolved-aqueous-air fraction (1.0×10^{-7}) boundary. The TH models are initialized to account for the geothermal temperature gradient and unsaturated hydrostatic pressure gradient in the DST area. The initialization was performed by adjusting the RH (or equivalently the air-fraction in the gas-phase held fixed at 0.9875) and the water infiltration rate to obtain a temperature of 24°C and a liquid saturation of 92 percent at the DST horizon. Although these boundary conditions are not appropriate for mountain-scale TH models, they are sufficiently removed from the DST area not to influence heat-driven TH behavior in the DST.

The HD is represented with a rectangular cross section (4.42 m wide by 4.42 m high). The heated portion of the HD is 47.5 m long. The lower 0.75 m of the HD is filled with a concrete invert with properties equal to those of the rock mass. The thermal bulkhead that separates the heated and unheated portions of the HD is made up of steel with fiberglass insulation and has an effective thickness of 0.07 m in the TH model. The influence of the steel on fluid flow is incorporated in the bulk permeability of the fiberglass; however, it is assumed that the steel is too thin to affect the thermal properties of the fiberglass insulation. To account for the condensation of water vapor on the bulkhead, the wet value of thermal conductivity of the fiberglass insulation was assumed to be a factor of 10 greater than that of dry fiberglass insulation. Because of the importance of heat loss through the thermal bulkhead, it is important to obtain thermal conductivity measurements of fiberglass insulation as a function of liquid-phase saturation and to apply those measurements to future TH-model calculations.

Because of its construction, the thermal bulkhead is a conduit for the loss of water vapor (and its associated latent heat) from the DST area. Further, binary gas-phase diffusion of air and water vapor provides a mechanism for vapor transport out of the HD and air transport into the HD. The current TH model assumes that the fiberglass insulation has zero capillarity; therefore, no van Genuchten parameters are assigned to the fiberglass insulation.

All nine in-drift heaters are represented in the model. The heaters are represented with a rectangular cross section (1.5 m wide by 1.5 m high). Along the axis of the drift, the first eight heaters (with the first heater being next to the bulkhead) are represented as being 5.2 m long, which includes the 0.6-m gap between the heaters. The last heater (at the far end of the HD) is represented as being 4.6 m long. The 9 heaters are placed 0.3 m above the floor (the upper invert surface). Heat flow through the cradles supporting the heaters is ignored. Because the in-drift heaters are effectively in contact with each other in the model (whereas in the field they are separated by 0.6 m) and because thermal conductivity of air is so small, heater-to-heater thermal-conductive heat flow is set to zero. However, heater-to-heater thermo-radiative heat flow is accounted for in the TH model.

The TH models used the NUFT nested-mesh option to provide finer gridblock resolution in the region of the DST area experiencing strongly driven TH behavior—namely, the region where boiling, dryout, condensate drainage, and two-phase reflux occur. The nested mesh allows for fine gridblock resolution concentrated in the region of strongly driven TH behavior and thereby reduces the computational burden. A series of ever-finer meshes are embedded in the root mesh, referred to as Mesh 1. Mesh 2 is embedded in Mesh 1. Mesh 3, which encompasses all of the

represented drifts in the DST area, is embedded in Mesh 2. Mesh 4, which encompasses an area just beyond the areal extent of the wing heater arrays, is embedded in Mesh 3. Mesh 5, which encompasses the heated portion of the HD and thermal bulkhead, is embedded in Mesh 4. Mesh 5, which has the finest gridblock dimensions, has a typical gridblock dimension of 0.3 m in the x and z directions for the first meter of rock surrounding the HD and wing heater arrays. The TH model has approximately 40,000 active gridblocks. Cross sections of the nested-mesh computational grid in the horizontal plane that passes through the axis of the drift heater array and through a vertical plane normal to the HD at its midpoint, are shown in Figures 8 and 9 for illustrative purposes.

6.1.3.5 Initial Conditions

The water infiltration flux used as input to these calculations was derived from a 1-D TH simulation of the stratigraphic column at the DST site to develop the initial conditions. In addition to satisfying the boundary conditions at the ground surface and at the water table, the temperature and water saturation at the DST horizon were required to be maintained at 24°C and 92 percent, respectively. These additional conditions were satisfied by varying the RH and water infiltration rate at the surface. This yielded a water infiltration rate of 0.218 mm/yr.

6.1.3.6 Heat Sources

The nine in-drift heaters are treated as discrete heat sources that are 1.5 m wide by 1.5 m high by 5.2 m long. The power levels are assumed to be identical for the drift heaters. The wing heaters, which flank the HD, are represented as four separate heater arrays: two outer arrays and two inner arrays. Each wing heater array is represented as a uniformly heated, smeared-heat source. The dimensions of each of the wing heater arrays are 4.77 m (in the x or lateral direction) and 46.9 m (in the y or drift axis direction). The outer wing heater arrays were assumed to have an areal power density that is 32.2 percent greater than that of the inner wing heater arrays. Element failures reported in a few individual wing heaters were not included in the model. The ratio of the heating powers of the outer and inner wing heaters is from DTN: MO9912SEPDOIHP.000.

The field-measured total wing heater power history and total drift heater power history were used to determine the time-varying heater power levels in the model. Over the first 1.5 years of heating, the total drift heater power averaged 52,239 W, or 5804 W per floor heater. Over the same period, total power of the outer wing heaters averaged 75,372 W, and total power for the inner wing heaters averaged 57,100 W. The areal loading density averaged 168.5 W/m² for the outer wings and 127.6 W/m² for the inner wings. The quality measurements of the total heating power are given in DTNs: MO9807DSTSET01.000, MO9810DSTSET02.000, and MO9906DSTSET03.000.

The purpose of using wing heater arrays in the DST is to cause a tabular region of dryout, which maximizes the tendency for condensate to perch in the rock above the dryout zone. Maximizing the perching of condensate (and minimizing condensate shedding) will maximize the tendency for two-phase refluxing (i.e., the heat-pipe effect) to occur above the dryout zone. Approximating the 50 wing heaters with a smeared-heat source will deter condensate from shedding between the wing heaters in the simulation. Prior to the coalescence of the dryout

zones surrounding each of the wing heaters, the smeared-heat-source approximation will therefore overpredict the perching of condensate above the dryout zone.

6.1.4 Large Block Test

This section describes the LBT as it pertains to numerical modeling that was done to simulate the thermal and hydrologic response of the LBT to a heating and cooling cycle. The calculations were performed with the NUFT 3.0.1s (to be verified (TBV), STN 10130-3.0.1s-00) code using the DS properties based on the DKM model and the AFM submodel (DTN: LB990861233129.001). Images of the simulated temperature fields, liquid-phase saturation fields, and temperature histories are used to examine the measured response of the block to the heating and cooling phases of the test. The model includes temporal details of the heating during the 375-day heating phase and the subsequent cooling phase. The total simulation time is 600 days.

6.1.4.1 LBT Background

The objective of the LBT was to create, maintain, and observe a planar, horizontal region of boiling in a representative block of fractured rock, so as to observe coupled thermal-hydrological-mechanical-chemical (THMC) behavior in a realistic environment. The size of the test was chosen so that the block of rock to be heated was large enough to contain several fractures, but was still small enough so that boundary conditions and rock heterogeneity could be adequately controlled and/or characterized. A nearly planar zone of boiling was created by imposing and maintaining a 1-D thermal gradient within the rock mass. The heating duration of the test was designed to provide a sufficient length of time for THMC processes to develop.

Specific goals of the LBT were:

- Study the dominant heat transfer mechanism in partially saturated, fractured rock
- Observation of condensate refluxing above a boiling zone
- Refinement of the spatial and temporal relationship between boiling isotherms and regions of drying in the rock mass
- Observation of rewetting following the cool-down of the block
- Observation of thermally driven rock deformation including fracture deformation
- Observation and monitoring of rock–water interaction.

The LBT was an integrated test, and many different types of data were collected. The heating phase of the test lasted for 375 days, and cooling of the block was monitored for six months. Wilder et al. (1997) present a description of the test and interim results.

6.1.4.2 Test Design and Layout

An outcrop area at Fran Ridge was selected to be the site for the LBT because of the suitable rock type exposed and the accessibility of the site. A 3 x 3 x 4.5 m block of fractured nonlithophysal Topopah Spring tuff was isolated at Fran Ridge (Figure 10).

A series of vertical and horizontal boreholes were drilled into the block. Instruments and heaters were installed within these boreholes and on the surface of the block. The instruments installed in the block included RTDs to measure temperatures, electrodes to conduct electrical resistivity tomography (ERT) to measure saturation, Teflon liners in boreholes for the NEU to measure saturation in boreholes, humicaps to measure RH, pressure transducers to measure gas phase pressure, conventional and optical multiple point borehole extensometers for measuring displacements along boreholes, fracture gauges mounted across fractures on the block surface to monitor fracture deformation, Rapid Estimation of K and Alpha probes to measure in situ thermal conductivity and thermal diffusivity, and visual observation of the drainage of water near the bottom of the block. Coupons of waste package materials and other introduced materials were placed within the block to study the effect of the heated environment on the materials. Labeled local microbes were introduced back into the block to study their survivability and migration. The design and construction of the LBT are documented in Wilder, et al. (1997).

The temperature measurements included the spatial and temporal variation of the temperature in the block and the thermal gradient on the insulated block surfaces. A layer of room temperature vulcanized material and Viton was installed on the block sides to make the walls essentially impervious to moisture. Three layers of insulation materials were installed on the outside of the moisture barrier. All of the instrument boreholes were sealed either by cement grout, packers, or a room temperature vulcanized/Teflon membrane. Straps were used to stabilize the block and insulation during the test.

To create a nearly 1-D thermal field within the block, heaters were placed in the rock to simulate a planar heat source at a height of 2.75 m from the top of the block, and a steel plate fitted with heating/cooling coils was mounted on the top of the block. This plate was connected to a heat exchanger to allow thermal control of the top surface. One heater of 450 watts was installed in each of the five horizontal heater boreholes.

The heating phase of the LBT began on February 28, 1997, and ended on March 10, 1998. The power history for the central heater, which is typical for all five units, is shown in Figure 11. The cooling of the block was monitored until September 30, 1998, when it was determined that the block had returned to ambient temperatures. During the heating phase, the block reached a maximum temperature of about 140°C at the heater horizon, and a heat exchanger was used to control the top temperature at about 60°C.

6.1.4.3 Model Geometry

A fully 3-D quarter-symmetry model is used to represent the entire large block. A schematic of the block, highlighting the modeled section and showing the locations of the five heater boreholes, is shown in Figure 12. The use of a quarter-symmetry section was reasonable because the block is relatively symmetric about the two vertical mid-planes. Moreover, homogeneous

fracture and matrix properties were assumed in all calculations based on the block being in a single stratigraphic unit. The three heater boreholes in the symmetry model, starting with the borehole in the east-west vertical mid-plane, are powered to one-fourth, one-half, and one-half of the full heater borehole power, respectively. Full power for each borehole was obtained by averaging the individual power history of each of the five heater boreholes. It is assumed that heat was delivered uniformly along the length of each heater.

The LBT model uses a Cartesian coordinate system with the positive z-direction oriented vertically downward. The grid of blocks is constructed with 25 increments in the x-direction, perpendicular to the heater axes, 21 increments in the y-direction, and 58 layers in the z-direction. Of the 60,900 grid blocks, 37,796 are active. The inactive blocks represent null blocks, which are removed from the calculations to allow the structure to stand out above the ground surface. Grid-block size in the x-direction varies from a minimum of 5 cm at the heater boreholes to a maximum of 15 cm inside the block. Inside the block, the maximum grid-block dimension is 20 cm in the y-direction and 12 cm in the z-direction. Grid size increases with depth below the block and with lateral distance from the block. The lower boundary of the model is about 370 m below the base of the block. The distance to the lateral boundaries from the center of the block is about 40 m and 50 m in the x- and y-directions, respectively.

6.1.4.4 Boundary and Initial Conditions

The upper boundary variables are established based on an average barometric pressure of 8.87×10^4 Pa (DTNs: TM000000000001.100, TM000000000001.104, TM000000000001.107) and a RH that yields an initial liquid-phase saturation of 0.75. This initial liquid-phase saturation is based on neutron probe measurements along boreholes in the block (DTNs: LL971204304244.047; LL980919304244.075). Monthly averaged air temperatures at Site 8 for 1997 (DTNs: TM000000000001.100, TM000000000001.104; TM000000000001.107; MO98METDATA110.000) are used for time-varying temperature of the atmosphere around the block. Site 8 is a Bureau of Land Management meteorology monitoring site at Fran Ridge, within Area 25 of the Nevada Test Site. Figure 13 shows the variation of monthly averaged temperatures at Site 8. Air temperatures for times later than 1997 were assumed to be identical to the values for the corresponding month in 1997. The top surface temperature was controlled at about 60°C. The actual temperature history measured at the top surface (DTN: LL970803004244.036) was used at the upper boundary for the simulations. Impervious insulation at the sides of the block permits some heat loss to the atmosphere (through the sides). Heat and moisture losses are also allowed through the top surface of the block. The lower boundary, 370 m below the base of the block, is set at 25°C to give a geothermal gradient of about 0.024°C/m, a gradient that is typical of the area. The four lateral boundaries are impervious and adiabatic.

A 1-D initialization run was done to establish the initial liquid-phase saturation, temperature, and gas pressure profiles used for 3-D calculations. The upper boundary temperature for initialization is 16.3°C, the mean atmospheric temperature measured at Site 8 in 1997.

6.1.4.5 Rock Property Sets

Hydraulic and thermal properties of the tsw34 modeling layer of the DS property set were used in model calculations because the hydrogeologic unit of the LBT area is part of the Tptpmn unit.

On July 3, 1997 (125 days after the heaters were turned on), additional insulation was blown into the sides of the block to decrease heat loss through the side into the atmosphere. To account for this change in the model, the thermal conductivity of the insulation was modified at 125 days, based on heat flux measurements across a layer of ultratemp insulation on the rock wall. Using the manufacturer-supplied thermal properties of the ultratemp, heat flux measurements were made across the material, then the flux measurements were applied to estimate the thermal conductivity of the full insulation system after 125 days. Up to 125 days, it is assumed that only the ultratemp insulation is applied. After 125 days, the thermal conductivity of the entire insulating system in the model is the value estimated from heat flux measurements. The major hydraulic and thermal properties of rock and insulators are summarized in Table 7.

6.2 COMPARATIVE ANALYSES

6.2.1 Single Heater Test

This section provides comparative analysis between TH measurements and corresponding base case simulations for the SHT.

6.2.1.1 Physical Model Analysis

The simulation results of the SHT model are compared to measured data. Measured data were obtained from strings of thermocouples installed in a set of boreholes that are essentially parallel to the axis of the heater. The specific thermocouples discussed in this section were those longitudinally nearest the mid-length of the heater. The first model comparison, shown in Figure 14, is made at the mid-length thermocouple (TMA-TC-1A-7) in the thermocouple borehole nearest the heater borehole.

Figures 15 and 16 compare the SHT model results to measured data from thermocouples TMA-TC-4A-6 and TMA-TC-5A-7, located about 70 cm directly below and above the heater, respectively (TMA-TC-4A-6 is about 6 cm further away from the heater) (CRWMS M&O 1999b, Table 3-1).

Figure 17 indicates the spatial variability associated with the SHT predictions radially away from the heater borehole in three different directions, upward (against gravity), downward (with gravity), and laterally (to the side). Since the curves are nearly identical, radially symmetrical heat transfer behavior is calculated (this cannot be assumed at the start of the modeling analysis). The measured data in the three directions are also tightly bunched, indicative of both conduction heat transfer and gas-phase pressure driven convection heat transfer.

Although the SHT model data represent the trends of the measured data quite well, the model results of the DS tend to underpredict the actual temperatures overall. This may be largely driven by three modeling features: the fracture permeability of the property set (see Table 4), the

gamma parameter in the AFM, and the use of non-local thermal properties for the thermal conductivities.

If the “effective” local fracture permeability near the sensor in the above boiling zone is actually lower than the $2.76 \times 10^{-13} \text{ m}^2$ value (Table 4) used in the DS property set TH analysis, the rate of convection heat transfer from the boiling zone (a region of high relative gas permeability) will actually be less than what the model predicts. Consequently, the thermocouple temperatures in the boiling zone will remain higher than the temperatures predicted by the model at this location (refer to Section 6.3.1 in which the Median k_b is used). The difference may also be driven by the conceptual model itself. If the AFM/DKM model retains more water in the matrix by restricting the ability of the model to transport vaporized water from the matrix to the fractures (a fracture spacing issue), the growth of the dryout zone around the heater will be stunted, and the temperature build-up (specifically in this boiling region) in the model is likewise not as great. Thus, the predicted temperatures within the boiling zone will be low due to the development of a dryout zone that is not as large with respect to actual.

Finally, although it would seem the property set, including thermal conductivity, derived mostly from test samples from the SHT block (Median k_b sensitivity case) would result in better simulations of the SHT, this is not the result. Rather, the base case (DS) and, to some extent, the other sensitivity property set (TSPA-VA) considered in the SHT analyses, which are derived from more widespread sampling, result in comparable agreement between measured and simulated temperatures (see Figure 18).

6.2.1.2 Statistical Measures: Measured Versus Simulated (DS property case) Temperatures

The following discussion of statistical measures is based on standard statistics (Bowker and Lieberman 1972), which have been modified to better adapt to interpretation of simulated TH behavior of the three thermal tests.

At any given time, the temperature gauges in the DST block are associated with a measured temperature value, $T_{mea,i}$, and a modeled temperature, $T_{sim,i}$, the latter obtained by spatial interpolation from the model grid nodes. The root mean square difference (RMSD) is given by

$$RMSD = \left[\frac{\sum_{i=1}^N w_i (T_{sim,i} - T_{mea,i})^2}{\sum_{i=1}^N w_i} \right]^{1/2} \quad (\text{Eq. 1})$$

The smaller the RMSD, the better the model fit to the data in a given temperature range.

At a given instant in time, the mean-difference (MD) can be evaluated from

$$MD = \frac{\sum_{i=1}^N w_i (T_{sim,i} - T_{mea,i})}{\sum_{i=1}^N w_i} \quad (\text{Eq. 2})$$

where N is the number of temperature gages used in the analysis, and w_i is the weighting factor given to the i^{th} temperature gage. If the MD were zero, then the model would not feature a systematic error of consistently over- or underestimating the temperature in a given range.

The third statistical measure used is the normalized absolute mean difference (NAMD), which is described as follows:

$$NAMD = \frac{\sum_{i=1}^N w_i (T_{sim,i} - T_{mea,i}) (T_{mea,i} - T_o)}{\sum_{i=1}^N w_i} \quad (\text{Eq. 3})$$

where: T_o = ambient rock temperature

Because of potential distortions and problems with precise measurement of ambient rock temperature, the NAMD was not applied when measured temperatures were within 5°C of ambient rock temperature.

The weighting factors, w_i , used in these three statistical measures are based on a frequency analysis of the temperature measurements, acknowledging that the sensors are not uniformly distributed throughout the test block. It is important to give equal importance to all temperature subranges in the total range of temperatures observed. For example, if only a few temperature gages are located in the “hot” zone close to the heater, as opposed to a large number of sensors located in “colder” areas, data in the “hot” temperature subrange would be given a larger weighting than data in the “colder” subrange. The total range of temperature measurements was divided into 20 equally sized temperature subranges, and the number of measurements falling into each subrange was calculated. Finally, the weighting factors for each subrange were defined as shown below:

$$w_j = 1 / N_j \quad (\text{Eq. 4})$$

where j denotes the temperature subrange considered. N_j gives the number of occurrences within this subrange. Each weighting factor, w_i , in equations 1 and 2 for locations within the j^{th} temperature range is the same. Weighting factors are only needed for populated temperature subranges.

The statistical measures for the SHT analyses are graphically shown in Figure 18. These three (RMSD, MD, and NAMD) statistical are used to assess agreement between simulated and

measured temperatures. This assessment is divided into three categories: all thermal sensors, thermal sensors above boiling (greater than 97°C), and thermal sensors below boiling (less than 97°C). The baseline property set, DS, results in RMSD and MD values that agree within 10°C of the measured temperatures throughout the 275 days of heating and in NAMD values within 10 percent of the measured temperature increase from ambient. This good agreement exists for the three statistical measures and the three temperature regimes considered. The other two property sets in Figure 18 are discussed in Section 6.3.1.

6.2.2 Drift Scale Test - TOUGH2 Simulations

6.2.2.1 Comparison of Measured and Simulated Temperatures

Twenty-six boreholes, grouped in five radial arrays originating from the HD, are dedicated to temperature measurements (Figures 4 to 6). These are two radial arrays of eight boreholes each in a vertical xz plane intersecting the HD at $y = 12$ m (boreholes 137 through 144) and $y = 23$ m (boreholes 158 through 165). There is one radial array of six boreholes at $y = 39$ m (boreholes 170 through 175), and two arrays of two vertical boreholes each intersecting the HD at $y = 3$ m (boreholes 133,134) and $y = 32$ m (boreholes 168, 169), respectively. RTDs are installed at nominal 0.3-m intervals in each of these 20-m-long boreholes. Simulated temperatures were interpolated from the 3-D TH model of the DST using the DS/AFM-UZ99 properties to the as-built locations of the approximately 1700 temperature sensors in all 26 boreholes for comparison with test data. In addition to these dedicated thermal boreholes, temperature measurements were also being taken in the mechanical boreholes and hydrology boreholes.

The comparison between simulations and measurements is illustrated by a few selected examples. Measured and simulated temperatures are compared by means of temperature profiles (i.e., temperature for RTDs along boreholes at a fixed time); and by means of temperature evolution (i.e., changes in temperature with time at selected sensors in some of the hydrology boreholes and one of the RTD boreholes). Additionally, statistical measures of the “goodness of fit” between measured and simulated temperatures are provided as a way to quantitatively compare simulated and measured temperatures. The simulated temperatures of the fractures are indistinguishable from the nearby matrix, implying that, for all practical purposes, the matrix and fractures are in thermal equilibrium. Thus, it is not necessary to distinguish between matrix and fracture temperatures for the subsequent discussion of temperature distributions in the DST block.

Temperature Profiles: Measured Versus Simulated

Figures 19 through 21 present a sequence of measured and simulated temperature profiles along boreholes 137 through 144 for 3, 12, and 18 months of heating, respectively. Temperature is plotted as a function of the distance from the borehole collar. The boreholes chosen are arranged in a cluster oriented radially outward (~20 m) from the HD (Figure 3). Boreholes 139 and 143 are horizontal and slightly above the wing heater horizon. Boreholes 137, 144 and 138 are oriented upward with angles of 0° and ±45° to the vertical axis, respectively, while boreholes 141, 142, and 140 are oriented downward with angles of 0° and ±45° to the vertical

axis, respectively. The latter three boreholes are collared in the concrete invert at the bottom of the HD.

Each of the RTD boreholes is equipped with up to 67 RTDs at approximately 0.3-m spacing. Symbols in Figure 19 through 21 indicate the location of the individual sensors. The simulated data, shown in the graphs at the bottom, are interpolated from the 3-D numerical grid. Generally, the measured and simulated temperature data compare favorably. The highest temperatures are obtained along the two horizontal boreholes 139 and 143, because of their proximity to the wing heaters. Also, the angled boreholes are slightly warmer than the vertical boreholes, due to the borehole orientation relative to the wing heater axes.

The temperature profiles in boreholes 139 and 143 (that are parallel to the wing heaters) reflect well the configuration of the wing heaters. Each wing heater has two sections: The inner section starts at about 1.67 m from the HD wall and ends at ~6.1 m. There is a gap of 0.66 m between the inner and outer wing heater, which terminates at ~11.2 m from the HD. At three months of heating (Figure 19), the measured temperature is ~97°C between 1 to 11 m from the borehole. The nominal boiling temperature indicates vaporization and condensation processes induced by the proximity to the wing heaters. At 12 months of heating (Figure 20), the temperatures between 1 to 11 m significantly exceed 100°C, indicating all liquid water in the borehole vicinity has boiled away, and the two-phase zone has moved out beyond the borehole horizon. In Figures 20 and 21, the temperature profiles in boreholes 139 and 143 show two distinct “humps” at 12 and 18 months of heating. First, temperature drops slightly in the zone between the HD wall and the start of the inner wing heaters. Temperatures in these two boreholes then increase with distance through the length of the inner wing heater, drop slightly owing to the gap between the inner and outer parts of the wing heater, before rising again along the length of the outer wing heater. Finally, temperatures fall off gradually beyond the tip of the outer.

In the case of measured data for these two boreholes, a noticeable zone of constant temperature of approximately 97°C appears around the tip of the outer wing heaters in both the 12- and 18-month graphs. This zone of constant temperature, often referred to as a “heat-pipe”, confirms the existence of a two-phase region of water and water vapor at the nominal boiling temperature of water at the prevailing pressure of approximately 89 kPa. The existence of such a heat-pipe zone also implies that pore water boiled away from areas near the HD and the wing heaters (being the hottest) condenses in or flows rapidly to the cooler rock just outside the tip of the outer wing heater. Temperatures in the other boreholes (at 45° or 90° to the wing heaters) in the cluster generally show a monotonic decrease away from the HD, except for a short temperature plateau (at the nominal boiling point of 97°C) within a few meters of the collar. The exact location of these two-phase boiling zones surrounding the dry region around the HD and the wing heaters is, of course, a function of time and the position of the particular borehole with respect to the HD and the wing heaters.

Overall, except for the horizontal boreholes, the measured temperatures appear to be marginally lower than the simulated values, in particular for regions of elevated temperatures above nominal boiling. The differences between the simulated and measured temperatures in the horizontal boreholes may be due to the lack of computational detail for the wing heater sources (they are smeared in the simulation). At the HD itself, the measured temperatures are lower than simulated temperatures by a few degrees centigrade. This may imply that the heat losses

occurring from the test block have not been adequately accounted for in the model. Another minor discrepancy between the measured and simulated temperatures is that the heat-pipe signature in the simulation results is less pronounced than that in the measured data. This issue is also discussed in Section 6.3.2.1.

Temperature Evolution: Measured Versus Simulated

In this subsection, measured and simulated temperatures as a function of time for selected sensor locations along borehole 160 are compared. Borehole 160, like borehole 139 in the previous subsection, lies parallel and slightly above the wing heater horizon. The upper graph in Figure 22 shows measured data for the temperature history through 18 months of heating at seven temperature sensors in borehole 160. The spikes in the measured data, shown in the top graph, arise from occasional power failures during heating. The sensors under consideration are: RTD-3, located at the HD wall; RTD-9 and RTD-17, located within the borehole length adjacent to the inner wing heater section; RTD-23 and RTD-33, located within the borehole length adjacent to the outer wing heater section; and RTD-44 and RTD-55, both toward the end of the 20-m borehole, several meters beyond the tip of the wing heaters. In the bottom graph, the simulated temperature evolution at the numerical grid elements closest to the sensor locations is shown. The measured temperature curves at RTD-23 and RTD-33 show distinct heat-pipe plateaus for a period of about 60 days, indicating gas-liquid two-phase conditions in the rock. These two sensors are located in the condensation zone just above the wing heaters. RTD-3 data represent the temperature evolution in the rock close to the drift wall. Although it is also in close proximity to the heat source, no heat pipe signature is evident in the data on the top graph. This is attributed to the vapor generated from the boiling of formation water around the HD being carried away into the open drift instead of condensing in the rock mass. Temperatures at RTD-44 and RTD-55, because of their distance from the heat sources, had not reached boiling after 18 months of heating. Overall, the simulated results correspond well with the measured data in both general trend and in magnitude of temperature values. However, the model appears to underestimate the temporal extent of the heat-pipe plateau as discussed in Section 6.3.2.1.

In Figures 23 and 24, the temperature evolution, at sensors located in hydrology boreholes 59 and 60, is presented. These are the hydrology boreholes closest to the HD, where borehole 59 is above and borehole 60 is below the HD, as shown in Figure 2. Of the four temperature sensors in each borehole, Sensor 1 is nearest to the collar of the borehole (i.e., closest to the OD), and Sensor 4 is nearest to the end of the borehole. In each of these figures, the upper plot represents the measured data, while the lower plot is derived from simulated results interpolated to sensor locations. The time evolution of temperatures in borehole 59 is first considered (Figure 23). Sensor 1 is farthest from the heat source and understandably shows the slowest rise in temperature with time. By the end of 18 months of heating, this sensor has reached a maximum measured temperature of 72°C. Sensors 2, 3 and 4 in the same borehole register (both in measured data and in simulation) result in much higher rates of temperature rise. At the end of 18 months of heating, they are at about 88-90°C. The measured and simulated temperatures agree very well.

Figure 24 shows the temperature as a function of time for all four sensors in borehole 60, both for measured data (top) and for simulated results (bottom). Again, that sensors 1 and 2 register the slowest rise in temperature. Sensor 3 in borehole 60 is located close to the outer wing heater

and has gone through an early fast rise in temperature. This was followed by a temperature plateau at about 300 days of heating (presumably the sensor was then located in the condensate zone just below the wing heater). The temperature plateau at the nominal boiling temperature of $\sim 97^{\circ}\text{C}$ is more noticeable in the measured data than in the simulated results. The subsequent rise in temperature past boiling signals that the drying has reached the location of Sensor 3. Sensor 4 in the same borehole registers slower temperature rise with time as it is farther from the heat sources. Toward 18 months of heating, a flattening out of the slope, with the temperature approaching nominal boiling was observed. The agreement between measurements and simulation results are again good.

6.2.2.2 Statistical Measures: Measured Versus Simulated Temperatures

For the purposes of calculating the MD, RMSD, and NAMD (Section 6.2.1.2), temperature measurements from all the operative sensors (approximately 1700) in the 26 RTD boreholes were considered: boreholes 133-134, 137-144, 158-165, and 168-175. The total number of sensors in these boreholes is large enough to provide a reasonable statistical estimate of the "goodness" of model results against the measured temperatures at the sensor locations. As mentioned earlier, the simulated temperatures at the above sensor locations are interpolated temperatures from the nearest grid-block centers. As shown in Figure 25, MD, RMSD, and NAMD for three different cases are presented: (1) all thermal sensors, (2) sensors measuring temperatures below 97°C , and (3) sensors measuring temperatures above 97°C . The results are given at 3, 6, 9, 12, 15, and 18 months after start of heating (December 3, 1997).

Considering results from all thermal sensors, Figure 25 shows that the MD increases slowly through successive months of heating. A positive MD implies that overall, the temperatures from TOUGH2 simulations are higher than the measured temperature. Thus, at 18 months of heating, simulated temperatures are on an average 3.7°C higher than measured temperatures. Considering the complicated nature of the DST and the uncertainties involved in modeling the thermal hydrology in the DST, such a good fit is indeed remarkable. The RMSD, though it increases rapidly during the early phases of heating, then reaches a somewhat steady value during later phases of heating. At 18 months, comparing results from all the sensors, the RMSD is 9.1°C , which also implies a reasonably good statistical fit between measured and simulated temperatures. The NAMD varies between 9 and 13 percent when measurements from all thermal sensors are included in the analysis.

Taking into account only those sensors that are recording temperatures below 97°C , the RMSD values are significantly lower than when all thermal sensors are considered. However, the MDs for these two cases are very similar through 18 months of heating. On the other hand, RMSDs from the case where only those sensors that are recording temperatures higher than 97°C are considered are higher than the "All Thermal Sensors" case. This implies that the model predicts more accurately for temperatures below nominal boiling than for those above. Below nominal boiling, thermal conduction is the dominant heat transfer mechanism. Above nominal boiling, temperature evolution is influenced not only by the heat transfer mechanism but also by the coupling of TH processes. More uncertainties are involved in modeling these coupled processes. To understand how the hydrological processes affect the temperature evolution, temperature, and hydrological measurements, it is necessary to evaluate this behavior against simulation results.

6.2.2.3 Analysis of Coupled Thermal - Hydrological Processes

Most of the key processes potentially involved in the TH response of the unsaturated fractured tuff to heat are reviewed with the help of a schematic diagram (Figure 26). As the formation temperatures approach 97°C (the nominal boiling point of water at the prevailing pressure of ~ 89 kPa at the DST), matrix pore water boils and vaporizes. Most of the vapor moves into the fractures, where it becomes highly mobile and is driven by the gas-pressure gradient away from the heat source. When the vapor encounters cooler rock, it condenses, and the local fracture saturation builds up. Part of the condensate may then imbibe into the matrix, where it is subject to a very strong capillary gradient towards the drier region around the heat source, giving rise to a reflux of liquid back to the heaters. If matrix imbibition is relatively slow, the condensate may build up in the fractures and eventually become mobile. Some fraction of the condensate in the fractures may flow back towards the drier region. However, as capillary forces are relatively weak in the fractures, a substantial amount of liquid may drain by gravity (down toward the heater from the condensation zone above the heater horizon and down away from the heater from the condensation zone below the heater horizon).

Occurrence of gravity drainage depends on the strength of evaporation-condensation and fracture-matrix interflow behavior. The stronger the vapor flux away from the heater and the condensate reflux towards the heater, the more obvious will be the heat-pipe signature in the temperature data (namely, a small local temperature gradient resulting from the persistence of liquid-vapor counter flow), and with time, the temperature remains at the nominal boiling point in this region. It is possible that particular matrix and fracture hydrological properties can give rise to such strong condensate reflux that a stable heat-pipe extends all the way to the HD, preventing the drying of rock and keeping the temperatures near the nominal boiling temperature.

The preceding discussions in Sections 6.2.2.1 and 6.2.2.2 demonstrate that measured temperatures in the DST compare well with simulated temperatures both qualitatively and quantitatively. Since heat conduction is the dominant heat transfer mechanism in the DST, it accounts for most of the temperature rise in the test block. The manifestation of TH coupling in the temperature data is primarily in the heat-pipe signatures. Figures 19 through 21 clearly illustrate the heat-pipe signatures in the measured temperature profiles. At 3 months of heating (Figure 19), the heat-pipe signature can be observed along and immediately above the inner wing heaters, indicating the existence of a condensation zone in that area. As heating continued, this two-phase condensation zone gradually moved away from the heat source, and the zone formerly wet became dry, with temperatures rising above nominal boiling temperatures. Thus, as heating progressed, the two-phase zone (Figure 21) arising from heating in the wing heaters moved out to the tip of the wing heaters, while the two-phase zone from the heat of the floor heaters in the HD moved just beyond the dry zone surrounding the HD. The heat pipe signature in the temperature at a given location is of limited duration because the return of liquid towards the drier-than-ambient zone is not sufficient to sustain a large two-phase zone, for the local properties of the middle non-lithophysal unit.

In addition to temperature signatures of the effect of TH coupling, the active hydrological testing data in the DST were evaluated. Since the dominant expression of TH coupled processes is the spatial redistribution and time evolution of the drying and condensation zones within the rock

mass, geophysical and hydrological measurements are being conducted periodically in the DST in an attempt to track the thermally-induced moisture movement in the rock mass. These active data are collected from cross-hole tomography by ground penetrating radar (GPR), ERT, NEU, and air-permeability measurements. Numerical simulations can give the time evolution of the moisture distribution in the matrix pores and the fractures. However, there is no one-to-one, direct correspondence of measured and simulated quantities; hence, a direct comparison of data and simulations is not possible. Rather, the complex thermal-hydrology of the DST must be investigated through careful interpretation and logical analysis of simulated results and available active hydrological testing data in order to make reasonable inferences.

Simulated Moisture Redistribution

In Figure 27, the simulated liquid saturations in the fractures in the vertical cross section of hydrology boreholes 57-61 are shown at 3 months and at 6 months after the start of heating. In Figure 28, the liquid saturations in the fractures in those boreholes at 12 and 18 months of heating are shown. These liquid saturations appear to be extremely low for this set of hydrology parameters (the scale of the liquid saturation is coded in rainbow color, from 0 percent in red to 15 percent in blue). The saturation contours indicate significant changes from the initial uniform saturation at ambient conditions of about 1.5 percent for this particular property set. At 3 months, the areas adjacent to the HD and the wing heaters became drier than ambient, with limited changes in saturations outside those areas. A halo of weak condensate build up is calculated at that time around the heated region, and a large area of increased fracture saturation is calculated below the heated region. At 6 months, a larger dry-out zone was observed. More noticeable, however, was the slow build-up of a condensate zone above (weak) and below (stronger) the HD. Some changes in saturations farther away from these zones are also noticeable.

At 12 months of heating, in addition to an increase in the extent of the dry-out zone, a very strong build-up of condensate below the heater horizon was predicted. However, the condensate zone above the HD seemed to be weakening further. At 18 months, the trends continued, and the condensate build-up below and to the sides of the HD were even more pronounced. These results seem to indicate the presence of gravity-driven flux in the fractures giving rise to the significantly wetter zone below the heater horizon than above, and shedding of mobilized water around the entire heated region. Results from active hydrological testing to determine whether the simulation is consistent with the time evolution of measured moisture redistribution in the fractures need to be examined. However, the simulated matrix liquid saturations are presented below before discussing the results of active hydrological testing as a basis for comparison.

Simulated liquid saturations in the matrix at 3 and 6 months of heating, again at the vertical cross section of hydrology boreholes of 57-61, are shown in Figure 29. The matrix liquid saturations at the same locations at 12 and 18 months of heating are shown in Figure 30. The liquid saturation is again coded in rainbow color (non-linearly), red for 25 percent and blue for 100 percent. The ambient preheat liquid saturation in the matrix is on the order of 95 percent, considerably wetter than the fractures. At 3 months of heating, no noticeable "dry-out" zone is observed around the HD, although the saturations have reduced considerably in that area. A small but symmetric condensate build-up zone is calculated above and below the HD. Figure 29 also shows that, after 6 months of heating, a dry-out zone has started to form around the HD,

particularly around the wing heaters. The wetter zone just outside the drier-than-ambient is expanding, nearly symmetrically.

At 12 months of heating (Figure 30), a complete dry-out zone exists around the HD. The wetter zone around it continues to be quite symmetric vertically. At 18 months of heating, however, the wetter zone in the simulation is beginning to become slightly thicker below the HD than above. In addition, the change in matrix liquid saturation, through successive months of heating, in the regions immediately outside the condensate build-up zone, is not appreciable. Together with the very asymmetric moisture distribution in the fractures (as shown in Figures 27 and 28), these results indicate that the gravity drainage of condensate in the fractures is on a faster time scale than the imbibition of condensate from the fractures into the matrix. This issue of relatively slower imbibition into the matrix compared to faster drainage in the fractures is discussed in Section 6.3.2.3.

Interpretation of Active Hydrological and Geophysical Testing Data

Active testing by air injection tests is carried out periodically throughout the DST to probe the redistribution of moisture in the DST rock mass due to heating (DTN: LB980120123142.004) with up to 18 months of heating have been reported (DTNs: LB980420123142.002, LB980715123142.002, LB981016123142.002, LB990630123142.001). In this subsection, these observations are correlated with the saturation redistribution results discussed in the previous subsection.

The active testing by air injection is aimed at detecting the change in moisture content in the fractures. Because the pre-heat liquid saturation is small in fractures, the measured permeability to air will approximately reflect the permeability of dry fractures. An increase in the fracture liquid saturation from condensation will be evidenced by a decrease in the local air-permeability value, as the relative permeability to air decreases with the presence of water. Each of the 12 hydrology boreholes (57-61, 74-78, and 185-186) is typically subdivided by high temperature packers into four zones. Each packed-off zone is equipped with sensors for temperature, pressure, and RH.

Air-injection tests were carried out in each zone before heating began. A complete set of air permeability tests continues to be carried out in each zone during heating periodically, at least once every three months. Estimated air-permeability values derived from the pressure response to these air injection tests were normalized to their pre-heat values. Wherever there was a more than 10 percent reduction in air-permeability value, the data were considered for comparative analysis. Figure 31 shows the permeability ratios in hydrology boreholes 57-59 (above the HD) and Figure 32 shows the permeability ratios in boreholes 60-61 (below the HD). The vertical axis of these figures is the normalized air permeability, whereas the horizontal axis is the date of testing. From Figure 31, it is observed that a trend of steady reduction in permeability as liquid saturation builds up has been established in zones 2 and 3 of borehole 59. The other two zones (zones 1 and 4) in borehole 59 also exhibit a decline in air permeability, though not as sharp as those in zones 2 and 3.

In Figure 32, zone 60-4 (except for a slight increase in August 1998) registered a sharp decline in air permeability, whereas that in zone 60-1 registered a modest drop. The air permeability at

zone 60-2 fell sharply early, but later maintained a low steady value. However, zone 60-3 exhibited a rather up-and-down pattern in the air-permeability ratios, reducing sharply at the beginning, rising sharply around 14 months of heating, and then falling slightly in the next quarter before rising again. These fluctuations are attributed to fracture heterogeneity giving rise to time dependent wetting and draining. Although the simulation results cannot capture fluctuations in air permeability values within a short time, most of these observations of permeability reduction are consistent with predictions of the time evolution of the condensate areas outside the drier-than-ambient area (Figure 27). Thus, the active test results appear to be in qualitative agreement with the simulated saturation data. However, it remains to be determined whether such positive correlation between simulated and observed results is sensitive to the hydrological property set assigned to the rock mass. This issue will be discussed in the sensitivity analysis (Section 6.3.2.3).

While the air-injection tests probe the moisture redistribution in the fractures, the bulk of the condensate resides in the matrix because of the larger matrix porosity. Geophysical measurements such as ERT, GPR, and NEU carried out periodically at the DST are all designed to monitor the changes in liquid saturation in the matrix pores. The geophysical measurements are consistent with the expansion of drying zones (around the heaters) with time, as illustrated by the simulated matrix liquid saturations discussed in the previous subsection (Figures 29 and 30). For example, a tomogram of saturation change from preheat ambient values derived from cross-hole GPR survey taken in January of 1999 is shown in Figure 33 (~13 months after heating) (DTNs: LB980120123142.006, LB990630123142.005). There is a decrease in matrix saturation around the HD and the wing heater, and an increase in matrix liquid saturation immediately outside of the drier-than-ambient region. For comparison, Figure 34 shows predicted changes in the matrix liquid saturation after 12 months of heating, in the same 2-D vertical section containing boreholes 64 through 68, in which the GPR survey was performed.

The large liquid saturation build up in the matrix within condensation zones also raises the plausibility of water seeping into the borehole sections residing at those locations. Seepage into a borehole section can also be promoted by fractures ending at the borehole wall. Since the numerical model does not account for site-specific small-scale heterogeneity in either the matrix or the fracture continua, it cannot predict the specific location where seepage might occur. However, the general location of potential seepage is expected to coincide with regions of high matrix water saturation. Indeed, water seepage into borehole sections did occur. Water was collected from borehole zones 60-2 and 60-3 in June 1998 (six months after heating) and again in August 1998. In November 1998 (11 months after heating), water was collected from borehole section 59-4. All borehole zones of the 12 hydrology boreholes were pumped periodically and water, if present, was collected. The simulated liquid saturation in both fractures and matrix at 6 and 12 months of heating as shown in Figures 27, 28, 29, and 30. It is clear from these figures that areas of increased matrix saturation coincide with borehole sections 60-2 and 60-3 at 6 months of heating. However, these areas have become dry as heating continues to 12 months, at which time the condensation area has expanded to include borehole section 59-4. The simulated liquid saturations are consistent with the borehole locations and time where water can be collected at the DST. However, no water was collected in several other instrumented locations with the same predicted saturations. This implies that the fracture geometry may be a significant factor for predicting seepage into boreholes near heated regions.

6.2.3 Drift Scale Test - NUFT Simulations

An overview of the TH behavior of the DST can be obtained by examining the contour-fill plots of temperature and liquid-phase saturation shown in Figures 35 through 42 for various cross-sectional planes through the drifts and the rock mass one year after the heating has begun. The material properties for this DST (NUFT) analysis are from the Tsw34 lithologic unit. The distribution of simulated temperatures and water saturation at day 365 occurring on the horizontal plane passing through the center of the wing heater borehole array is shown in Figures 35 and 36. These figures show the high temperatures and drying created by the wing heaters. The simulated temperatures and water saturation on cross-sectional planes normal to the axis of the HD are shown in Figures 37 and 38 for a vertical cross-section located at $y = 23.0$ m.

One year after heating began, the calculated temperature and water saturation distributions indicate that the dryout zones surrounding the HD and wing heater arrays have coalesced. At this time, a 30 m wide heated zone encompasses the wing heater-array area, and much of the rock between the wing heaters and the HD. In the wing heater areas and in the rock adjacent to the much of the HD, water saturation has been reduced 30 to 40 percent, with a maximum water saturation of about 65 percent along the HD wall. A distinct zone of condensate shedding is also evident around the entire perimeter of the superheated zone. The vertical and lateral extent of the dryout zone has grown considerably by this time. Furthermore, after one year of heating, the merging of the dryout zones is complete at the middle and the end of the wing and drift heater arrays, and the greatest extent of dryout occurs at the midpoint (in the axial or y direction) of the DST. The nominal boiling point isotherm (97°C) in the vertical cross section close to the mid-plane of the HD ($y = 23.0$ m, Figure 37) completely encloses the HD and the wing heater arrays. Also, at this time, the upper and lower contours of the nominal boiling-point isotherm are nearly horizontal for all three vertical cross sections (Figures 37, 39, and 41), indicating a tabular boiling region. These results indicate that the wing heater arrays have achieved their design objective of generating a broad tabular region of dryout that helps maximize the tendency for condensed water to remain isolated in the rock above the dryout zone and away from the HD.

6.2.3.1 Comparison of Simulated and Measured Temperatures

Comparison of Temperature Histories

The simulated and measured temperature histories after 12 and 18 months of heating are shown in Figure 43 for all sensors in borehole 137 (vertically upward), using the DS property set. The maximum difference between the simulated and measured locations of specific temperatures is about 1 m, and the maximum difference between the simulated and measured temperatures at specific locations is about 10°C .

The simulated and measured temperature histories over the first 18 months of heating at five selected sensors in each of six selected boreholes are plotted in Figures 44 through 48. The selected boreholes are 158-162 and 80, respectively. The selected sensors are the No. 2, 5, 10, 40, 67 sensor in each of these holes. Borehole 80 runs parallel to the axis of the HD on the OD side of the HD. It is drilled from the CD parallel to the HD axis and above the HD. Boreholes 158-162 lie in a single vertical plane that intersects the HD normal to its axis and lie on the OD side of the HD. Boreholes 158 and 162 extend vertically upwards and vertically

downwards from the HD while borehole 160 extends horizontally towards the AOD. Boreholes 159 and 161 are inclined at 45 degrees to the horizontal plane and lie above and below the horizontal plane, respectively.

The results for boreholes 158-162 allow response to heating of the DST to be studied within a single vertical plane at a location that is relatively unaffected by end effects. Boreholes 158 and 162 allow comparison of the differences between locations directly above and below the drift, while borehole 160 allows the effects of the wing heaters to be studied. Finally, borehole 80 allows observation of the temperature changes along a line parallel to the HD lying some distance above the wing heater array.

The simulated temperature histories for the DS and the measured temperature histories are compared in Figures 44 through Figure 48. These plots show that, in general, the match is extremely good at all times at distances far from both the drift and the wing heat sources. The match near the HD at early duration times is quite poor for borehole 158 which extends vertically upward from the roof of the HD while it is very good for borehole 162 which extends vertically downward from the floor of the HD. The predicted temperature is significantly below the measured temperature at small times at the crown (roof), and this error decreases progressively as one moves along the drift wall from the crown of the HD towards its invert (floor). In contrast, at long duration times, the predicted temperatures are in very good agreement with the measurements at the crown of the drift while they increasingly overpredict the temperature as one moves toward the floor until becoming quite poor at the invert of the HD.

In borehole 80, which runs parallel to the HD (Figure 48), the temperatures in the middle portion sufficiently far from the thermal bulkhead and the other end of the HD are quite well predicted at times less than 182 days. This is because borehole 80 is sufficiently distant from the HD. However, at longer times, the match degrades. At sensors #30 and #44, the simulation temperatures are identical, and between about 275 and 400 days, they are predicted to be a constant temperature at about 97°C, indicating a relative stable condition of slow boiling of the water at this location. Subsequently, the temperature rises beyond 97°C, and the process that leads to this dryout condition is not well predicted by the model. In Figure 48, sensor #2 of borehole 80 seems to exhibit the effects of seasonal barometric pressure fluctuations due to leakage past the thermal bulkhead.

Comparison of Temperature Profiles

The simulated temperature profiles for the DS property set and measured temperature profiles for two selected boreholes at 100, 182 and 365 days of heating are presented in Figures 49 and 50. Figure 49 shows the simulated and measured temperature profiles along the horizontal borehole 160 that extends radially over the wing heater array. The decline in temperature between the HD and the wing heaters and the double-humped temperature fluctuation due to the unheated section between the wing heater arrays can be clearly seen in the measured temperature profile at 182 and 365 days. This double-hump in these temperature profiles is not captured by the smeared heat source modeling approximation. The excellent agreement of the far-field temperature profiles is shown in this plot.

Figure 50 shows the simulated and measured temperature profiles along the horizontal borehole 80 that runs parallel to the heater-drift about 3.2 m vertically above and about 10 m laterally from the drift axis. The very good agreement between measured and simulated temperature at short durations in the mid length of the borehole is because this borehole is in the far-field. At longer times, the agreement becomes poorer. In the mid length of this borehole, the measured temperatures fluctuate up and down with a spatial periodicity of a few meters in wavelength; this is due to the discrete heat sources in the wing heater boreholes that are spaced 1.9 m apart. The simulated temperatures do not exhibit this periodicity because the wing heaters are modeled as smeared heat sources.

6.2.3.2 Statistical Measures: Measured Versus Simulated Temperatures

The root mean square difference (RMSD), mean difference (MD), and normalized absolute mean difference (NAMD) between the simulated and measured temperatures were selected to serve as measures of the goodness-of-fit of the simulated values to the measured values. The calculated RMSD, MD and NAMD for the DS property set for all temperature sensors are plotted as a function of time in Figure 51. These results show that, for the DS property set, the RMSD above 97°C is generally higher than the RMSD below 97°C. At times greater than 182 days, RMSD does not vary significantly with time. The MD shows that temperature is overpredicted by the model at long duration times for temperatures both above and below 97°C. The NAMD for all thermal sensors ranges from 9 to 26 percent, whereas for boiling regions, the NAMD is lower.

In general, the comparison between the simulated and measured temperatures is poor for all sensors located very close to the heat source at early times (less than 100 days). This is a result of the computational grid spacing being too coarse to resolve the large temperature gradients that are generated near the heat sources at the early times. At longer times in excess of one year, the results improve significantly as the temperature profiles smooth out. At early times, the agreement between calculated and measured temperatures is best for the vertical boreholes. For the horizontal boreholes, the comparison between the simulated and measured temperatures is good in the area close to the HD; however, the simulated temperatures are higher than the measured temperatures over much of the wing heater arrays, with the greatest difference occurring over the outer half of the wing heater arrays.

The regions for which there is good agreement between predicted and measured temperature fall into two categories: (1) regions with sub-boiling temperatures, and (2) regions that are close to the HD at and near boiling temperatures.

The good agreement in the sub-boiling-temperature region indicates that heat flow is dominated by heat conduction and that the assumed value of wet thermal conductivity is reasonable. Because of the high liquid-phase saturation (92 percent) in the sub-boiling region, the wet value of thermal conductivity is applicable in that region. Because the effective bulk permeability in the DST area is much less than the threshold value at which buoyant gas-phase convection begins to affect heat flow (Buscheck and Nitao 1994, p. 1), it is likely that heat flow in the sub-boiling region is dominated by heat conduction.

The good agreement between simulated and measured temperatures in the region close to the HD indicates the following: (1) thermal radiation is adequately represented in the TH model, and

(2) heat flow in the rock is dominated by heat conduction and the dry value of rock thermal conductivity is adequately represented in the TH model.

Heat Transfer within the Heated Drift

The heat flux distribution in the rock adjacent to the HD is dominated by thermal radiation in the drift (Hardin 1998, p. 3-10) which accounts for about 80-90 percent of the total heat transfer. The good agreement between simulated and measured temperatures in the vicinity of the HD indicates that thermal radiation is well represented in the model. However, the temperature at the apex of the drift is consistently underpredicted by the calculations whereas the temperature at the floor of the drift is well predicted. This may be due to the impact of natural convection within the drift by which a significant amount of heat is transferred from the bottom of the floor heaters to the apex of the HD. Estimates based on an analytical correlation for natural convection heat transfer within concentric cylinders show that although the total heat transferred by natural convection is small compared to that transferred by radiation, local maxima in the heat flux occur at the bottom surface of the heater (which does not contact the invert in the simulation) and the apex of the drift.

The heat flux transferred by natural convection at the apex of the drift can account for as much as 35 percent of the total heat flux at this location. The heat flux at the drift invert is unaffected because a minimum in the convective heat flux occurs at this location. Differences exist between the equations that govern natural convection in free-air and in porous-media. The effective thermal conductivity and permeability of the pseudo-porous medium properties that represent the drift-air-space must be selected to be dependent on the temperature difference between the floor heater and the drift-wall. This is done to improve the accuracy of computation of the heat transferred by natural convection. While the effect of natural convection within the drift may affect local heat transfer to the drift crown, the simulated and measured vertical temperature profiles above the HD do not indicate the presence of a two-phase reflux (or heat-pipe) area above the HD; therefore, the heat-pipe effect does not significantly affect heat flow in the vicinity of the HD.

Temperature Profiles near Wing Heaters

The poor agreement between the simulated and measured temperatures in the outer wing heater-array areas may be the combined result of several causes. First, the smeared representation of the inner- and outer- wing heat sources appears to be too coarse. This is indicated by the inability of the calculated temperature profiles to accurately follow the peaks and valleys of the measured temperature profiles both in the radial direction and in the axial direction with respect to the HD. Temperature profiles are measured in the horizontal boreholes that run parallel to the HD (e.g., borehole 80) exhibit the peaks and valleys are separated by a distance approximately equal to the spacing of the wing heater boreholes (about 1.9 m). This can also be seen to be occurring in the radial direction in the temperatures measured in horizontal boreholes (e.g., borehole 160) where a valley occurs in the temperature profile between $x=8$ m to $x=10$ m. The 2 m distance coincides with the unheated section between the inner and outer wing heater elements that is 0.66 m in length and is centered at approximately $x=8.8$ m. The power consumed by the individual heater elements should be used to more accurately represent the distribution of heat generation, rather than a uniform heat generation rate. It may also be

necessary to use a finer computational mesh in this area both to represent the heat sources more accurately and to accommodate the sharp changes in the temperature profiles that arise as a result of proximity of some measurement boreholes to the heater arrays.

Second, it appears that the TH model is overpredicting the spatial extent of matrix dryout. Consequently, the simulated values of liquid-phase saturation should be regarded as being too low in the outer wing heater-array areas. The overprediction of dryout and temperature rise in the wing heater-array areas is probably a result of a combination of effects. These effects include the influence of vapor flow along the wing heater boreholes (Section 6.2.3.4), an estimated infiltration flux that is too low, and other neglected effects summarized in Section 6.4.3.

6.2.3.3 Comparison of Simulated and Measured Water Saturation Distributions

Simulated water saturations for the DS property set are compared in this section to saturation ratios determined from ERT measurements (Blair et al. 1998, Section 3). The electrical resistivities are measured through twelve ERT boreholes containing a total of 200 electrodes. Eight of these boreholes drilled from the HD, containing 140 electrodes, form vertical planes through the HD axis. The remaining four ERT boreholes drilled from the OD, containing 60 electrodes, form vertical planes normal to the axis of the HD. Images of resistivity change were calculated from resistivity data collected before and during the heating episode. The changes in resistivity are sensitive to both temperature and water saturation, with increasing temperature and water saturation decreasing resistivity. Therefore, in areas of increasing temperature and increasing dryness, the effect of increase in temperature on resistivity is partially offset by the decrease in water saturation. The Waxman Smits model (Waxman and Thomas 1974, pp. 213-214) was used to calculate the water saturations at a given location after accounting for the effect of temperature variations. The water saturation ratio in the ERT images is the water saturation during the heating event divided by the initial water saturation (both values were estimated by the same ERT method).

The simulated water saturations and the water saturation ratios estimated from ERT measurements for the vertical cross-section passing through the axis of the HD, and two vertical cross-sections normal to the axis of the HD, are presented. The latter cross-sections shown in Figure 52, are located approximately at $y=4.6$ m and $y=24.9$ m, respectively, from the thermal bulkhead.

The simulated water saturations and the ERT water saturation ratios are presented in Figures 53 through 56. The simulated water saturations were calculated at 100, 182 (0.5 yr.), 365 (1 year) and 547 days (1.5 years)-of heating while the ERT water saturation ratios were estimated from resistivity and temperature measurements at 105, 182, 371 and 558 days of heating. These comparisons must be considered to be semiquantitative because of uncertainties in the measurement and interpretation of the ERT data (Blair et al. 1998, Section 3, pp. 3-8). The error in comparing the simulated results against the measured data due to differences between the measurement and simulation times is expected to be negligible because these differences are small and there were no sudden externally induced changes during the intervening periods. When comparing these two sets of images, it should be noted that the ERT images represent the ratio between the current and initial water saturations while the simulated images represent the

water saturation itself. Furthermore, the simulations assumed an initial water saturation of 92 percent near the DST while the ERT water saturation ratios were evaluated using the estimated initial water saturations which varied from point to point according to the heterogeneity of the local rock properties. Also, attention should be paid to the differences in the color scales used in these two sets of images because the water saturation represented by a given color in the two sets of image maps could be quite different.

The changes in the simulated water saturations show two growing regions of decreasing water saturation associated with the heater drift and the wing heater arrays, respectively. The saturation estimates indicate that a relatively large region of drying develops around the wing heaters while smaller drying regions develop around the HD. At early times, less than 0.5 year, there are significant differences between the ERT saturation ratio and simulated saturation distributions, with the ERT images indicating that saturation changes primarily occur near the wing heaters while the simulations indicate that drying is concentrated near the HD. These differences persist up to 0.5 year of heating, and then gradually disappear with increasing time. After 1 year and 1.5 years of heating, both sets of images show that the zones of drying around the wing heaters and HD have merged and have the same overall character with differences only in the details of the shapes of the dryout zones. The significant differences between the ERT water saturation ratio and the simulated saturation distributions at early times can be the result of errors in both of these two different sets of results. For example, the ERT simulations at small times appear to be excessively smeared out around the wing heaters; this could be the result of numerical interpolation errors. Also, the significant deviations between simulated and measured temperatures gives rise to the possibility that there are significant corresponding errors in the simulated water saturations at small times.

An important observation that can be made from the simulated saturation maps is that there are zones of water saturation higher than the initial water saturation (indicated by zones of deeper blue color than the light blue color in the far field) just beyond the drying zones that surround the heated region. These zones of higher than initial water saturation represent zones of condensation of water evaporated from the drying zones that are located nearer to the heat sources. Their presence can also be detected in the measured temperature data as plateaus in the temperature-time history plots at approximately the boiling temperature of 97°C. These condensation zones can also be seen in the ERT images as dark blue or violet patches at approximately the same locations as the more continuous dark blue bands present in the simulated saturation images. The patchiness of the condensation zones in the ERT images could be the result of heterogeneities in the rock material property, and initial water saturation distributions that are not represented in the NUFT simulations.

NEU was also used to measure the distribution of moisture content along boreholes in the DST. NEU was conducted in boreholes 47 to 51, 64 to 68, 79, and 80 (CRWMS M&O 1997b). As shown in Figures 4, 5, and 6, the NEU holes were grouped into two arrays (borehole array 47 to 51 and borehole array 64 to 68) that are perpendicular to the HD, and two longitudinal horizontal boreholes (79 and 80) parallel the HD. The borehole Array 47 to 51 and Array 64 to 68 form vertical cross sections from the OD to the HD, intersecting the HD at about 6.4 and 26.5 m from the bulkhead respectively. Boreholes 79 and 80 are about 3.5 m above the midpoint of the wing heater planes. Teflon tubes were grouted in the holes, so that the holes are open for the NEU while sealed from the drift environment. The inner diameters of the Teflon tubes were 5.4 cm

for boreholes 79 and 80, and 4.95 cm for boreholes 47 to 51 and boreholes 64 to 68. Cement grout was used for the sealing. The free water in the cement grout will have strong influence on the measured neutron counts; however, the neutron data are analyzed by taking the difference between the pre-heat baseline measurements and the subsequent measurements during the test. Therefore, the effects of the water in the cement grout on the measured moisture content in the rock mass are minimized. NEU is one of the methods that can provide accurate measurement of the moisture content in rock mass, with good spatial resolution. However NEU can only sample a region about 10 to 15 cm in radius along a hole. Therefore neutron data should be used to monitor the moisture distribution in small regions along holes, and as standards for the results of imaging techniques, such as ERT and GPR, that can monitor moisture distributions over large regions. The DTNs of the neutron data presented in this report are LL980409604244.059 and LL990708904243.033.

The measured neutron data at nominal times of 3, 6, 12, and 18 months of heating are shown in Figures 57 through 64. Not all of the NEU was conducted exactly on those dates, but the difference in the dates is no more than one month. For example, for boreholes 64 and 65, the data for the 12 months of heating were measured on 11/19/98, instead of 12/3/98; the data for the 18 months of heating were measured on 5/10/99, instead of 6/3/99. The data presented here are the difference fraction volume water along those holes. In calculating the difference fraction volume water content, the data obtained in the first measurement during the heating phase (nominally in February 1998) were treated as the baseline, and were subtracted from the data measured on later dates. (The pre-heat measurements were not used as baseline data because they were measured using a different tool, and the calibration information of that tool has not yet been incorporated in the data reduction.) It has been verified that the moisture contents in the rock mass had not changed much in February 1998. Therefore, a zero in Figures 57 through 64 means no change since February 1998; a value of +0.01 means the water contents has increased by 1 percent of the volume of the rock. Fraction volume water is a better way of representing the moisture content than liquid saturation because its value is independent of the porosity, which may be spatially and temporally variable. At the DST location, water content can vary from about zero after dry out to about 10 to 12 percent at full saturation. Liquid saturation in the rock mass can be calculated from the data presented by dividing them by the porosity. For example, at a porosity of 10 percent, a 2 percent fraction volume water means 20 percent saturation.

Because of the timing of the NEU and the uncertainty in the in situ porosity of the rock mass, the comparison of the neutron data with the simulated water saturation in the matrix is semiquantitative. Comparing the neutron data in Figure 60 with the water saturation simulated by NUFT in Figure 56 and TOUGH2 in Figure 34 shows that in general the simulated saturation agrees well with the neutron data, especially in the drying region and the increase in moisture content outside of the drying region. The measured increase in moisture content is shown in discrete bands, instead of zones, as in the simulation. The two images in each figure, for example Figure 60, show the spatial variability of the measured results. The array represented by the other set of neutron boreholes (Nos. 47 to 51 – not shown), which is about 6.4 m from the bulkhead, indicates much less drying than that of boreholes 64 to 68, which is about 26.5 m from the bulkhead. This may be caused by the thermal and hydrological leakage in the bulkhead, in addition to the heterogeneous nature of the rock mass. Figures 61 through 64 show the measured moisture content along the two longitudinal, boreholes 79 and 80, at the four times. The cross section location of boreholes 80 and 79 in Figures 34 and 55 is $z = 3.5$ m and $x = -8.25$ and

8.25 m, respectively. The measured moisture content in these two holes seems to be much less than the simulated one. In other words, the TOUGH2 and NUFT simulations seem to overpredict the matrix liquid saturation in the region above the heaters. The increased moisture content measured by NEU near the end of borehole 80 has been corroborated by observation of water in that hole.

6.2.3.4 Influence of Vapor Flow along Wing Heater Boreholes

For the base-case TH model, simulated temperatures are considerably higher than the measured temperatures for the wing heater arrays, particularly for the outer third of the wing heater arrays. The potential importance of vapor flow along the wing heater boreholes was investigated (Blair et al. 1998, Section 6) using a sensitivity-analysis of the DST in which the horizontal permeability in the x direction (i.e., the direction parallel to the wing heater boreholes) in the plane of the wing heaters was increased by a factor of 1000. This approximate method was adopted to avoid the very high computational burden that would have been imposed by explicitly representing the 50 wing heater boreholes. The increased horizontal permeability in this alternative TH model was intended to represent the effect of the 50 wing heater boreholes acting as preferential conduits for the flow of water vapor and latent heat into the HD.

The influence of vapor and heat flow along the wing heater boreholes was clearly evident in this sensitivity analysis at 75 days after the initiation of heating. Vapor flow leaving the wing heater holes carried latent heat away from the wing heater area, lowering the temperature; this transported latent heat increased the temperature in the rock between the wing heater arrays and the HD. Unlike the base-case TH model which predicted a region of sub-boiling conditions between the wing heater arrays and the HD, the case with the leaking wing heater boreholes exhibited boiling temperatures in that region. The flow of water vapor and latent heat into the HD increased both the temperature and RH in the HD.

The wing heater boreholes also had a significant effect on the liquid-phase saturation in the wing heater area and on the rock between the wing heater arrays and the HD. The wing heater boreholes facilitate additional overall dryout. Because the wing heater boreholes relieve the gas-phase pressure buildup that would otherwise occur near the wing heater arrays, boiling can occur at lower temperatures, which effectively limits the throttling of dryout.

6.2.3.5 Influence of Barometric Pumping

Previous model simulations of the DST (Blair et al. 1998, pp 15 to 16) included barometric pressure fluctuations within the drift showed that the RH in the HD, particularly in the area close to the thermal bulkhead, is strongly affected by the fluctuation in barometric pressure in the DST area. Because the thermal bulkhead provides negligible resistance to gas flow, fluctuations in barometric pressure on the cold side of the thermal bulkhead are quickly transmitted to the hot side of the thermal bulkhead. Consequently, the gas-phase pressure history in the heated portion of the HD is essentially the same as that in the unheated portion of the HD.

RH is given by the relation (Morris 1992, p. 1828):

$$RH = P_{\text{gas}}(1 - X_{\text{ag}})/P_{\text{sat}}(T) \quad (\text{Eq.5})$$

where P_{gas} is the total gas-phase pressure, X_{ag} is the mole fraction of air of the gas phase, and $P_{\text{sat}}(T)$ is the saturated vapor pressure at the local temperature T .

The primary cause for the fluctuation in measured RH is the fluctuation in X_{ag} in the HD. An increase in X_{ag} results in a decrease in RH . The fluctuation in X_{ag} (and RH) occurs from two effects: (1) gas-phase advection of air across the thermal bulkhead and (2) binary diffusion of air and water vapor across the thermal bulkhead.

When P_{gas} in the rock is greater than P_{gas} in the HD, water vapor is advected from the rock into the HD. Prior to the period of vigorous boiling in the rock, barometric-pressure highs can result in P_{gas} in the drift being greater than P_{gas} in the rock, thereby preventing water vapor from entering the drift. If P_{gas} in the drift is high enough, it can also cause air to be advected into the HD through the bulkhead. Even if air is not advected into the HD through the bulkhead, air can enter the drift by binary gas-phase diffusion. If the barometric pressure high causes the gas phase in the drift to be stagnant, air will diffuse into the HD through the bulkhead. If barometric pressure is low, water vapor will tend to advect into the HD from the adjacent rock; this vapor flow will then be advected out of the HD through the bulkhead; the flow of water vapor out of the HD through the bulkhead opposes the tendency for air to be diffused into the drift. Consequently, during barometric pressure lows, air is being continually displaced from the drift, thereby lowering X_{ag} and increasing RH .

The influence of barometric pumping on TH conditions was computed in the vicinity of the thermal bulkhead (Blair et al. 1998, pp. 15 and 16). During barometric pressure lows, water vapor exits the HD through the thermal bulkhead, transporting latent heat out of the bulkhead. During barometric pressure highs, the direction of gas through the bulkhead is reversed; therefore, water vapor and latent heat are not lost during barometric pressure highs. At all times, there is a loss of heat through the thermal bulkhead resulting from heat conduction; the conductive heat loss increases as the temperature on the hot side of the bulkhead increases. However, for early time (< 60 days) the heat loss out of the thermal bulkhead is small and responds weakly to changes in barometric pressure.

For later times (> 60 days), temperatures begin to exceed the nominal boiling point, substantially increasing the rate of vapor generation in the rock. Because boiling substantially increases the flow rate of water vapor leaving the bulkhead, the loss of latent heat (during barometric pressure lows) increases rapidly for $t > 60$ days. During barometric pressure highs, because the flow of water vapor out of the bulkhead is greatly reduced or even stopped, there is much less heat loss through the bulkhead. During barometric pressure highs, heat conduction is the dominant mode of heat loss through the bulkhead. Because the temperature on the hot side of the bulkhead is continually rising, the conductive heat loss through the bulkhead continually increases with time and thus, even during barometric pressure highs, the trend over time is for increasing heat loss.

The latent-heat flux out of the bulkhead could be measured by allowing the water vapor to leave the bulkhead through a sufficiently large diameter pipe (e.g., 3-in. diameter) and into a condenser where the rate of condensate generation would be measured. Flow resistance through a 3-in. pipe would be negligibly small compared to partially sealed leaks in the thermal bulkhead; therefore, the pipe would be the preferential flow path where the majority of water vapor would exit the thermal bulkhead.

RH in the drift was observed to respond strongly to barometric pressure pumping. For early time (< 60 days), the relationship between the simulated and measured RH in the HD on the hot side of the thermal bulkhead is quite good. However, for $t > 60$ days, the simulated values of RH are much greater than the measured values of RH . The causes for this difference are still under investigation.

The current model assumes that temperature in the unheated portion of the HD is uniform as a result of drift ventilation. If the vertical temperature distribution in the drift on the cold side of the bulkhead were represented in the model, it is more likely that a thermally-driven flow instability would be predicted. Cold air would enter the HD through the lower bulkhead, while hot water vapor would leave the HD through the upper bulkhead. Because the current model underrepresents buoyancy effects in the HD and through the bulkhead, the simulated vapor flow out of the bulkhead occurs in roughly a 1-D piston-like fashion, whereby air is displaced by water vapor out of the bulkhead. If the TH model accounted for thermally-driven flow instabilities, it would allow more air to remain in the drift, thereby simulating a lower RH in the HD than is simulated by the current TH model. Alternatively, sufficiently large-diameter pipe could be installed in the lower region of the thermal bulkhead to serve as the primary conduit for vapor leaving the thermal bulkhead, which would tend to lessen the influence of thermally-driven flow instabilities on the flow of water vapor through the thermal bulkhead.

6.2.4 Large Block Test

This section compares the NUFT calculations with temperatures and liquid-phase saturations measured in the field. The simulation results using the DS property set are first compared with measured data to evaluate how well they match. Simulation results using the DS are then compared to results generated using the MS and the two sets of results compared to measured data.

A statistical goodness-of-fit analysis is performed to compare simulated and measured temperatures along Borehole TT1, a vertical borehole that contained RTD sensors that measured temperatures in the rock. Three statistical measures of goodness-of-fit are used; the RMSD, MD and NAMD between measured and simulated temperatures, as defined in Section 6.2.1.2. The boundary and initial conditions are identical to those presented in Section 6.1.3 for the DS property set.

6.2.4.1 Drift Scale Property Simulation Results Versus Measurements

Figure 65 shows the simulated versus measured temperature profile along Borehole TT1 at six times from 30 to 400 days. The model, with the DS property set, shows some overprediction of temperature at earlier times, but the difference between simulated and measured temperatures decreases at later times. At 300 days and 400 days (25 days after power shutdown), the agreement is excellent.

The statistical measures for the LBT analyses are graphically shown in Figure 66. These three RMSD, MD, and NAMD statistical measures (Section 6.2.1.2) are used to assess agreement between simulated and measured temperatures. This assessment is divided into three categories: all thermal sensors, thermal sensors above boiling (greater than 97°C), and thermal sensors

below boiling (less than 97°C). The baseline property set, DS, results in simulated temperatures that agree well with the measured temperatures throughout the initial 400 days of heating. This good agreement exists for the three statistical measures and the three temperature regimes considered.

Figure 67 compares simulated and measured temperature histories at two sensor locations along TT1. Sensor TT1-14 (2.76 m below the top of the block, at the heater plane) became superheated at about 25 days. The sharp increase in temperature at 125 days was due to the addition of extra insulation at that time. The reduction and subsequent flattening-out of temperatures starting at about 220 days reflects reduction in heater power in an effort to stabilize the maximum block temperatures at about 140°C. The simulated temperature history at sensor TT1-14 matches the measured data fairly well in the time ranges 0 to 25 days and 225 to 375 days. The model, using the DS property set, overpredicts temperature in the time range 25 to 225 days. The simulated cool-down lags the measured cool-down by a few degrees. Model overprediction, particularly between 25 and 225 days, may reflect that the rock properties do not adequately match the field conditions at the LBT. The overprediction might also be partially caused by: a two events where rainfall may have infiltrated into the block causing cooling; or possibly by overestimating the effectiveness of the block wall insulation in the model.

The history for sensor TT1-19 (1.76 m below the top of the block, and 1 m above the heater plane) is similar to that observed for sensor TT1-14, except that temperature changes due to additional insulation and heater power reduction are less evident because the location is at a greater distance from the heater plane. This sensor was calculated to remain in the sub-boiling zone for most of the test, except for a brief period between 150 days and 235 days when the temperature was predicted to rise less than about 5°C above boiling. The measured temperatures approached but did not exceed boiling.

Figure 68 shows the liquid-phase saturation profile along TN3. Model results are compared to liquid-phase saturations measured in the field by neutron probe (DTNs: LL971204304244.047, LL980919304244.075). The field measurement times, 103, 361, and 501 days are compared at model times of 100, 365, and 500 days. The small differences between model and measured times should have a negligible effect on the comparisons since saturation changes develop relatively slowly. The simulated dryout zone develops slowly and remains smaller than the measured zone at all three times. At about 100 days, the model dryout zone is poorly developed with no point on the profile having a liquid saturation less than 0.375, half the initial saturation. (A point that has a liquid saturation less than half the initial value is defined to be included in the dryout zone.) In contrast, the measured dryout zone is well developed at 100 days, showing a thickness of about 0.75 m and a minimum liquid saturation of about 0.12. The measured data also show a distinct recondensation zone approaching full saturation at about 1.3 m below the heater horizon, and a small recondensation zone about 0.5 m below the upper surface of the block. The measured data show sharp fluctuations in saturation not observed in the simulation. This difference is probably due to heterogeneities in the thermohydrologic properties of the fractured rock not incorporated into the property set. At about 365 days (10 days before power shutdown), the simulated dryout zone is fully developed with a thickness of 1.4 m, but continues to lag the measured dryout zone thickness. The recondensation zones above and below the heater horizon are still evident at 365 days, and the geometry is very similar to that observed at

100 days. At 500 days (125 days after power shutdown), measured recondensation zones above and below the heater horizon persist, while the simulation shows no significant recondensation.

ERT surveys were conducted to monitor temporal changes in liquid-phase saturation along planes within the Large Block. It was assumed that all resistivity changes are sensitive only to temperature and liquid-phase saturation. Rough changes in liquid-phase saturation were obtained by analyzing the resistivity change tomograph to remove the effects of electrical resistivity changes due to temperature.

Figure 69 compares images of liquid-phase saturation calculated using the DS (DTN: LB990861233129.001) with saturation ratios obtained by ERT measurements in the field (DTNs: LL980913304244.072, LL980916704244.073). Simulation results are shown at 275, 340, 365, and 385 days for an east-west section close to the center of the block. ERT tomographs of saturation ratio are presented for the same section at approximately the same times. The saturation ratio at each given time and location is the saturation normalized by the initial value. Therefore, a ratio less than 1.0 implies drying and a ratio greater than 1.0 implies wetting. The initial liquid-phase saturation in the simulation is 0.75, based on NEU (Section 6.1.4.4).

The most significant difference between the ERT and simulation images is that distinct saturation decreases observed along vertical features for the ERT results are not observed for the simulation. The edges of the ERT dryout zone are jagged and not well defined, while the simulation shows a well-defined, oval-shaped dryout zone with smooth edges. At about 275 days, both the ERT and simulation show substantial dryout in and adjacent to the heater horizon. However, the ERT dryout zone has some anomalies, the most significant being a nearly vertical spike about 1 m from the west wall. The spike advances close to the top of the block. Saturation increases from the ERT are spotty and dispersed, while the simulation shows very small saturation increases above and below the heater plane. At 365 days, the images are similar in shape to those for 275 days, but the dryout zone has grown about 10-20 percent in area. At 365 and 385 days (10 days after power shutdown), the ERT images seem to suggest re-wetting of the rock while the model shows a sustained dryout zone. However, the ERT measurements are less reliable at these later times because the high contact impedance for the electrodes in dry rock makes it difficult to drive a sufficiently large current through the rock.

The difference in dryout behavior between the simulation results and ERT measurements are due to the use of a homogeneous material property set to model the highly fractured heterogeneous rock. The vertical dryout spikes observed in the ERT results are probably due to increased drying along vertical fractures or fractured zones.

6.2.4.2 Discussion of Simulation Results

Figures 70 through 75 show images of simulated temperature and liquid-phase saturation distributions after 30, 100, 200, 300, 400, and 600 days of testing using the DS property set. The images are shown for a north-south section through the center of the block. The dryout develops slowly during the early phase of the test but grows into a substantial dryout area by the time of power shutdown (375 days). At 30 days, the dryout areas around individual heaters have not coalesced, but the superheated areas have coalesced. This implies that condensate flow between

heaters has essentially stopped sometime prior to 30 days, but some flow at the walls is still evident. Even at later times, condensate drainage apparently continues at the walls because of the low temperatures in the rock adjacent to the insulation. The thickness of the dryout area grows to a maximum of approximately 1.4 m sometime between day 300 and power shutdown.

The simulated temperature and liquid-phase saturation profiles along the block at several times are shown in Figure 76. The figure shows profiles along a vertical line with x-y coordinates (0.30, 0), midway between the center heater and an adjacent heater. The temperature profile is asymmetric in the low temperature region, having a flatter gradient above the heater horizon because the upper boundary temperature is fixed at about 60°C for most of the heating phase. The thickness of the superheated area is about 0.63 m at 30 days and grows to maximum of about 2.3 m at 200 days. Peak temperature shown in the profile is about 147°C at 200 days. The temperature field collapses rapidly following power shutdown at 375 days. The peak profile temperature at 400 days, 25 days after power shutdown, is about 58°C. At 500 days, the peak occurs at the top of the block and is only 25°C.

Temporal changes in the geometry of the dryout area are also shown in Figure 76. The dryout area is fairly symmetric, indicating that the asymmetry observed in the temperature profile and gravity effects have not influenced the shape of the area significantly. No dryout area is seen at 30 days, and only a very small zone is predicted to develop at 100 days. For times 200 days and later, dryout area thicknesses of about 0.7 m to 1.4 m are predicted. No significant rewetting is predicted to occur in the dryout area between power shutdown at Day 375 and 600 days. Only very minor condensate buildup is predicted below and above the heater horizon. The maximum predicted saturation is less than 2 percent above the initial value of 75 percent. The rapid collapse of the temperature field after power shutdown is in sharp contrast to the sustained dryout area. No reflux areas are evident in the simulation.

6.3 SENSITIVITY STUDIES

DTNs for the TH property sets used in these sensitivity studies are provided in Tables 4 through 7, and in Table 9.

6.3.1 Single Heater Test

In this section, the DS property set is compared to a locally measured Median k_b and to the previous base case hydrologic property set applied to the thermal hydrology models used in support of TSPA-VA. The locations used in the comparison are identical to those of Figures 14 through 17. The results, which are shown in Figures 77 through 80, are discussed below.

In some locations (Figures 77 and 79), the thermal and hydrologic property set obtained from local measurements (the Median k_b set) most accurately represents the temperature measurements made at the SHT location. The TSPA-VA property set is generally inferior to the other two property sets considered in the SHT simulations in terms of both graphical analyses at these same locations and in the overall thermal statistics (Figure 18). The property values used in the Median k_b set are given in Table 4. In particular, this property set results in good agreement between measured and simulated TH data in the above boiling areas shown in some (Figures 77 and 79, for example) and acceptable but lesser agreement in other locations

(Figure 78). The agreement using the Median k_b property set is most likely due to the reduction in bulk permeability, which is about one order of magnitude lower than that of the DS property set. This restricts the heat flow out of the above boiling area which in turn tends to drive the temperatures up (e.g., convective cooling is restricted in the Median k_b case such that heat must primarily leave the boiling area by conduction).

The statistical measures for the SHT analyses are graphically shown in Figure 18. These three (RMSD, MD, and NAMD) statistical measures (see discussion in Section 6.2.1.2) are used to assess agreement between simulated and measured temperatures. This assessment is divided into three categories: all thermal sensors, thermal sensors above boiling (greater than 97°C), and thermal sensors below boiling (less than 97°C). The two sensitivity property sets, Median k_b and TSPA-VA, result in simulated temperatures that agree sufficiently well with the measured temperatures throughout the 275 days of heating. Although agreement between simulated and measured temperatures is acceptable, the TSPA-VA property set produces simulated temperatures that are generally inferior to those resulting from either of the other two property sets with respect to the measured temperatures. Except for the NASD low temperature regime, these trends in statistical measures hold for the three statistical measures and the three temperature regimes considered.

6.3.2 Drift Scale Test - TOUGH2 Simulations

6.3.2.1 Scope of the Sensitivity Analysis

The key parameters influencing the TH processes in fractured tuff at the DST are thermal conductivity, permeability, porosity, relative permeability, and capillary pressure characteristics (which include van Genuchten α and m) of the matrix and fractures. It has been shown in Section 6.2.2.1 that the TOUGH2 temperature predictions compare well with the DST measurements. Since heat conduction is the dominant heat transfer process, the agreement between data and simulations possibly implies that the thermal conductivity of the DST block is reasonably well represented by the parameter values used in numerical model. The TH processes such as gravity drainage of condensate in the fractures and the imbibition of water into the matrix are controlled by the hydrological properties. These coupled processes primarily affect the drying and wetting phenomena that can be indirectly compared with the active hydrological testing data.

The TH coupling also gives rise to subtle second order effects in the temperature, such as the presence/or absence and duration of heat-pipe signatures. The extensive set of data from the DST affords an opportunity to place constraints on the parameter values of the hydrological properties. Therefore, in this section, a sensitivity analysis on the key parameters mentioned above is presented. It is investigated whether varying these key parameters will result in substantially different model predictions and whether, by virtue of their match with the data from the DST, the appropriate parameter ranges can be determined. Since fracture-matrix interaction plays a crucial role in controlling hydrological processes, an alternative conceptual model for the fracture-matrix interaction is evaluated in the sensitivity analysis.

The base case property set used in the simulations presented in Section 6.2 originates from the UZ Drift Scale Property Set (DTN: LB990861233129.001) as mentioned in Section 6.1.2.6.

Since it was derived from the UZ Drift Scale Property set, and since it employs an AFM, this property set is referred to as DS/AFM-UZ99 in Table 5. The other tests used the same or similar properties in their DS property set cases (Tables 4, 6, and 7). The base case property set was derived from calibration runs for ambient conditions (Section 6.1.2.6).

For this sensitivity analysis, the classical dual-permeability formulation (Pruess 1991) was used, rather than the AFM, for the interaction between matrix and fracture. A different set of key thermal and hydrological parameters was also used. This set of properties takes advantage of site characterization data specific to the DST. For example, thermal conductivity values (for wet and dry samples) derived from laboratory measurements of rock cores from the thermal test area in Alcove 5 of the ESF were utilized. Further, based on the laboratory measurements of the liquid saturation of the cores from the DST block, the calibration runs for a property set were conducted to match the liquid saturation at the DST horizon to that value. Additionally, for the same calibration run, only the data in borehole SD-9, which is the surface-based borehole that is closest to the thermal test area, were used. This property set is denoted as the DKM-TT99 (for DKM-TT99, see Table 5) property set. This property set has been used for pretest predictions (Birkholzer and Tsang 1997, pp. 18-20) and analysis of DST results through the early phases of heating (Tsang et al. 1998, pp. 2-26 and 2-27). Table 5 provides a comparison of the key parameters used in the DS/AFM-UZ99 and DKM-TT99 models.

In the next few subsections, results are presented regarding the influence on TOUGH2 simulations of these key parameters, individually and in combination with each other. This type of sensitivity analysis also provides an opportunity, by separately comparing simulation results from the two property sets with measured data, for determining whether the parameter values are within acceptable limits. Also, a comparative analysis of the simulation results from the two property sets helps to elaborate and illustrate competing physical processes and to establish the dominant ones at different times and locations. With these as objectives, the following subsections will show how the thermal and hydrological properties affect the simulation results.

6.3.2.2 Thermal Conductivity and Temperature Predictions

Table 5 shows that for the base case property set (DS/AFM99-UZ99), the wet and dry thermal conductivities are 2.33 W/m°C and 1.56 W/m°C, respectively. On the other hand, they are 2.0 W/m°C and 1.67 W/m°C for the DKM-TT99 property set. Thus, the wet thermal conductivity is about 17 percent higher for the base case compared to DKM-TT99. The dry thermal conductivity, however, is lower for the base case than for DKM-TT99. In this section, how these thermal conductivities affect the temperature distribution in the rock mass under investigation is explored.

In Figures 81 through 83, the simulated temperature profiles with the DKM-TT99 for boreholes 137-144 at 3, 12, and 18 months of heating, respectively are shown. These are to be compared to their counterparts generated with the base case, in Figures 19 through 21. The temperature profile plots look similar for the two property sets, and both compare well with measured data. The same similarity can be observed in temperature evolution plots, as demonstrated in Figure 84 (to be compared to Figure 22) for the evolution of temperatures in borehole 160. Since temperature distribution in the rock mass is predominantly governed by thermal conduction, these similarities will suggest that temperature distribution in the rock mass

at the DST is not very sensitive to thermal conductivity. It appears that the thermal conductivity values from the two property sets are both in the acceptable range. The only noticeable difference in the temperature distribution obtained from the two property sets is the extent of the heat-pipe signature. Since convective heat transfer plays the most important role in determining the extent and duration of heat-pipe signals, the coupling between the thermal and the hydrological processes, rather than the thermal conductivity, is responsible for these minor differences in temperature distribution in the rock.

In Figures 85 and 86, the contours of temperature distributions around the HD in the vertical cross section of hydrology boreholes 57-61 at 6 and 18 months of heating, respectively, are shown. In these two figures, the contour plot at the top is the prediction from the base case DS/AFM-UZ99 model, whereas the one at the bottom is that from the DKM-TT99 model. As expected, the contour plots for temperature distribution appear similar for the two cases under consideration. However, subtle differences arise between the two sets, which can be accounted for by the different thermal conductivity of the two property sets. After six months of heating, the contours in Figure 85 show higher temperature near the heat source for the base case. This can be attributed to the smaller dry thermal conductivity of the base case (given that the heat capacity is almost identical for the two property sets for the tsw34 modeling layer). Modeling of the tsw34 modeling layer is emphasized more than the tsw33 and tsw35 layers because the entire set of DST thermal sensors are located in tsw34. After 18 months of heating, the temperature contours in Figure 86 for the base case are closer together (higher gradient) than for the DKM-TT99 property set in the near-boiling region away from the heat source. This can be attributed to the higher wet conductivity in the base case. The temperature contour plots for the other hydrology boreholes, although not shown here, appear similar.

The statistical measures developed in Section 6.2.1.2 for the accuracy of temperature predictions by TOUGH2 simulations were also compared for the two property sets, as judged against measured temperatures. As before, all the operative sensors in the 26 RTD boreholes were selected and compared to temperatures measured by those sensors with interpolated simulated temperatures at the sensor locations at a specific time. Figure 25 presents a comparative study of RMSD, MD, and NAMD for the two property sets (DS/AFM-UZ99 and DKM-TT99). Statistical measures are comparable for the two property sets, indicating that temperatures are not strongly affected by the range of thermal conductivity values. The thermal conductivity values used in the simulations lie within an acceptable range for the DST block.

6.3.2.3 Hydrological Properties and Saturation Redistribution

Figure 87 compares fracture liquid saturations in the vertical cross section of hydrology boreholes 57-61 at 18 months after the start of heating. The top contour plot corresponds to simulations with the base case property set, DS/AFM-UZ99, and the bottom contour plot corresponds to DKM-TT99 properties. The distribution of liquid saturations for these two different sets of properties looks almost identical. An extended dry-out zone appears around the HD, out to the extent of the wing heaters on both sides of the HD. Away from this dry-out zone, and above the HD, some condensate builds up. In addition, a very asymmetric distribution of condensate is predicted in the fractures above and below the HD, with a stronger build-up below than above, indicating strong gravity-driven drainage in the fractures. However, although the two plots agree well qualitatively and seem to capture the same underlying hydrological

processes, the saturation scales used in plotting them are quite different. The base case plot is drawn to the scale (0.0, 0.15); and the DKM-TT99 plot is drawn to the scale (0.05, 0.5). Figure 87 is reproduced in Figure 88, but this time the two plots are drawn to the same saturation scale of (0.05, 0.5). Now they appear different. The fractures in the base case are extremely dry compared to the DKM-TT99 case. The very low ambient saturation in the fractures for the base case is partially a result of its higher porosity compared to DKM-TT99. Except for this distinction, however, it has already been demonstrated that the underlying physical processes are probably well captured by both the property sets.

Since moisture redistribution in the fractures is fundamentally a function of water and vapor mobility, it is mainly governed by capillary pressure and relative permeability characteristic curves (both in the liquid and in the gas phase), which themselves are governed by the van Genuchten parameters (for these present simulations). Figure 89 shows the capillary pressure in both the fractures and the matrix as a function of equivalent liquid saturation for the two property sets. The capillary suction at a specified equivalent saturation in the base case property set is weaker than that in the DKM-TT99 property set. Figure 90 plots the relative permeability as a function of equivalent liquid saturation in the liquid phase for the two cases. Contrary to capillary pressure, the liquid-phase relative permeability in the base case is higher than that in DKM-TT99, even though only slightly. Therefore, water in the fractures would drain more readily in the base case property set because of its higher fracture liquid relative permeability and weaker capillary suction, and liquid saturation would not build up as readily in the base case as for the DKM-TT99 property set.

These predictions from the alternative property sets can be evaluated against active hydrological testing data, specifically, air injection test results. Figure 91 shows the gas-phase relative permeabilities for these two property sets, both for the fractures and the matrix. The important observation is that, for the range of fracture saturation changes associated with the base case property sets (2 percent ambient in tsw34 to about 10 percent maximum during the heating phase), the gas-phase relative permeability should remain virtually unchanged as indicated by Figure 91. However, air injection testing (Figures 31 and 32) has shown substantial reduction in air permeability (to about a quarter of the initial preheat values) in many zones of the hydrology boreholes. These zones have been identified to correspond to zones of simulated increased liquid fracture saturation at various phases of heating (Figures 27 and 28). The observed reduction in air permeability is attributed to condensate build-up in the fractures. The base case property set appears somewhat off the mark in predicting (quantitatively) such reductions in air permeabilities. On the other hand, for the DKM-TT99 property set, simulated fracture liquid saturation increases from about 10 percent at ambient to about 50 percent maximum in the condensation zones during heating. Figure 91 indicates that, for this range of increase in liquid saturation, the air permeability drops by approximately a factor of 4. This is more consistent with air injection measurements and suggests that the DKM-TT99 property set better predicts the fracture saturation redistribution than the DS/AFM-UZ99 property set.

Figures 92 and 93 present the predicted liquid saturations in the matrix at 6 and 18 months of heating, respectively, for the vertical cross section of the hydrology boreholes 57-61, using the DKM-TT99 property sets. The matrix liquid saturations at those times and at that same location for the base case property set were presented earlier (Figures 29 and 30). Comparison of these contour plots for matrix saturations with the two different property sets establishes a few

important points. First, the ambient matrix saturation (~92 percent) in the DKM-TT99 is slightly lower than in the base case property set (~95 percent). Second, the zone of condensation build up around the HD and the wing heaters is less symmetric for the DKM-TT99 property set than in the base case, with a bigger condensation zone below the HD than above. This asymmetry in the saturation redistribution in the zone immediately outside the drier-than-ambient area is observed from six months of heating through 18 months of heating with the DKM-TT99 property set. In contrast, the base case property set results predict that the matrix saturation in the condensate zone is very symmetric through the early phases of heating, with an asymmetric distribution only beginning to develop after 18 months of heating.

Saturation build-up in the matrix pores takes place from imbibition of condensate as it continues to drain down the fractures. Because drainage through fractures is not countered by the vaporization process below the HD as it is above, more imbibition into matrix pores should occur below the HD than above. This also implies that there will be a stronger saturation build-up in the matrix below the HD than above. These expected phenomena appear to be consistent with the saturation redistribution in the matrix obtained at all phases of heating with the DKM-TT99 property set, and only at later phases of heating with the base case property set.

The rather symmetric saturation distribution with the base case property set at early phases of heating can be understood from its hydrological properties. The base case property set is derived using the AFM. The AFM implements a reduced fracture-matrix interaction area compared to the classical DKM that makes the entire fracture-matrix area available to flux transfer (as in the case of DKM-TT99). The reduced matrix-fracture interaction in the AFM naturally leads to less imbibition of condensate into the matrix from the fractures (as compared to that for the classical DKM). As a result, drainage in the fractures dominates over imbibition into the matrix. The drainage in the fractures is further enhanced by the weaker capillary suction with the base case property set. Thus, water boiled away by heat is immediately drained through the fractures, with very little chance of matrix saturation building up at early phases of heating. However, as more and more water is boiled, the cumulative effect of condensate build-up in the matrix below the HD from the slight imbibition becomes apparent. In short, imbibition in the matrix takes place over a much larger time scale for the base case property set scenario than for the DKM-TT99 property set. Current ERT data indicate an asymmetry in the matrix saturation distribution around the HD, even during the early phases of heating. This asymmetry again points to the DKM-TT99 property set capturing the hydrology of the DST better than the DS/AFM-UZ99 property set, although the differences are very subtle and minor.

6.3.3 Drift Scale Test - NUFT Simulations

6.3.3.1 Sensitivity of DST Simulations to Input Data

The sensitivity of the DST simulation results to variation of parameter values over a realistic range is assessed in this section using the four different property sets that were presented in Table 3. Of these property sets, the DS represents the set of data developed using property values for the DST horizon in the stratigraphic section at the site. Given that the DST test is a short term test spanning only a few years, the test is expected to probe and be influenced by only the near field of the test. As such, the DS property set is viewed as the most realistic property set for simulating the response of the DST, and was selected as the base case for this report.

The MS property set utilizes property values that are derived from various levels in the stratigraphic column at the site, and is expected to represent in some sense the average behavior at the site (Section 6.1.3.3). The main difference between the MS and DS property sets is that the fracture permeability of the rock at the DST horizon in the MS property set is about two orders of magnitude greater than the fracture permeability of the DS property set. The MSLK property set is a modified version of the MS property set with less saturation-dependence of thermal conductivity for rock at the DST horizon. In the CON property set, water and moisture flow are suppressed and heat conduction is the only allowed transport process. The only difference in the thermal data between the CON property set and the DS and MS property sets are the changes in the state of hydration of the rock material in the DST horizon. In the CON property set, the thermal conductivity of rock is decreased from one constant value to another when a specific alteration temperature is exceeded. The specific heat of the rock is allowed to first increase with temperature to a new value at a specified temperature and then decrease to the initial value when a second temperature is exceeded; the total "additional energy" of the high heat capacity temperature range is intended to account for the latent heat of pore water that is evaporated from the rock in that temperature range.

6.3.3.2 Sensitivity of Temperature to Input Data

The DST was simulated over a 1.5 year period. The simulated and measured temperature profiles for each of the four property sets (DS, MS, MSLK and CON) are plotted for the same sensors and boreholes considered previously in Section 6.2.2.2. The measured temperatures and the simulated results for all four property sets for selected sensors are presented in Figures 94 through 99 for boreholes 158-162 and 80 respectively. The simulated temperature profiles for all four property sets and the measured temperature profiles for two selected boreholes at 100, 182 and 365 days of heating are given in Figures 49 and 50. Figure 49 shows the simulated and measured temperature profiles along the horizontal borehole 160 that extends radially over the wing heater array. Figure 50 shows the simulated and measured temperature profiles along the horizontal borehole 80 that runs parallel to the HD about 3.2 m above the center of the HD and the plane of the wing heater array. These figures show, in general, that the sensitivity to differences in TH properties is least in the sub-boiling range. Examination of the property differences in the property sets indicates that fracture permeability has a stronger influence in the near- and above-boiling regimes than the range of thermal conductivities investigated. As discussed in Section 6.2.3.1, the error is large near the heat sources at shorter durations for all property sets due to the coarseness of the computational grid. The grid does not resolve high temperature gradients that exist at these locations at early times.

6.3.3.3 Sensitivity of Goodness-of-Fit of Temperature Results to Input Data

The statistical measures for the DST - NUFT analyses are graphically shown in Figure 51. These three (RMSD, MD, and NAMD) statistical measures (as defined in Section 6.2.1.2) are used to assess agreement between simulated and measured temperatures. This assessment is divided into three categories: all thermal sensors, thermal sensors above boiling (greater than 97°C), and thermal sensors below boiling (less than 97°C). The sensitivity property sets considered (MS, MSLK, and CON) result in simulated temperatures that agree well with the measured temperatures throughout the initial 550 days of heating. The overall trends of the three statistical measures and three temperature regimes considered are similar for the three sensitivity

cases, except for poorer agreement for the above-boiling temperature distributions simulated with the CON property set.

6.3.4 Large Block Test

6.3.4.1 Drift Scale Property Simulation Versus Mountain Scale Property Simulation

Figure 100 shows simulated temperature profiles along TT1 computed using the DS and MS property sets, plotted together with the measured profile. The profiles are plotted at 100, 200, 300, and 400 days. While both the DS and MS property modeling results generally overpredict temperatures, the DS results are closer to the measured data. At 100 days, the DS and MS property results are very close, with the temperatures from the MS property results about 4°C higher at the heater horizon. However, both simulations consistently overpredict the temperatures. At 200 days, the two property sets are in better agreement with the measured profile, but there continues to be overprediction in the superheated area where the MS property results show greater disagreement than the DS property results. At 300 days, excellent agreement between DS property results and measured data is observed. The MS property results at this time show good agreement with measured data, but continue to overpredict temperatures in the superheated area. At 400 days, 25 days into the cool-down phase, both property sets produce results in good agreement with the measured data, with the DS property results giving a slightly better match.

A comparison of the liquid saturation profiles for the two property sets, shown in Figure 101, explain the differences observed between the two temperature profiles. Liquid saturation profiles are shown at 100, 200, and 300 days. The dominant feature of the profiles at all three times is a substantially larger dryout area for the MS property simulation. The MS property set has a fracture permeability that is nearly two orders of magnitude greater than the fracture permeability for the DS property set. The higher permeability permits more rapid vapor losses from the hot areas to the cold areas, causing faster drying in the hot areas. The drier hot areas, with a lower thermal conductivity, then transfer heat by conduction at a slower rate and therefore experience a greater temperature rise. The higher fracture permeability therefore explains the reason why simulations with the MS consistently predict higher temperatures in and adjacent to the heater horizon.

The degree of agreement between measured temperatures and the simulation results using the two property sets (DS and MS) is examined by comparing the RMSD, MD, and NAMD for profiles at various times from 30 days through 500 days (Figure 66). As shown earlier in the temperature profiles (Figure 100), the DS property set consistently gives a lower RMSD than the MS property set. For both property sets, the match with measured data improves with time during the heating phase. The MD is also generally smaller for the DS property set, suggesting better agreement with measured data. Again, the match of both property sets consistently increases with time.

Results of this comparative analysis to assess the performance of the NUFT model using the DS and MS property set are summarized as follows:

- Simulation results obtained using the DS property set show better agreement with the measured temperatures than simulation results obtained using the MS property set
- Both property sets generally overpredict temperatures in and adjacent to the heater horizon, but the degree of overprediction is less for the DS property set
- The RMSD and MD for both property sets indicate that the agreement with measured data generally increases as the test progresses
- The dryout area modeled using the DS property set is significantly smaller than the areas modeled using the MS property set and areas measured by NEU probe.
- The ERT vertical spike of dryout implies high fracture permeability, consistent with the MS property set.

6.3.4.2 Sensitivity of LBT Simulations to Property Sets

This section presents a sensitivity analysis to examine the effect of changes in the thermal and hydraulic properties of the rock on the temperature field developed in the Large Block. Five cases are addressed (see Table 3). The results for all cases are plotted in Figure 66.

Case DS is the DS property set described in Section 6.1.2.6, and Case MS is the MS property set described in Sections 6.1.3.3 and 6.3.3.1, and in Table 7. The MSLK property set is identical to the MS properties, except the dry and wet thermal conductivities are modified to 1.67 and 2.00 W/m°C, respectively. The original dry and wet thermal conductivity values were 1.56 and 2.33 W/m°C, respectively. The mountain scale with a higher fracture permeability (MSFP) property set is also based on the MS properties, but with the fracture permeability for the entire portion of the block above the heater horizon increased two orders of magnitude ($1.7 \times 10^{-9} \text{ m}^2$) after 30 days of heating. The permeability was increased to examine the possible thermohydrologic effects of significant fracture opening above the heater horizon during the heating phase.

The CON property set is a conduction-only analysis with thermal conductivity and specific heat varying with temperature to mimic the effects of boiling. The conductivity is 2.33 W/m°C for temperatures less than 100°C and 1.56 W/m°C for temperatures 100°C and above. The specific heat is 948 W/kg°C for temperatures less than 95°C, 4567.94 W/kg°C between 95 and 114°C, and 948 W/kg°C above 114°C. This methodology is that practiced by the design organization using the ANSYS heat transfer model software, which does not include mass transfer capability. The methodology allows some consideration of saturation and latent heat (evaporation) effects on heat transfer. The simulation for the CON case was done using the conduction-only module of NUFT where all fluid flow is deactivated. Since radiation is not used in the LBT analysis, conduction is the only active heat transfer mechanism.

The statistical measures for the LBT analyses are graphically shown in Figure 66. These three (RMSD, MD, and NAMD) statistical measures (defined in Section 6.2.1.2) are used to assess agreement between simulated and measured temperatures. This assessment is divided into three categories: all thermal sensors, thermal sensors above boiling (greater than 97°C), and thermal sensors below boiling (less than 97°C). The sensitivity property sets considered (MS, MSFP, MSLK, and CON) result in simulated temperatures that agree well with the measured temperatures throughout the 375 days of heating. The overall trends for the four sensitivity cases are similar for the three statistical measures considered and for the three temperature regimes considered. Although the statistical measures varied as much with time as with property set, the MSFP property set had the best match (lowest statistical measure values), and the MS properties had the worst match, particularly for the high temperature data.

Following is a summary of the temperature statistics for all temperatures in the block.

- DS, CON, and MSFP show the best overall agreement with field temperatures.
- MSLK shows the worst agreement, in all three temperature ranges, overpredicting temperature for nearly the entire test.
- The RMSD and MD are highest in the range of 30 to 100 days and lowest at 200 to 300 days.
- The worst period of overprediction of temperature, 30 to 100 days, was prior to the two potential rainwater infiltration events at 106 and 188 days, which are thought to have substantially cooled sections of the block.
- All cases overpredict until about 150 days with improved prediction at later times.
- Higher fracture permeability above the heater horizon (MSFP) significantly reduced the high overprediction of temperature observed with the MS properties prior to about 270 days.
- MSFP shows the best agreement with measured temperatures in the superheated range.

When all thermal sensors are considered, the statistical measures do not show major differences among the five cases. In general, the match with measured data steadily improved with duration of heating. The positive MD indicates that all the cases generally overpredict temperatures. The degree of overprediction is highest for MSLK case and lowest for the MSFP and CON cases.

The improved match seen in Figure 66 with MSFP properties compared to MS properties shows that opening of fractures above the heater horizon can cause a reduction of temperatures in the block. The mechanism for this temperature reduction is probably higher convective heat losses through the top of the block.

Slightly improved thermal agreement for the conduction-only model should not be interpreted to mean that conduction-only models could compete with full TH models in these analyses. First, a conduction-only analysis is limited in that information on phase change, fluid movement, and

chemical transport is not obtained. Second, a more detailed sensitivity analysis that varies a wider range of thermohydrologic parameters in the TH cases will improve agreement with measured data, while supplying critical information on fluid movement. Thirdly, the conductions only property set did not perform as well in the DST (NUFT) analyses in Figure 51 as it did in the LBT analysis, based on results provided.

Figure 102 shows the 200-day temperature profiles along borehole TT1 for the five property sets and the measured data. As with the goodness-of-fit analysis, the CON and DS property sets show the best agreement with measured data and the MS and MSLK property sets show the worst agreement. Also, the simulations generally overpredict temperature in and adjacent to the heater horizon except for the MSFP property set. A distinct reflux zone, seen only faintly in the measured data, is observed above the heater horizon for the MSFP case.

Results of this LBT sensitivity analysis using the five property sets are summarized as follows:

- Simulation results obtained using the CON and DS property sets show better agreement with the measured temperatures than simulation results obtained using the MS and MSLK property set.
- All five property sets generally overpredict temperatures in and adjacent to the heater horizon. The degree of overprediction is less for the MSFP, CON, and DS property sets and greater for the MSLK property set.
- The RMSD and MD statistical measures for all five property sets indicate that the agreement with measured data generally increases as the test progresses.
- Higher fracture permeability above the heater horizon using the MSFP property sets reduced the high overprediction of temperature observed with the MS property set but showed a large and strong reflux zone not seen in the measured data.

6.4 SUMMARY OF ANALYSIS

6.4.1 Single Heater Test

In general, the drift scale hydrologic property set provides an overall adequate match of the observed trends of the SHT temperature measurements (Figure 18). Although somewhat cooler than the measured results in the boiling zone, this property set matches the below boiling measured data reasonably well. Also, as repository design moves towards a cooler design, the predictions of the TH models against measured data in the below or nearly boiling regions takes on added importance. From the graphical results, it is observed that the below boiling predictions are markedly better. Additionally, the measured temperatures of the SHT clearly indicate an absence of the two-phase counterflow process. The current property set and active fracture conceptual model properly simulate this conduction-dominated behavior. These observations indicate that the property sets currently in use perform relatively well while representing a thermal perturbation. Since the hydrologic property sets are calibrated to reproduce ambient conditions without specific recourse to reproducing the thermal perturbation of a field test or total repository heating, the reasonable temperature and saturation predictions

indicate that the simulations are addressing the key physical processes at the temporal and spatial scales of the tests. The only way in which the hydrologic property sets and conceptual flow models can be tested against a thermal perturbation is in a controlled experiment such as the LBT, SHT, or the DST.

Previous hydrologic property sets, used in TSPA VA models, underpredicted the heating trends of the SHT. The drift scale property set also underpredicts temperatures, to a certain extent, in the boiling region. However, the comparison is markedly better moving from the TSPA-VA property set results to the Drift Scale (base case) property set results being used in the TSPA-SR. Based on the results of the SHT model comparison of the DS property simulations to measured temperatures, it is reasonable to use the drift scale hydrologic property set in the TSPA-SR thermal hydrology models.

6.4.2 Drift Scale Test - TOUGH2 Simulations

Results from TOUGH2 simulations of the TH processes in the DST were compared with the measured temperature data obtained through the first 18 months of heating and with periodic active hydrological testing data. A complex numerical grid that follows the as-built configurations of the DST as far as possible was generated to carry out the TOUGH2 simulations. Rock properties from the UZ Drift Scale Flow/Transport property set were used. In this property set, an AFM was implemented to model the fracture-matrix interaction area reduction, the liquid- and gas-phase relative permeabilities, and the capillary pressure.

Temperatures predicted by the TOUGH2 simulations are in good agreement with measured temperatures (Figure 25). Statistical measures established that the simulated temperatures were within acceptable margins of measured temperatures. It was also demonstrated that the liquid saturations in the fractures were extremely low, with an asymmetric distribution of saturations in the condensate zone just outside the drier-than-ambient area around the HD (with more condensate below the HD than above). The extremely low ambient water saturations in the fractures were attributed to the high porosities assigned to them. The asymmetric saturation distribution was attributed to the weak capillary suction and strong gravity-driven drainage. The liquid saturations in the matrix showed a symmetric build-up of condensate outside the drier-than-ambient zone around the HD, at least through the early phases of heating. Only in later phases of the heating cycle is there evidence of asymmetric build-up of the condensate in the matrix. Reduced fracture-matrix interaction areas and weak matrix-imbibition in a sensitivity analysis resulted in slow build up of asymmetry in matrix liquid saturations.

As part of a sensitivity analysis, thermal conductivities, liquid- and gas-phase permeabilities, and capillary pressures were identified as key parameters. The DKM-TT99 property set was selected to investigate how changes in the key parameter values would affect the simulation results. Even though the thermal conductivity values were different in the two property sets (DS/AFM-UZ99 base case and DKM-TT99), the temperature distributions were not greatly affected. A comparison of the statistical measures for the two property sets confirmed this further. In conclusion, the temperature distribution was not very sensitive to the ranges of thermal conductivity values used, and the thermal conductivities in the two property sets appear to be within an acceptable range. However, trends of MD and RMSD for the two property sets seem

to indicate that the rock mass in DST favors the dry thermal conductivity of 1.67 W/m°C and a wet thermal conductivity of 2.33 W/m°C.

Coupled TH processes are expected to contribute to second order effects on the temperature, and subtle second order differences did appear in the temperature distributions obtained from the two property sets. While the DKM-TT99 property set showed heat-pipe signatures at selected locations that were larger than the measured heat-pipe signatures at those locations, the converse was true for the base case property set. Since the heat-pipe signatures were mostly governed by convective heat transfer, the results were not as sensitive to the range of rock thermal properties investigated as they were to the range of rock TH properties.

Fractures in the DKM-TT99 property set appeared to be considerably wetter than those in the base case property set, both in the ambient liquid saturations and in the condensation build-up zone. The liquid saturations in the fractures also demonstrated a strong asymmetric build-up of condensate below the heater horizon. Saturation changes in the fractures from their ambient conditions with the DKM-TT99 property set were found to be more consistent with the air-injection test results. While the simulated saturation changes in the fractures with the base case property set would predict almost no reduction in air-permeability values, those with the DKM-TT99 property set resulted in predictions of air-permeability reductions consistent with field observations. The ambient matrix saturation in the DKM-TT99 property set was slightly lower than for the base case property set, and condensate build up was more asymmetric in the former through the entire duration of heating considered in this report. Early and consistent asymmetric distribution of matrix liquid saturations with the DKM-TT99 property set is attributed to stronger imbibition into matrix pores from the fractures owing to a combination of higher fracture-matrix interaction areas and stronger capillary suction in the fractures. ERT data indicated that for the condensation zones around the HD, the rock was wetter below the heater horizon than above. All these seem to favor the DKM-TT99 in capturing TH processes at the DST. However, based on the results of investigative analysis and systematic sensitivity analysis, both property sets are considered to have produced results that were within acceptable limits of the measured data from the DST.

6.4.3 Drift Scale Test - NUFT Simulations

Comparisons (Figure 51) between simulated and measured temperatures during the first six months of the DST show a tendency for the models to overpredict temperatures in the wing heater-array areas, particularly in the outer third (plus or minus x direction) of the wing-heater arrays. Several factors that are currently not considered in the base-case TH model contribute to this overprediction of temperature and other inaccuracies in prediction of temperature elsewhere in the DST block:

- Approximation of the circular cross section of the heater drift geometry by a square cross-section of equal area. This approximation affects accuracy of the calculations immediately adjacent to the heater drift wall and at early times when the changes at the HD are confined to this region. However, the overall pattern of heat, water and water vapor is not seriously affected.

- Smearred representation of the wing heater arrays. This approximation affects the accuracy of the calculations in the immediate neighborhood of the array. Again, this approximation does not seriously affect the overall pattern of heat, water and water vapor in the DST. Nonetheless, assumptions related to heater power should be further investigated to ensure future simulations properly reflect test conditions.
- Approximate modeling of in-drift conduction and convective heat transfer using the pseudo-porous medium approximation.
- Neglect of the near-field damage zone, and neglect of the initial drying of the near field due to ventilation during construction and to water and water vapor drainage from the rock mass into the HD during the early heating phase.
- Neglect of preferential vapor flow and its associated latent heat along the wing heater boreholes entering the HD and exiting the thermal bulkhead.
- Smearing of wing heater array heat sources deters drainage of condensate between the wing heater boreholes, thereby preventing much of the buildup of condensate that occurs above the wing heater arrays at early stages of the simulations.
- Neglect of nonequilibrium fracture-matrix flow that can allow condensate drainage to proceed much further before being imbibed by the rock matrix. Allowing condensate to drain far below the heater horizon increases heat convection away from the immediate DST area, which would lower simulated temperatures in the DST.
- Lack of measurements of the thermal conductivity of wet fiberglass insulation to adequately represent conductive heat loss out of the bulkhead. The current base-case model probably underrepresented this heat loss.
- Use of tuff properties to represent the concrete invert. Properties for concrete used in the TSPA-VA should be incorporated into the model since they better account for the effect of the heat of hydration and for the influence of fractures and joints in the concrete.
- Lack of representation of the concrete liner in part of the drift. This could be incorporated in the TH model along with improved hydrologic properties for concrete mentioned previously.
- Lack of heterogeneity of fracture properties in the TH model. These could assess whether local heat pipes, small-scale buoyant gas-phase convection cells, or focused condensate drainage might occur within highly fractured zones and thereby result in regions of preferential heating or preferential cooling.

Improved modeling of the HD geometry using a stepped approximation to the circular cross-section can be done at increased cost of performing the radiation computations within the HD. Likewise, the wing heater arrays can be more accurately represented using a finer grid in those locations to capture the gaps between the individual heaters in axial and radial directions.

However, this will only affect the local temperature comparisons, and not the overall patterns of heat and mass flow. It is feasible to embed a finer grid for a limited subset of the wing heaters to "sample" these effects.

The conduction and convective heat transfer within the pseudo-porous medium that represents the air within the HD only partially accounts for the heat transferred by these two modes. The impact of this approximation significantly affects only the local temperature field at the apex of the drift crown because radiation dominates the total heat transfer. However, this approximation can partially account for the measured temperatures that are significantly higher at the drift crown apex than the predicted temperatures. The pseudo-porous medium approximation can be used to better represent this difference by using a thermal conductivity that is dependent on the waste package to drift wall temperature difference. This can be done using heat transfer correlations available in the literature for natural convection between concentric cylinders occupied by air and by an air-filled porous medium.

The initial dryout due to construction ventilation and early water or water vapor drainage into the HD should be considered in future DST analyses. Also, heterogeneity of fracture properties and nonequilibrium fracture flow can be readily accommodated in the TH model.

Addressing the preferential vapor flow and condensate drainage along the wing heater boreholes would require that the wing heater boreholes be discretely represented in the TH model. The additional computer processing from the usage of the DKM has little local benefit near a smeared-heat-source representation of the wing heater arrays.

Improved modeling of the thermal bulkhead requires laboratory measurements of dry and wet fiberglass insulation thermal conductivity as well as the monitoring of the moisture loss out of the thermal bulkhead. The moisture loss out of the bulkhead is probably the most significant TH modeling uncertainty at this time. Accurate modeling of the concrete invert may also require laboratory measurements.

6.4.4 Large Block Test

Results of the sensitivity analysis using the five property sets are summarized as follows:

- Simulation results obtained using the CON and DS property sets show better agreement with the measured temperatures than simulation results obtained using the MS and MSLK properties.
- All five property sets generally overpredict temperatures in and adjacent to the heater horizon, but the degree of overprediction is less for the MSLF, CON and DS properties and greater for the MSLK properties.
- The RMSD and MD statistical measures for all five properties sets indicate that the agreement with measured data generally increases as the test progresses (Figure 66).
- Higher fracture permeability above the heater horizon reduced the overprediction of temperature observed with MS properties but showed a strong reflux zone not seen in the measured data.

- The dryout zone modeled using the DS properties is significantly smaller than the zones modeled using the MS properties and the zones measured in the test.

6.5 THERMAL TEST MODEL VALIDATION

The purpose of this AMR is to compare process and performance assessment (PA) model predictions to data obtained from three in situ tests of varying duration (275 days to over 18 months) and scale (a few meters to over ten meters of above-boiling temperatures). Temperature data were used for the comparisons, with a semi-quantitative comparison of hydrological data. A number of TH property sets have been used in PA and design calculations, whereas this AMR uses alternative sets of TH property sets in the conceptual and mathematical models developed to calculate repository performance during the thermal pulse that will be caused by the radioactive decay heat.

Each of the simulations of the thermal tests in this AMR can be considered a model. These models have a high degree of similarity to the repository PA models, since the purpose of the AMR is to provide an analysis of the validity of those models within the limited temporal and spatial scales of the field tests. The use of alternative input property sets in each of these models could be regarded as alternative models, if the properties are considered a part of the models themselves. The following sections describe the models used for each field test, including an assessment of their validity for the intended purpose.

The validation criteria described in this section are based on the statistical measures for temperature defined in Section 6.2.1.2, namely the RSMD and the MD. The RSMD, which is calculated as a weighted average at several times during the thermal pulse for each of the models, is a measure of the variability of the difference between measured and simulated values. The MD, also calculated as a weighted average at several times during the test, is a measure of the bias of the difference between measured and simulated values. The NAMD, which includes the weighting, provides the normalized absolute difference between measured and simulated temperatures. Because NAMD tends to overstate the differences when measured temperatures are near ambient, temperatures within 5 °C of ambient are not considered. For the average of these times, a value within 10°C for both RSMD and MD and a NAMD of less than 20 percent are established as validation criteria for the purpose of these field test models. The criteria were applied to the "all data" category. For completeness, the "above boiling" and "below boiling" categories were also provided in the respective tables for the four sets of simulations.

It is premature to develop hydrology validation criteria for these models. This is because of the preliminary nature of the analysis of hydrologic processes in these tests, as discussed in Sections 6.2.2, 6.2.3, 6.2.4, 6.3.2, and 6.3.4. Development and application of such criteria is deferred to a later report.

6.5.1 The Single Heater Test as Simulated by the TOUGH2 Model

TOUGH2 (Pruess 1991) is a computer code developed for a number of earth science applications, with the current model designed to support UZ flow and transport under both ambient and thermally perturbed conditions, for a repository in unsaturated fractured rock. The conceptual model implemented by the software includes dual continua for fractures and matrix

and an AFM for the interaction between the two continua. Heat transfer modes include radiation, convection, and conduction. Multiple species, including liquid water and water vapor can be transported due to pressure gradients, gravity, and capillary forces. Latent heat effects are included in both the heat and mass transfer. These conceptual models are discussed in considerable detail in the Unsaturated Zone Flow and Transport Process Model Report (CRWMS 2000b) and its supporting AMRs, particularly CRWMS 2000c, CRWMS 2000d, and CRWMS 2000e.

The geometry, boundary conditions, initialization procedure, and alternative property sets to be used in this model were described in Sections 4.1, 5.1, 5.2, and 6.1.1. The results of the comparisons of measured and simulated temperatures for the SHT are discussed in Sections 6.2.1 and 6.3.1. These results are summarized in Figure 18 and in Table 10.

Table 10. Model Validation Results for the Single Heater Test TOUGH2 Model^a

Criterion	RMSD	MD	NAMD
	Average "All Data" ≤10°C	Average "All Data" ≤10°C	≤20% (for reference only, not applied)
	Average(Max)	Average(Max)	Average(Max)
DS Property Set			
All data	7 (7) °C	-3 (-5) °C	8 (10) %
Above boiling data	9 (10) °C	-7 (-9) °C	7 (9) %
Below boiling data	4 (6) °C	-1 (-3) °C	8 (10) %
Median k_b Property Set			
All data	5 (6) °C	0 (-3) °C	8 (9) %
Above boiling data	6 (8) °C	-3 (-6) °C	5 (7) %
Below boiling data	4 (5) °C	1 (2) °C	10 (11) %
TSPA-VA Property Set			
All data	9 (10) °C	-5 (-6) °C	10 (11) %
Above boiling data	13 (15) °C	-11 (-14) °C	11 (12) %
Below boiling data	4 (5) °C	-1 (-2) °C	9 (11) %

^a The average values are presented, with the worst case values also shown in parentheses. Acceptable results, based on the stated criteria, are indicated in bold italic font. All Data values were compared to the criteria to evaluate acceptability.

From the perspective of temperature prediction, the Median k_b property set is preferred for simulating the SHT with TOUGH2. The DS and TSPA-VA property sets, also meet the criterion of the model validation. However, this model validation does not fully address hydrological behavior as well as mechanical and geochemical aspects of the tests. Since the focus in this AMR was selection of properties that could be most appropriate for PA and design calculations, validation of the repository conceptual models adapted to the field tests has been addressed at a very limited extent.

6.5.2 The Drift Scale Test as Simulated by the TOUGH2 Model

TOUGH2 (Pruess 1991) was used in a similar manner as discussed in the previous section (Section 6.5.1).

The geometry, boundary conditions, initialization procedure, and alternative property sets to be used in this model were described in Sections 4.1, 5.1, 5.3.1, and 6.1.2. The results of the comparisons of measured and simulated temperatures for the DST-TOUGH2 model are discussed in Sections 6.2.2 and 6.3.2. These results are summarized in Figure 25 and in Table 11.

Table 11. Model Validation Results for the Drift Scale Test TOUGH2 Model^a

Criterion	RMSD	MD	NAMD
	Average "All Data" ≤10°C	Average "All Data" ≤10°C	≤20% (for reference only, not applied)
	Average(Max)	Average(Max)	Average(Max)
DS/AFM-UZ99 Property Set			
All data	8 (9) °C	3 (4) °C	11 (13)%
Above boiling data	10 (11) °C	3 (7) °C	8 (10) %
Below boiling data	5 (6) °C	3 (5) °C	15 (23) %
DKM-TT99 Property Set			
All data	8 (11) °C	2 (4) °C	11 (12) %
Above boiling data	10 (13) °C	3 (6) °C	8 (10) %
Below boiling data	5 (6) °C	2 (4) °C	12 (15) %

^a The average values are presented, with the worst case values shown in parentheses. Acceptable results, based on the stated criteria, are indicated in bold italic font. All Data values were compared to the criteria to evaluate acceptability.

From the perspective of temperature prediction, the both the DS/AFM-UZ99 and DKM-TT99 property sets both meet the validation criteria. However, this model validation does not fully address hydrological behavior as well as mechanical and geochemical aspects of the tests. Since the focus in this AMR was selection of properties that could be most appropriate for PA and design calculations, validation of the repository conceptual models adapted to the field tests has been addressed at a very limited extent.

6.5.3 The Drift Scale Test as Simulated by the NUFT Model

NUFT (Nitao 1993) is a computer code developed for a number of earth science applications, with the current model designed to support UZ flow and transport under both ambient and thermally perturbed conditions, for a repository in unsaturated fractured rock. The conceptual model implemented by the software includes dual continua for fractures and matrix and an AFM for the interaction between the two continua. Heat transfer modes include radiation, convection, and conduction. Multiple species, including liquid water and water vapor can be transported due to pressure gradients, gravity, and capillary forces. Latent heat effects are included in both the heat and mass transfer. The state of the art numerical methods allow nested grids and extremely

high computational efficiency. The NUFT conceptual models are discussed in more detail in another AMR (CRWMS M&O 2000f).

The geometry, boundary conditions, initialization procedure, and alternative property sets to be used in this model were described in Sections 4.1, 5.1, 5.3.2, and 6.1.3. The results of the comparisons of measured and simulated temperatures for the DST-NUFT model are discussed in Sections 6.2.3 and 6.3.3. These results are summarized in Figure 51 and in Table 12.

Table 12. Model Validation Results for the Drift Scale Test NUFT Model^a

Criterion	RMSD	MD	NAMD
	Average "All Data" ≤10°C	Average "All Data" ≤10°C	≤20% (for reference only, not applied)
	Average(Max)	Average(Max)	Average(Max)
DS Property Set			
All data	10 (11) °C	1 (6) °C	16 (26) %
Above boiling data	12 (16) °C	8 (12) °C	11 (15) %
Below boiling data	8 (11) °C	-1 (-6) °C	17 (27) %
MS Property Set			
All data	9 (11) °C	1 (4) °C	14 (20) %
Above boiling data	10 (12) °C	4 (4) °C	8 (10) %
Below boiling data	8 (10) °C	2 (6) °C	17 (21) %
MSLK Property Set			
All data	11 (13) °C	3 (7) °C	16 (22) %
Above boiling data	12 (15) °C	8 (9) °C	11 (12) %
Below boiling data	9 (11) °C	2 (6) °C	19 (23) %
CON Property Set			
All data	14 (19) °C	6 (12) °C	15 (17) %
Above boiling data	19 (25) °C	15 (21) °C	15 (19) %
Below boiling data	6 (8) °C	-1 (-2) °C	12 (18) %

^a The average values are presented, with the worst case values also shown in parentheses. Acceptable results, based on the stated criteria, are indicated in bold italic font. All Data values were compared to the criteria to evaluate acceptability.

From the perspective of temperature prediction, the DS and MS property sets meet the acceptance criteria. However, the MSLK, and CON property sets do not meet the criteria of the model validation because their RMSD values exceed the acceptance criterion of 10°C. This is discussed further in Section 6.5.5. However, this model validation does not fully address hydrological behavior as well as mechanical and geochemical aspects of the tests. Since the focus in this AMR was selection of properties that could be most appropriate for PA and design calculations, validation of the repository conceptual models adapted to the field tests has been addressed at a very limited extent.

6.5.4 The Large Block Test as Simulated by the NUFT Model

NUFT (Nitao 1993) was used in a similar manner as discussed in the previous section (Section 6.5.3).

The geometry, boundary conditions, initialization procedure, and alternative property sets to be used in this model were described in Sections 4.1, 5.1, 5.4, and 6.1.4. The results of the comparisons of measured and simulated temperatures for the LBT are discussed in Sections 6.2.4 and 6.3.4. These results are summarized in Figure 66 and in Table 13.

Table 13. Model Validation Results for the Large Block Test NUFT Model^a

Criterion	RMSD	MD	NAMD
	Average "All Data" ≤10°C	Average "All Data" ≤10°C	≤20% (for reference only, not applied)
	Average(Max)	Average(Max)	Average(Max)
DS Property Set			
All data	6 (9) °C	2 (8) °C	9 (18) %
Above boiling data	7 (11) °C	2 (11) °C	6 (12) %
Below boiling data	6 (9) °C	2 (8) °C	10 (18) %
MS Property Set			
All data	7 (9) °C	3 (8) °C	10 (18) %
Above boiling data	8 (13) °C	4 (6) °C	7 (14) %
Below boiling data	6 (9) °C	2 (8) °C	10 (18) %
MSFP Property Set			
All data	6 (9) °C	2 (8) °C	9 (18) %
Above boiling data	5 (6) °C	0 (4) °C	4 (5) %
Below boiling data	6 (9) °C	2 (8) °C	10 (18) %
MSLK Property Set			
All data	8 (11) °C	5 (8) °C	12 (19) %
Above boiling data	11 (17) °C	9 (17) °C	10 (18) %
Below boiling data	7 (10) °C	4 (8) °C	11 (19) %
CON Property Set			
All data	6 (10) °C	2 (9) °C	10 (22) %
Above boiling data	6 (10) °C	1 (9) °C	6 (10) %
Below boiling data	6 (10) °C	1 (9) °C	11 (22) %

^a The average values are presented, with the worst case values also shown in parentheses. Acceptable results, based on the stated criteria, are indicated in bold italic font. All Data values were compared to the criteria to evaluate acceptability.

From the perspective of temperature prediction, the LBT NUFT model met the acceptance criteria for all five property sets. However, this model validation does not fully address hydrological behavior as well as mechanical and geochemical aspects of the tests. Since the focus in this AMR was selection of properties that could be most appropriate for PA and design calculations, validation of the repository conceptual models adapted to the field tests has been briefly addressed.

6.5.5 Summary of Thermal Test Model Validation

The DS property set satisfies the thermal test model validation criteria for all four models (SHT-TOUGH2, DST-TOUGH2, DST-NUFT, and LBT-NUFT). Similarly, the MS, Median- k_b , TSPA-VA, DKM-TT99, and MSFP property sets also satisfied the validation criteria for the models in which they were tested. However, the MSLK and CON property sets satisfied the criteria for the LBT-NUFT model, but did not when applied to the DST-NUFT model. Consequently, only 2 of 14 property sets did not meet the RMSD criteria (although they satisfied the MS and NAMD criteria). The other 12 property sets satisfied all three criteria.

Further work is planned to identify in which geometric regions, and temperature and saturation ranges the two models (discussed above) perform differently. Then, the specific model features, such as treatment of the drift shape or mesh coarseness, can be evaluated and modified to improve the model performance. For the purpose of this report, the "acceptability" of the integrated model (including conceptual model, mathematical formulation, zoning, properties, boundary conditions, and initial conditions) is not an issue because 1) the aspects other than property sets were acceptable when alternative property sets were used, and 2) the purpose of the AMR was to compare multiple property sets to measured data. Finally, it was not expected that all property sets would produce the same temperatures; thus, a range of statistical measures were expected.

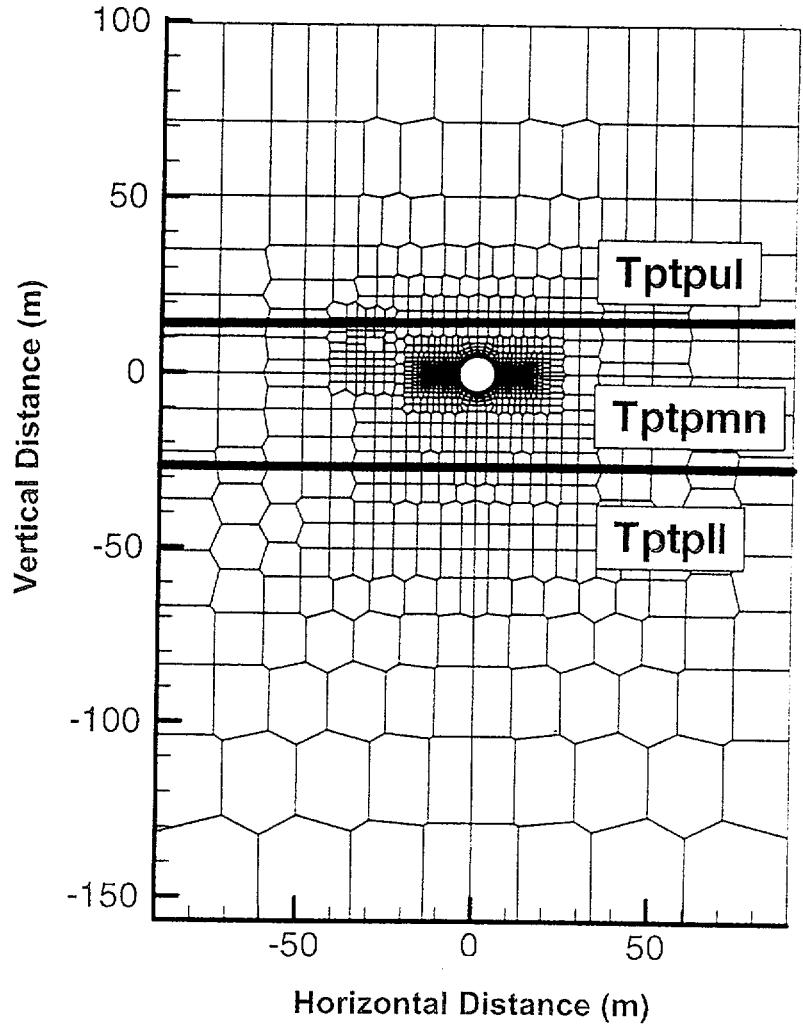


Figure 1. Vertical Cross Section of DST (TOUGH2) Numerical Grid Intersecting the HD at $Y \cong 10$ m from the Bulkhead and Containing Hydrology Boreholes 57-61

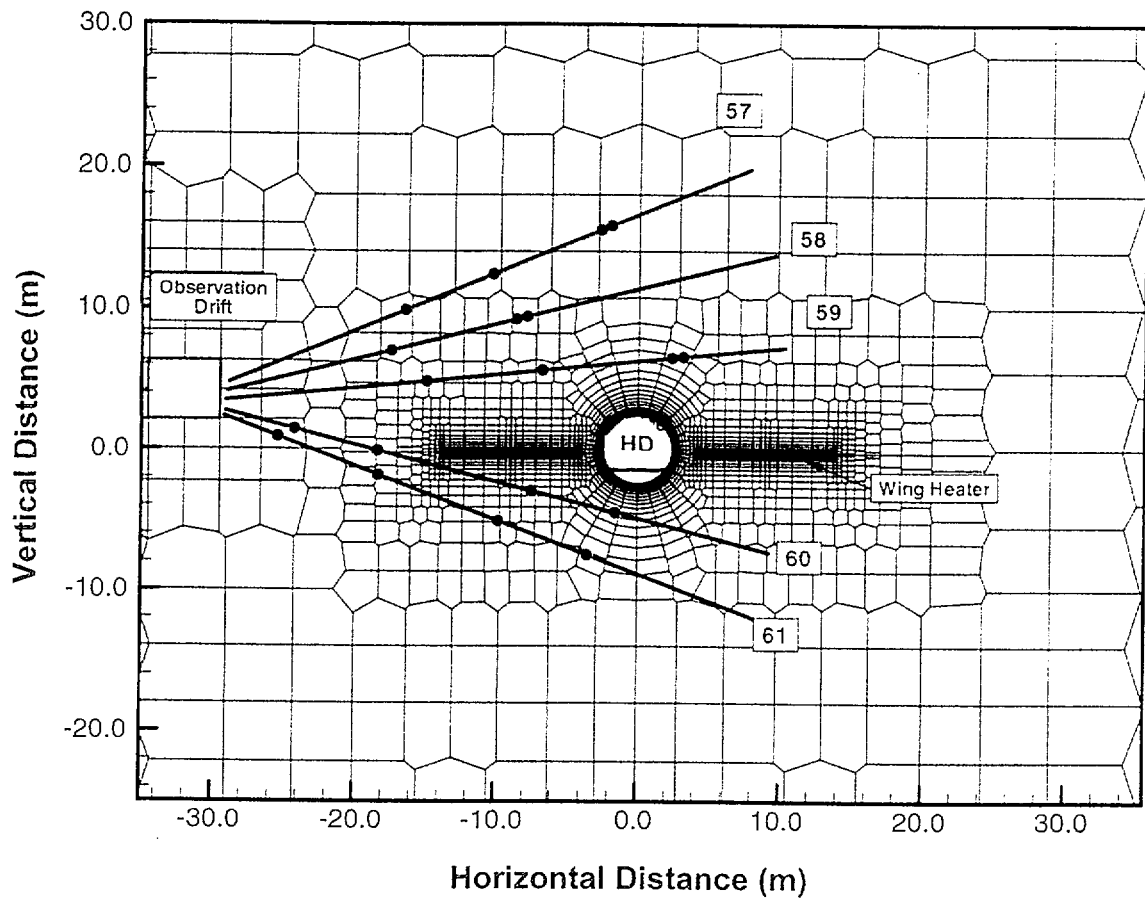


Figure 2. Detailed View of Vertical Cross Section of DST (TOUGH2) Numerical Grid through Plane Containing Hydrology Boreholes 57-61

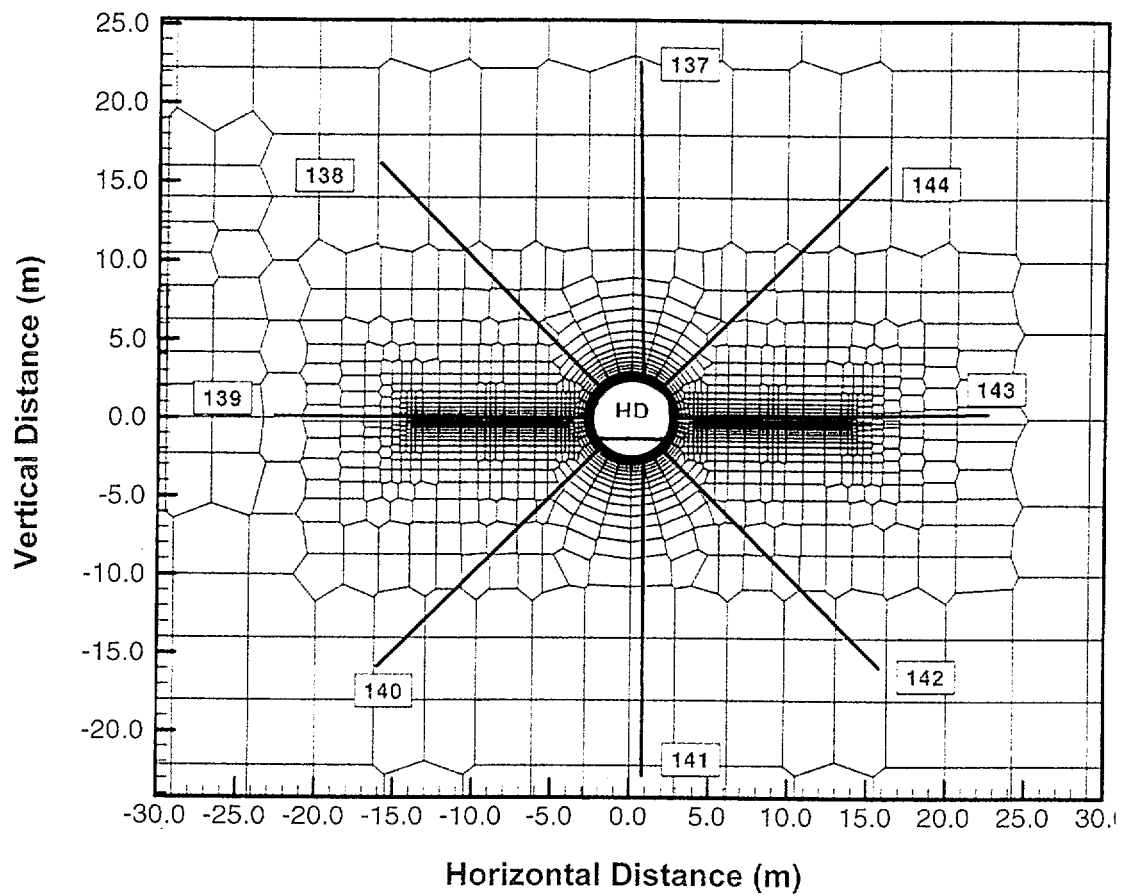
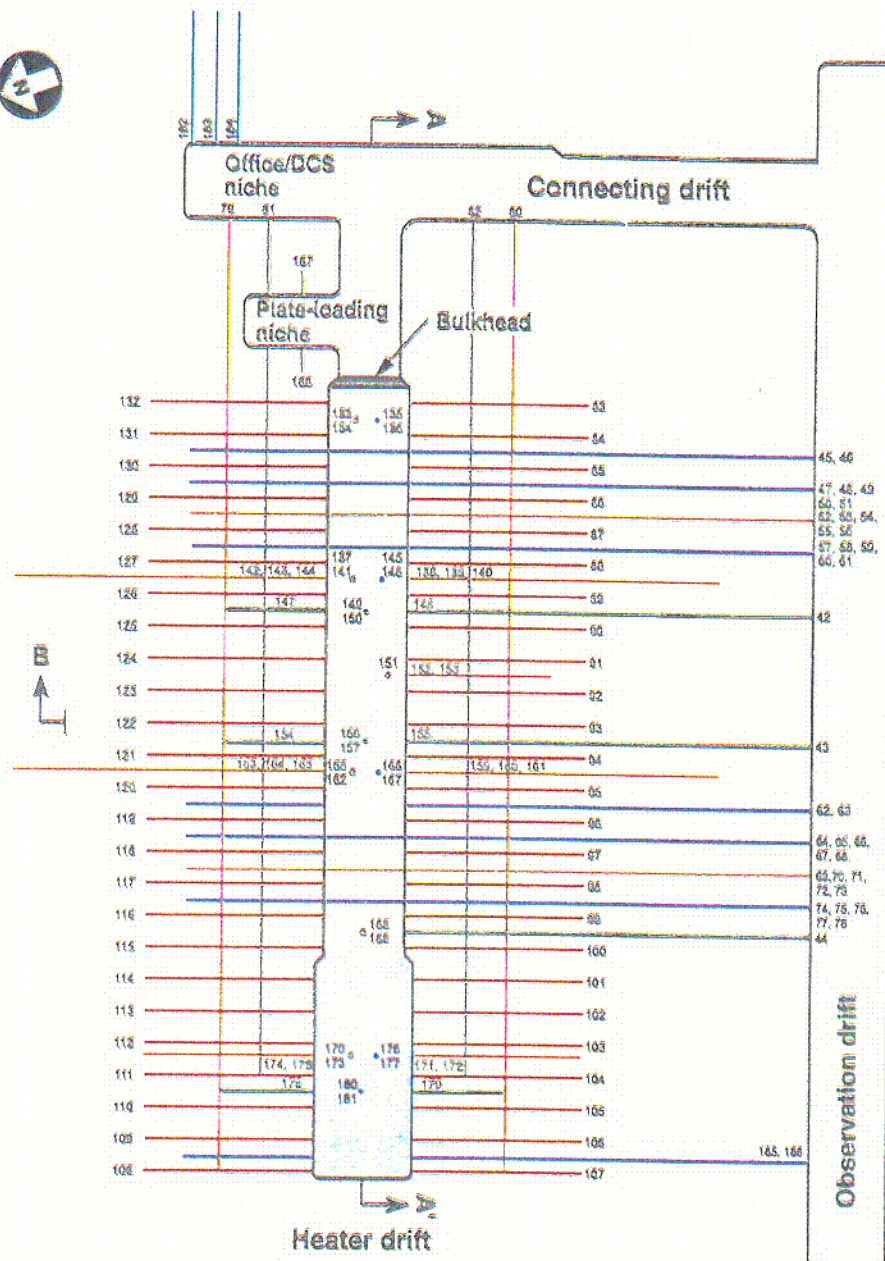
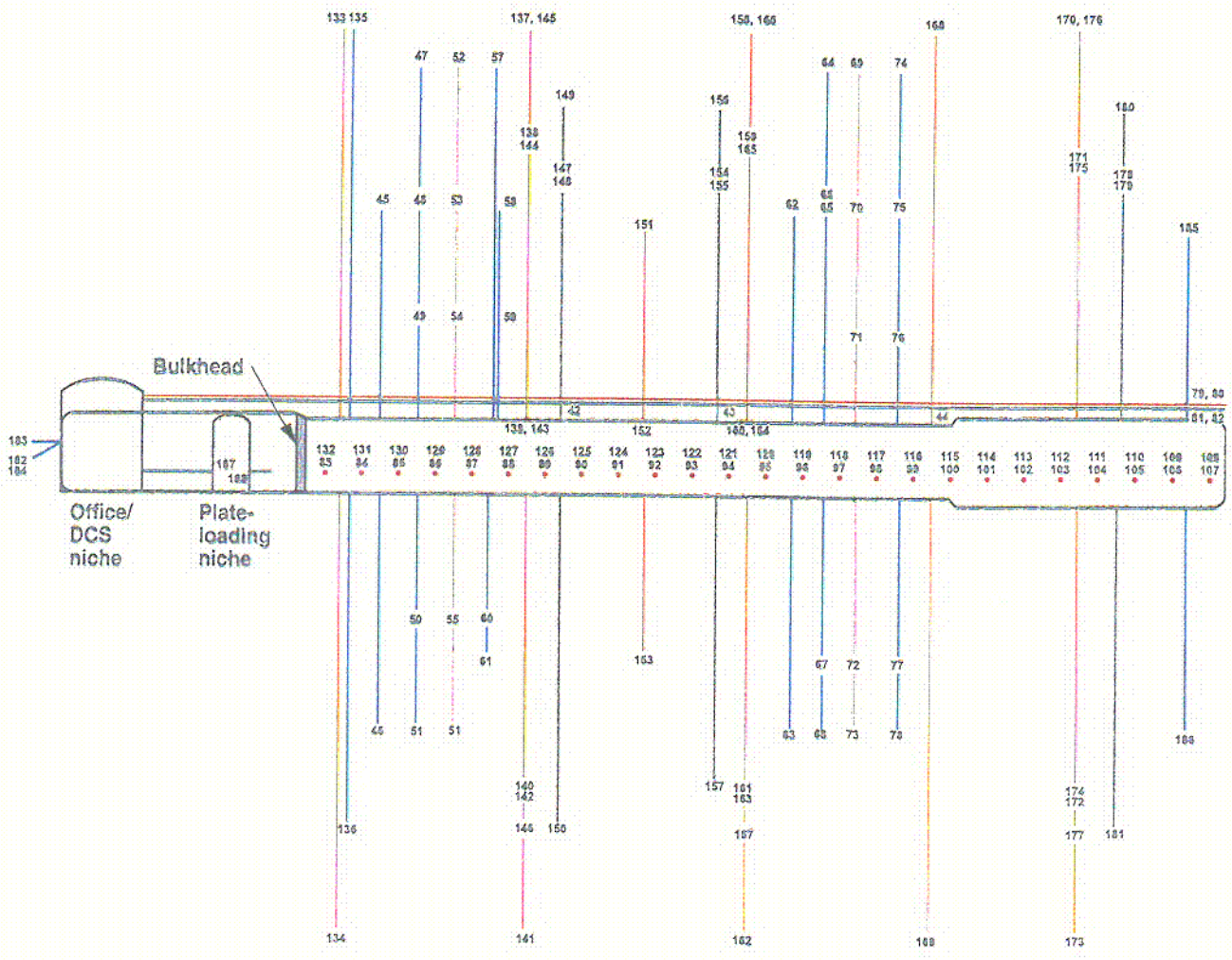


Figure 3. Detailed View of Vertical Cross Section of DST (TOUGH2) Numerical Grid through Plane Containing RTD Boreholes 137-144, Looking into the HD from the Bulkhead



- | | | | |
|--------------------------|--------------|---|--|
| LEGEND: Boreholes | | LEGEND: Ground support system | |
| Wing heaters | Hydrological | Rockbolts and welded wire used throughout heated drift for safety and stability purposes only | |
| Thermal | Chemical | Cast-in-place concrete | |
| Mechanical | | | |

Figure 4. Plan View of the DST

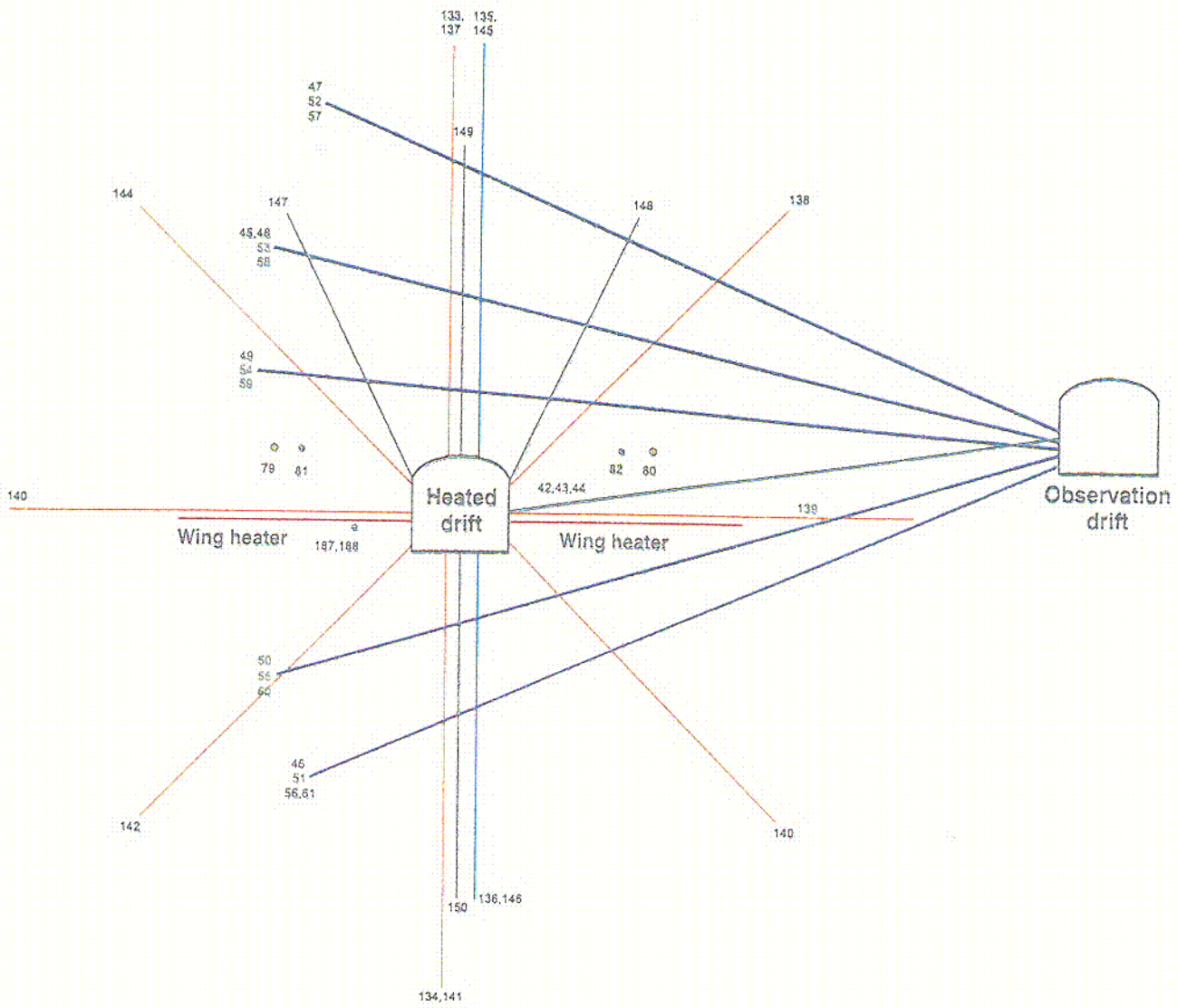


LEGEND: Boreholes

- Wing heaters
- Thermal
- Mechanical
- Hydrological
- Chemical

Figure 5. Cross Section (A-A') Parallel to the Heated Drift in the DST

C2



LEGEND: Boreholes

- Wing Heaters
- Thermal
- Mechanical
- Hydrological
- Chemical

Figure 6. Cross Section (B-B') Orthogonal to the Heated Drift in the DST

CB

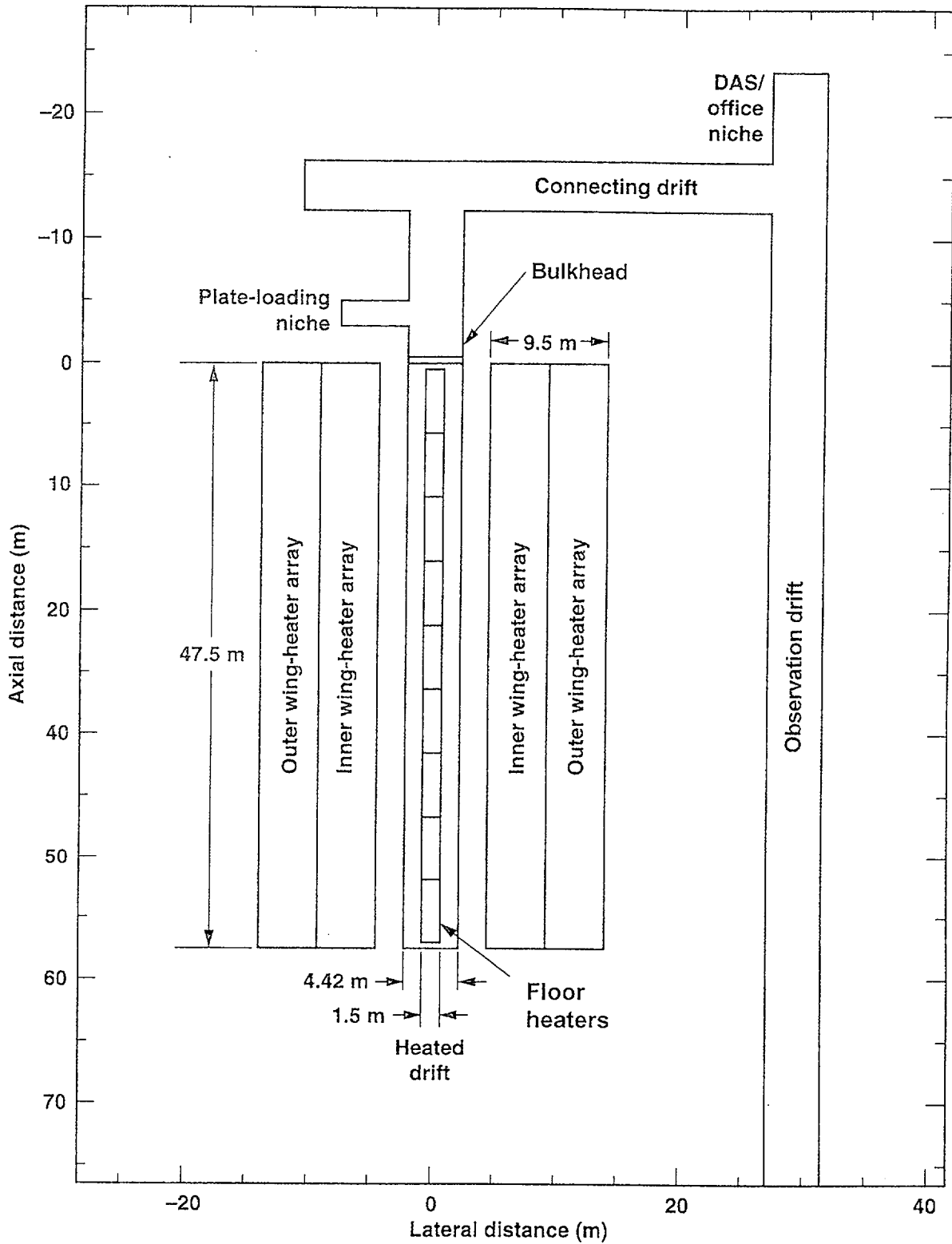


Figure 7. Idealized NUFT Computational Domain Used for Computing the TH Response of the DST

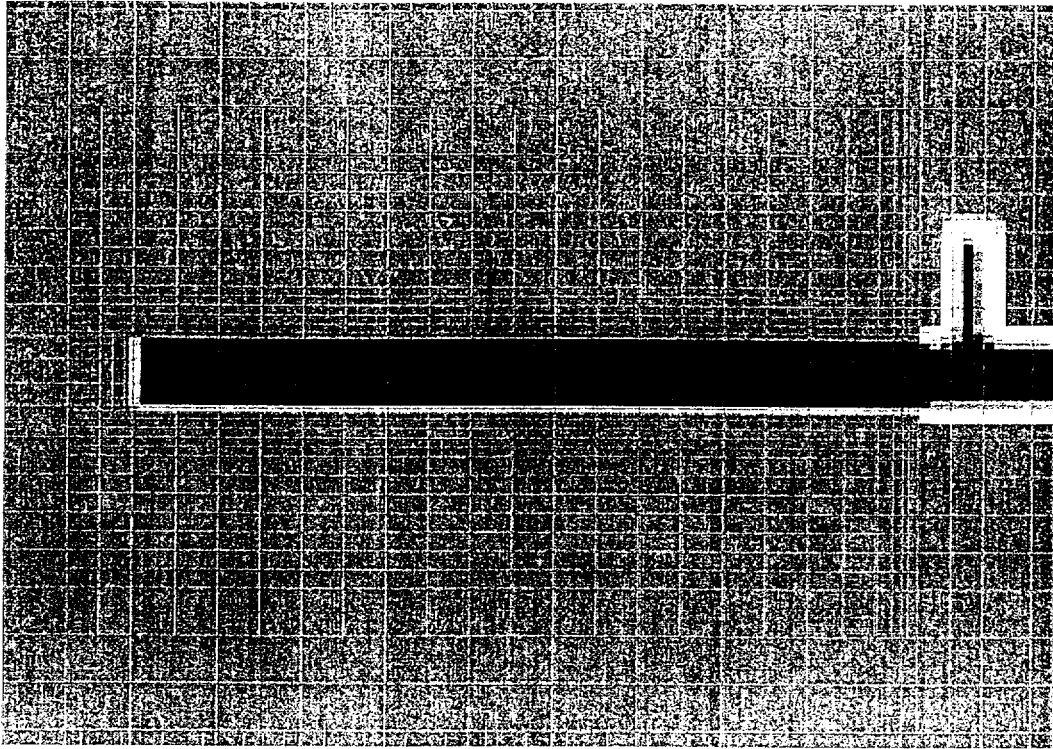


Figure 8. Horizontal Cross Section Passing through the Axis of the HD of the Nested-Mesh Finite Difference Computational Grid Employed for the DST (NUFT) Calculations

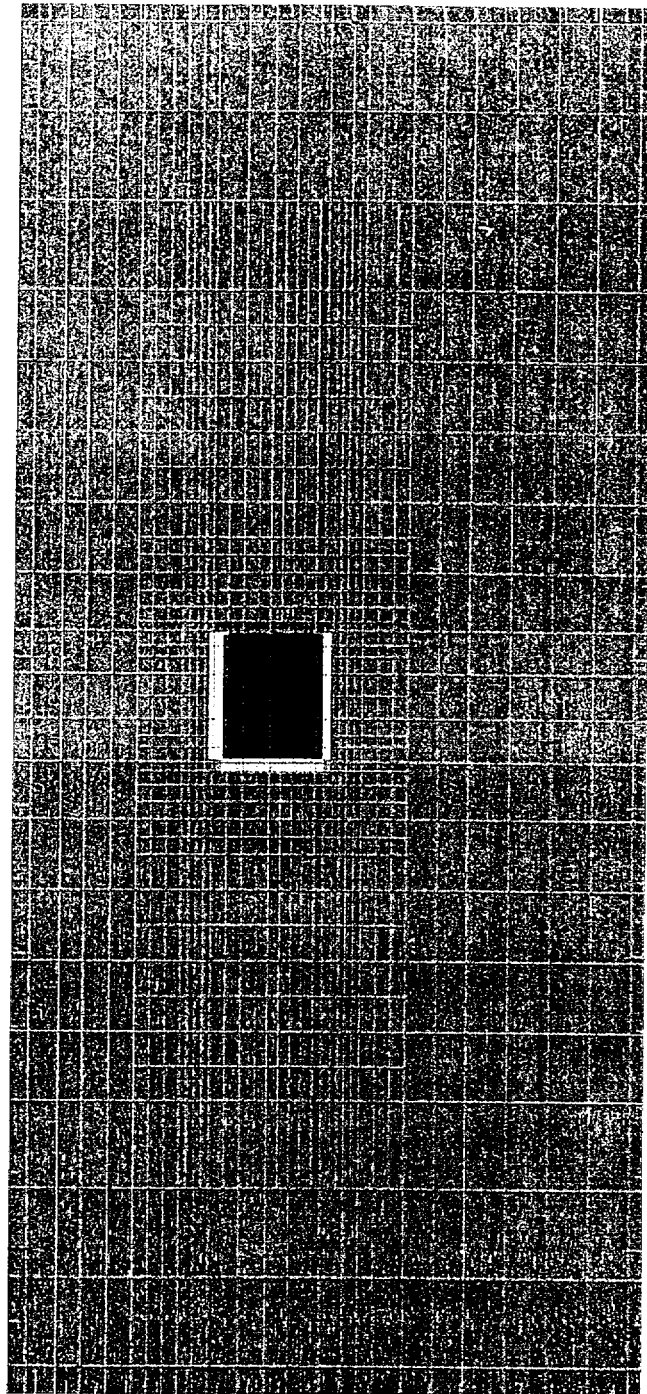


Figure 9. Vertical Cross Section Passing through the Mid-Point of the HD of the Nested-Mesh Finite Difference Computational Grid Employed for the DST (NUFT) Calculations

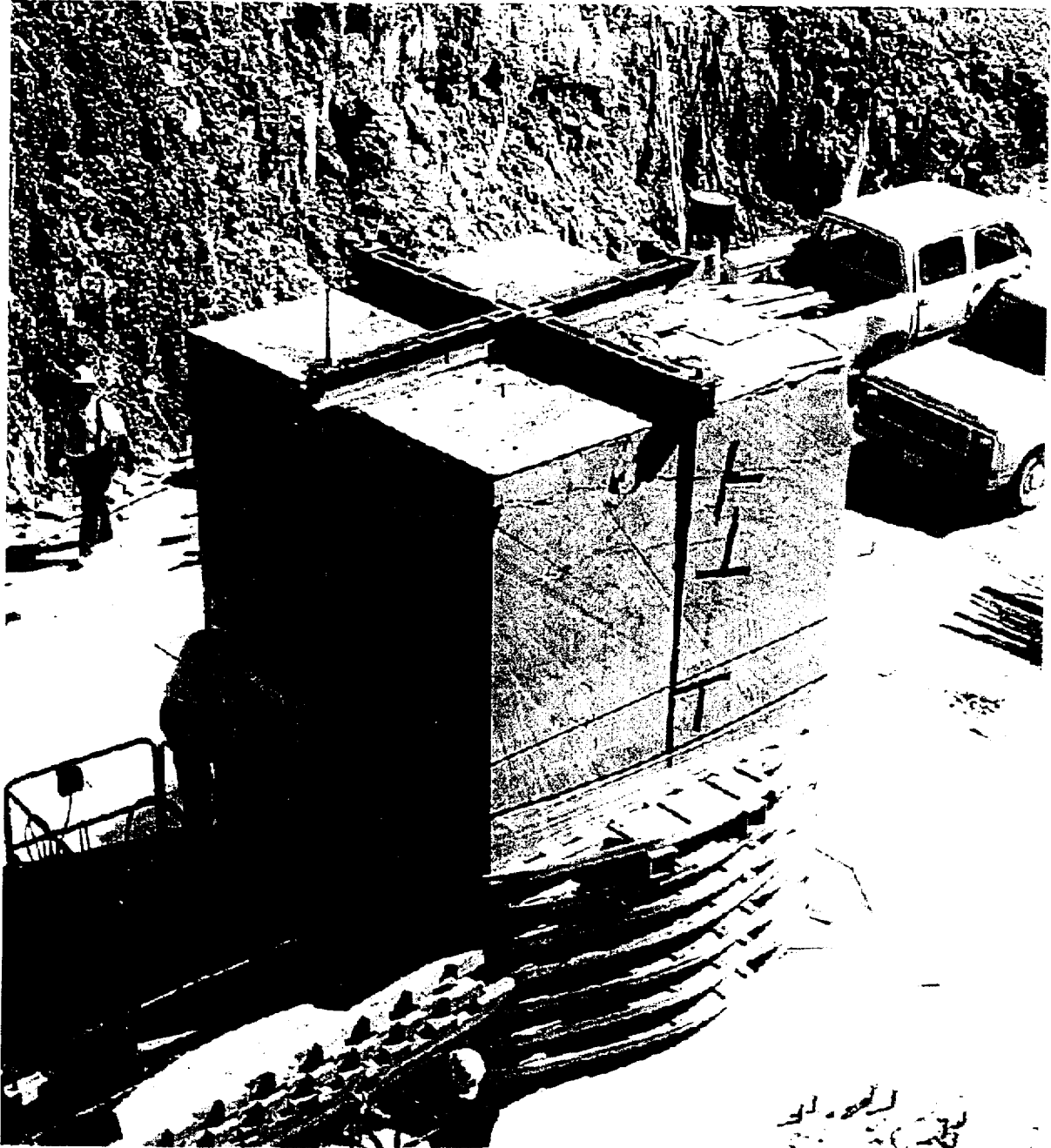


Figure 10. Photograph of Large Block Test (LBT) Site

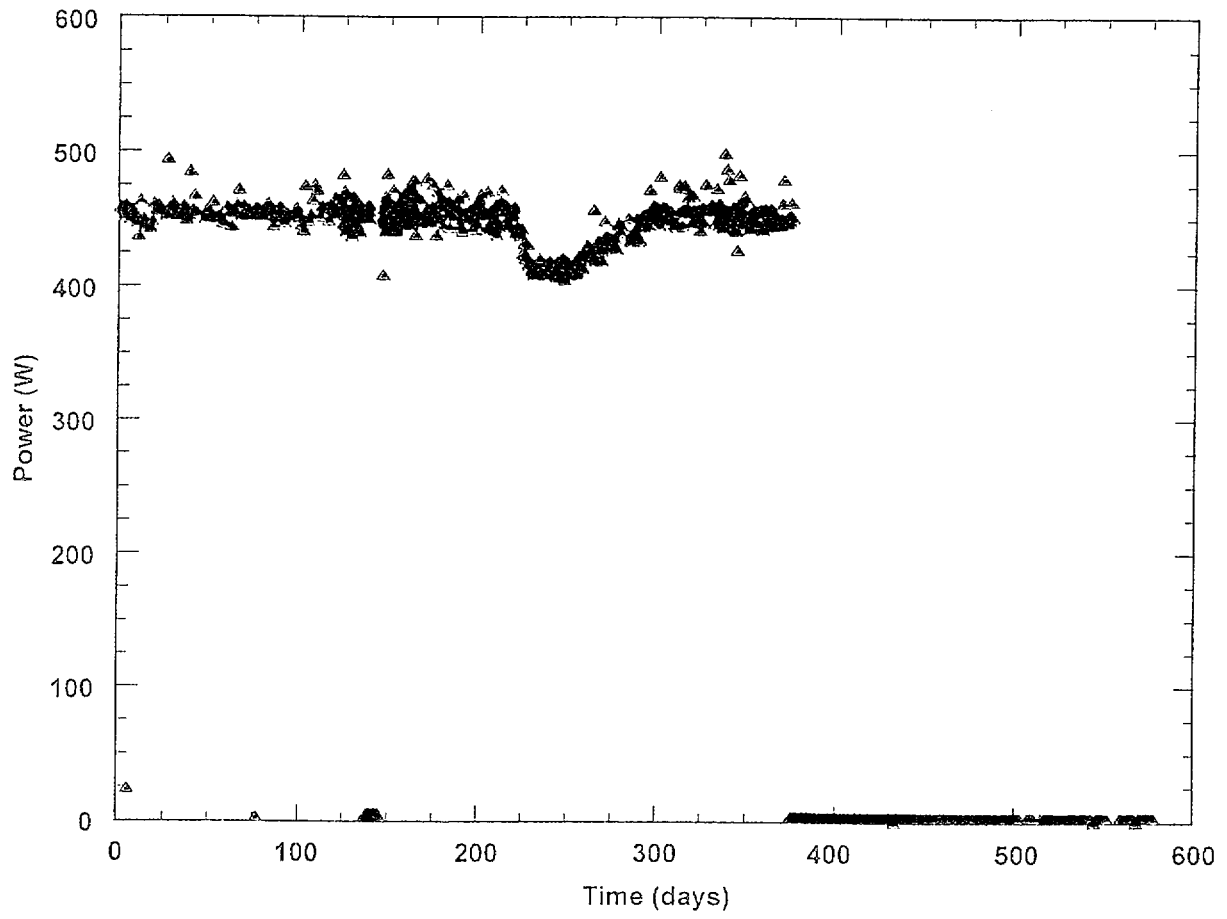


Figure 11. LBT Heating Power History for Heater No. 3

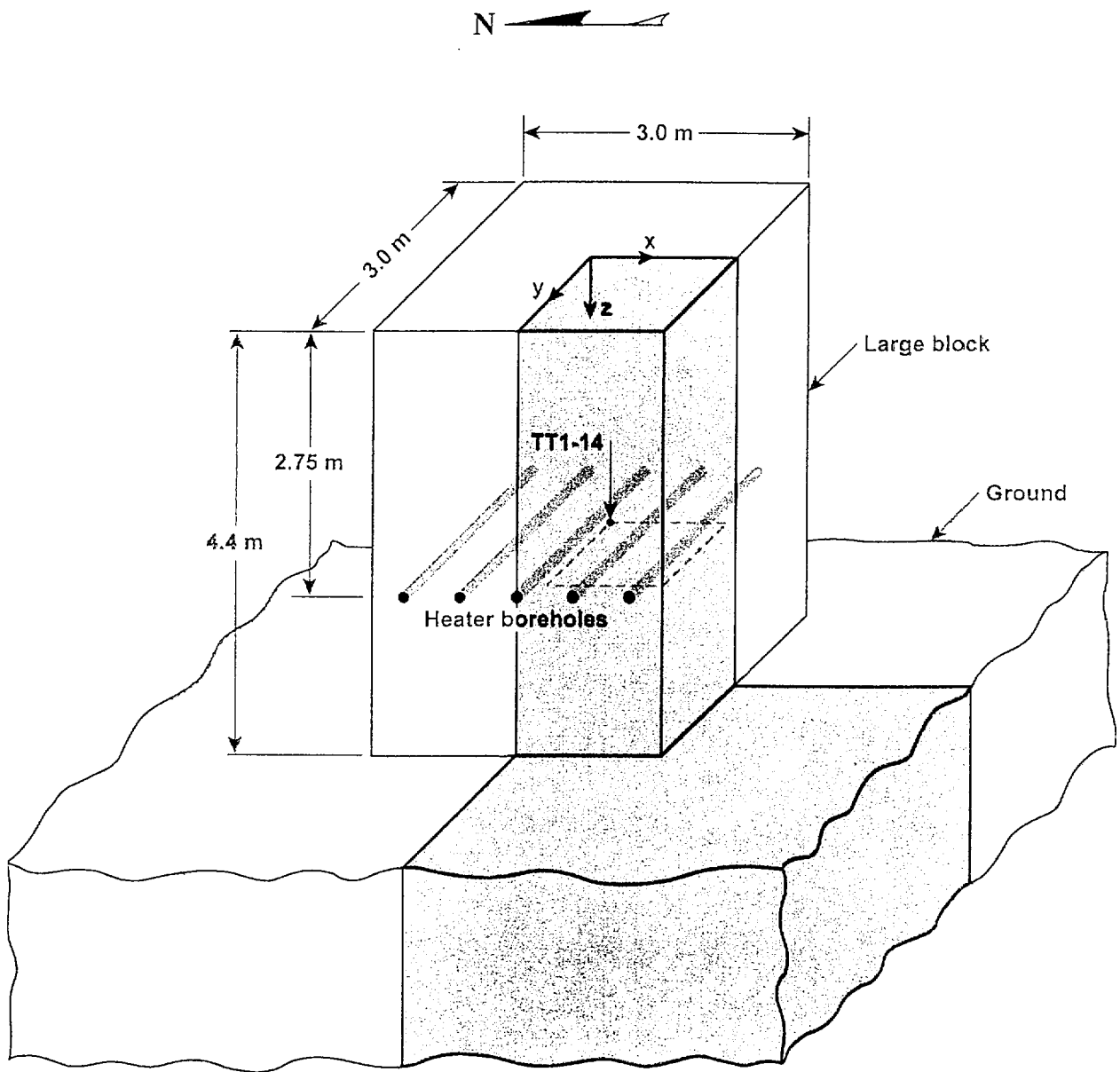


Figure 12. Schematic of the LBT Model Geometry (NUFT)

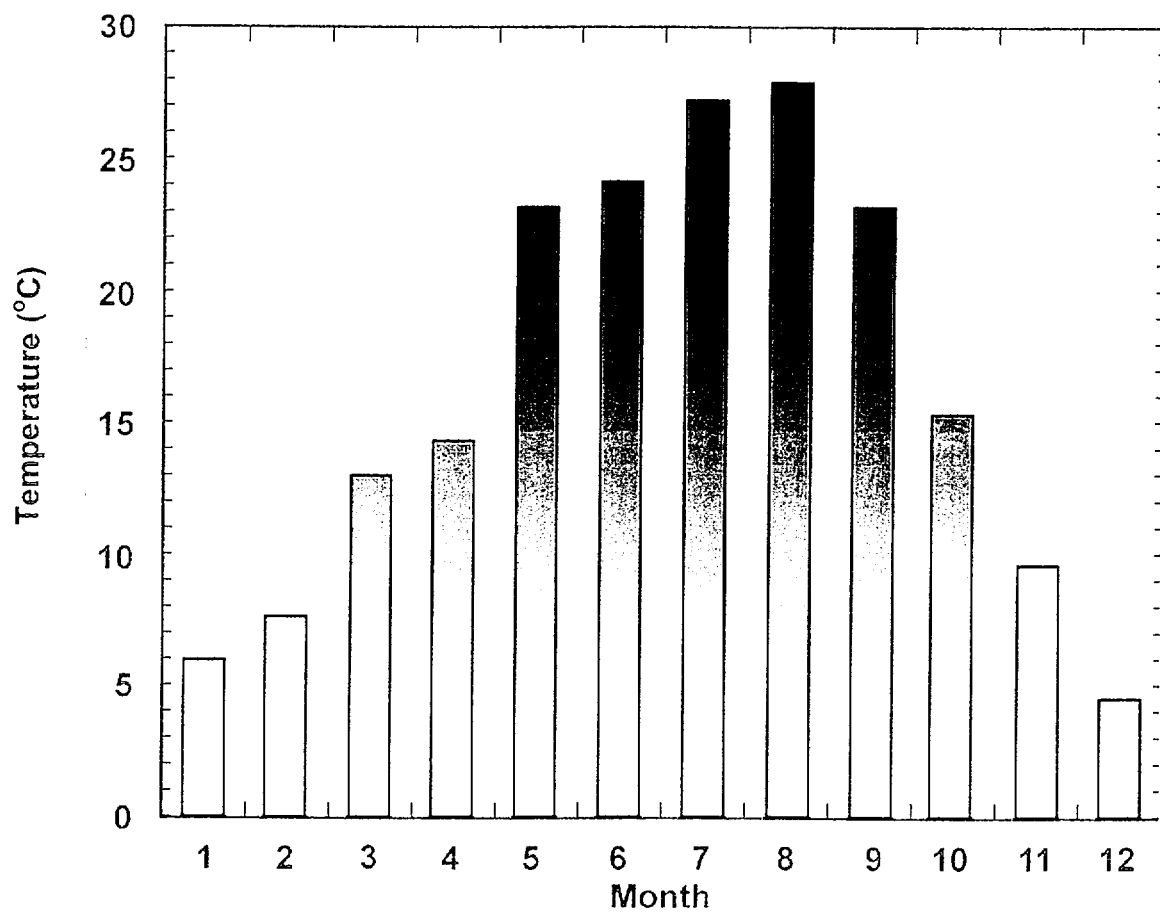


Figure 13. Monthly Average Air Temperature During 1997 Measured at Site 8 in Fran Ridge

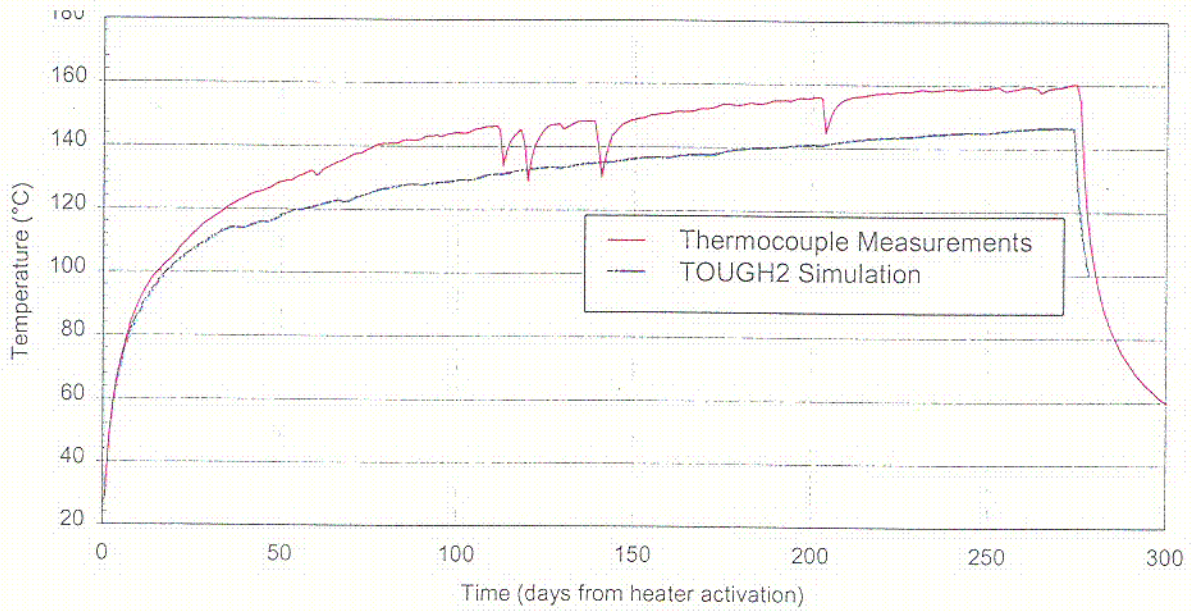


Figure 14. Comparison of the TOUGH2 Simulation Using the Drift-Scale Property Set and the SHT Measured Temperatures at Thermocouple Location TMA-TC-1A-7 (22 cm horizontally away from the heater center)

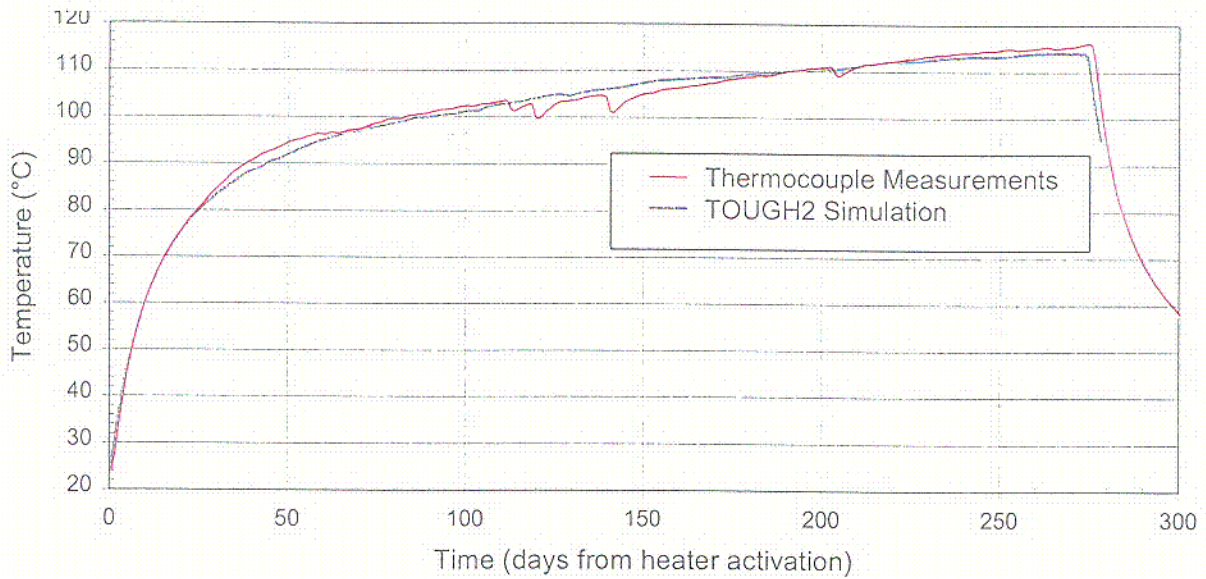


Figure 15. Comparison of the TOUGH2 Simulation Using the Drift-Scale Property Set and the SHT Measured Temperatures at Thermocouple Location TMA-TC-4A-6 (73 cm below the heater center)

c4

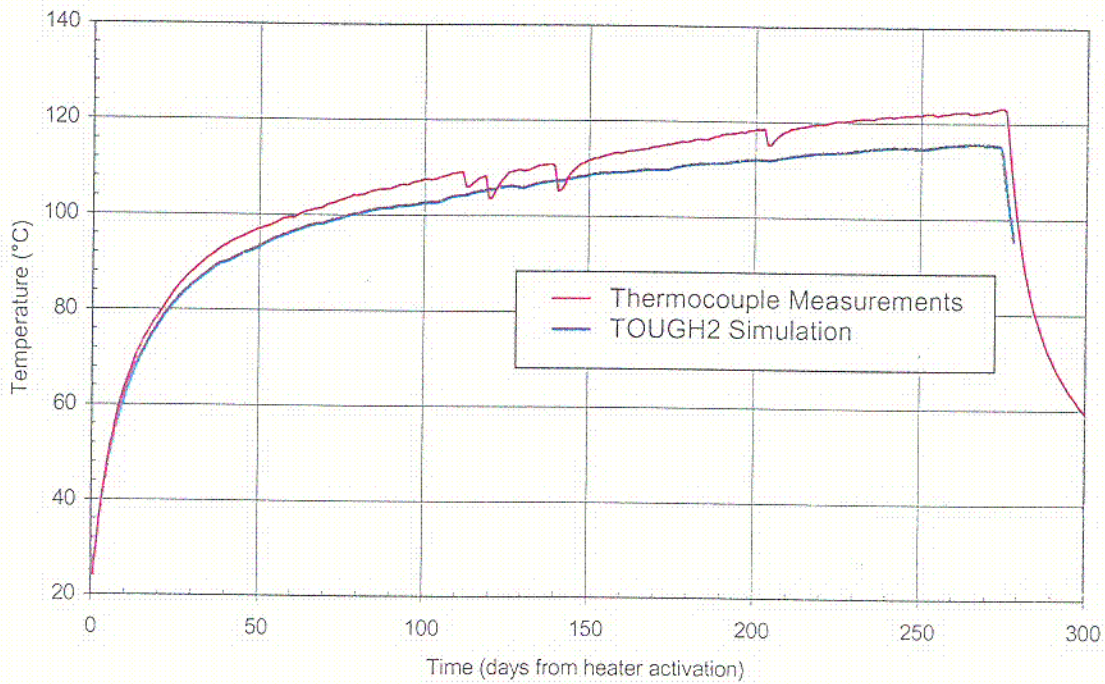


Figure 16. Comparison of the TOUGH2 Simulation Using the Drift-Scale Property Set and the SHT Measured Temperatures at Thermocouple Location TMA-TC-5A-7 (66 cm above the heater center)

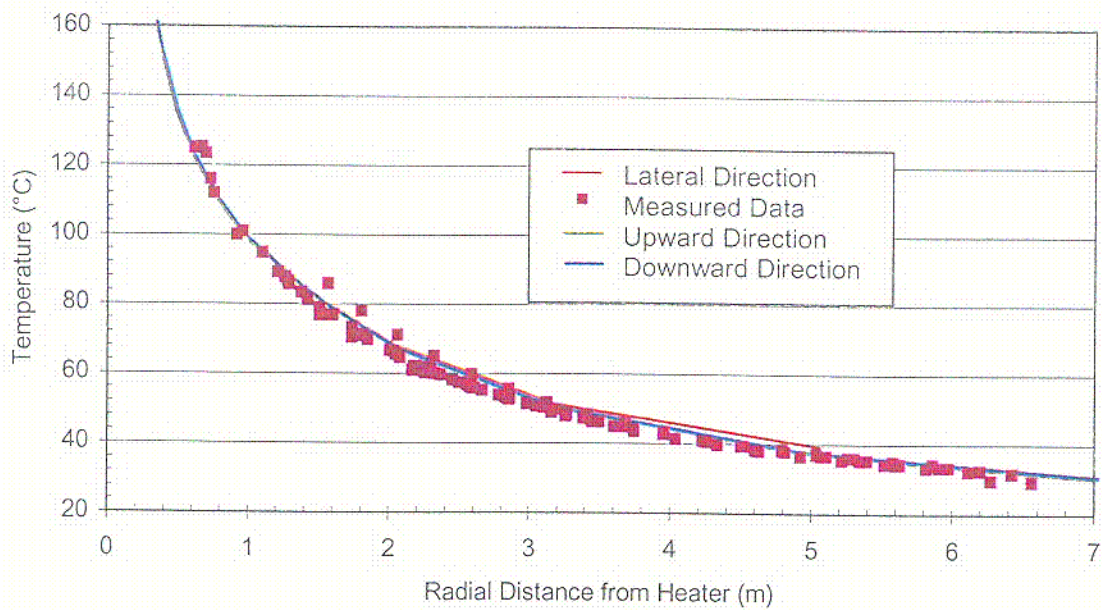


Figure 17. Comparison of the TOUGH2 Simulation Using the Drift-Scale Property Set and the SHT Measured Temperatures Radially Around Heater Mid-Length

C5

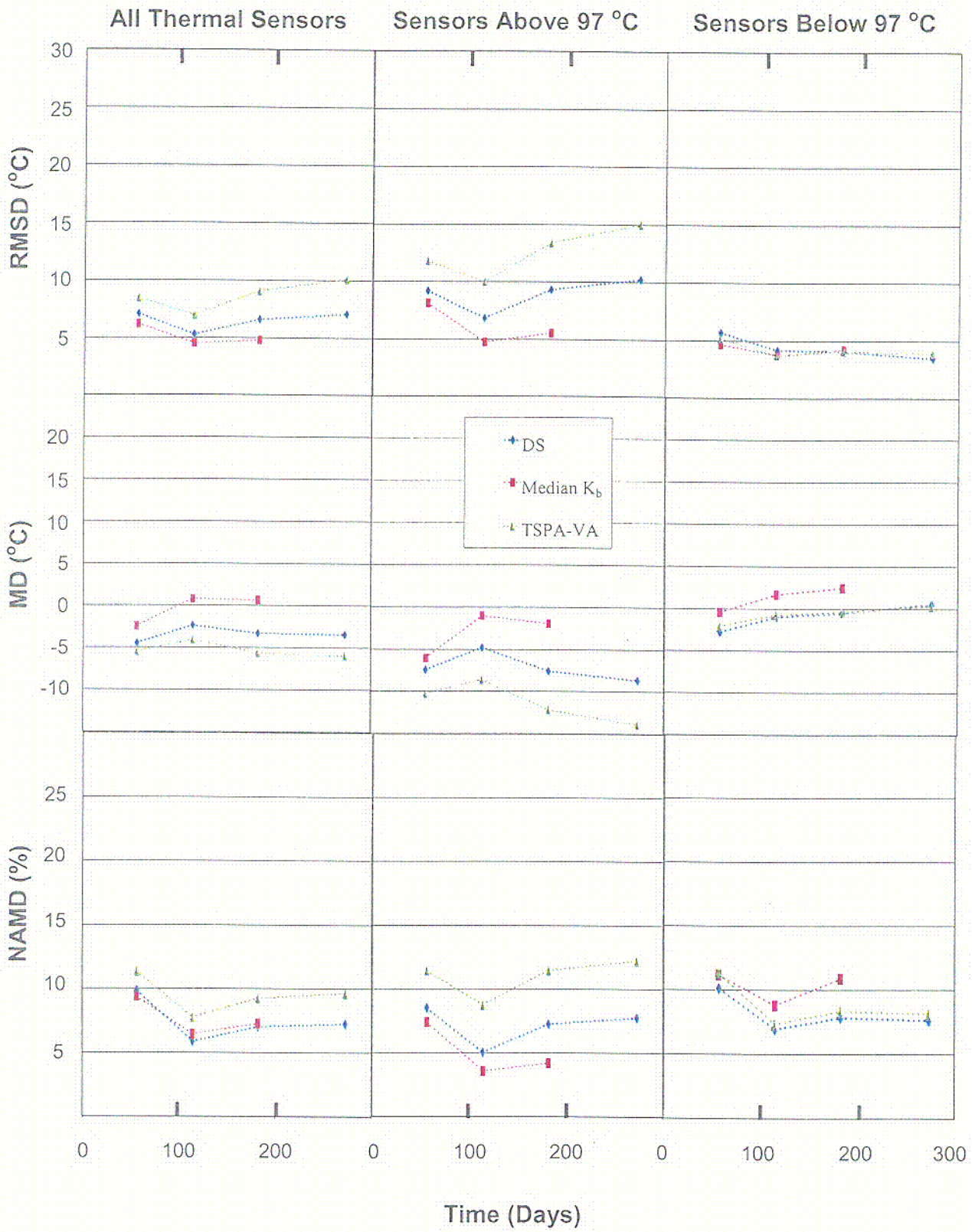


Figure 18. Statistical Measures for SHT Thermal Analyses

Cle

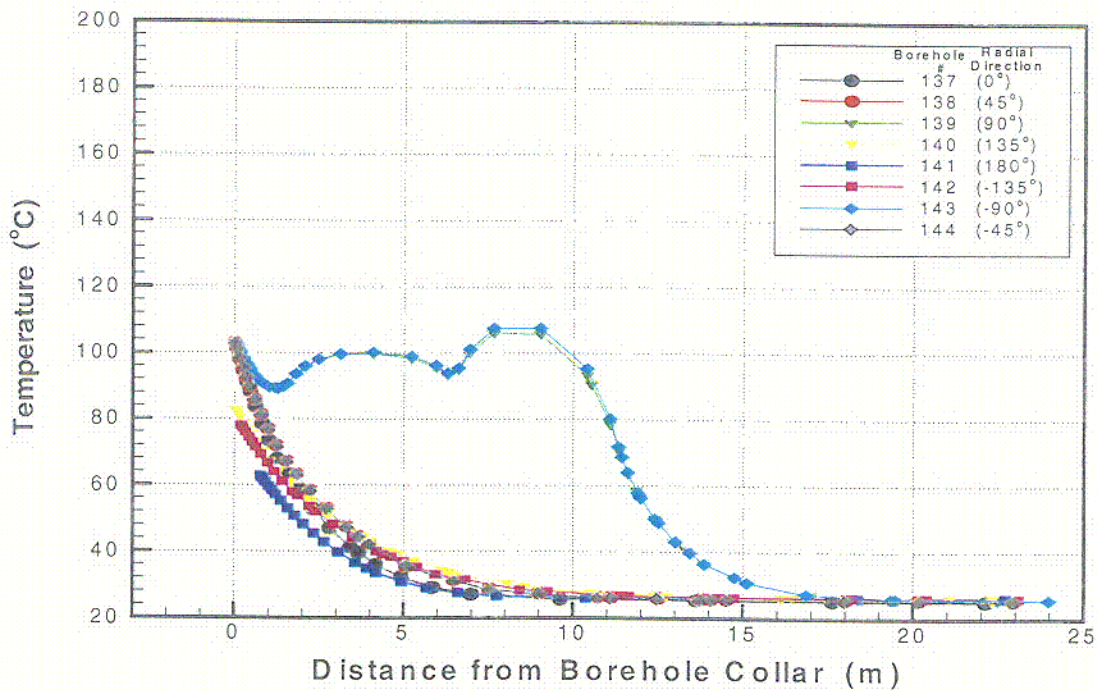
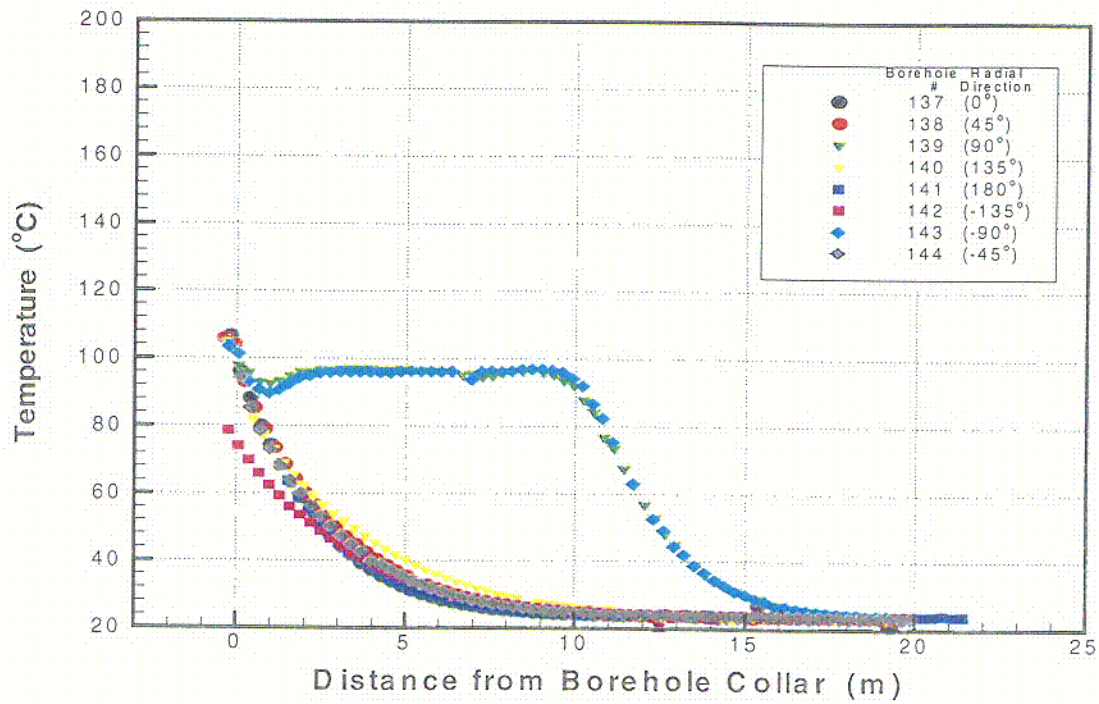


Figure 19. Measured (top) and TOUGH2 Simulated (bottom) DST Temperatures as a Function of Distance of Sensor Locations from Borehole Collars in RTD Boreholes 137-144 after 3 Months of Heating. The DS/AFM-UZ99 Properties were used in the Simulation.

C7

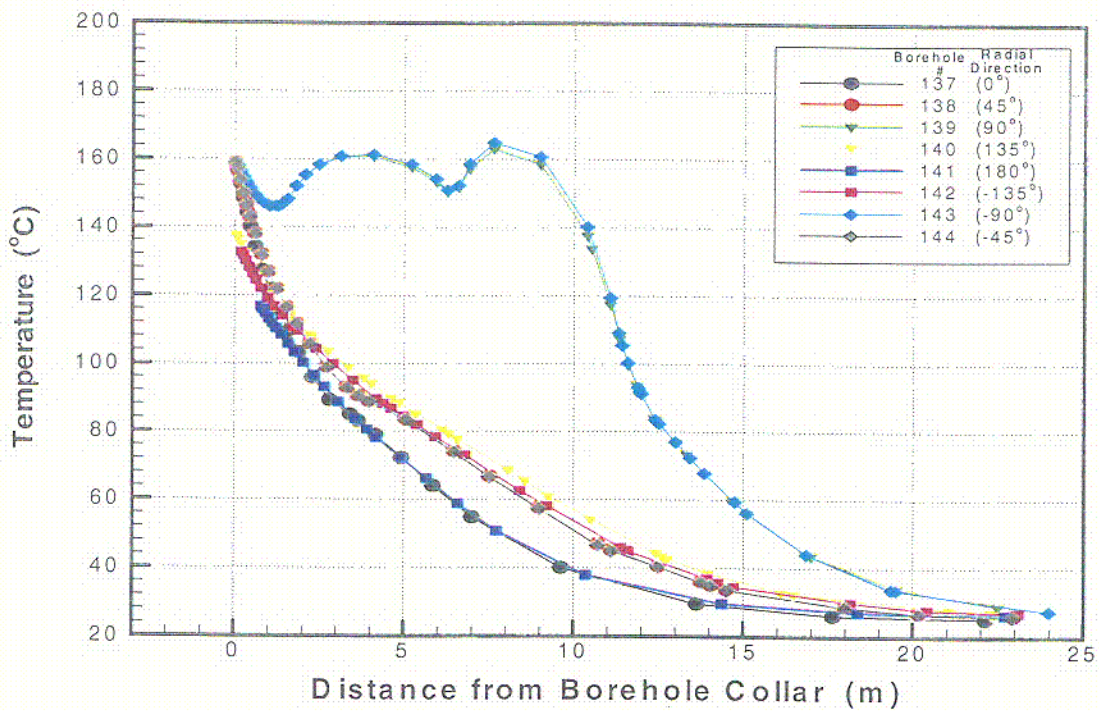
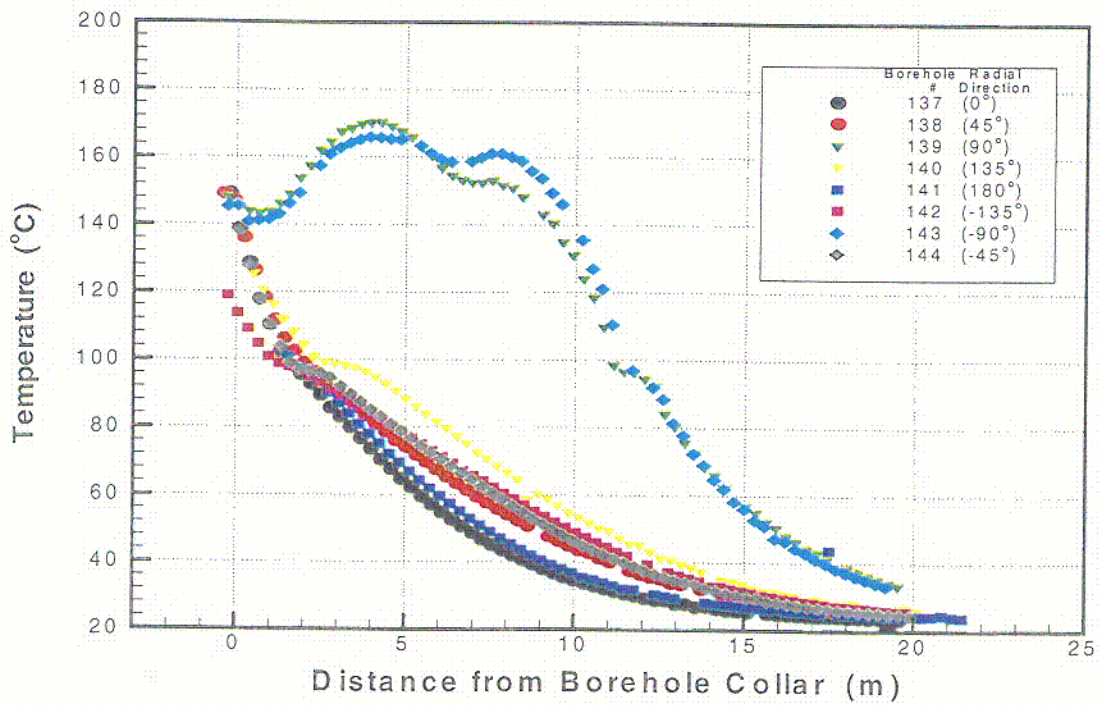


Figure 20. Measured (top) and TOUGH2 Simulated (bottom) DST Temperatures as a Function of Distance of Sensor Locations from Borehole Collars in RTD Boreholes 137-144 after 12 Months of Heating. The DS/AFM-UZ99 Properties were used in the Simulation.

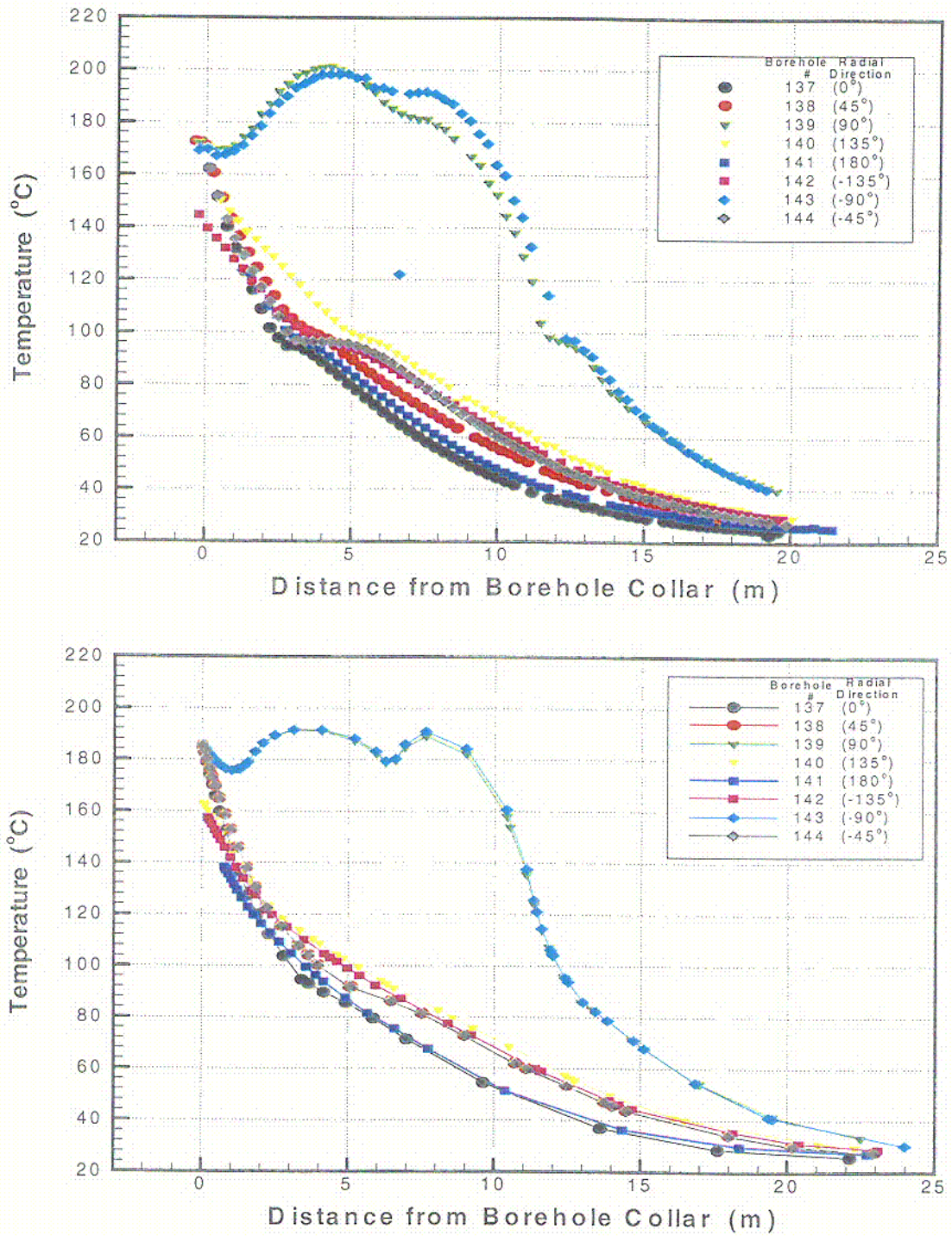


Figure 21. Measured (top) and TOUGH2 Simulated (bottom) DST Temperatures as a Function of Distance of Sensor Locations from Borehole Collars in RTD Boreholes 137-144 after 18 Months of Heating. The DS/AFM-UZ99 Properties were used in the Simulation.

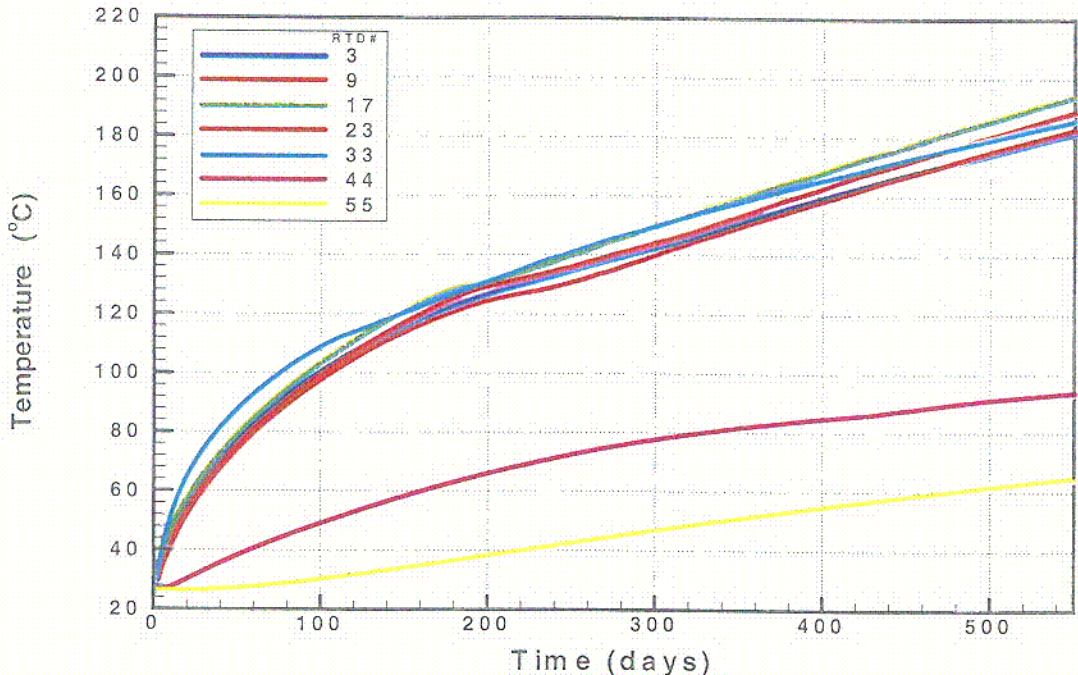
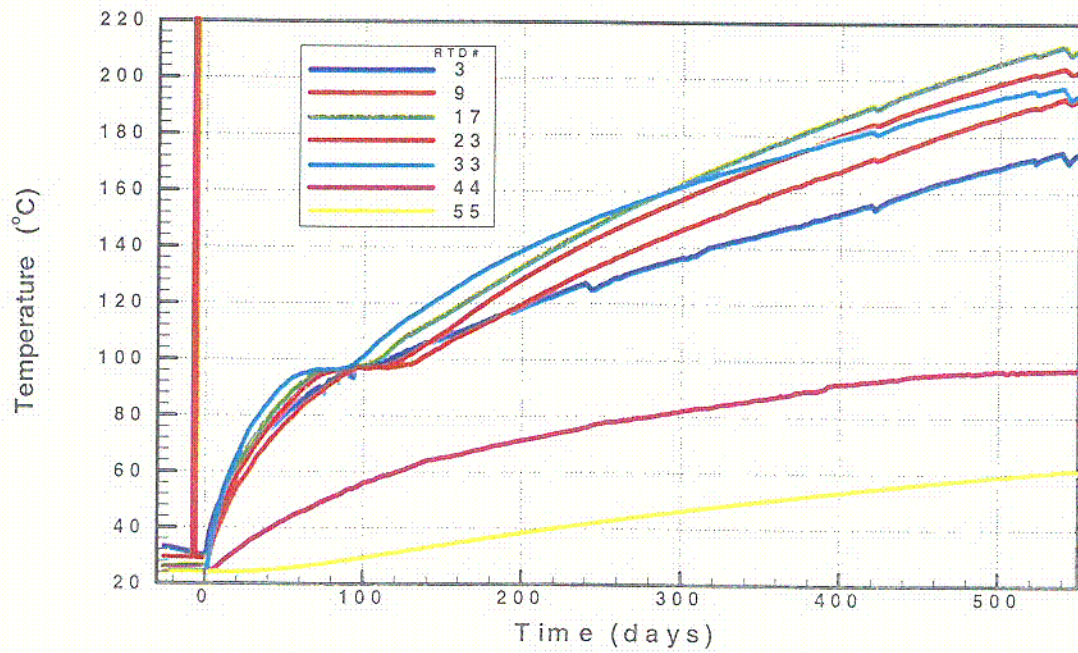


Figure 22. Measured (top) and TOUGH2 Simulated (bottom) DST Temperatures as a Function of Time at Selected Sensor Locations of Borehole 160 (Horizontal near the Wing Heaters). The DS/AFM-UZ99 Properties were used in the Simulation.

C10

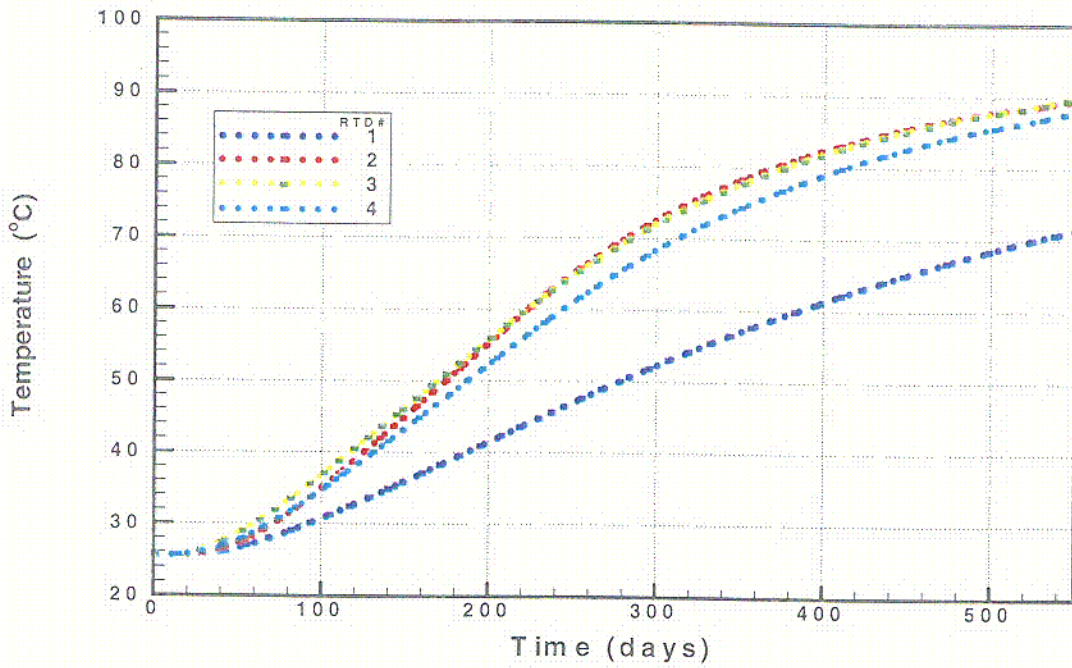
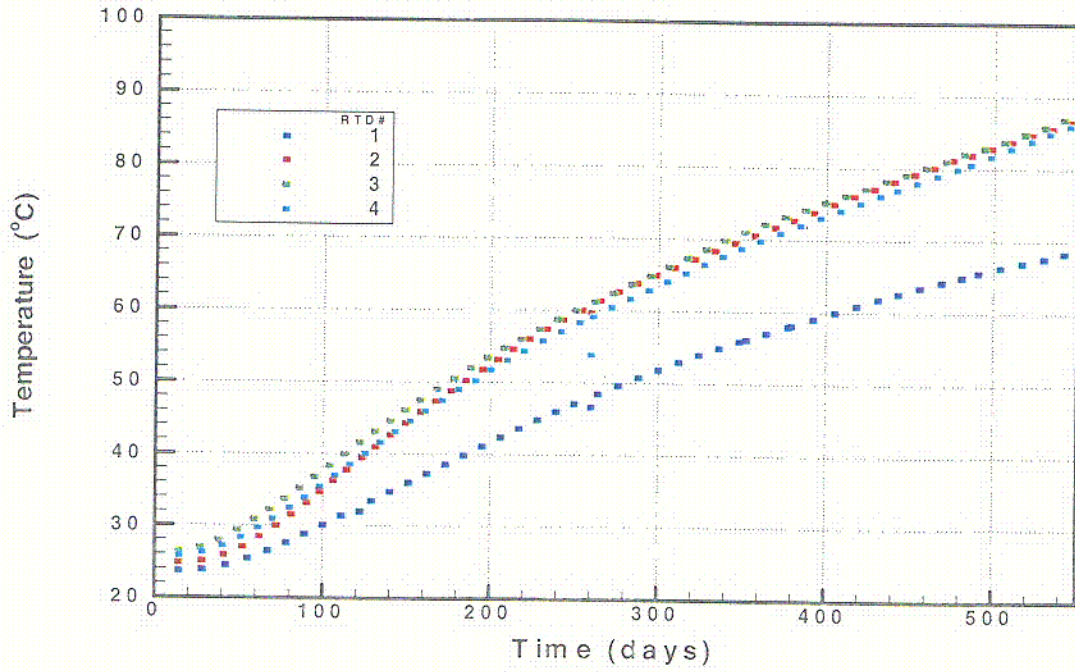


Figure 23. Measured (top) and TOUGH2 Simulated (bottom) DST Temperatures as a Function of Time at All Sensor Locations of Borehole 59, above the Heated Region. The DS/AFM-UZ99 Properties were used in the Simulation.

CH

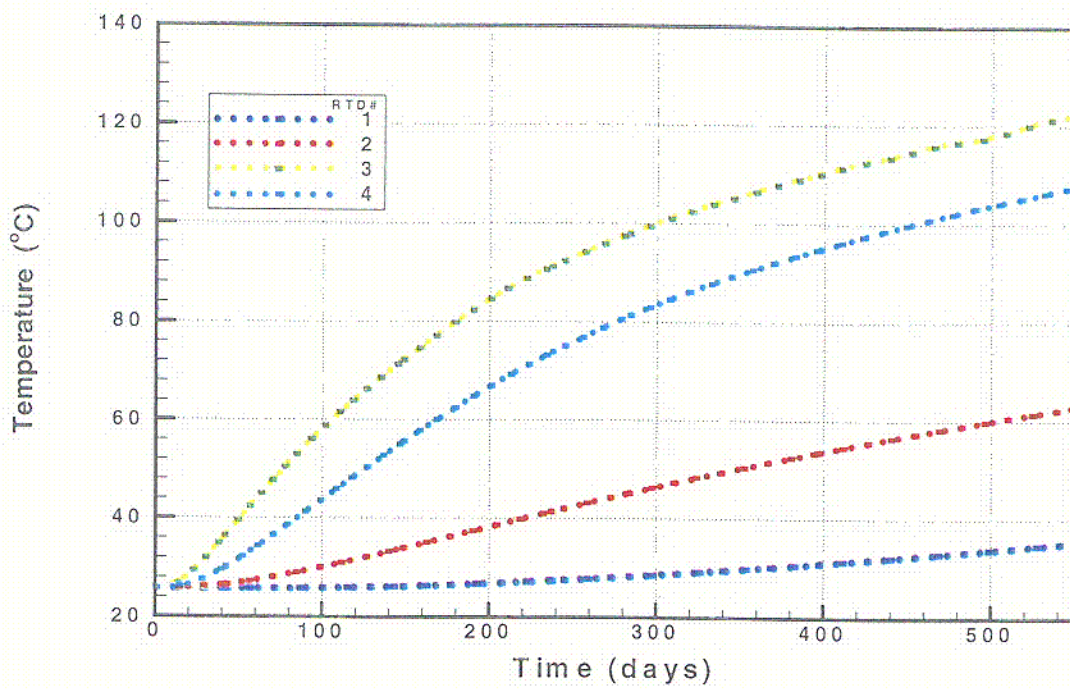
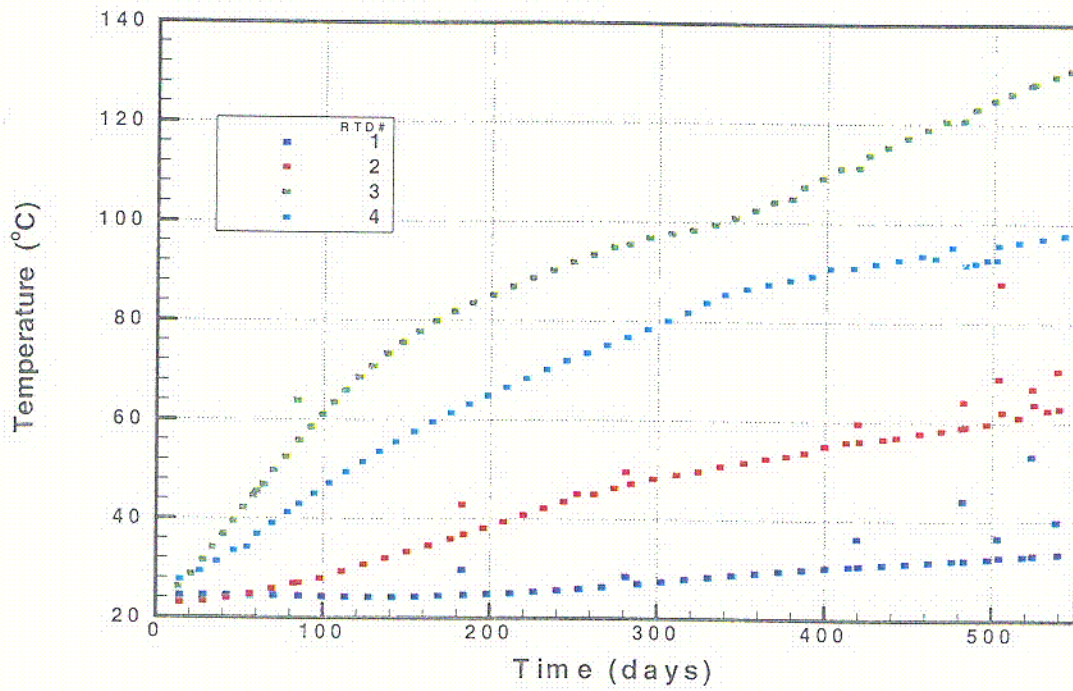


Figure 24. Measured (top) and TOUGH2 Simulated (bottom) DST Temperatures as a Function of Time at All Sensor Locations of Borehole 60, below the Heated Region. The DS/AFT-UZ99 Properties were used in the Simulation.

C12

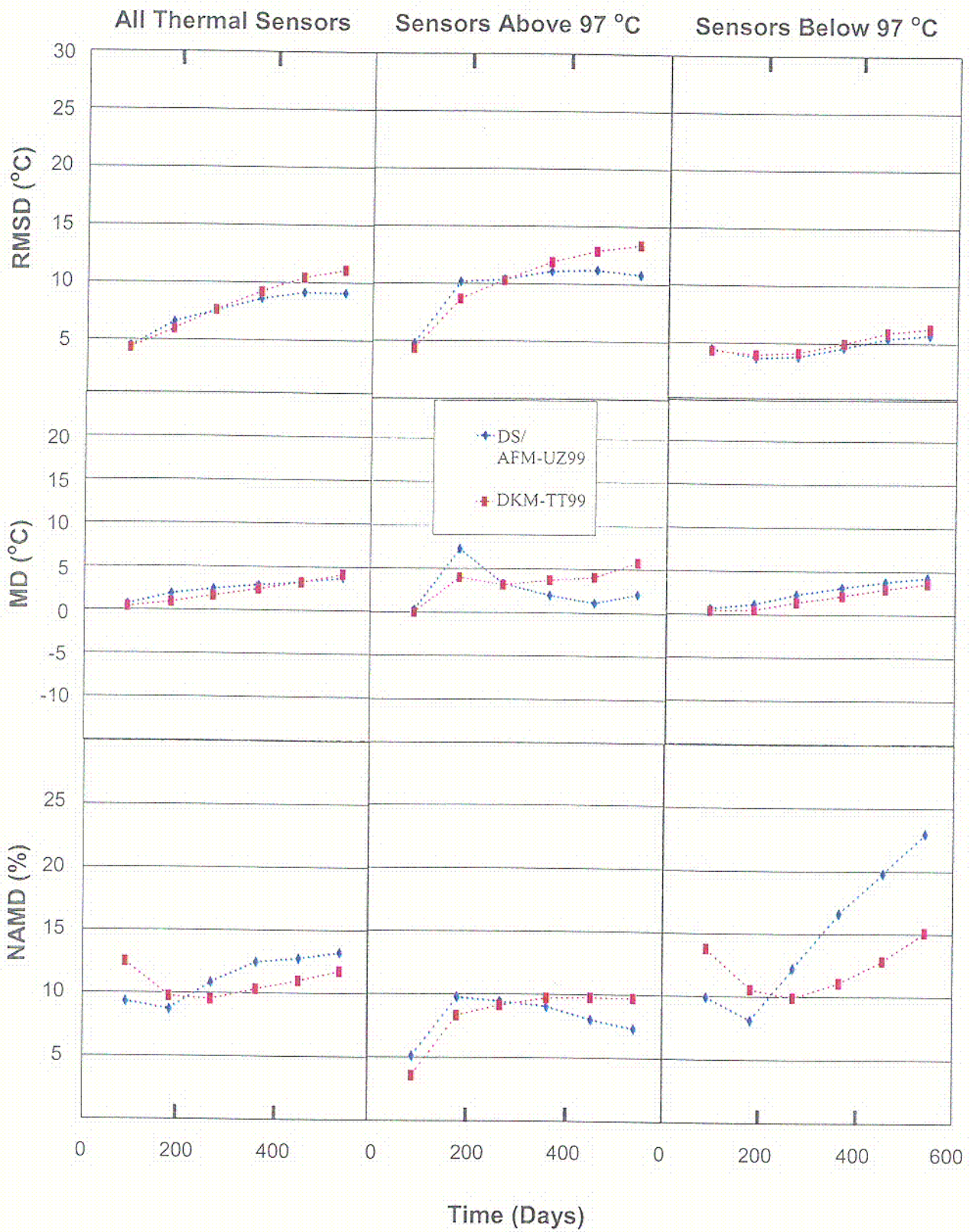


Figure 25. Statistical Measures for DST TOUGH2 Thermal Analyses

213

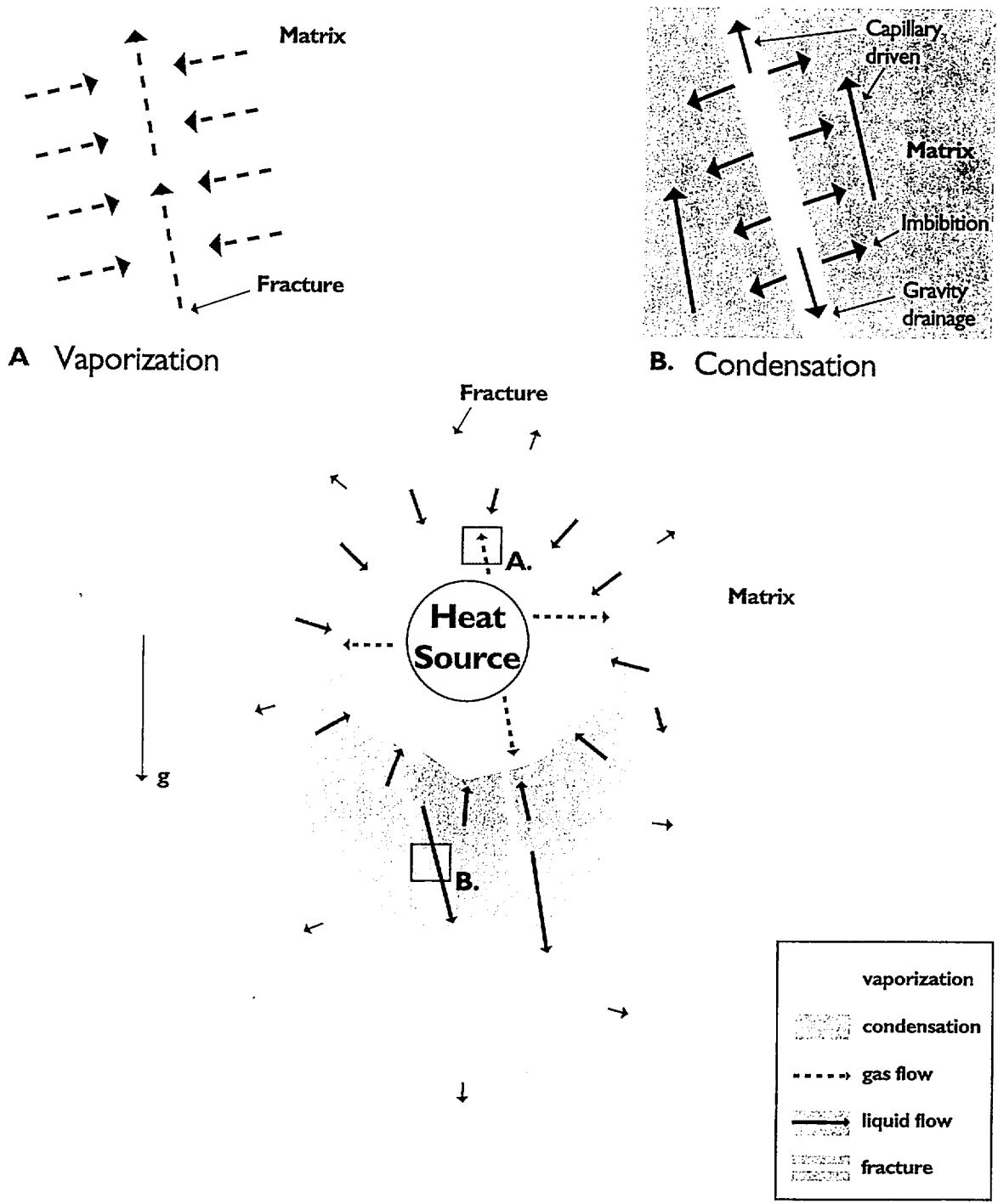


Figure 26. Schematic Representation of Thermal Hydrological Processes in an Unsaturated Fractured Geological Medium

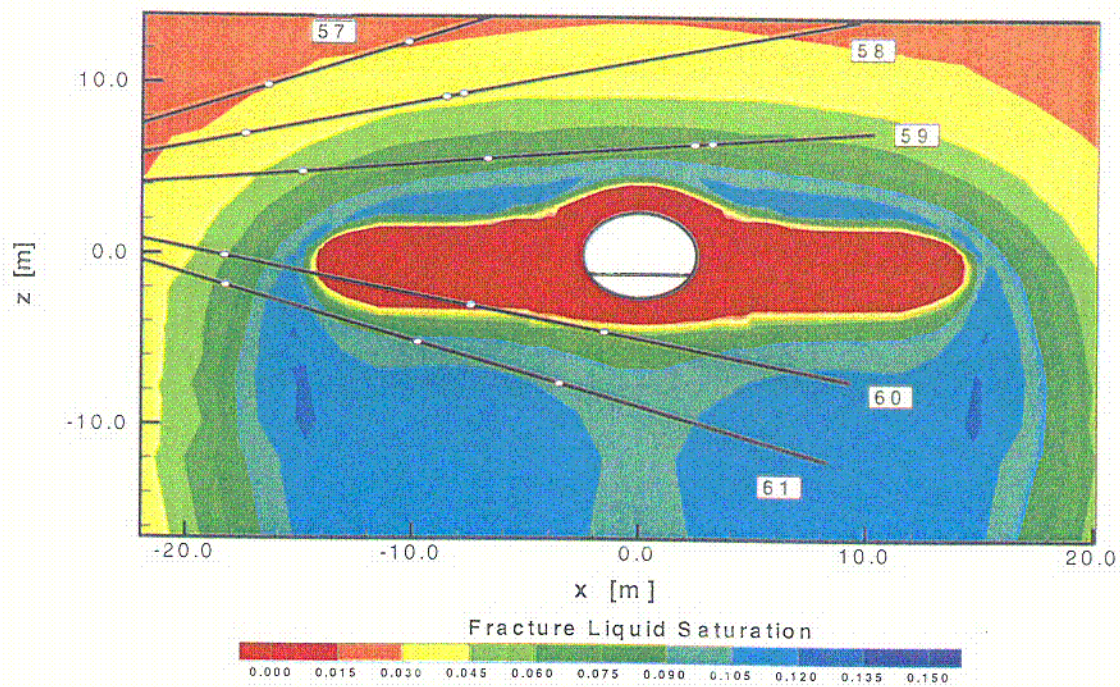
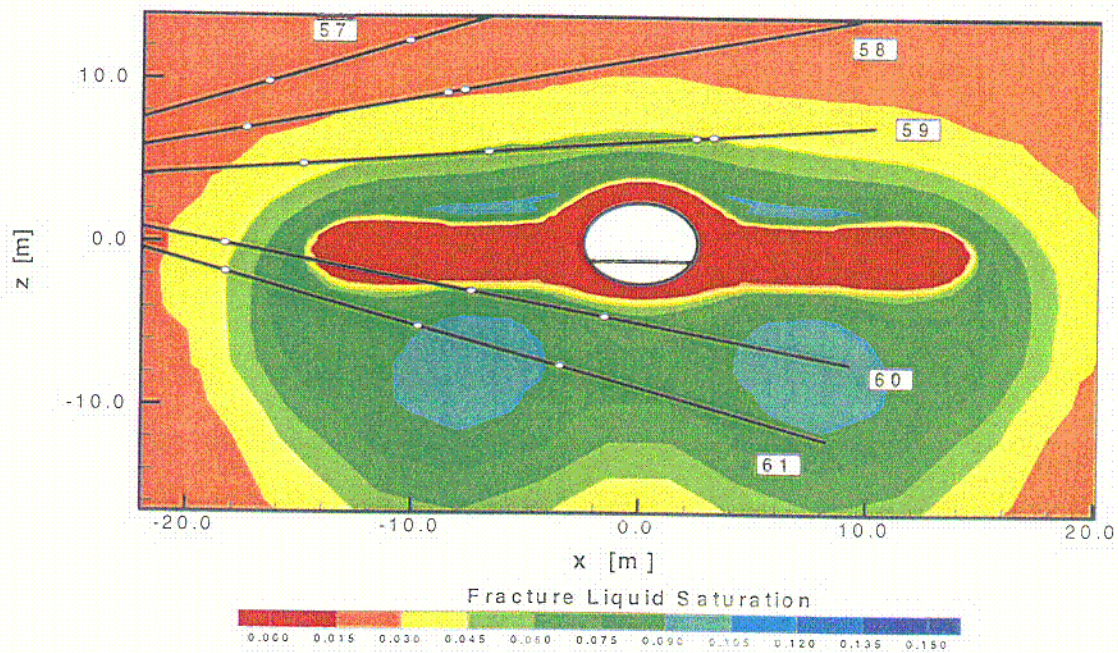


Figure 27. TOUGH2 Simulated Fracture Liquid Saturation in the Plane of Hydrology Boreholes 57-61 After 3 Months (top) and 6 Months (bottom) of DST Heating, Using the DS/AFM-UZ99 Properties

C14

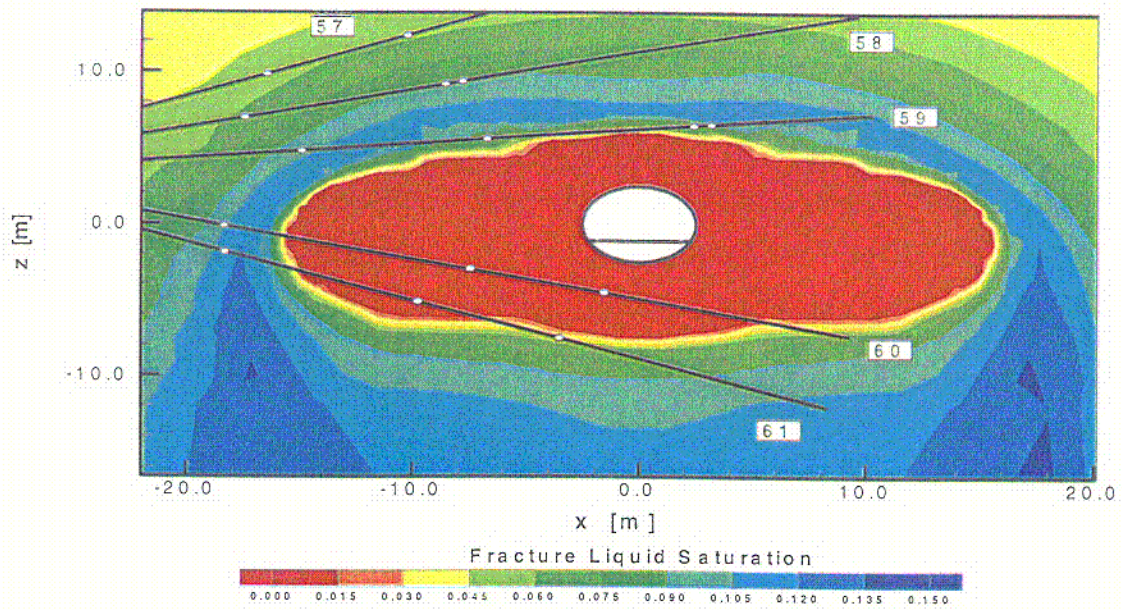
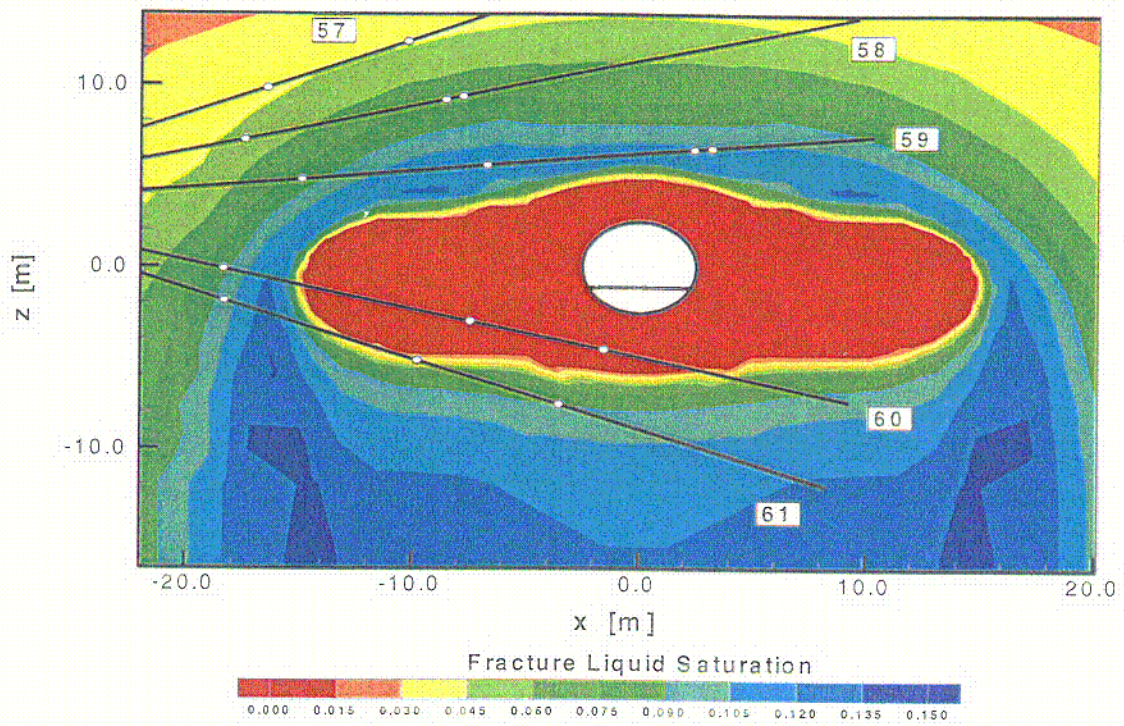


Figure 28. TOUGH2 Simulated Fracture Liquid Saturation in the Plane of Hydrology Boreholes 57-61 After 12 Months (top) and 18 Months (bottom) of DST Heating, Using the DS/AFM-UZ99 Properties

C15

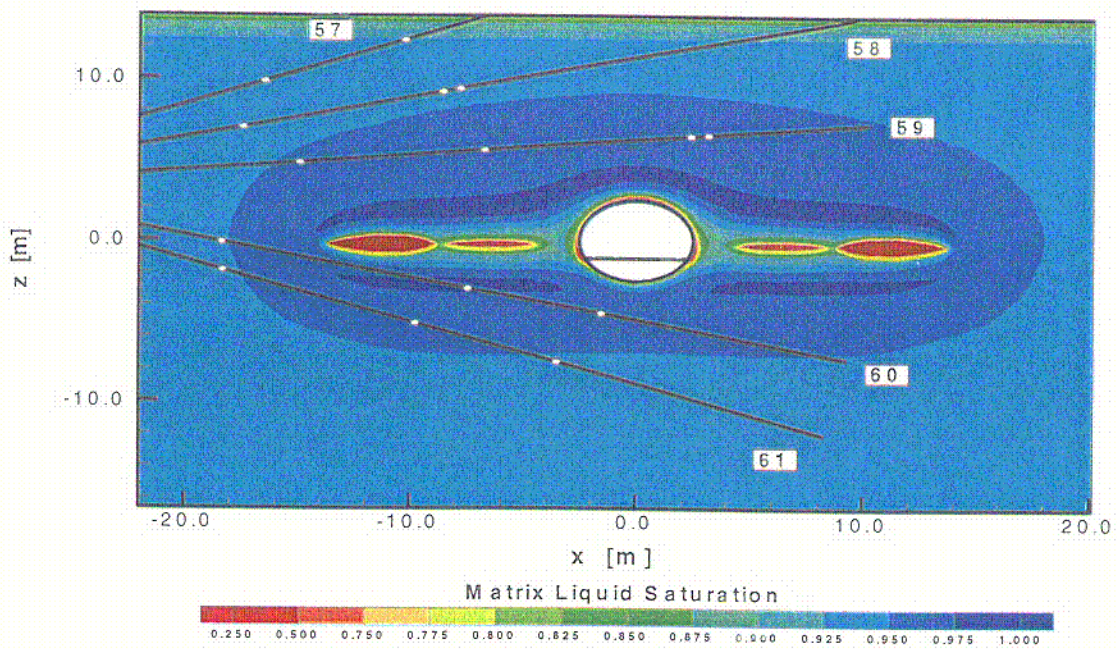
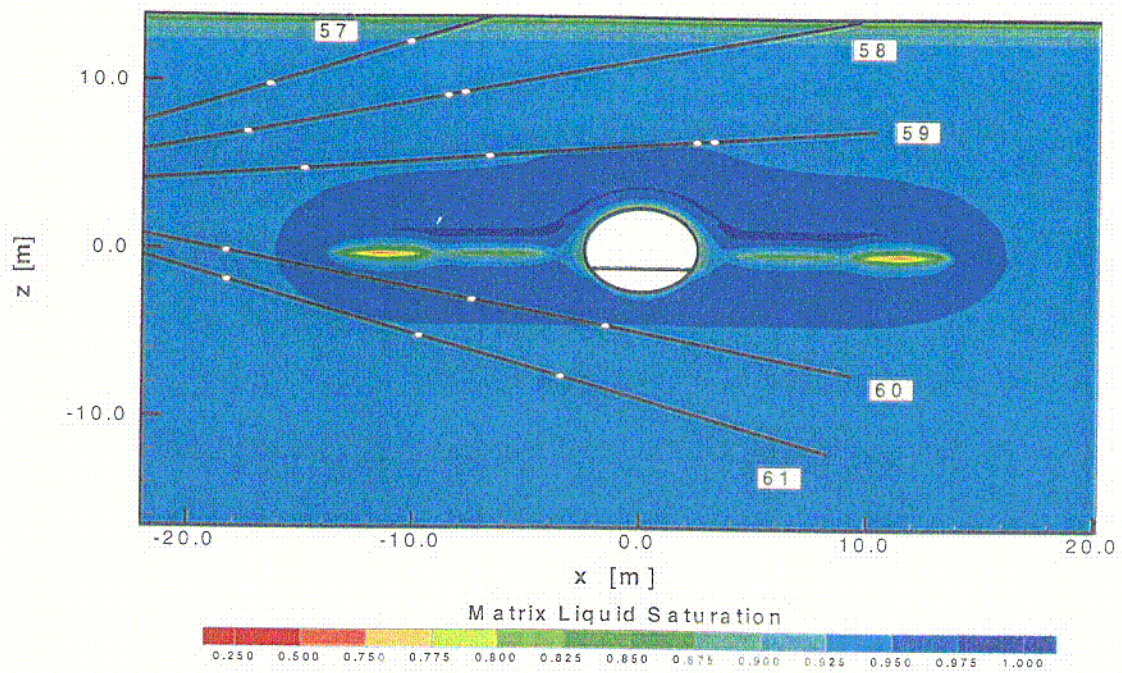


Figure 29. TOUGH2 Simulated Matrix Liquid Saturation in the Plane of Hydrology Boreholes 57-61 After 3 Months (top) and 6 Months (bottom) of DST Heating, Using the DS/AFM-UZ99 Properties

CLG

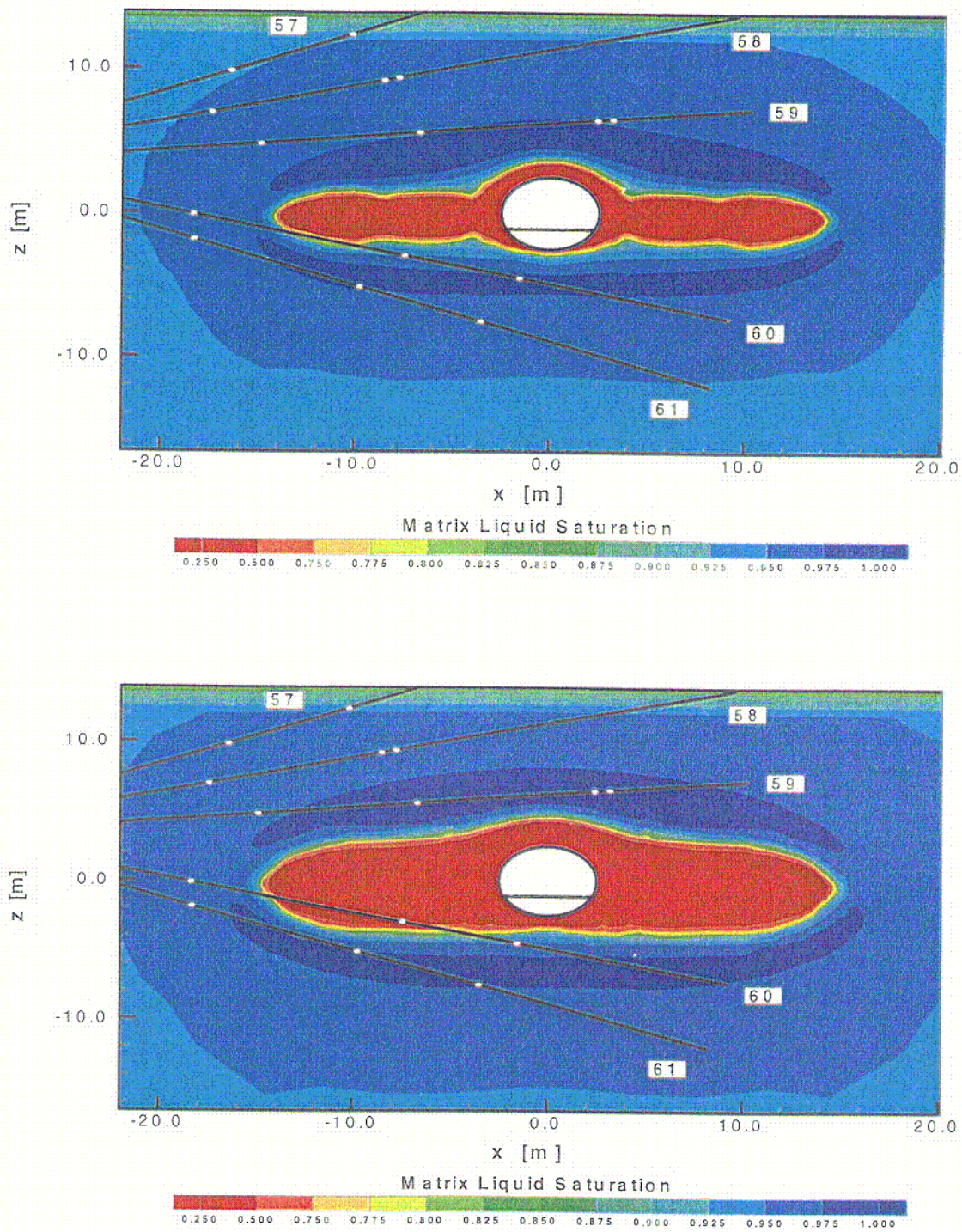


Figure 30. TOUGH2 Simulated Matrix Liquid Saturation in the Plane of Hydrology Boreholes 57-61 at 12 Months (top) and 18 Months (bottom) of DST Heating, Using the DS/AFM-UZ99 Properties

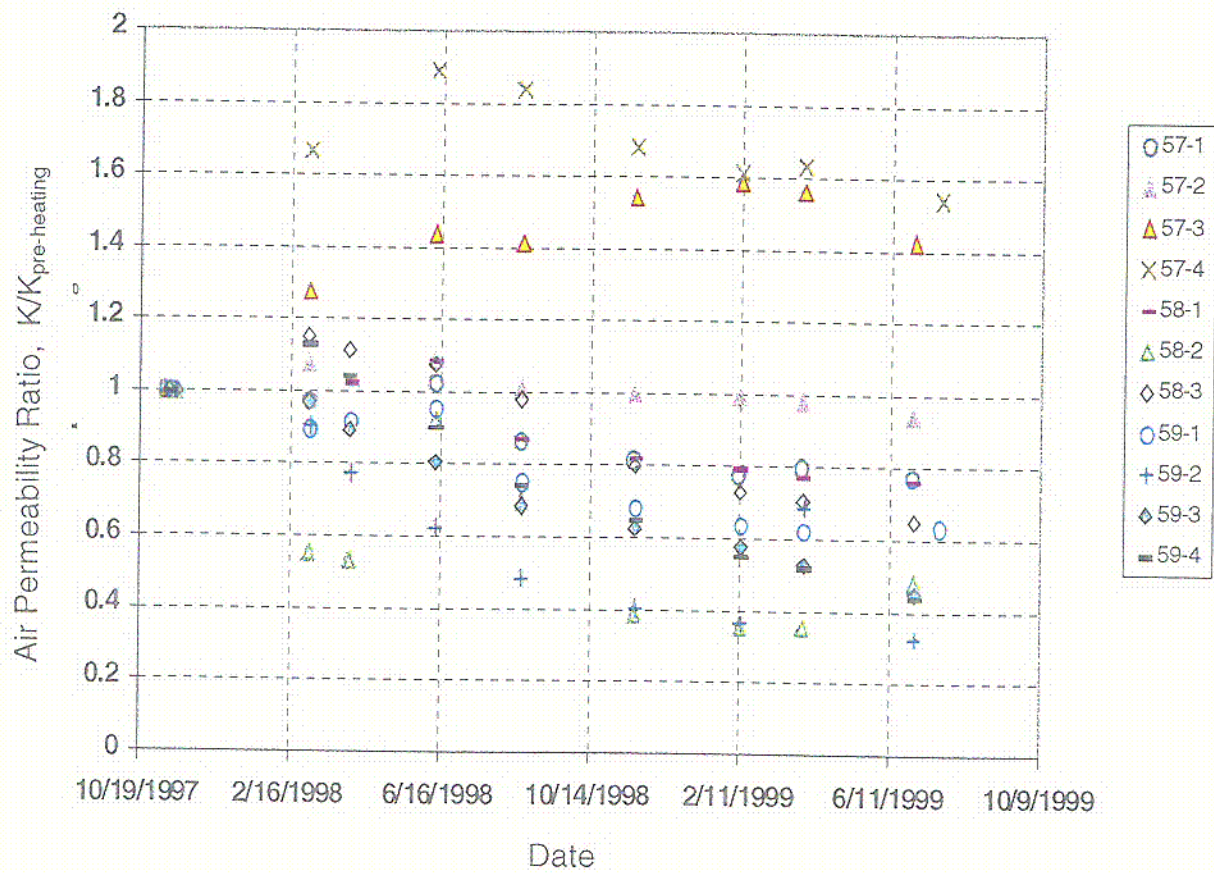


Figure 31. Changes in Air Permeability Values with Respect to Pre-Heat Values as Obtained Through Air-Injection Tests in DST Hydrology Boreholes 57-59 Above the Heated Drift

C18

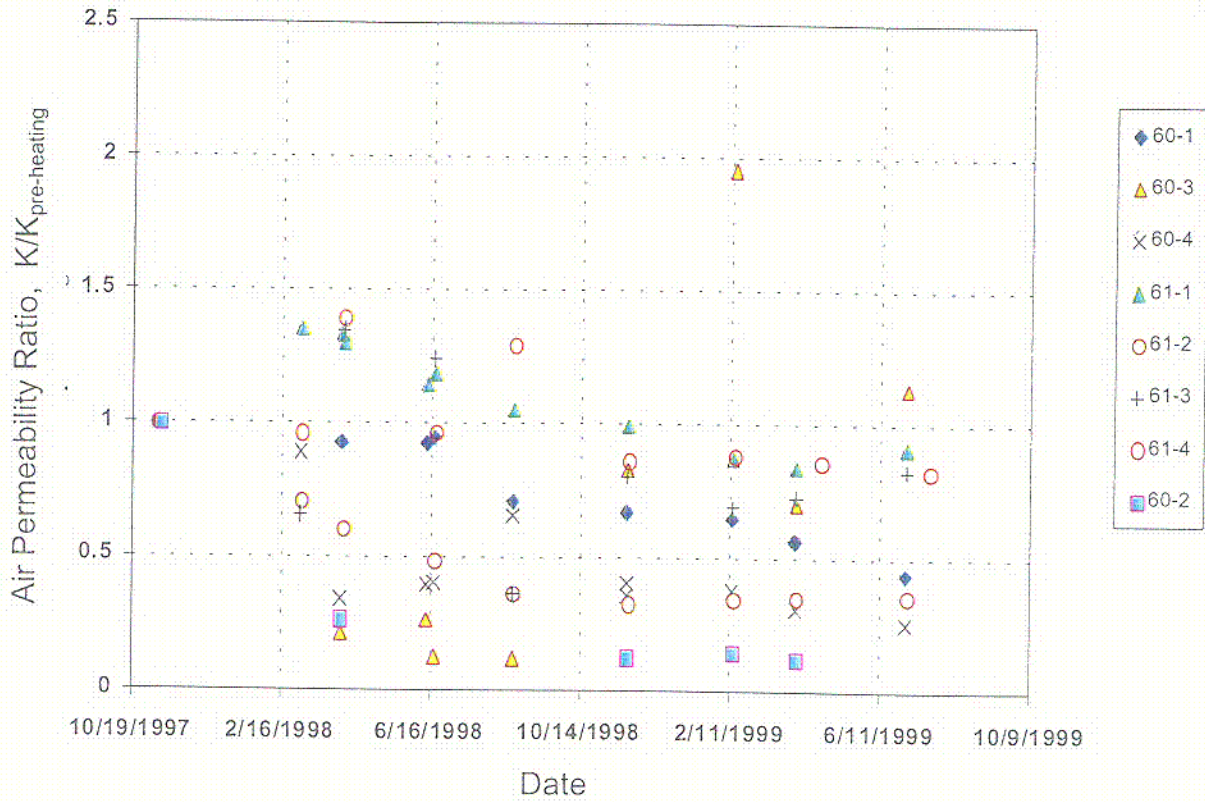


Figure 32. Changes in Air Permeability Values with Respect to Pre-Heat Values as Obtained Through Air-Injection Tests in DST Hydrology Boreholes 60-61 Below the Heated Drift

c19

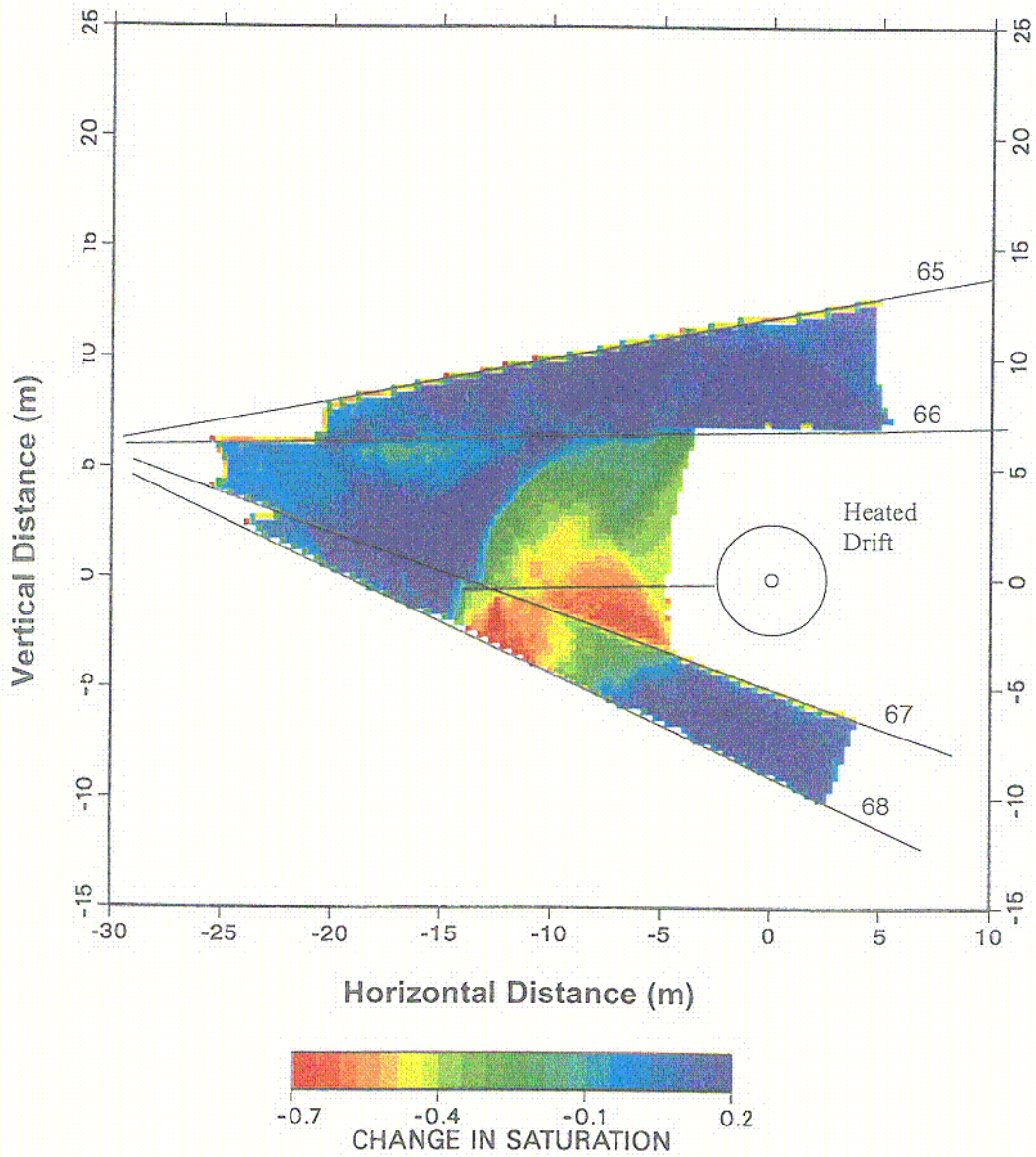


Figure 33. Tomogram Showing Saturation Change from Pre-Heat Ambient Values Derived from a Cross-Hole Radar Survey Taken in January of 1999 (~13 months of heating) in the Plane of DST Boreholes 64-68

C20

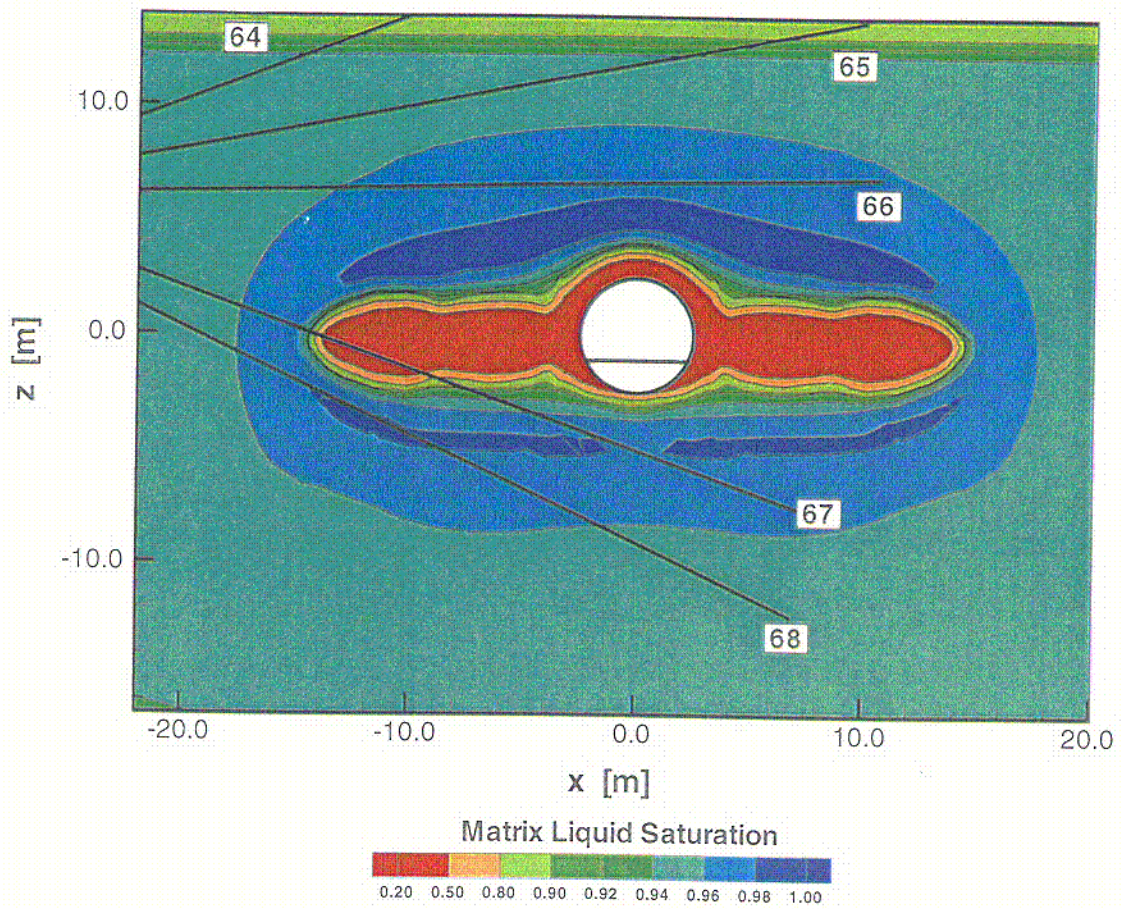


Figure 34. TOUGH2 Simulated Matrix Liquid Saturation in the Plane of DST Boreholes 64-68 After 12 Months of Heating, Using the DS/AFM-UZ99 Properties

C21

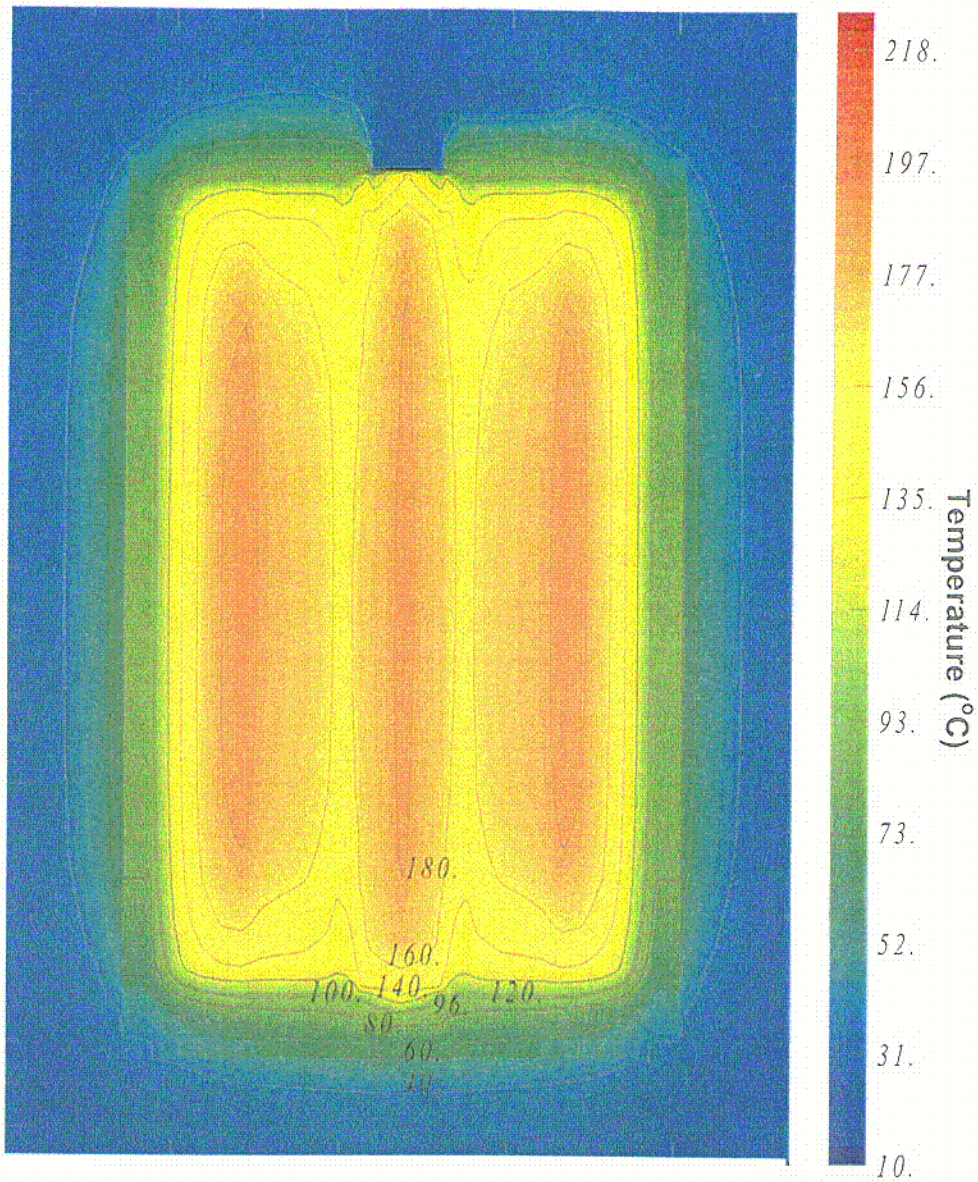


Figure 35. Distribution of the Simulated Temperature on a Horizontal Plane through the Wing Heater Arrays (Z=-0.5 m) at 365 Days for the DS DST NUFT Analyses

C22

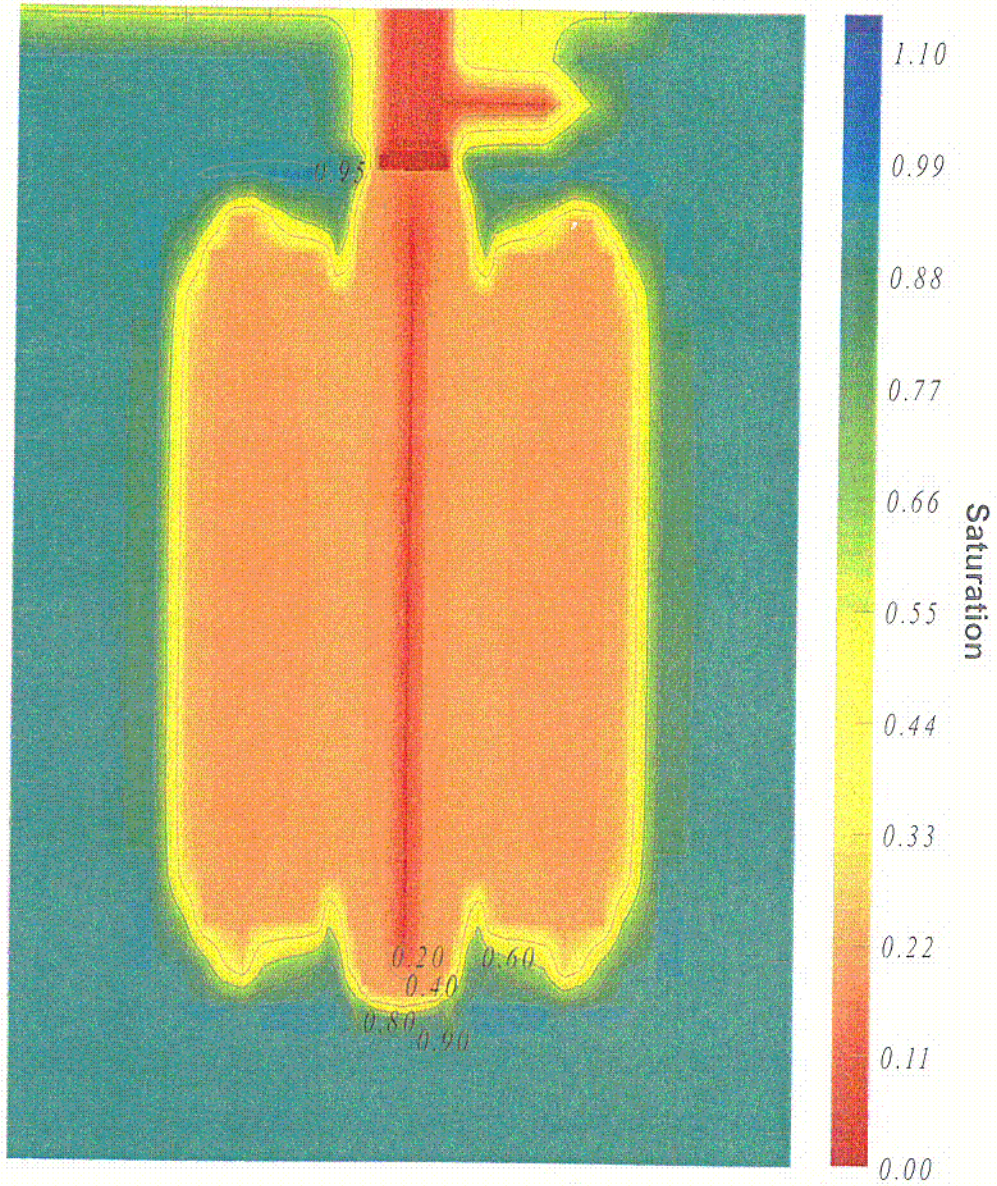


Figure 36. Distribution of the Simulated Water Saturation on a Horizontal Plane through the Wing Heater Arrays ($Z=-0.5$ m) at 365 Days for the DS DST NUFT Analyses

C23

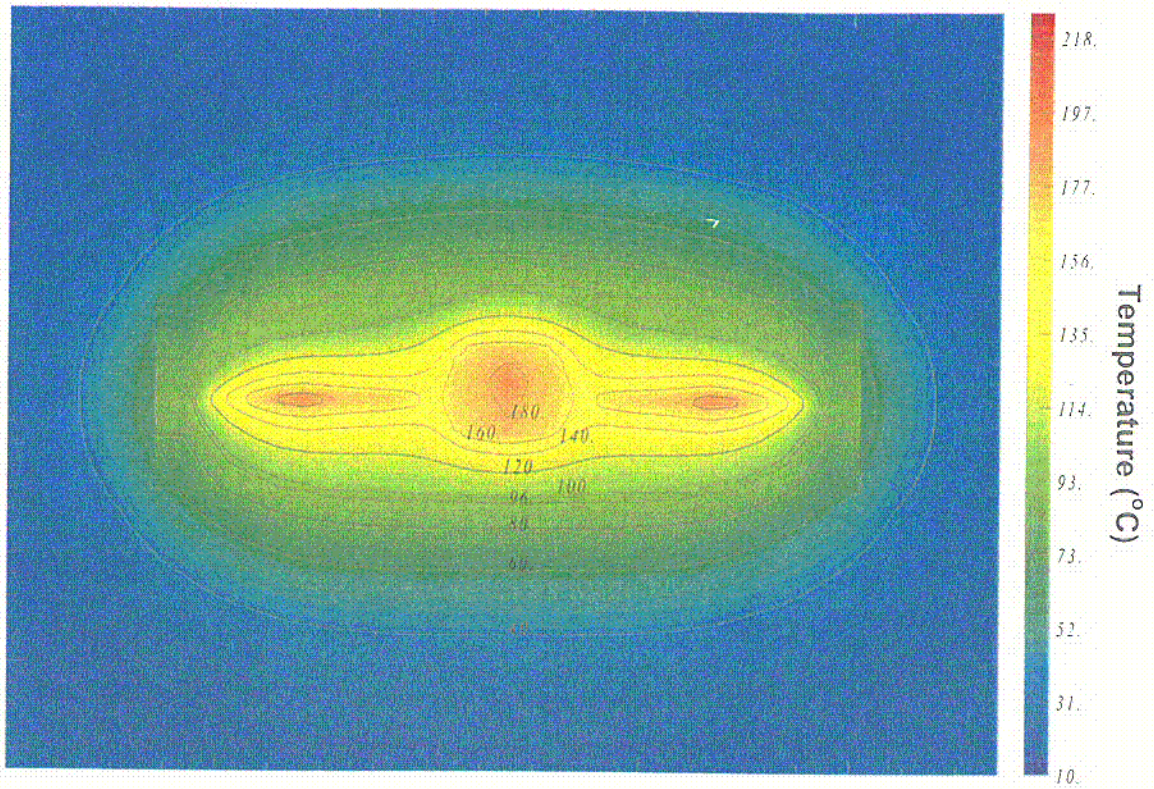


Figure 37. Distribution of the Simulated Temperature on a Vertical Slice through the Mid-Length of the DST at 365 Days for the DS DST NUFT Analyses

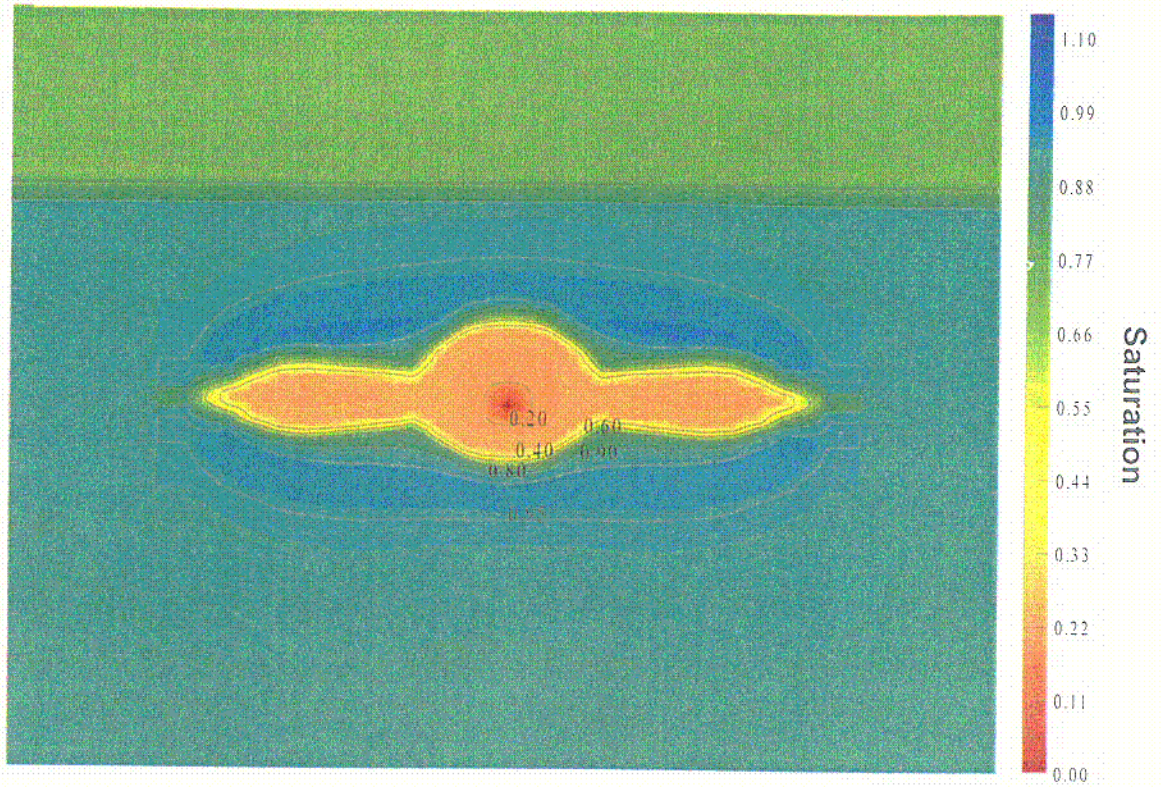


Figure 38. Distribution of the Simulated Water Saturation on a Vertical Slice through the Mid-Length of the DST at 365 Days for the DS DST NUFT Analyses

C25

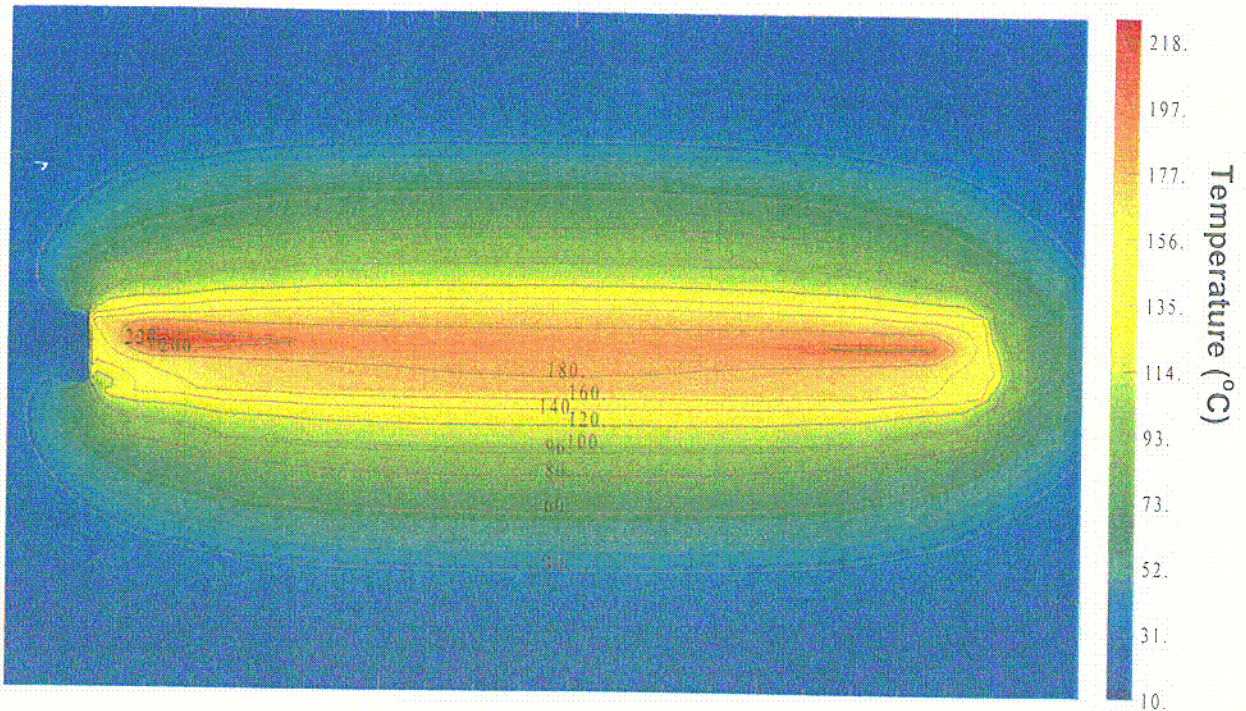


Figure 39. Distribution of the Simulated Temperature on a Vertical Plane through the Longitudinal Axis of Heated Drift Array ($X=0m$) at 365 Days for the DS DST NUFT Analyses

026

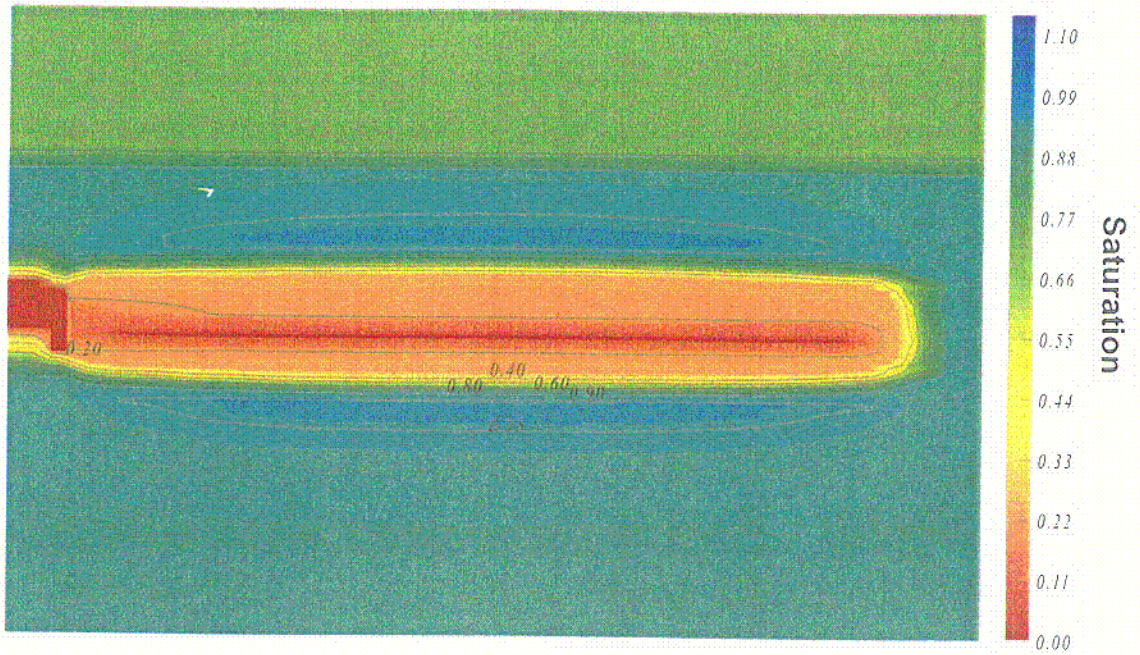


Figure 40. Distribution of the Simulated Water Saturation on a Vertical Plane through the Longitudinal Axis of Heated Drift Array ($X=0m$) at 365 Days for the DS DST NUFT Analyses

C27

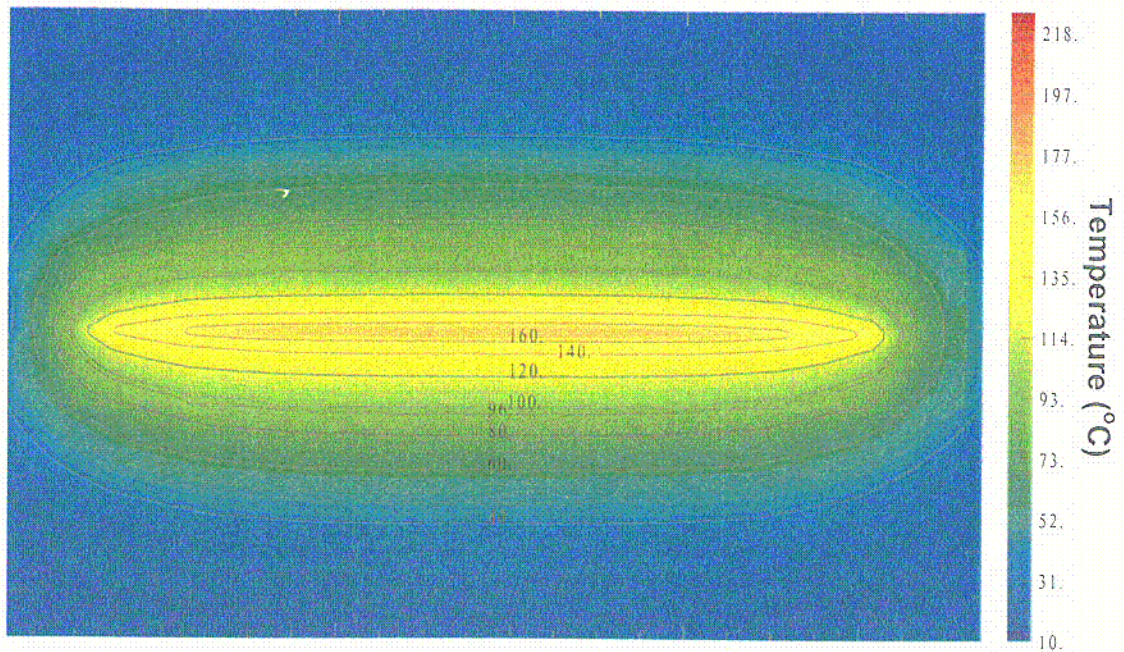


Figure 41. Distribution of the Simulated Temperature on a Vertical Plane Normal to Wing Heater Array (X=-6.24 m) Near the Center of the Inner Wing Heater Array at 365 Days for the DS DST NUFT Analyses

C28

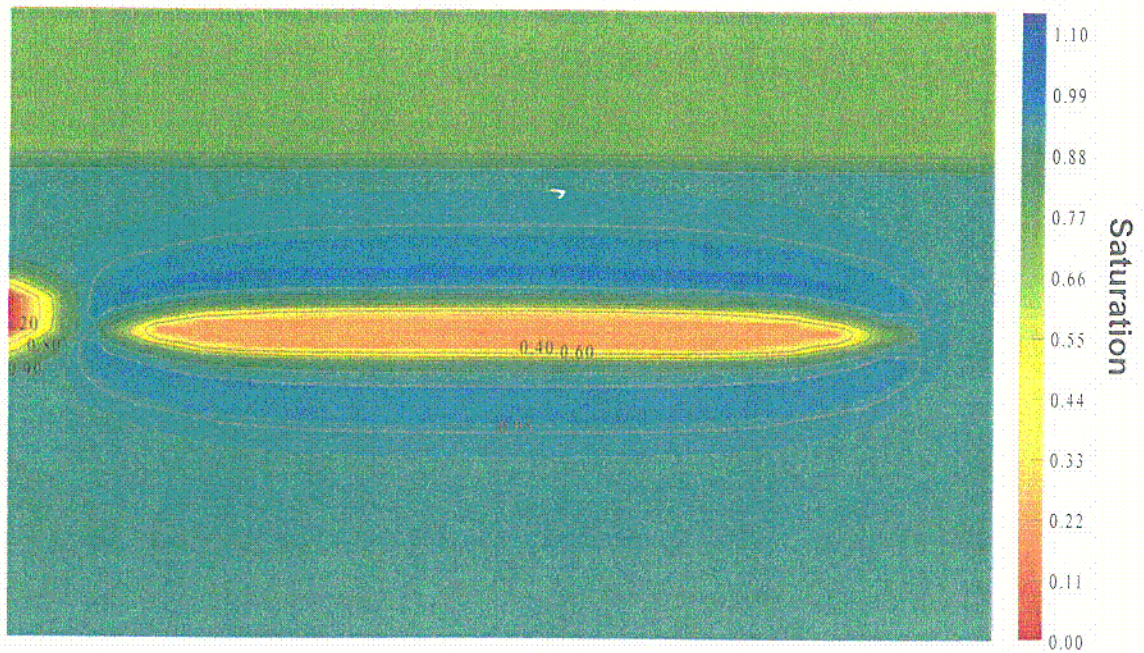
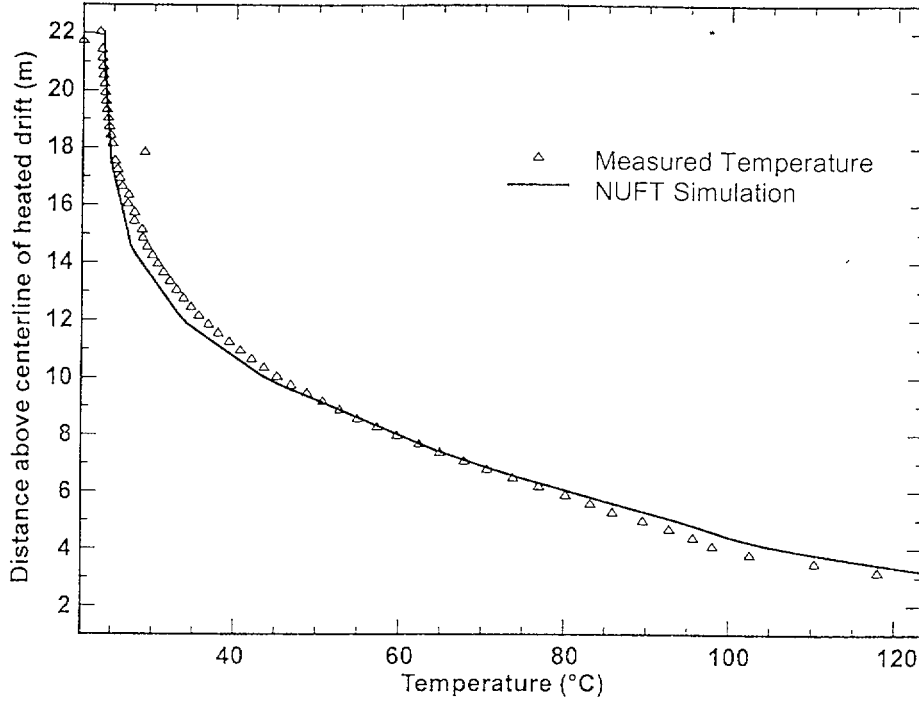


Figure 42. Distribution of the Simulated Water Saturation on a Vertical Plane Normal to Wing Heater Array (X=-6.24 m) Near the Center of the Inner Wing Heater Array at 365 Days for the DS DST NUFT Analyses

C29

(a) 12 Months



(b) 18 Months

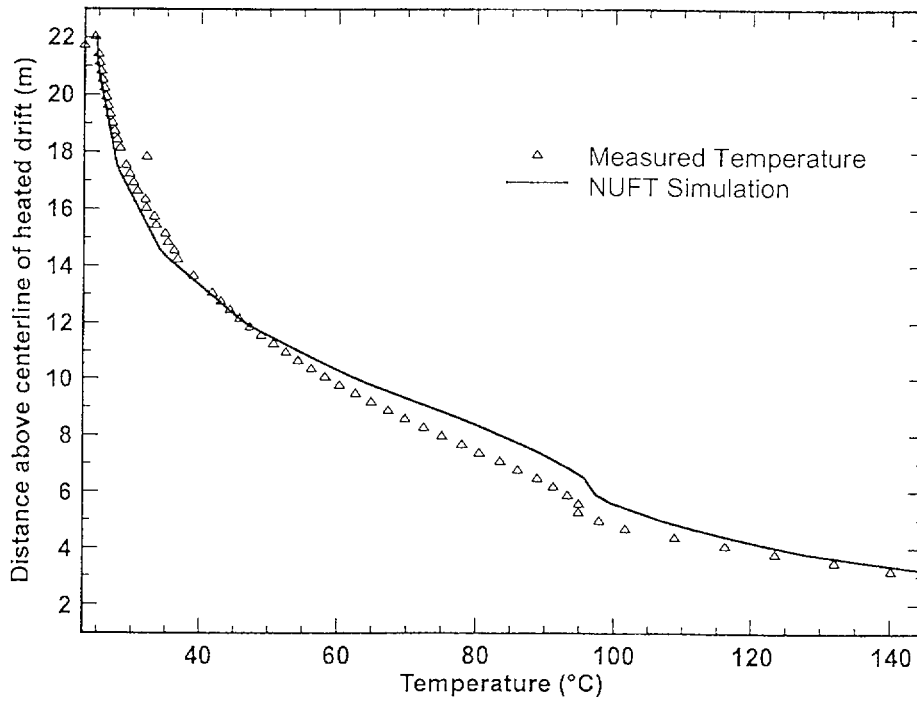


Figure 43. Comparison of NUFT Simulated and Measured Temperatures from the DST, Along Borehole 137 (Vertical Upward) at (a) 12 Months and (b) 18 Months

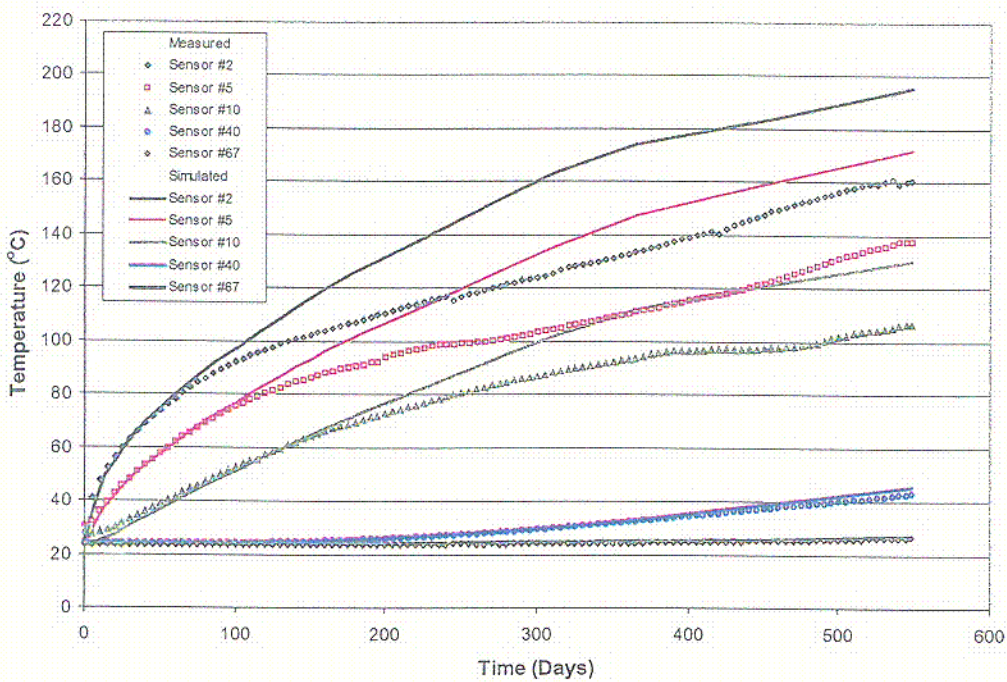
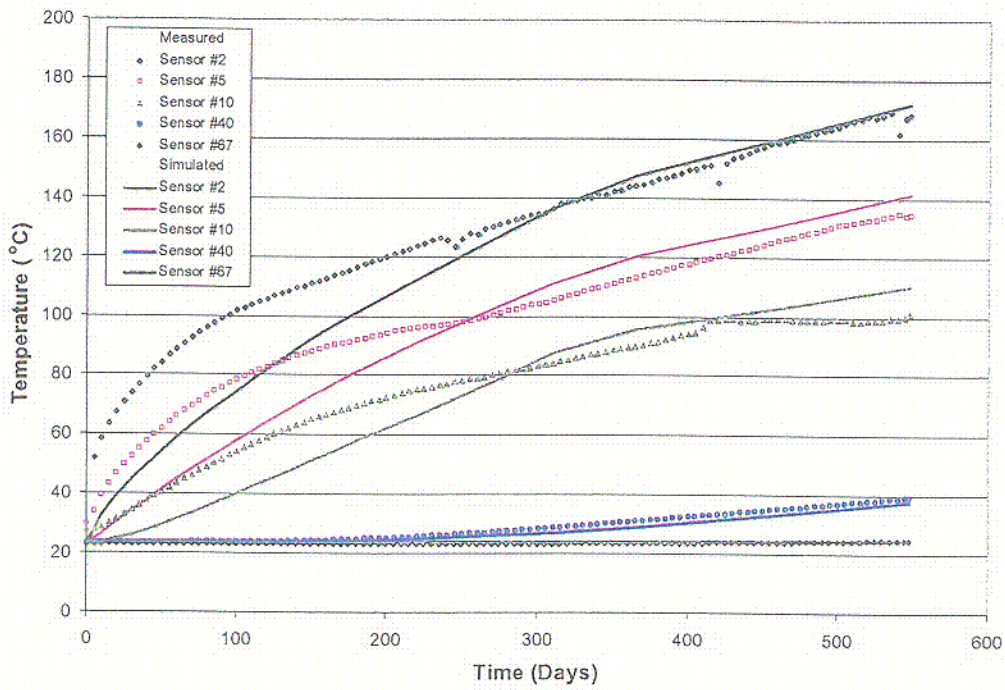


Figure 44. Comparison of NUFT Simulated and Measured Temperature Histories for Sensors No. 2, 5, 10, 40, and 67 Over the 18 Months in Borehole 158 (Vertical up, top) and Borehole 162 (Vertical down, bottom) for the DST, Using the DS Property Set

C30

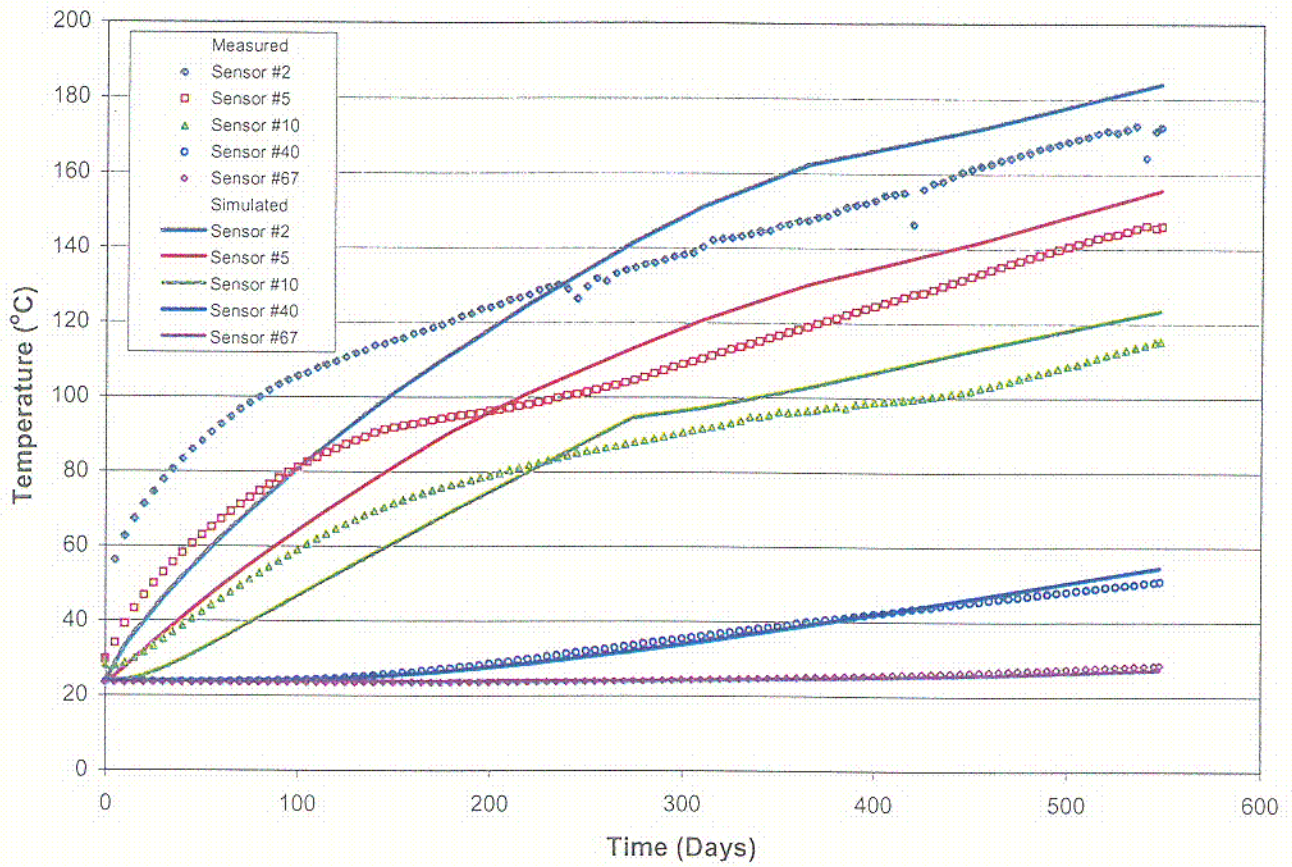


Figure 45. Comparison of NUFT Simulated and Measured Temperature Histories for Sensors No. 2, 5, 10, 40, and 67 over 18 Months in Borehole 159 (45° Upward) for the DST, Using the DS Property Set

C31

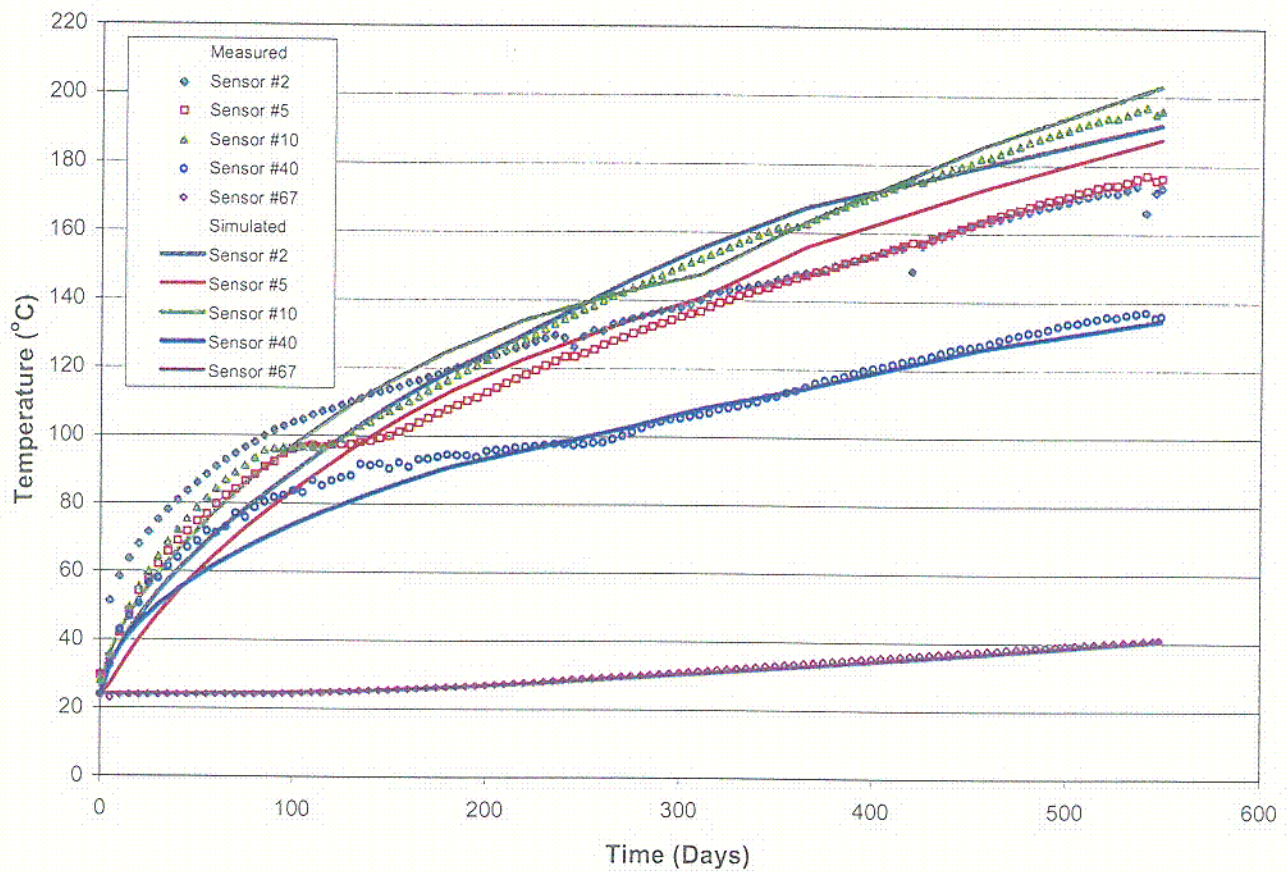


Figure 46. Comparison of NUFT Simulated and Measured Temperature Histories for Sensors No. 2, 5, 10, 40, and 67 Over the 18 Months in Borehole 160 (Horizontal near the Wing Heaters) for the DST, Using the DS Property Set

C32

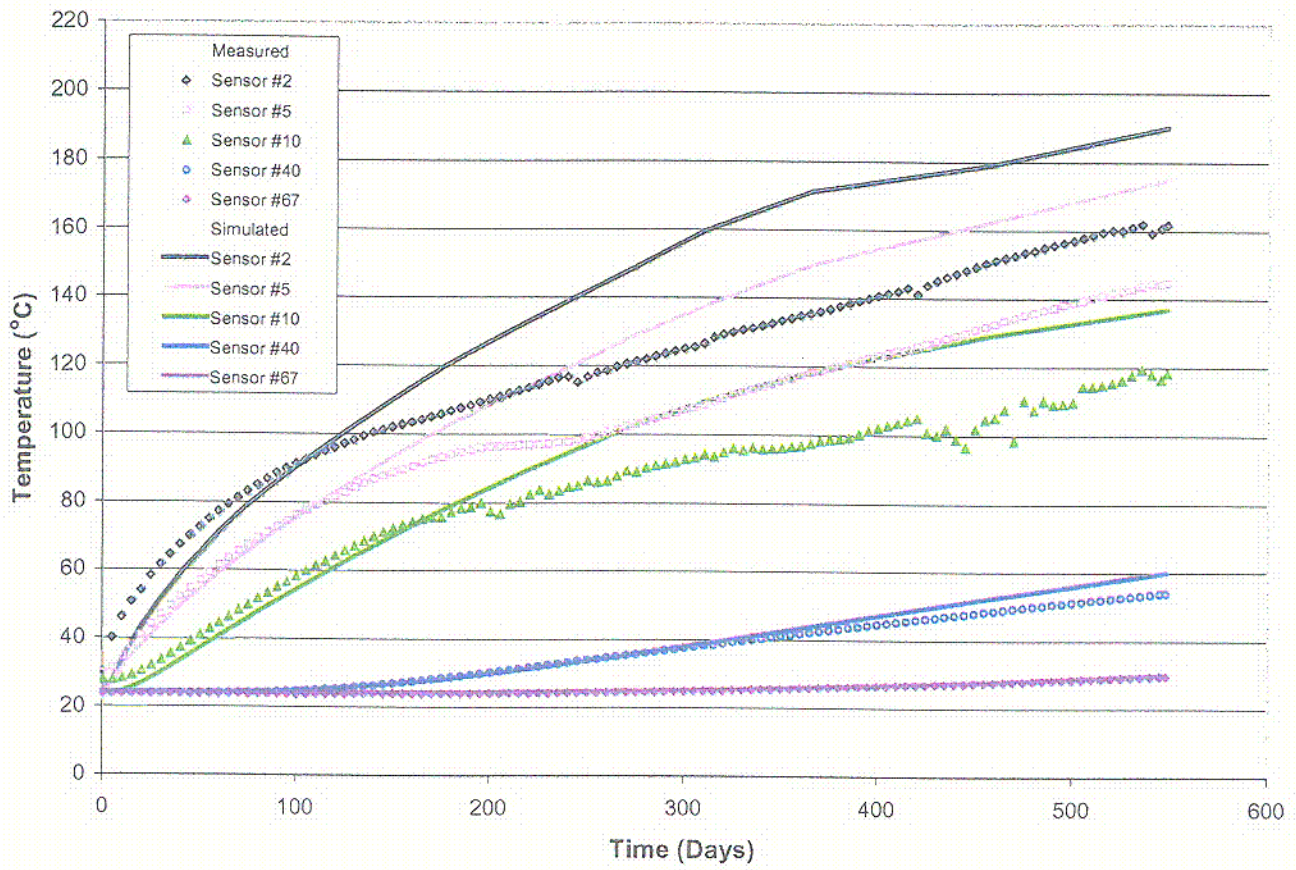


Figure 47. Comparison of NUFT Simulated and Measured Temperature Histories for Sensors No. 2, 5, 10, 40, and 67 Over the 18 Months in Borehole 161 (45° Downward) for the DST, Using the DS Property Set

C33

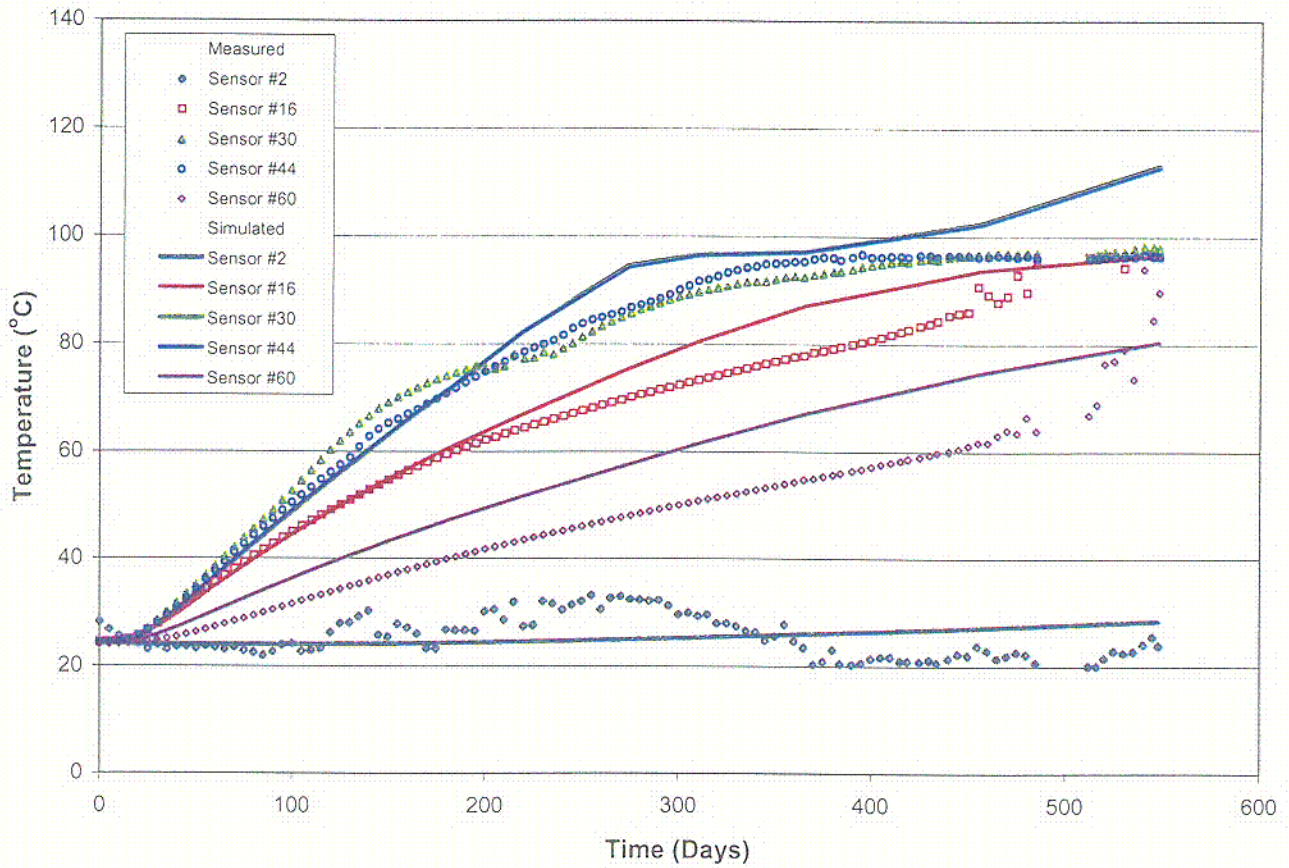


Figure 48. Comparison of NUFT Simulated and Measured Temperature Histories for Sensors No. 2, 16, 30, 44, and 60 Over the 18 Months in Borehole 80 (Parallel to the Drift Slightly Above and to the Side) for the DST, Using the DS Property Set

C34

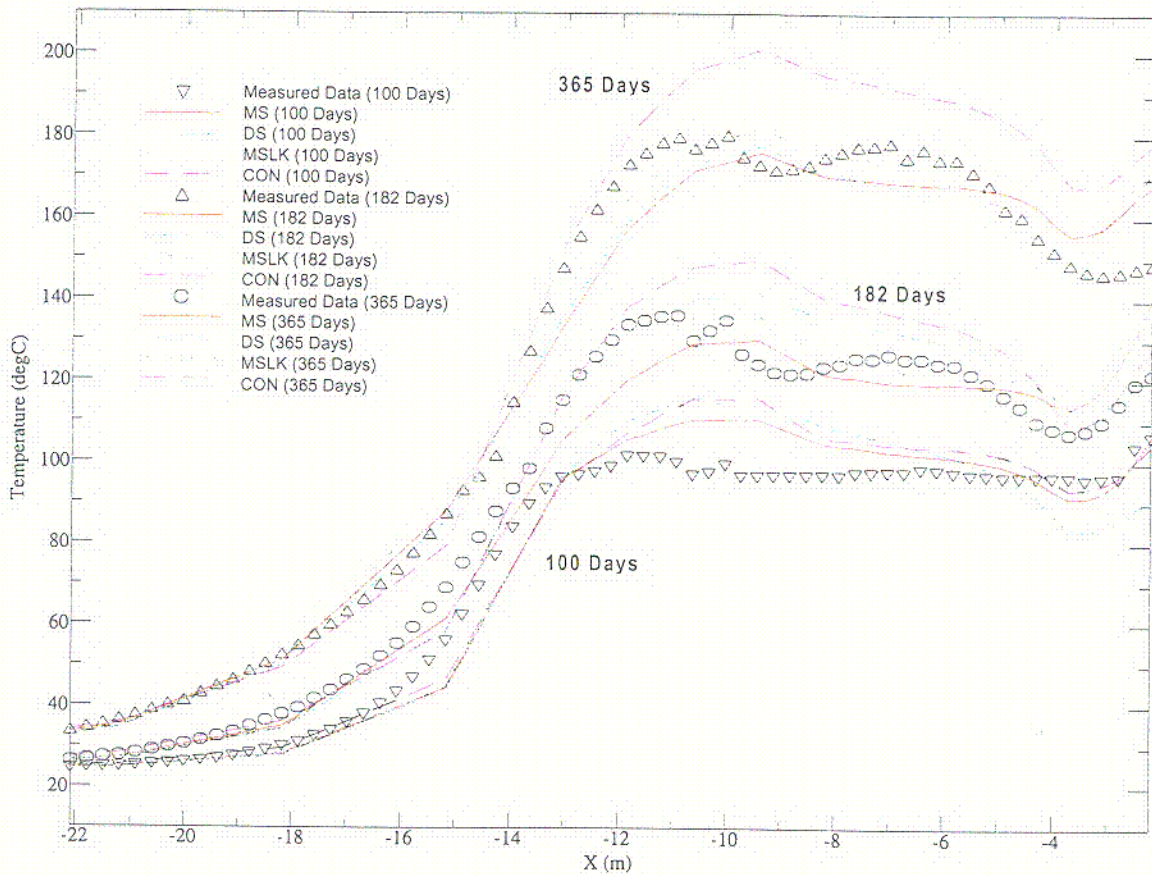


Figure 49. Comparison of NUFT Simulated and Measured Temperature Along Borehole 160 (Horizontal Near the Wing Heaters) at 100, 182, and 365 Days of Heating for the DST

C35

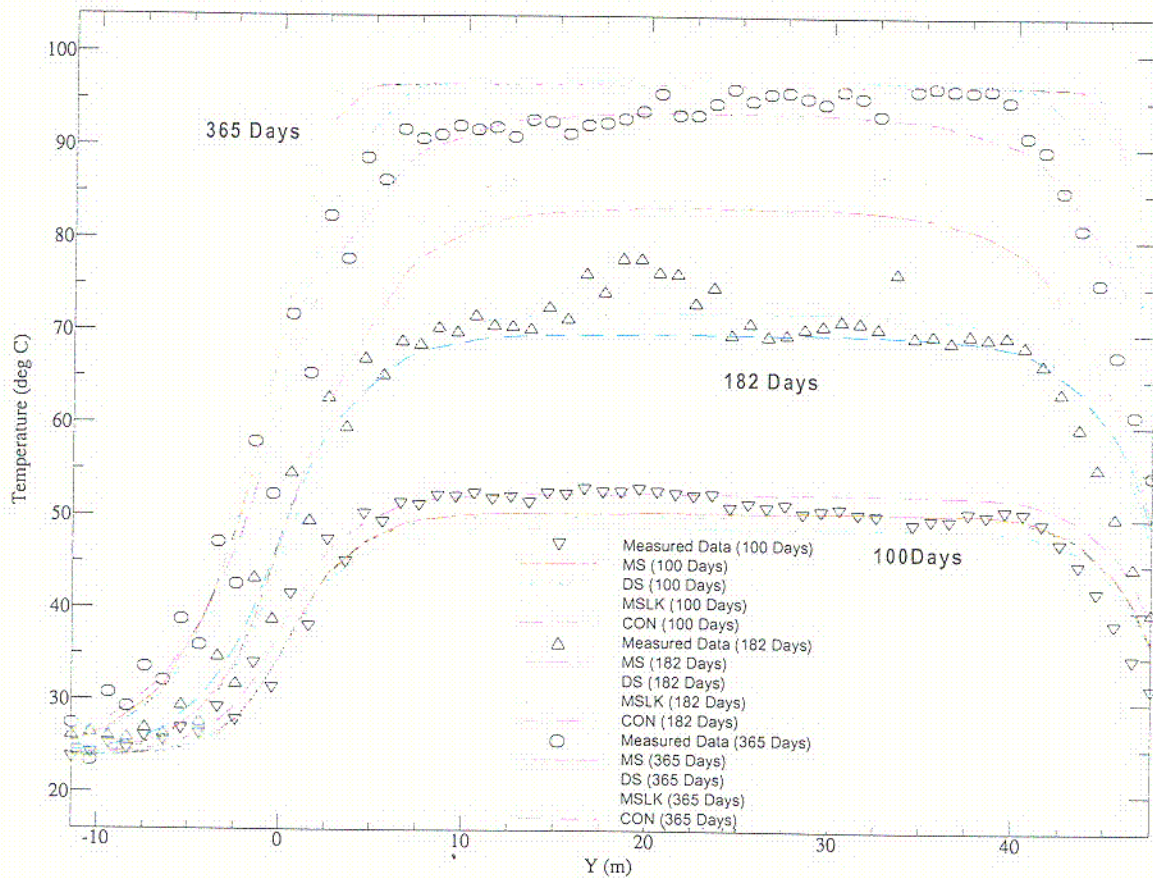


Figure 50. Comparison of NUFT Simulated and Measured Temperature Along Borehole 80 (Parallel to the HD, Slightly Above and to the Side) at 100, 182, and 365 Days of Heating for the DST

C36

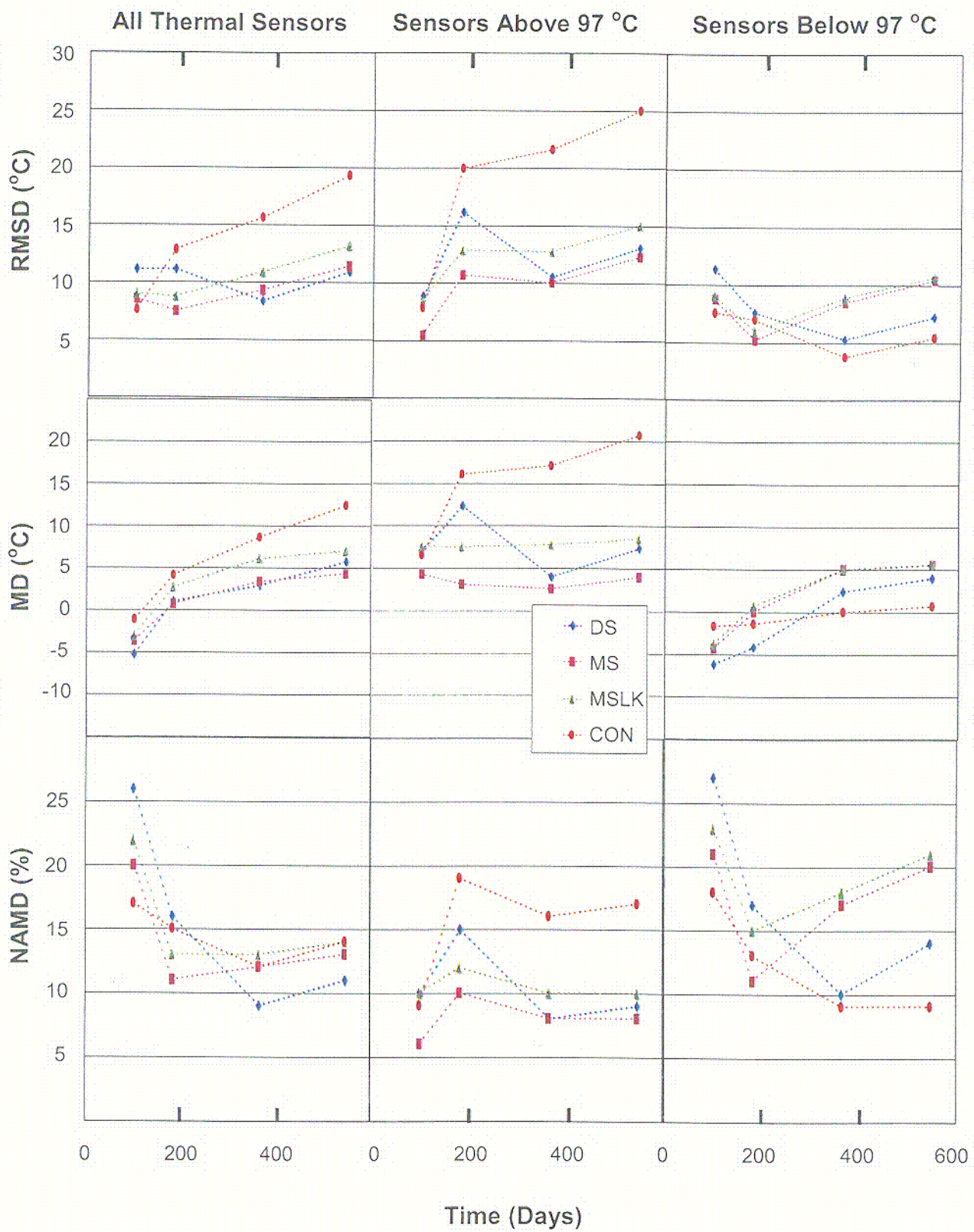
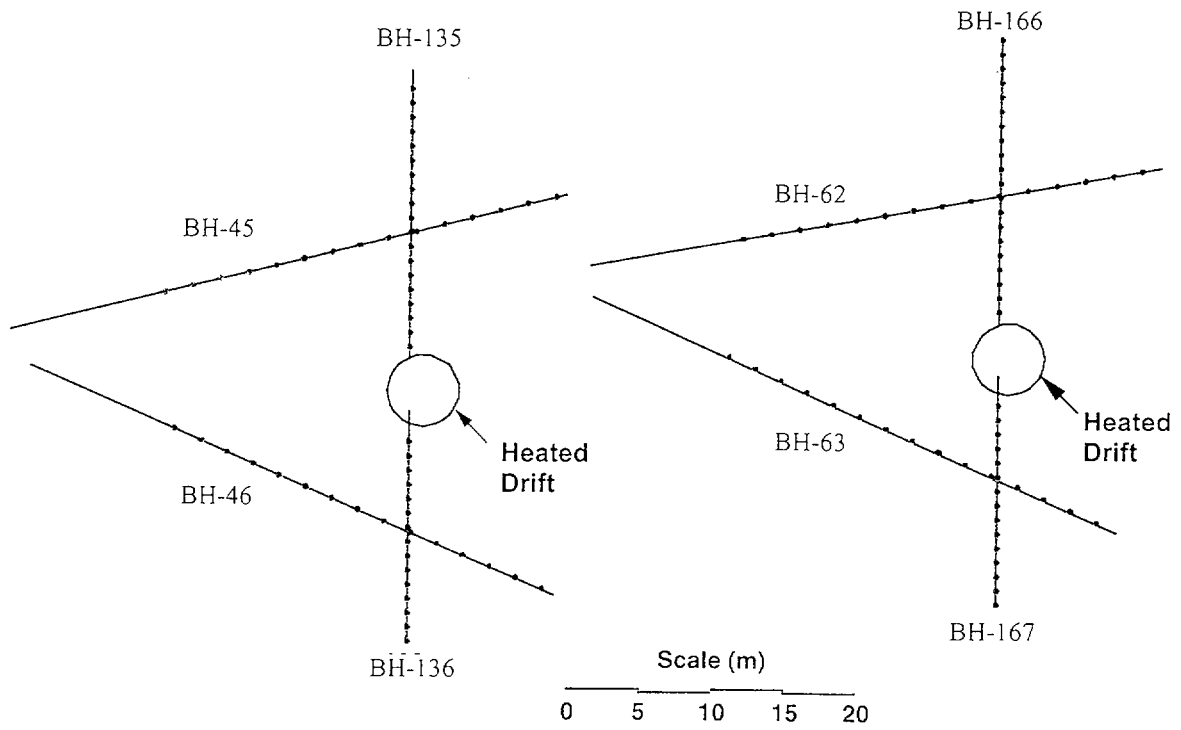


Figure 51. Statistical Measures for DST NUFT Thermal Analyses

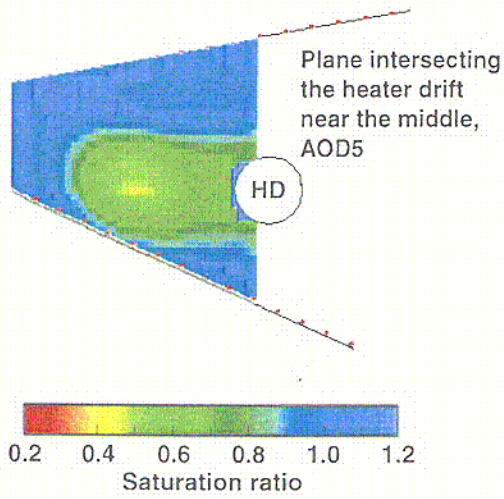
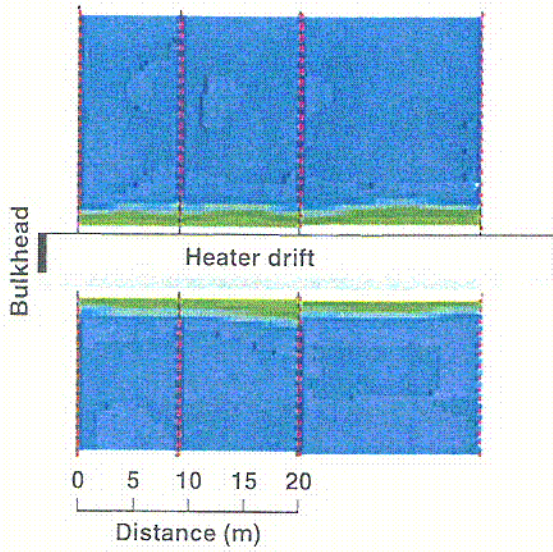
C37



NOTE: The electrodes within each borehole are shown by small circles. The electrode spacing is 1m for boreholes drilled from the HD and 2m for boreholes drilled from the OD.

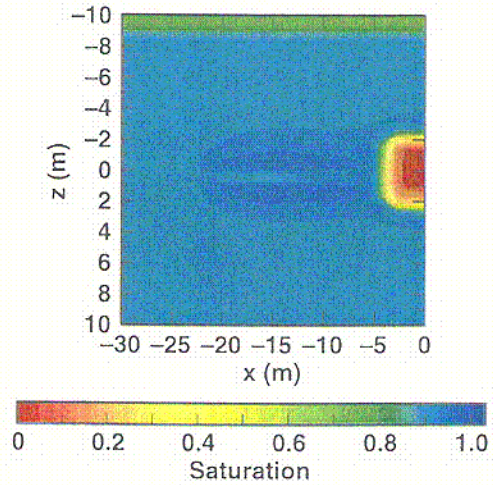
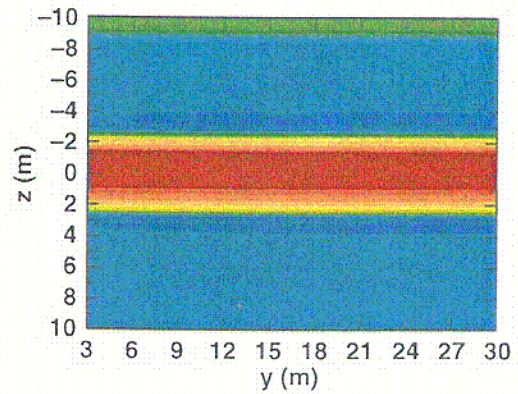
Figure 52. Two Cross-Sections Orthogonal to the HD Showing the Location of the ERT Boreholes Drilled from the OD and Selected Boreholes Drilled from the HD of the DST

Measured (ERT)



(a)

Simulated



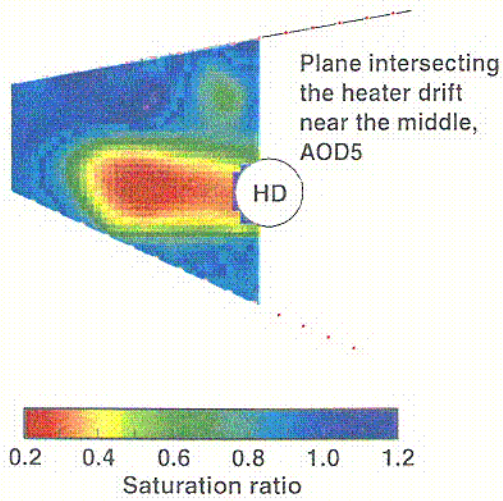
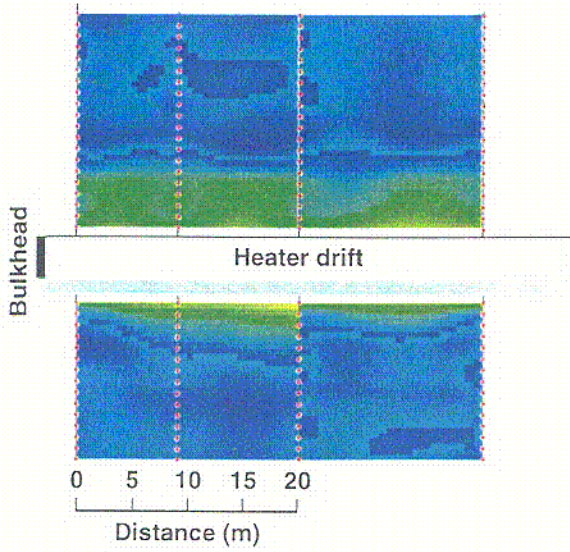
(b)

NOTE: Measured ERT-derived water saturation ratio (at 105 days) distributions for the (a) longitudinal cross-section through the HD axis and (b) transverse cross-section OD#5 (Boreholes 62, 63).

Figure 53. Comparison of Distributions of Measured and Simulated (NUFT) Water Saturation at 100 Days for the DST, Using the DS Property Set

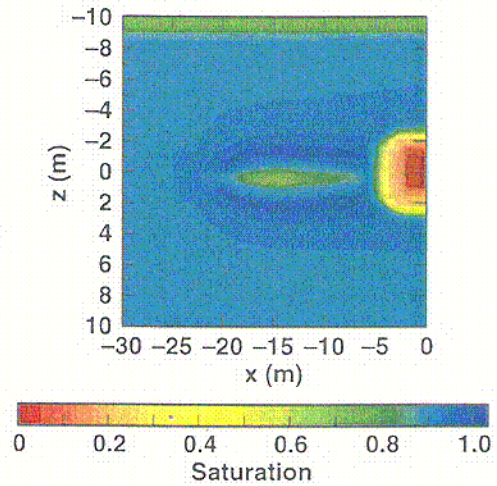
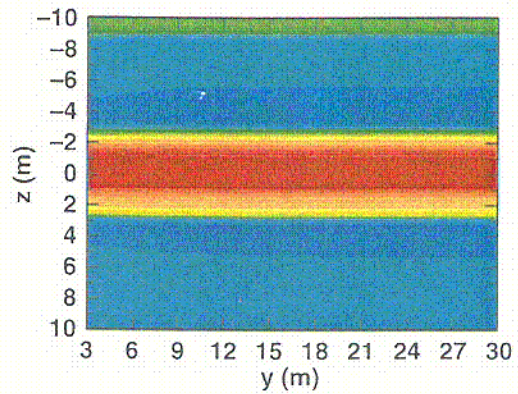
C38

Measured (ERT)



(a)

Simulated



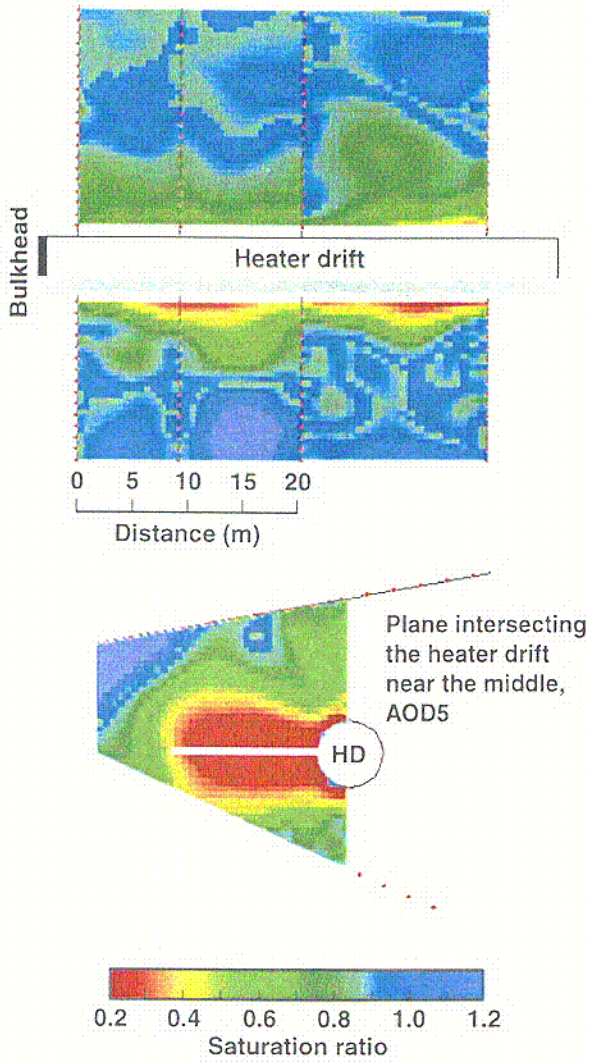
(b)

NOTE: Measured ERT-derived water saturation ratio (at 182 days) distributions for the (a) longitudinal cross-section through the HD axis and (b) transverse cross-section OD#5 (Boreholes 62, 63).

Figure 54. Comparison of Distributions of Measured and Simulated (NUFT) Water Saturation at 182 Days for the DST, Using the DS Property Set

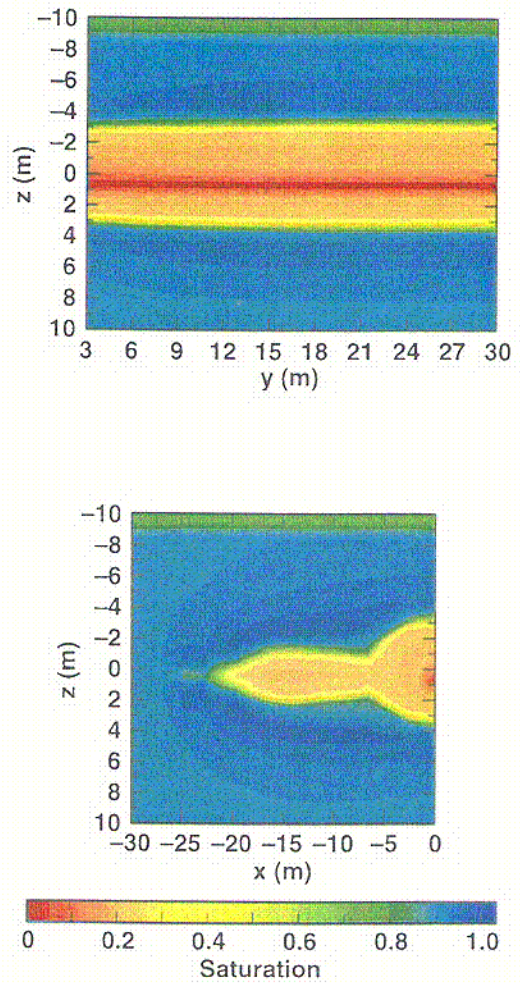
C39

Measured (ERT)



(a)

Simulated



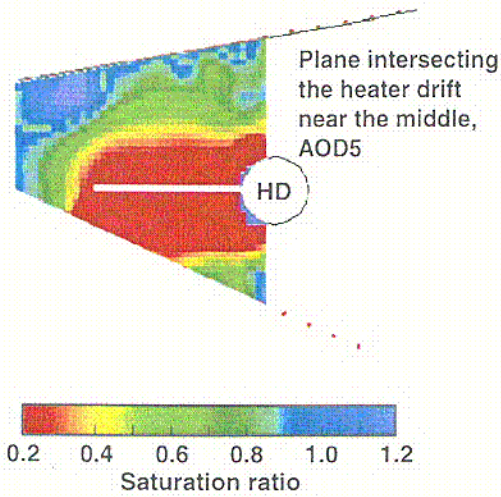
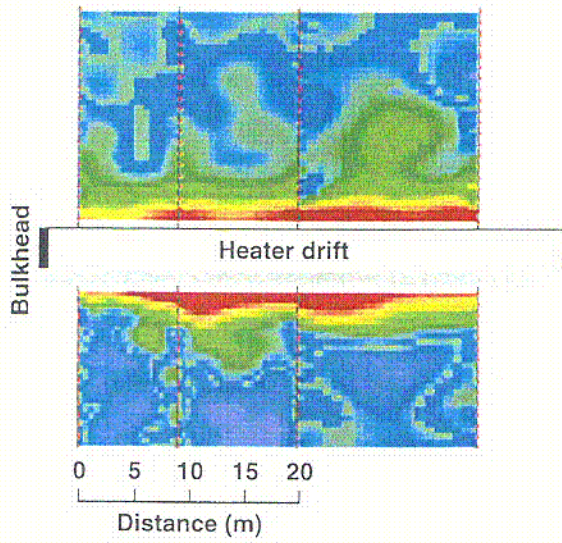
(b)

NOTE: Measured ERT-derived water saturation ratio (at 371 days) distributions for the (a) longitudinal cross-section through the HD axis and (b) transverse cross-section OD#5 (Boreholes 62, 63).

Figure 55. Comparison of Distributions of Measured and Simulated (NUFT) Water Saturation at 365 Days for the DST, Using the DS Property Set

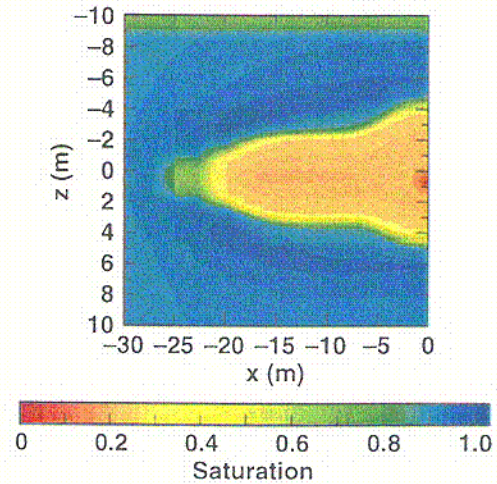
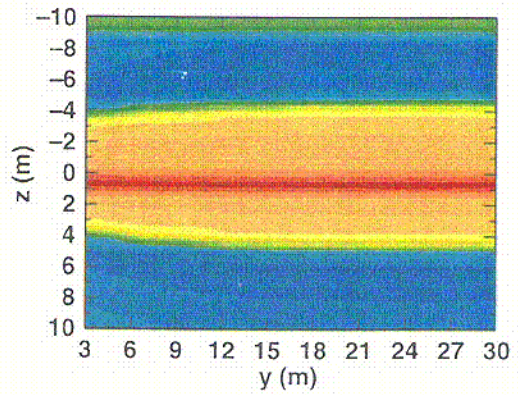
C40

Measured (ERT)



(a)

Simulated



(b)

NOTE: Measured ERT-derived water saturation ratio (at 558 days) for the (a) longitudinal cross-section through the HD axis and (b) transverse cross-section OD#5 (Boreholes 62, 63).

Figure 56. Comparison of Distributions of Measured and Simulated (NUFT) Water Saturation at 547 Days for the DST, Using the DS Property Set

C41

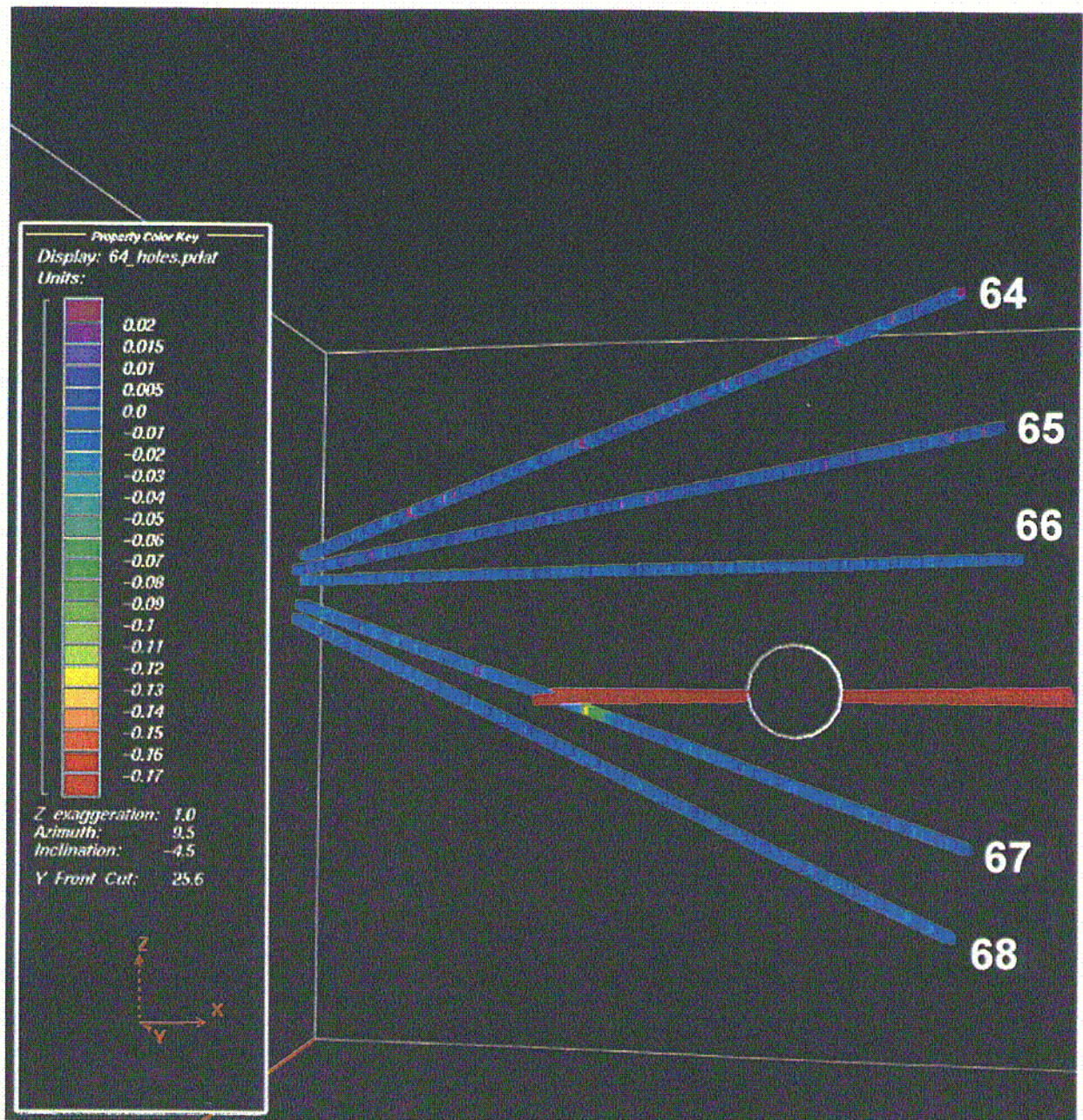


Figure 57. Fraction Volume of Water Content in DST Boreholes as Measured by Neutron Logging Boreholes 64 to 68 for Nominal Heating Duration of 3 Months.

C42

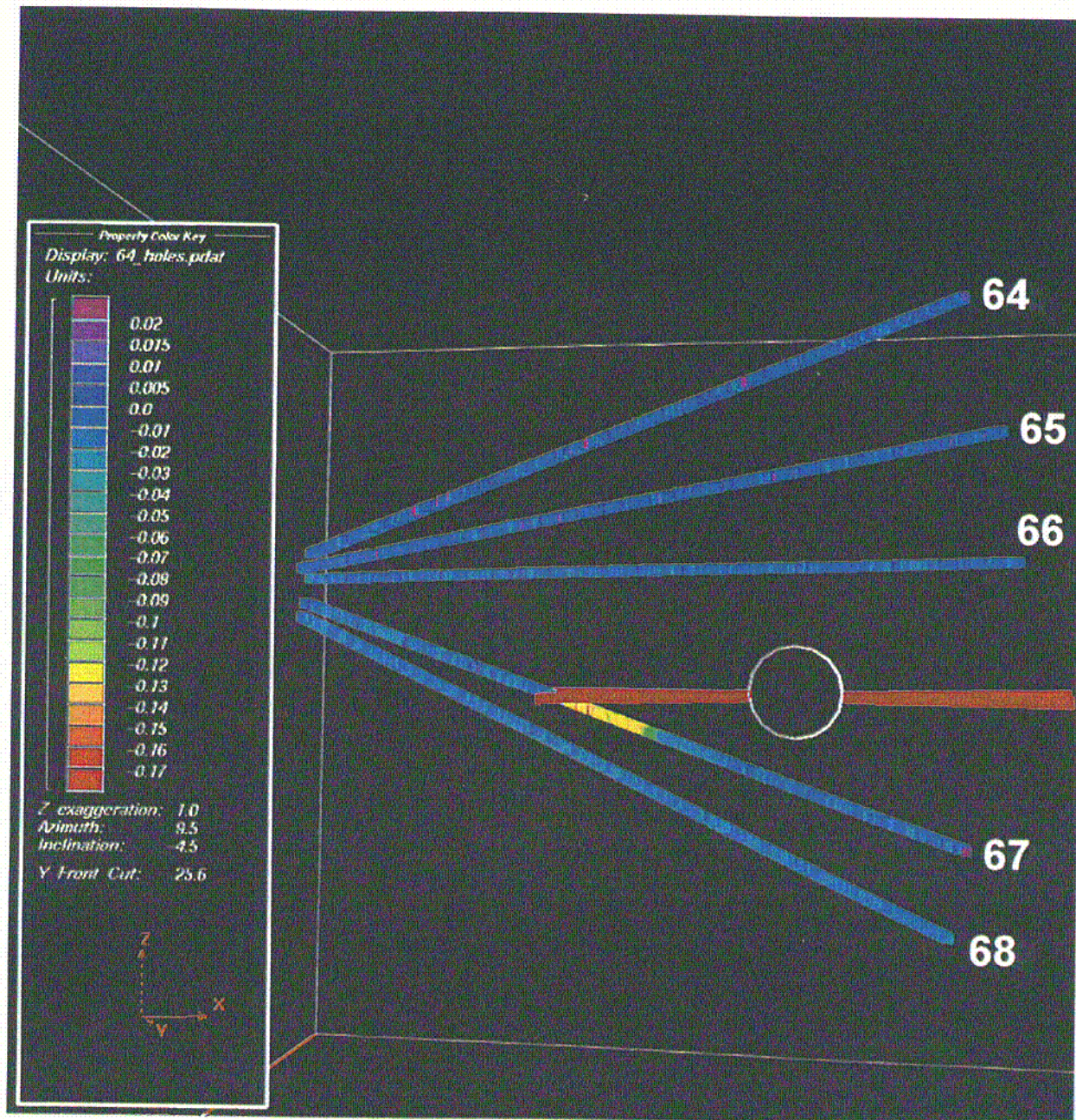


Figure 58. Fraction Volume of Water Content in DST Boreholes as Measured by Neutron Logging Boreholes 64 to 68 for Nominal Heating Duration of 6 Months.

C43

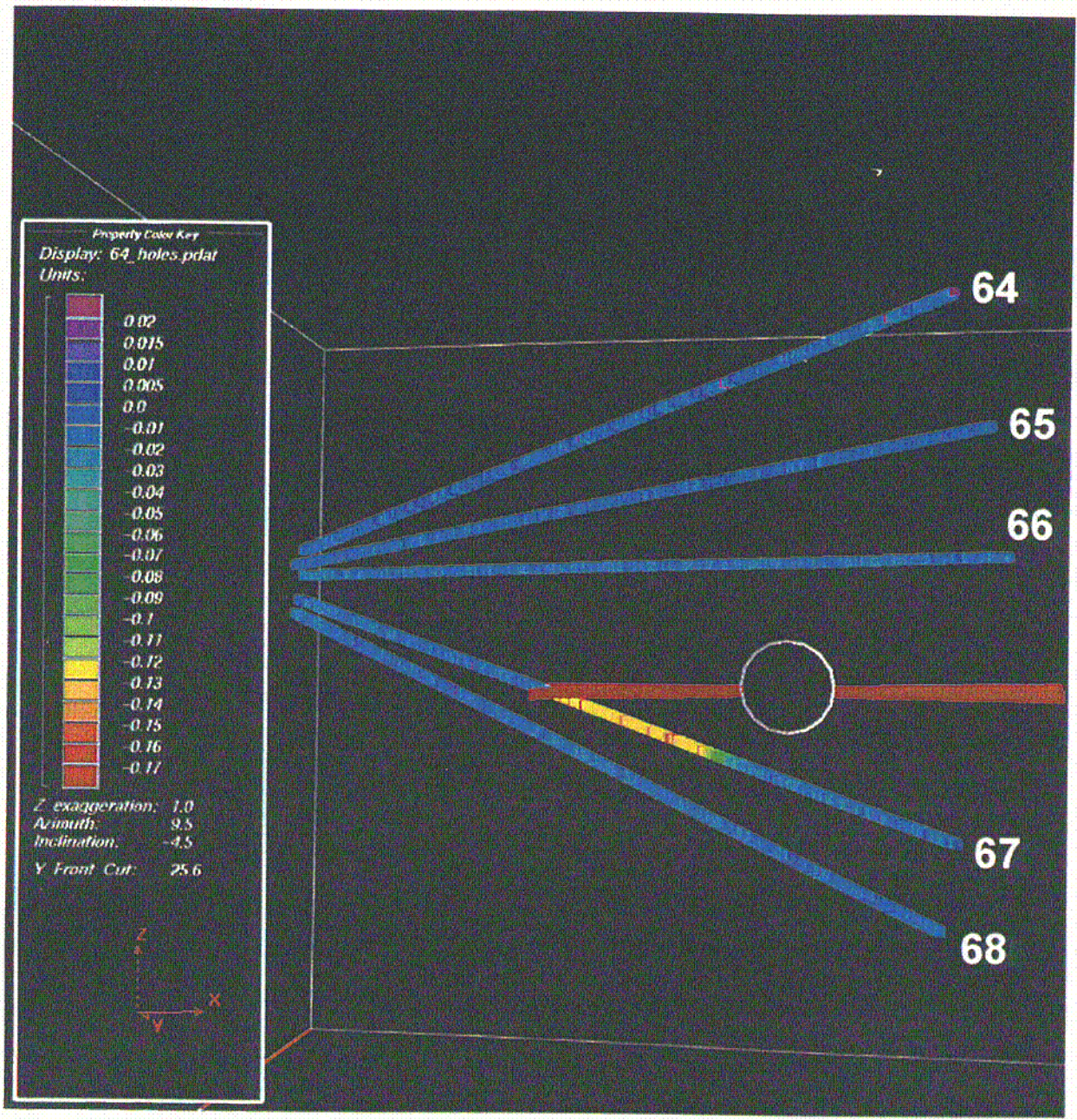


Figure 59. Fraction Volume of Water Content in DST Boreholes as Measured by Neutron Logging Boreholes 64 to 68 for Nominal Heating Duration of 12 Months

C44

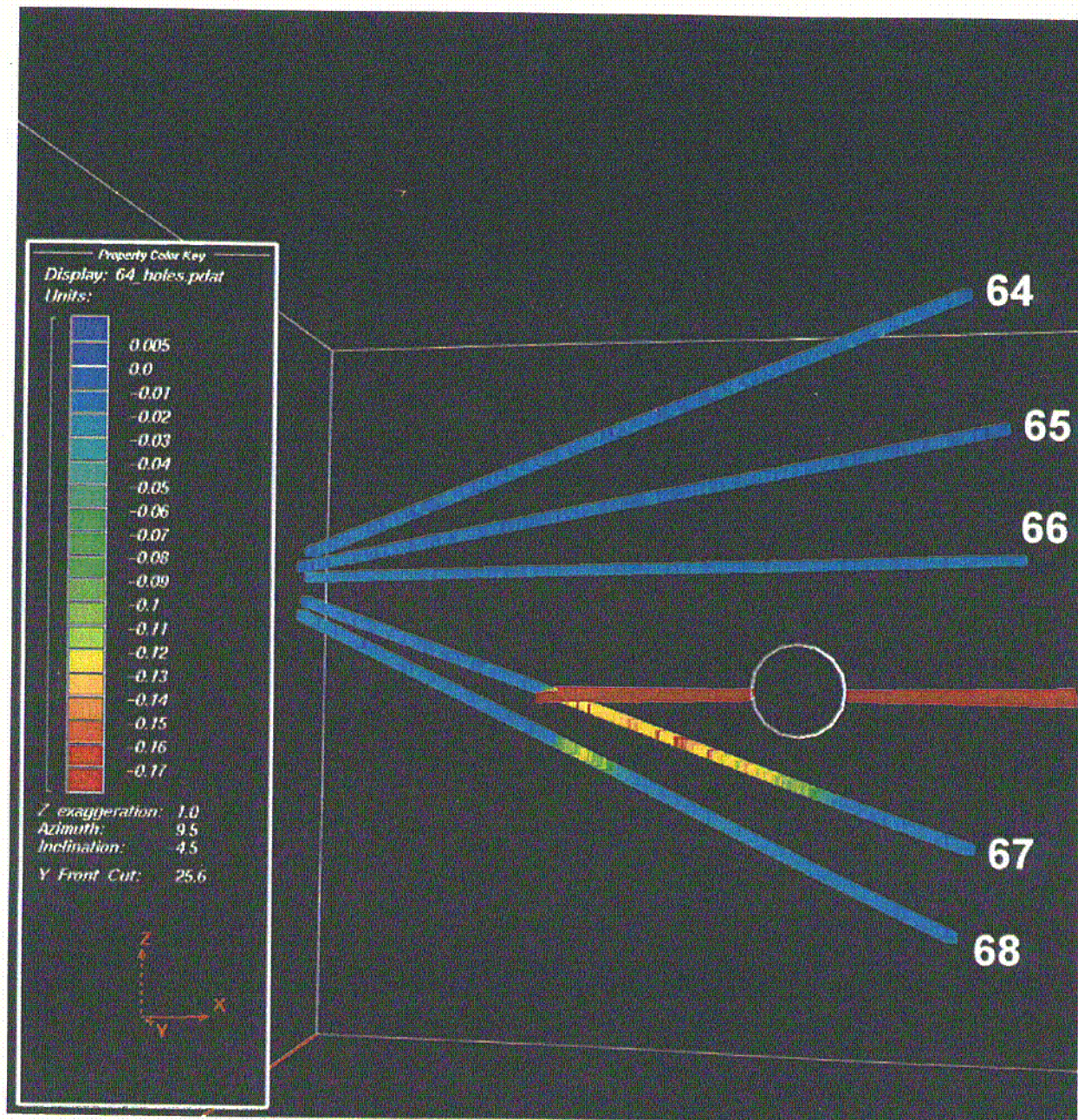


Figure 60. Fraction Volume of Water Content in DST Boreholes as Measured by Neutron Logging Boreholes 64 to 68 for Nominal Heating Duration of 18 Months

C45

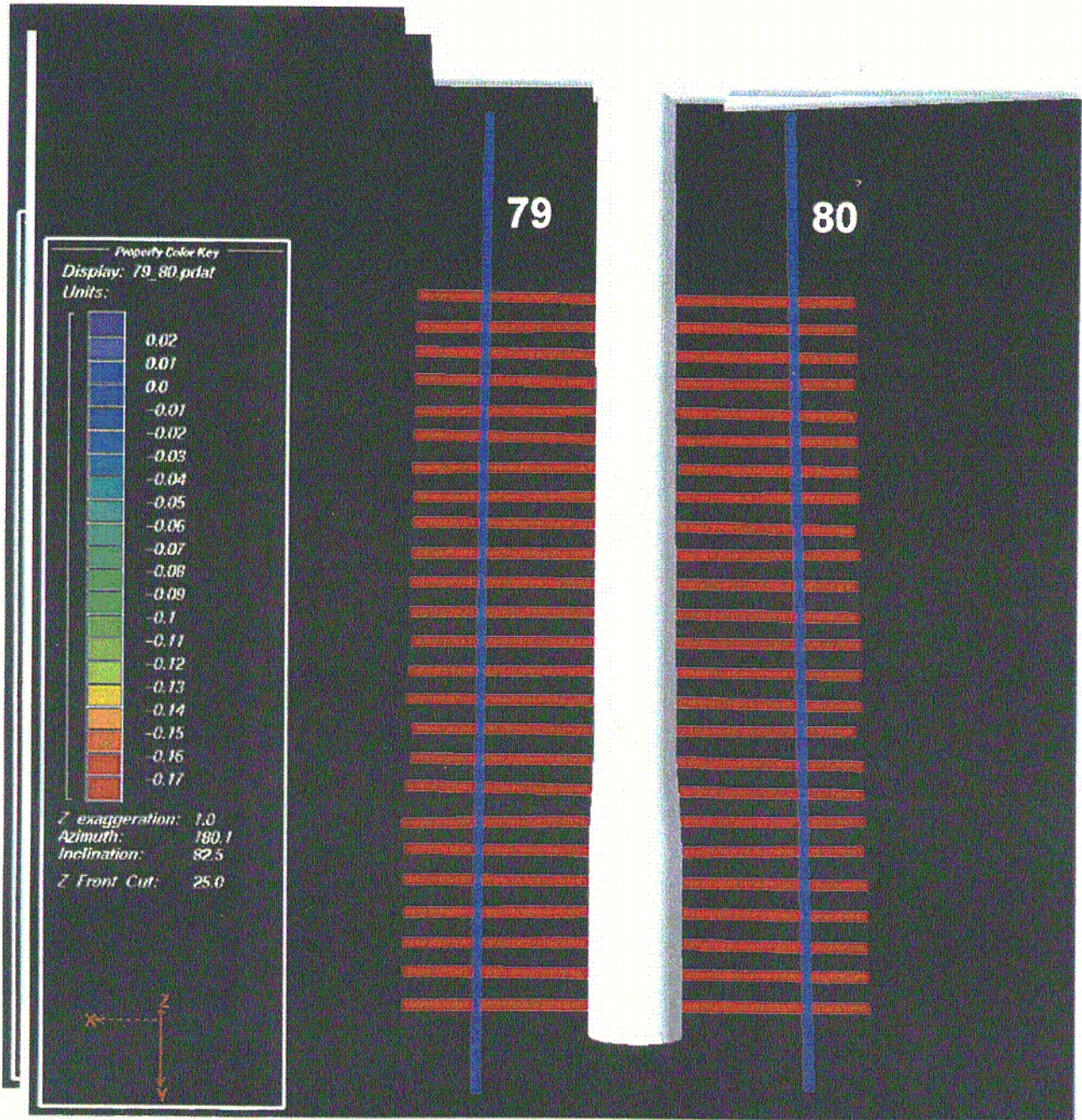


Figure 61. Fraction Volume of Water Content in DST Boreholes 79 and 80 as Measured by Neutron Logging for Nominal Heating Duration of 3 Months

c46

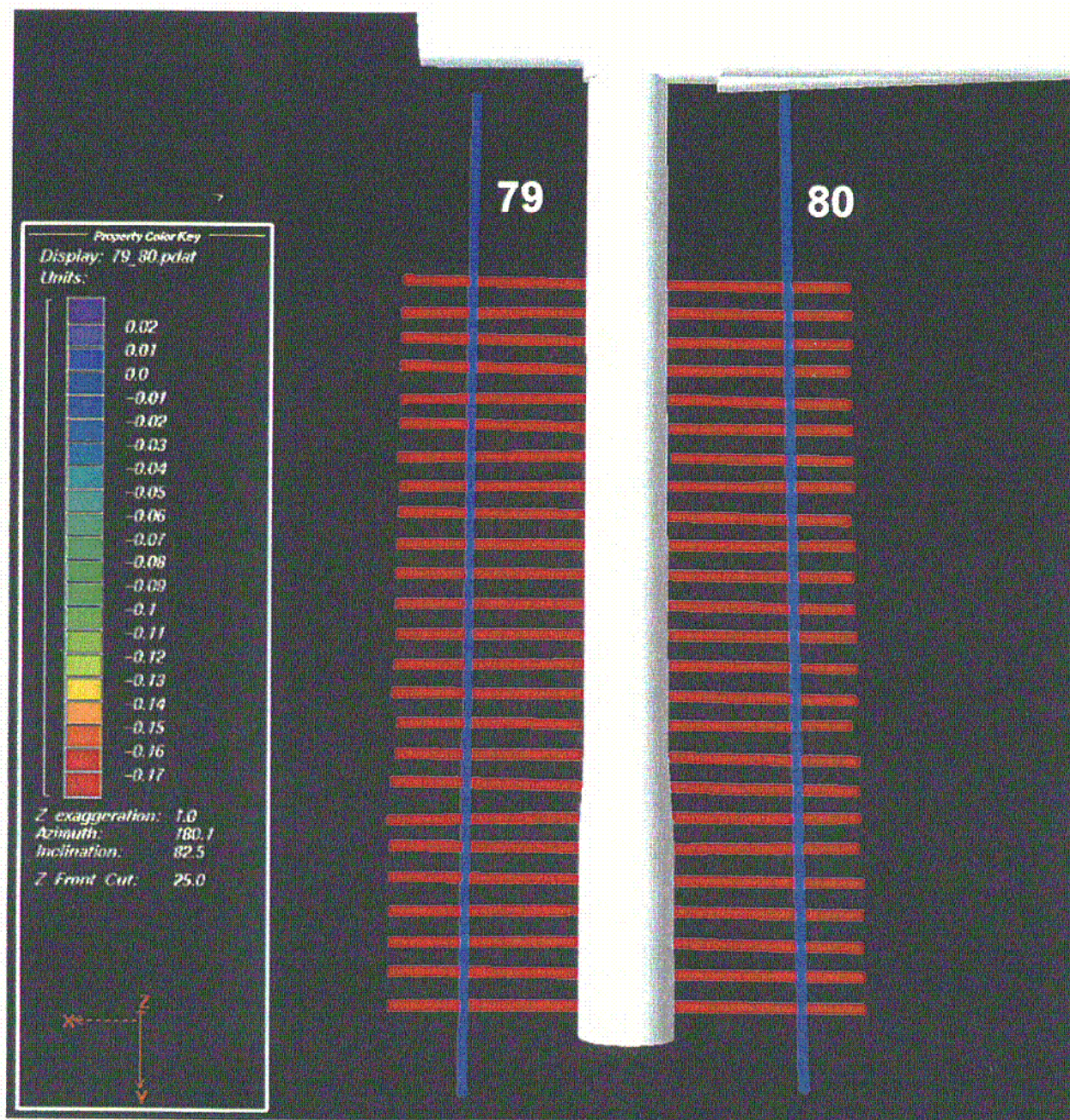


Figure 62. Fraction Volume of Water Content in DST Boreholes 79 and 80 as Measured by Neutron Logging for Nominal Heating Duration of 6 Months.

C47

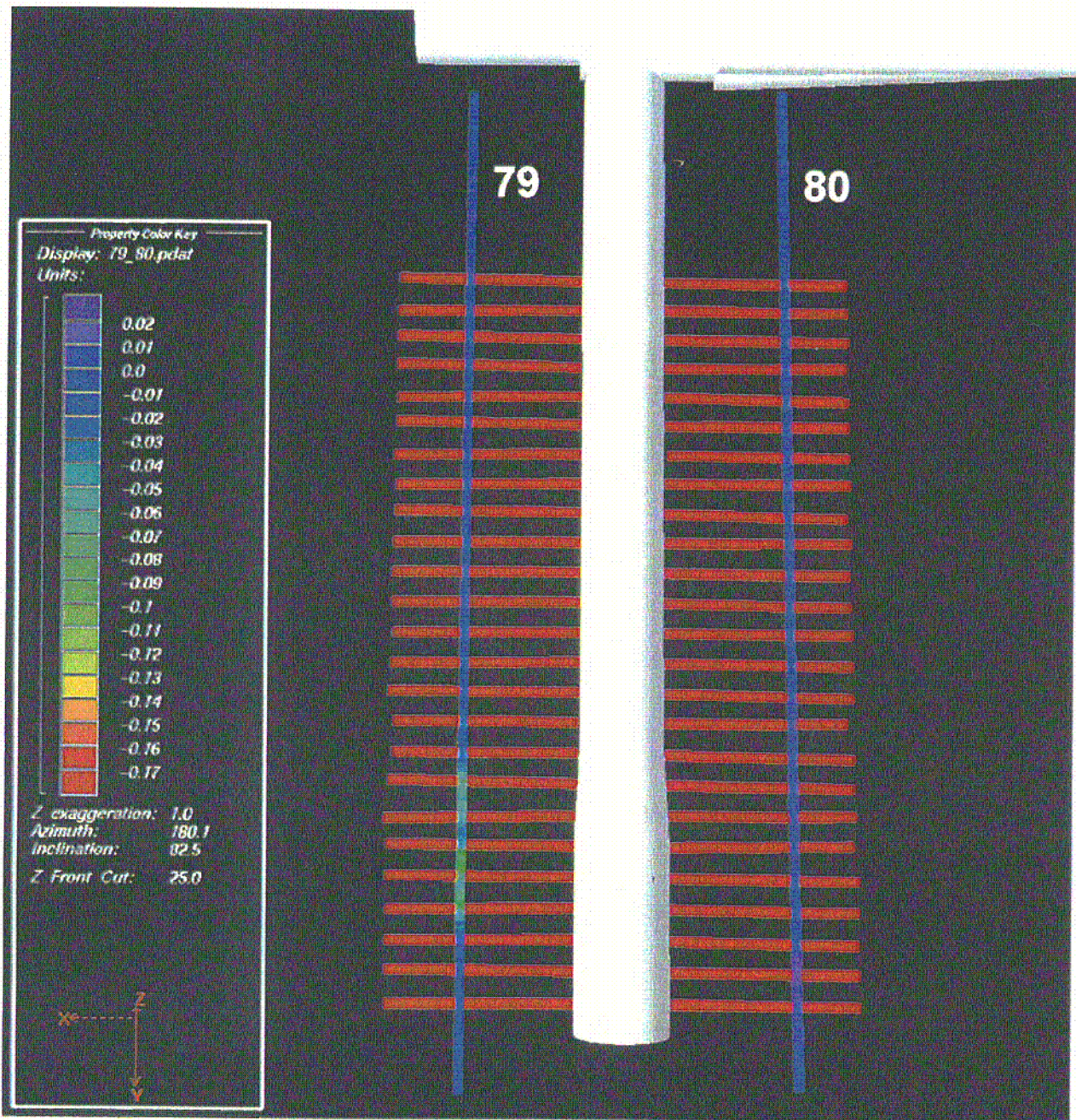


Figure 63. Fraction Volume of Water Content in DST Boreholes 79 and 80 as Measured by Neutron Logging for Nominal Heating Duration of 12 Months.

c48

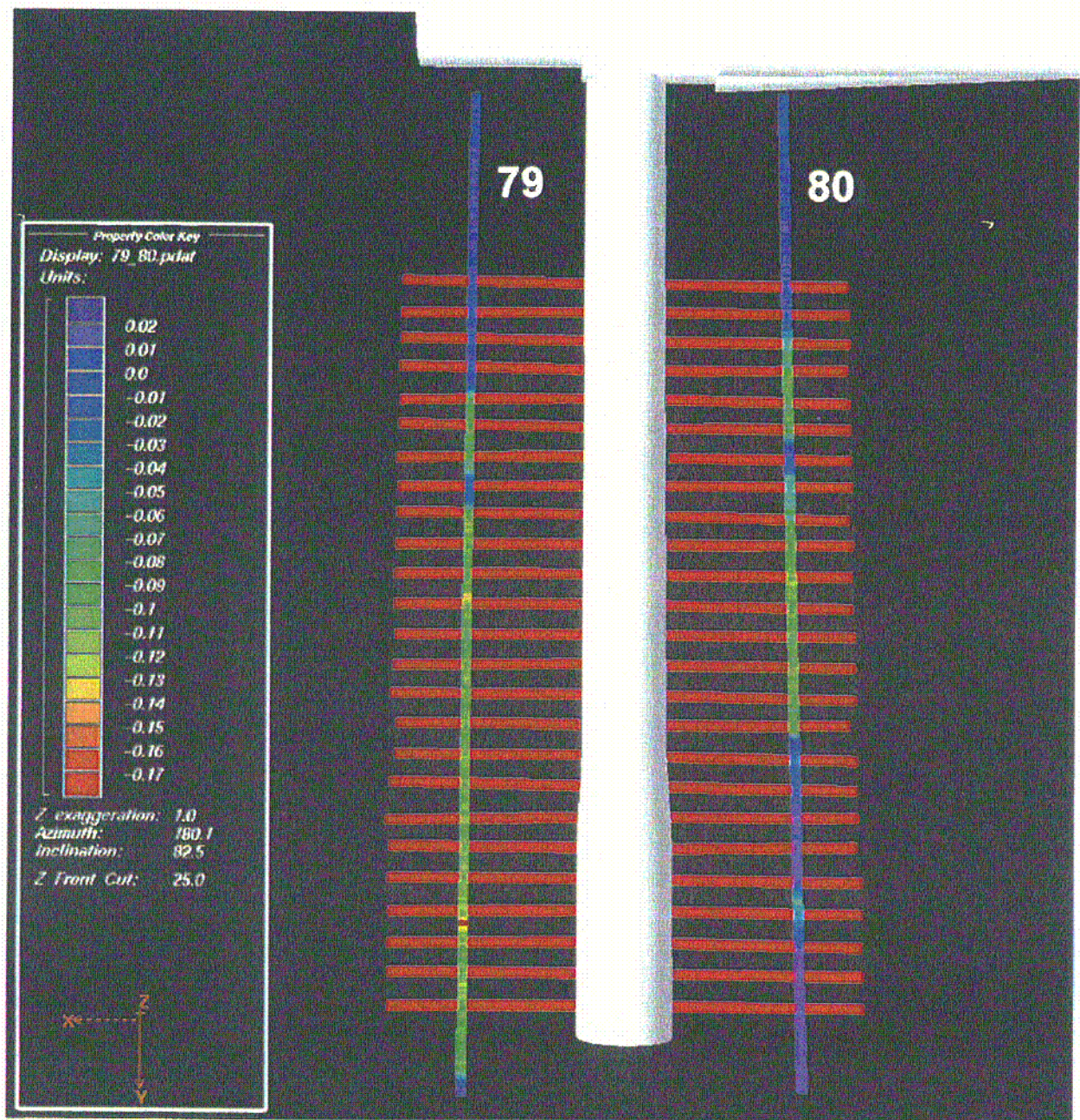


Figure 64. Fraction Volume of Water Content in DST Boreholes 79 and 80 as Measured by Neutron Logging for Nominal Heating Duration of 18 Months.

249

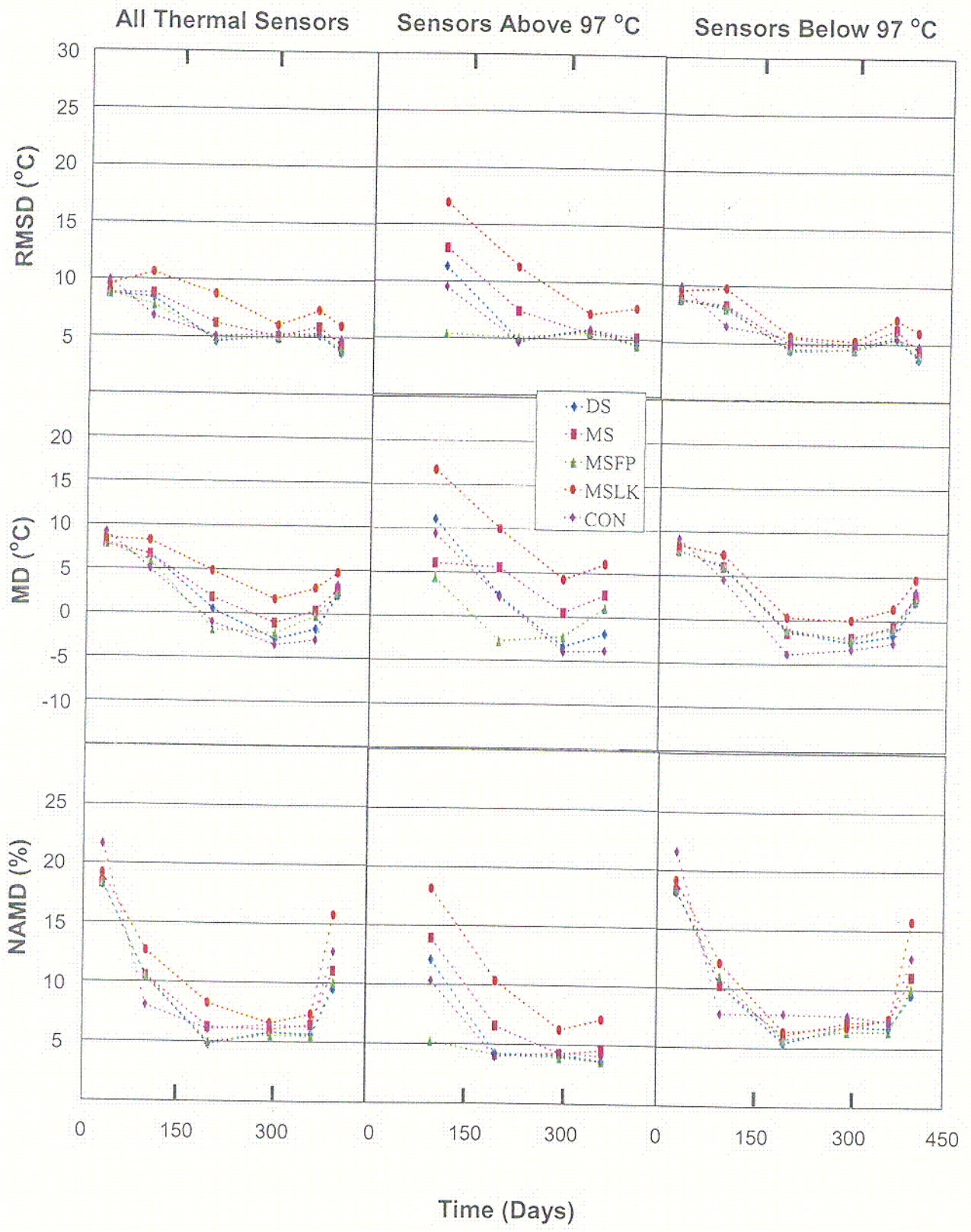


Figure 66. Statistical Measures for LBT Thermal Analyses

C50

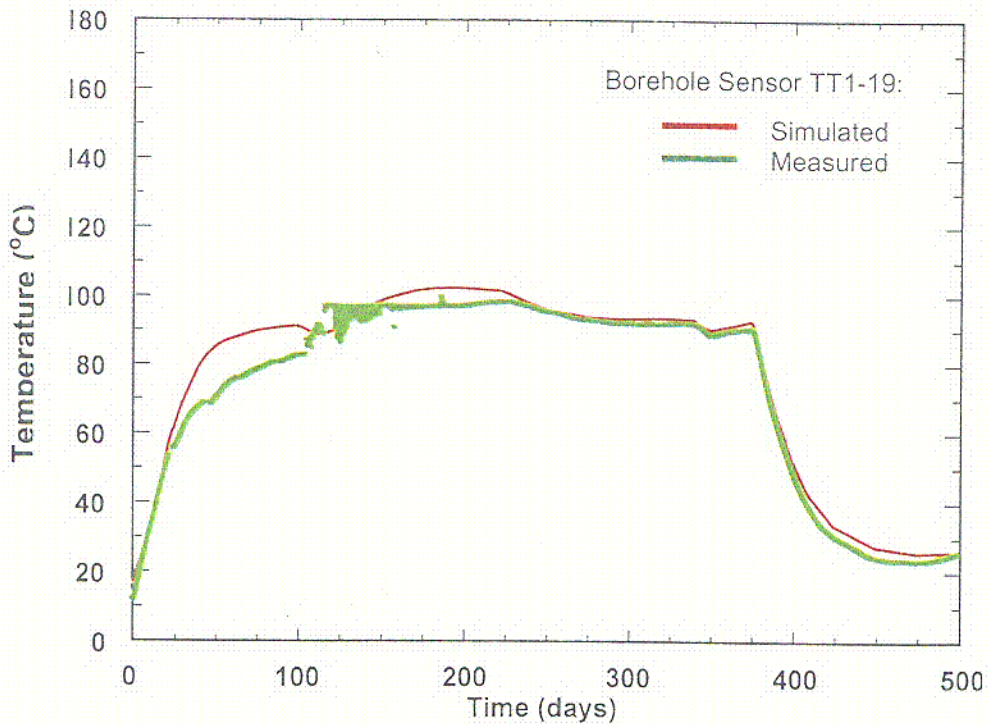
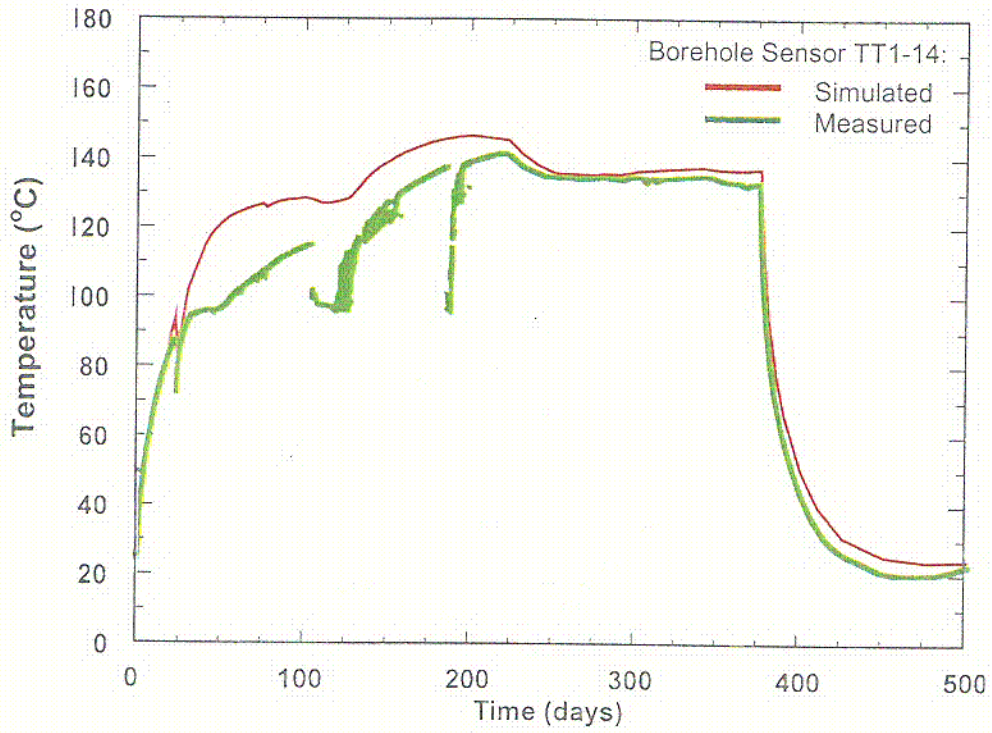


Figure 67. Simulated Versus Measured Temperature Histories for Sensors TT1-14 and TT1-19 at Borehole TT1 of the LBT. The DS Property Set was Used in the Simulation.

251

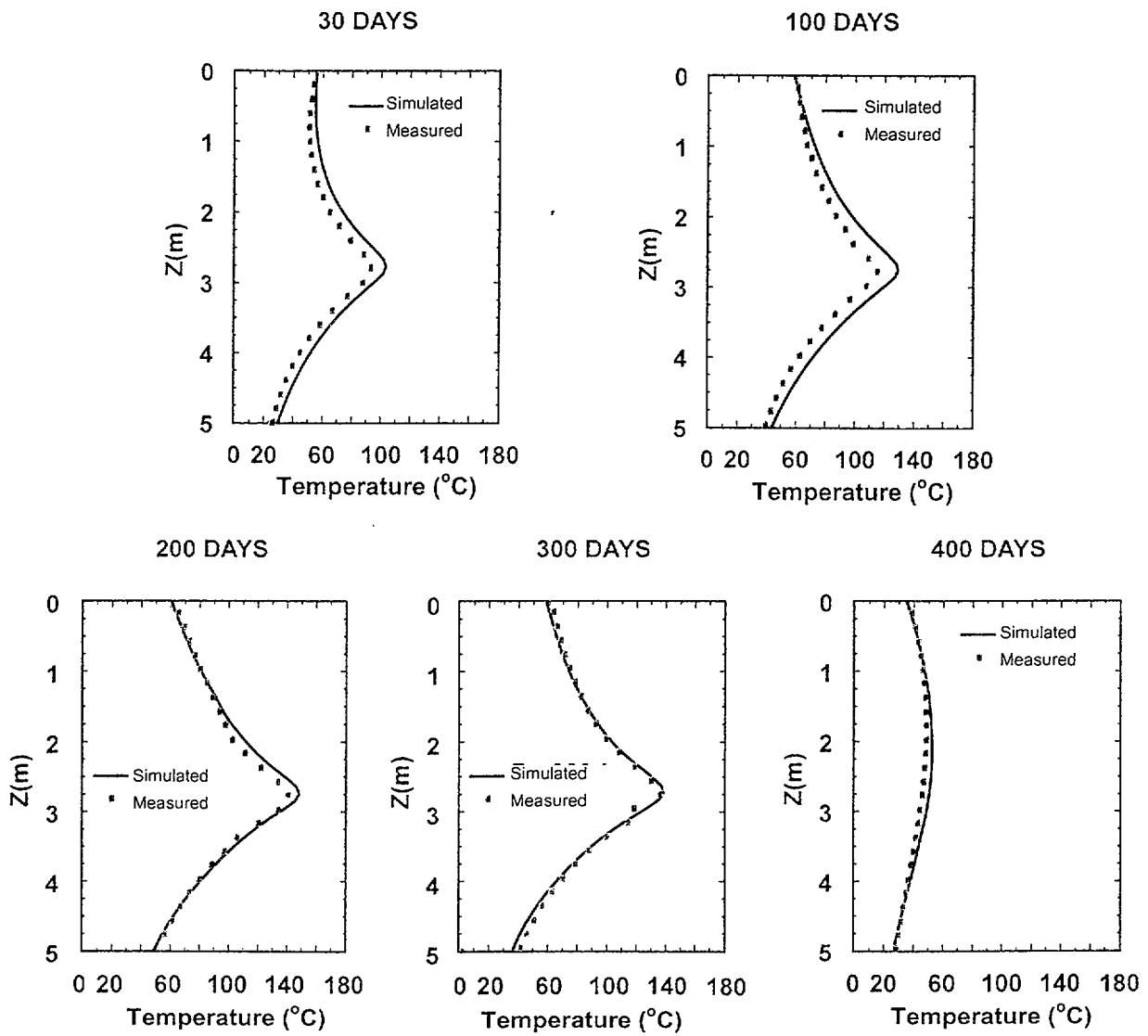


Figure 65. Simulated Versus Measured Temperature Profile for Borehole TT1 of LBT. The DS Property Set was Used in the Simulation. The Heaters were Active for 375 Days

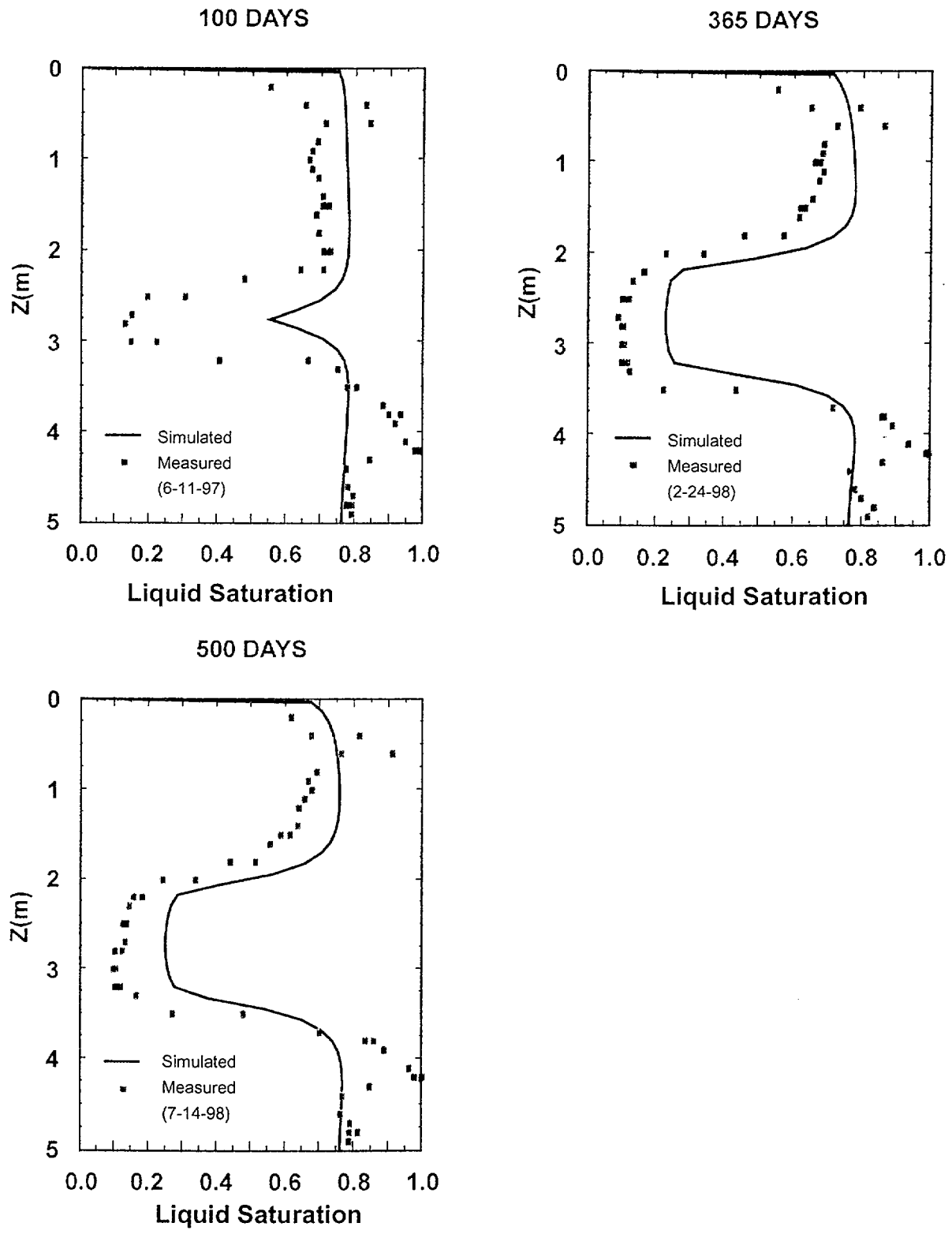


Figure 68. Liquid Saturation Profile Along Borehole TN3 for the LBT. The DS Property Set was Used in the Simulation

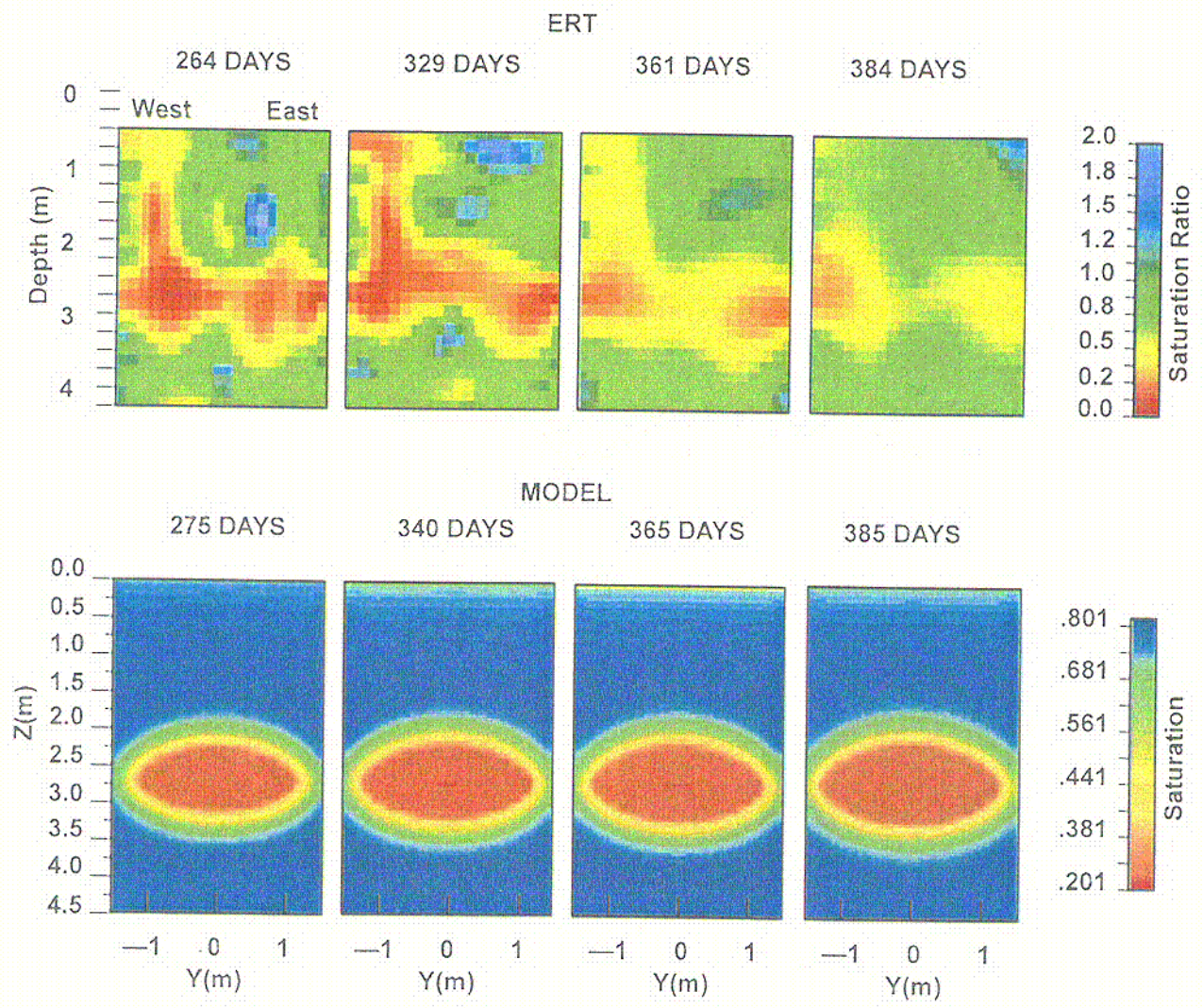


Figure 69. Comparison of ERT Measurements and Simulated (DS-LBT) Water Saturations

C52

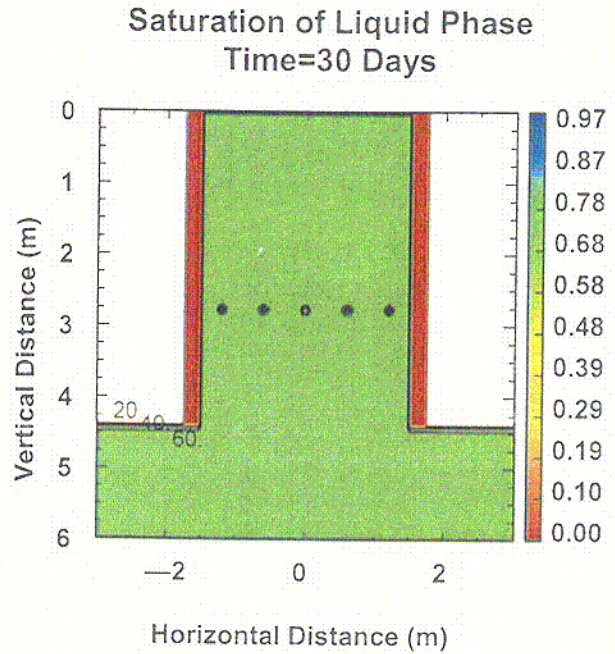
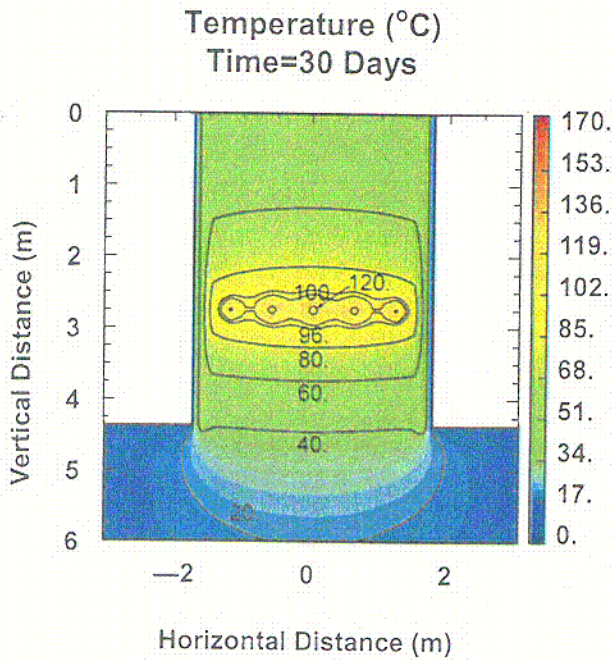


Figure 70. Image of Simulated Temperature and Liquid-Phase Saturation Distribution at 30 Days for the LBT, Using the DS Property Set

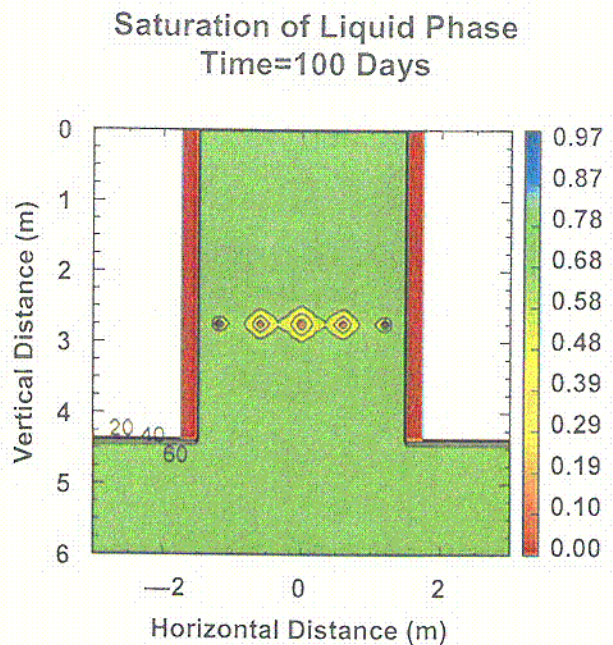
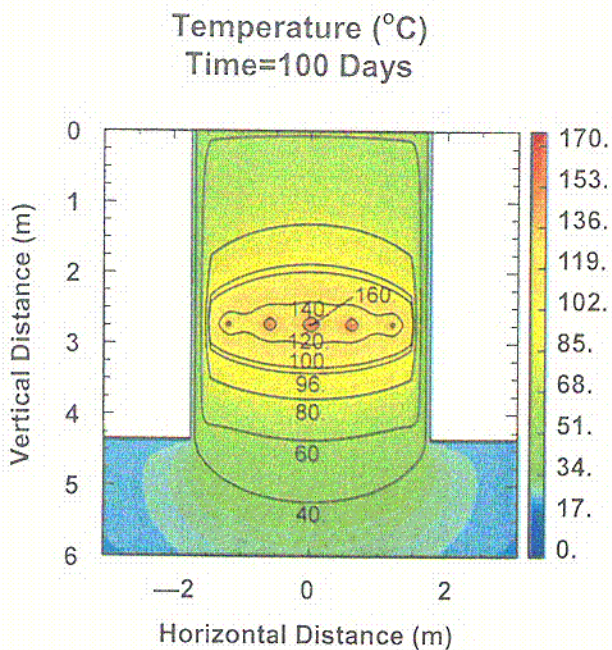


Figure 71. Image of Simulated Temperature and Liquid-Phase Saturation Distribution at 100 Days for the LBT, Using the DS Property Set

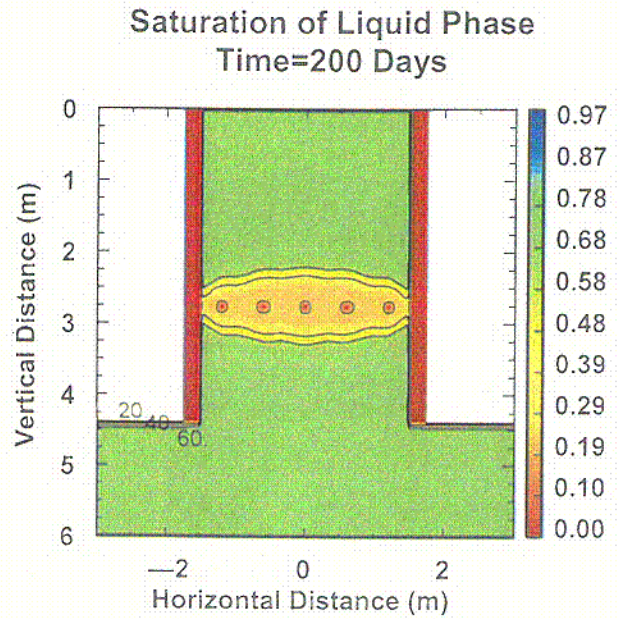
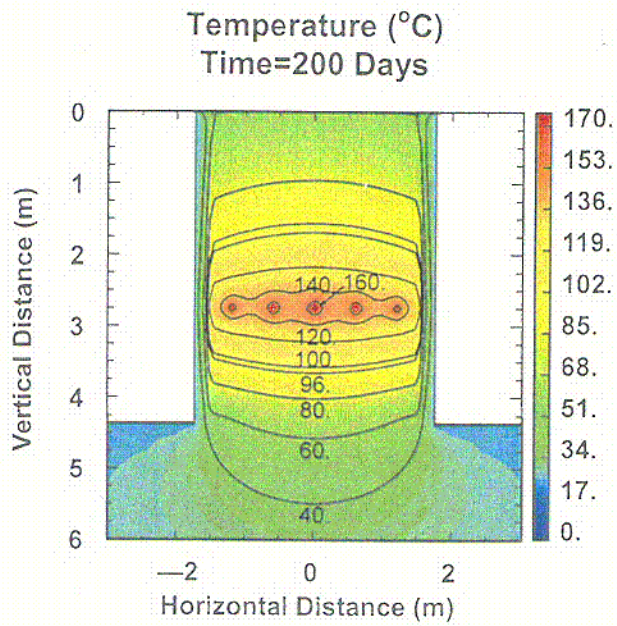


Figure 72. Image of Simulated Temperature and Liquid-Phase Saturation Distribution at 200 Days for the LBT, Using the DS Property Set

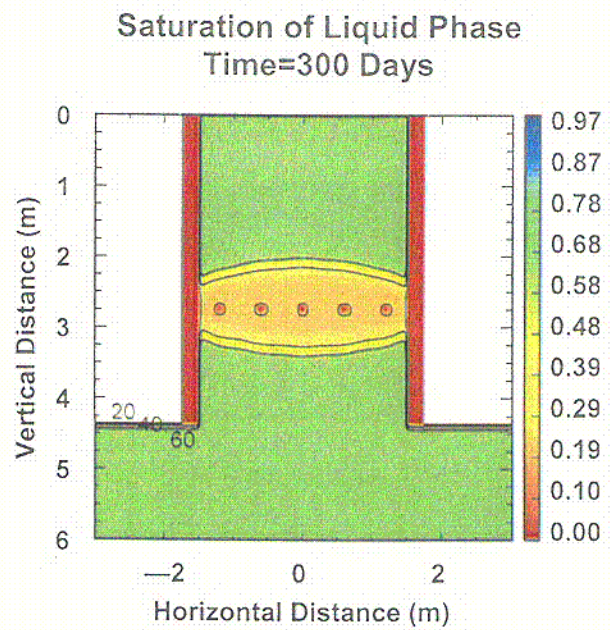
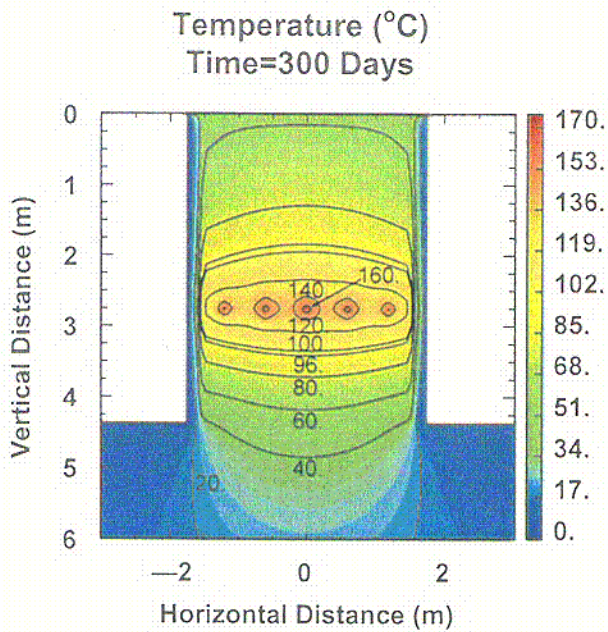


Figure 73. Image of Simulated Temperature and Liquid-Phase Saturation Distribution at 300 Days for the LBT, Using the DS Property Set

C54

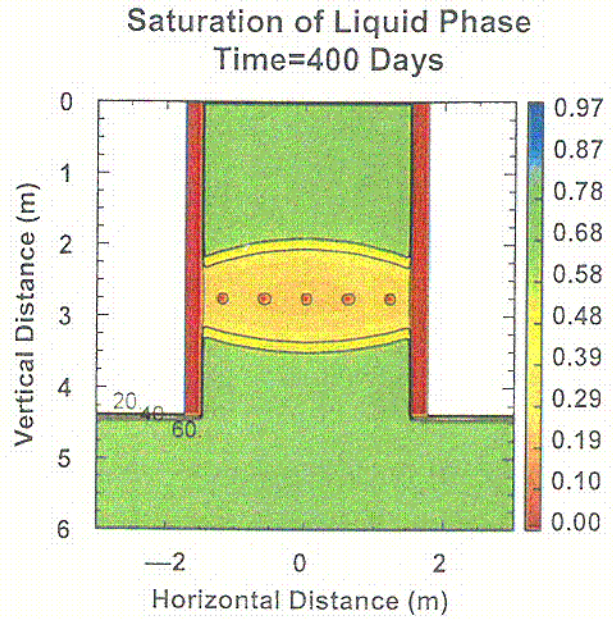
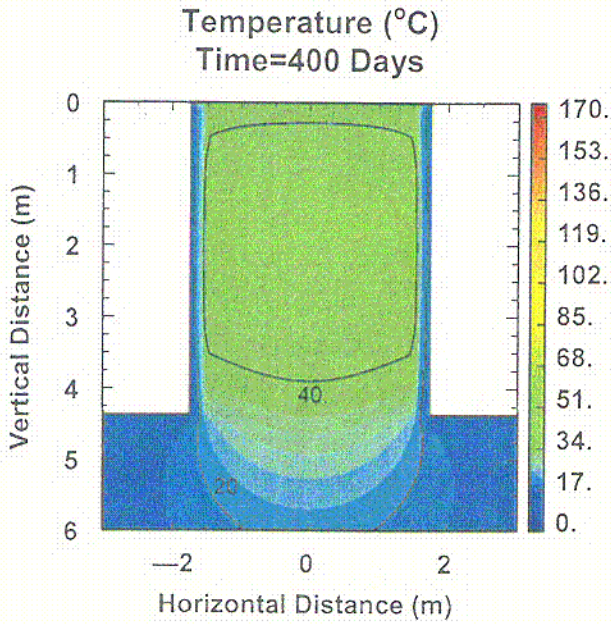


Figure 74. Image of Simulated Temperature and Liquid-Phase Saturation Distribution at 400 Days for the LBT, Using the DS Property Set

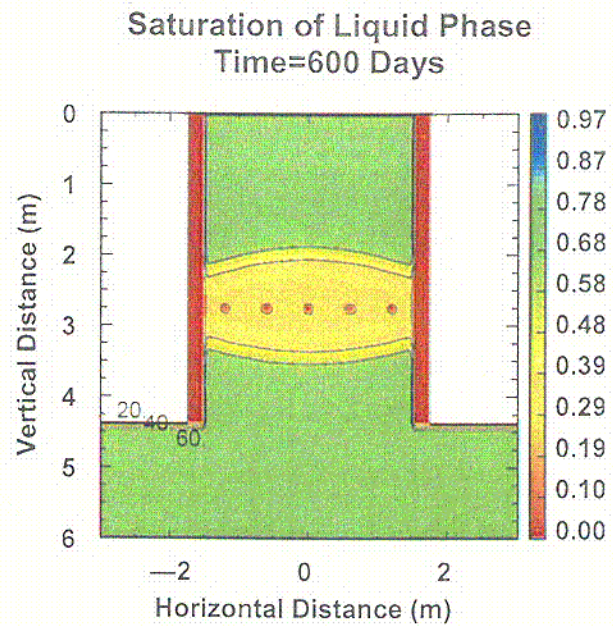
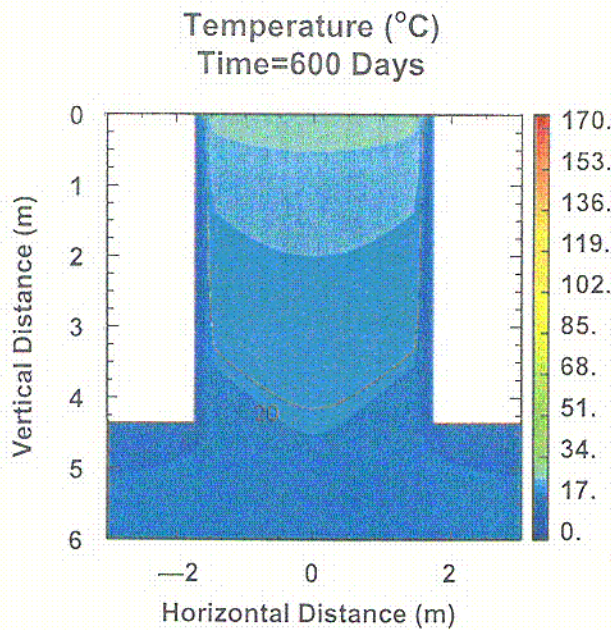


Figure 75. Image of Simulated Temperature and Liquid-Phase Saturation Distribution at 600 Days for the LBT, Using the DS Property Set

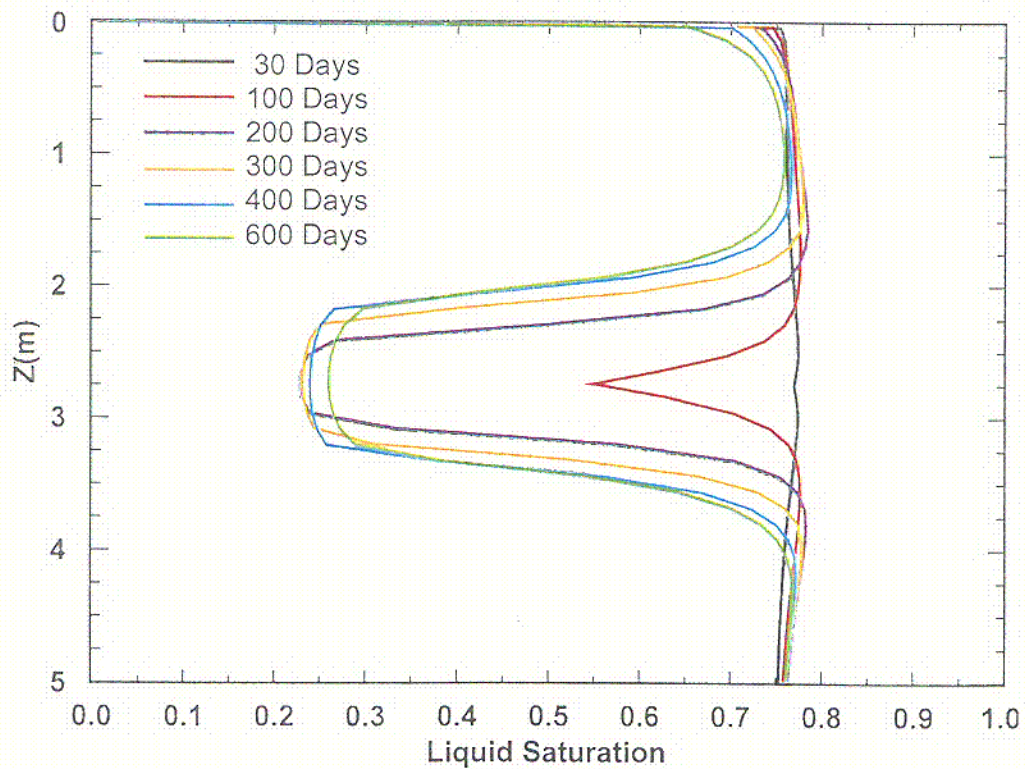
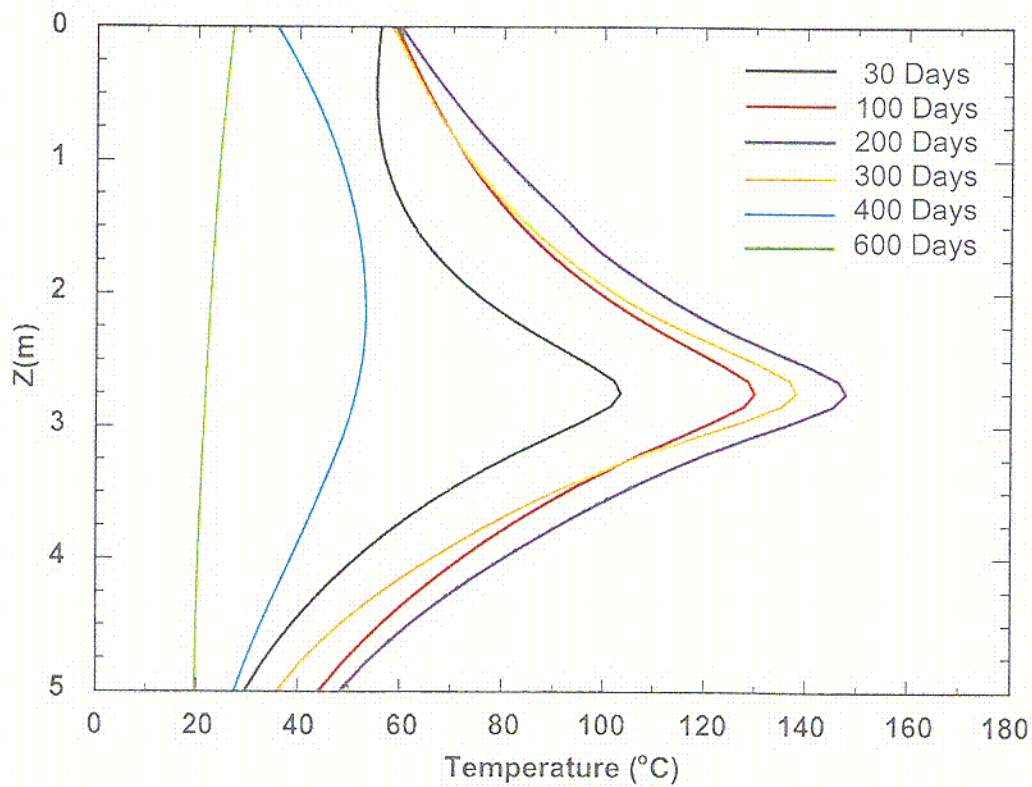


Figure 76. Simulated Temperature (top) and Liquid-Phase Saturation (bottom) Profiles along the LBT Block

C56

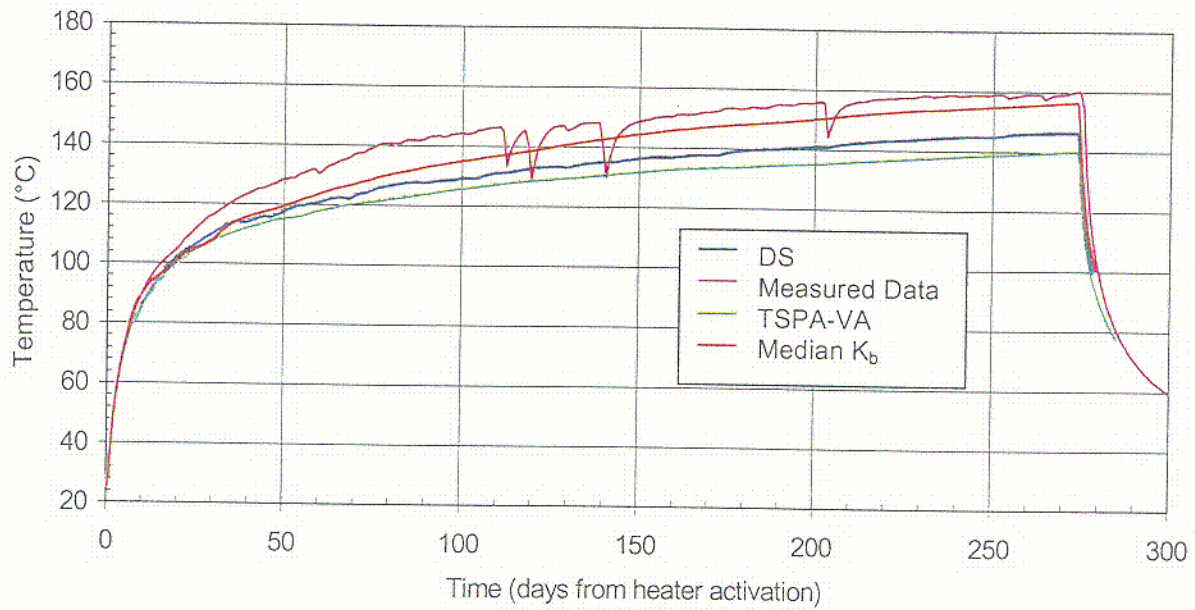


Figure 77. Comparison of Three SHT TOUGH2 Simulations (Property Sets: DS, Median k_b , and TSPA-VA) and Measured SHT Temperatures at Thermocouple Location TMA-TC-1A-7

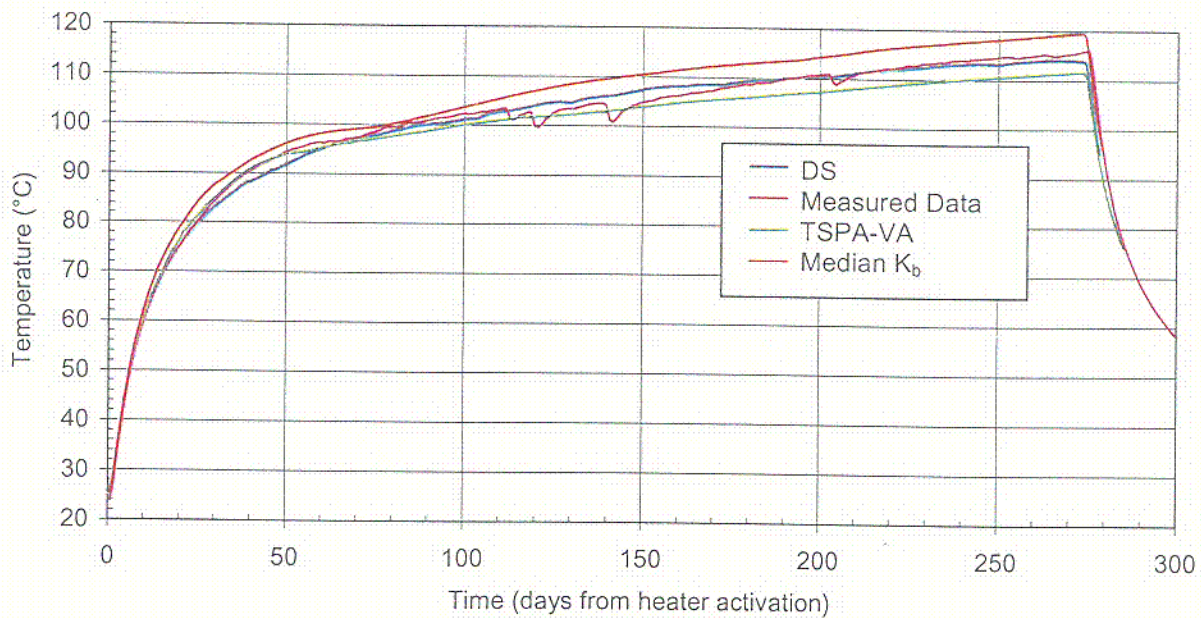


Figure 78. Comparison of Three SHT TOUGH2 Simulations (Property Sets: DS, Median k_b , and TSPA-VA) and SHT Measured Temperatures at Thermocouple Location TMA-TC-4A-6

C57

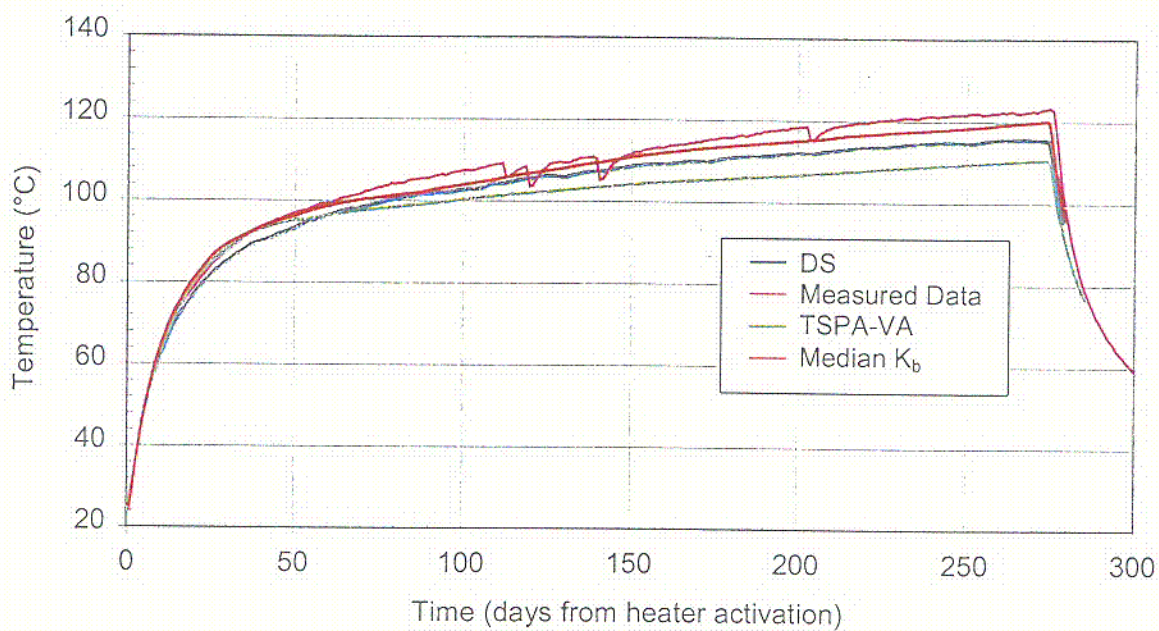


Figure 79. Comparison of Three SHT TOUGH2 Simulations (Property Sets: DS, Median k_b , and TSPA-VA) and Measured SHT Temperatures at Thermocouple Location TMA-TC-5A-7

C58

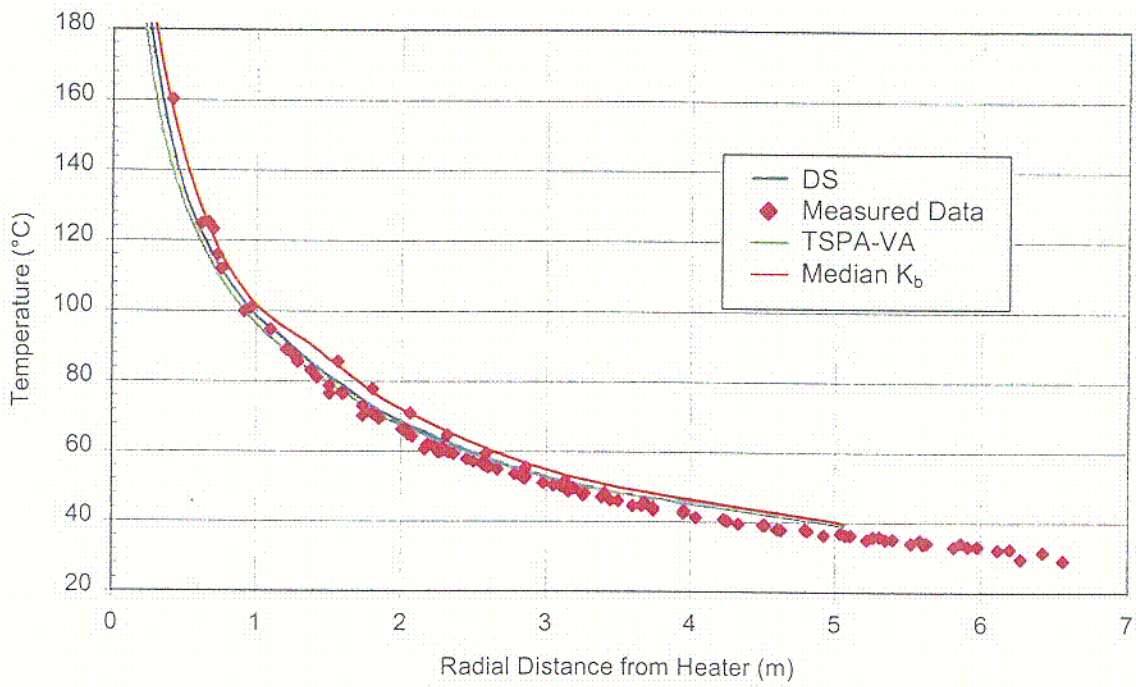


Figure 80. Comparison of Three SHT TOUGH2 Simulations (Property Sets: DS, Median k_b , and TSPA-VA) and SHT Measured Temperatures Radially Around the Heater Mid-Length

C59

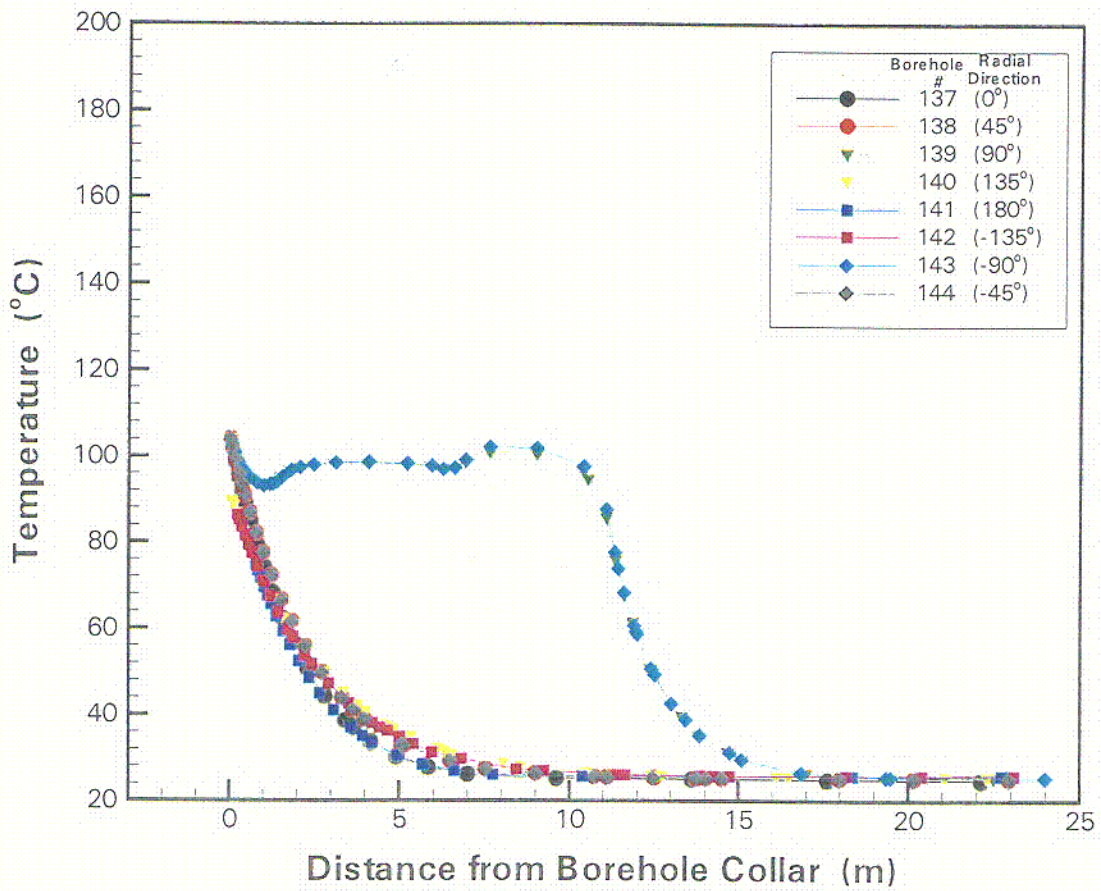


Figure 81. TOUGH2 Simulated Temperatures along RTD Boreholes 137-144 after 3 Months of DST Heating (Case: DKM-TT99)

C60

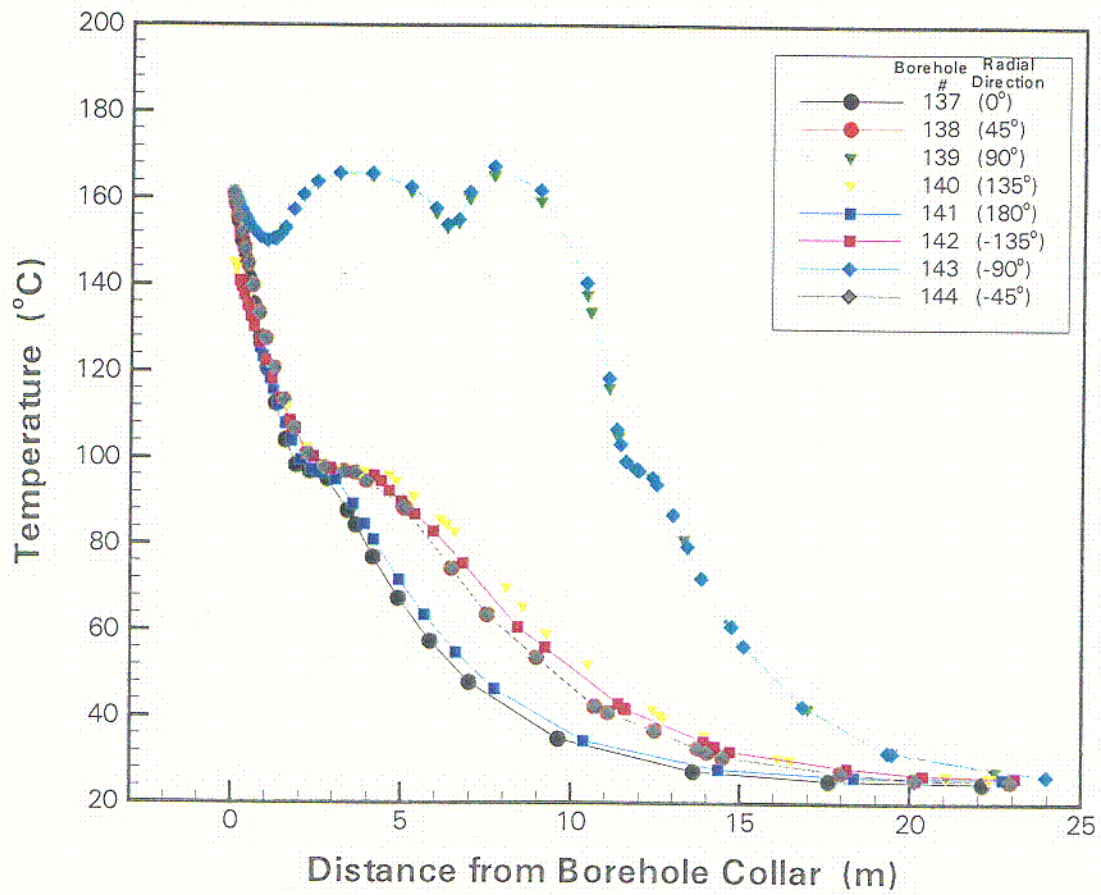


Figure 82. TOUGH2 Simulated Temperatures along RTD Boreholes 137-144 after 12 Months of DST Heating (Case: DKM-TT99)

261

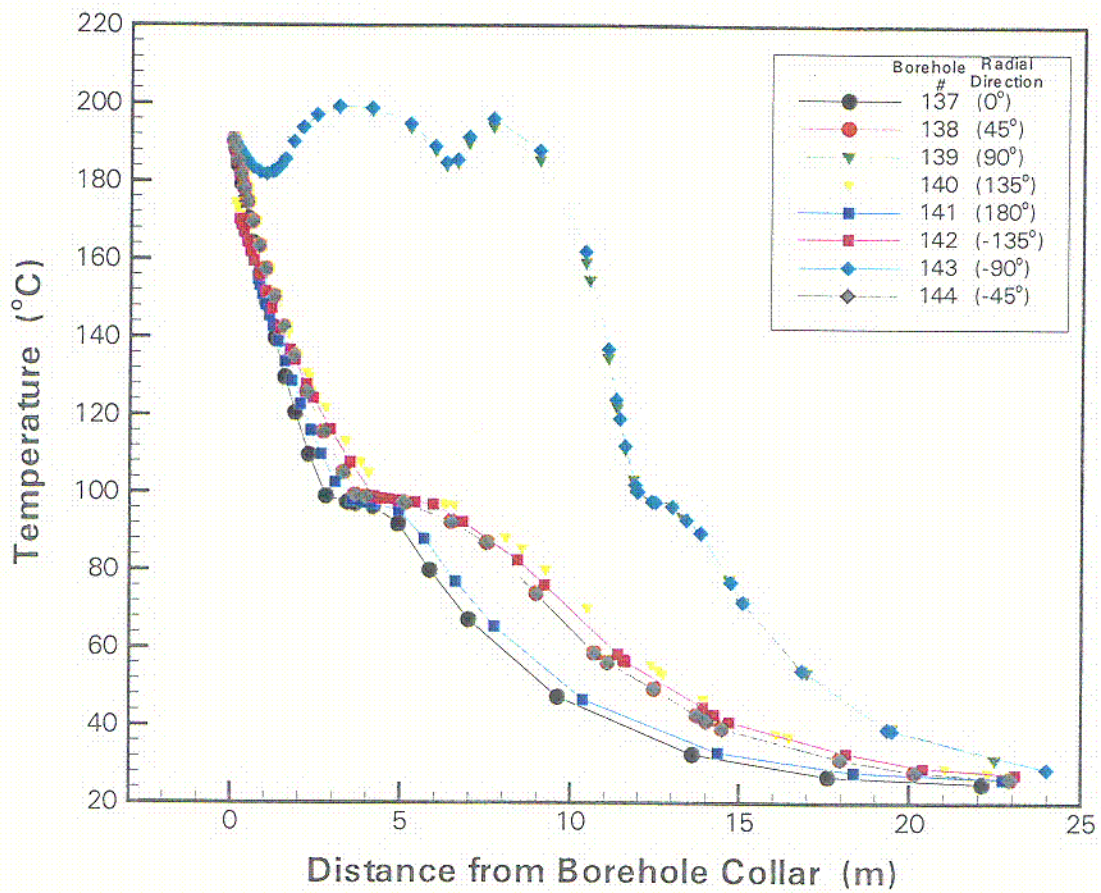


Figure 83. TOUGH2 Simulated Temperatures along RTD Boreholes 137-144 after 18 Months of DST Heating (Case: DKM-TT99)

C62

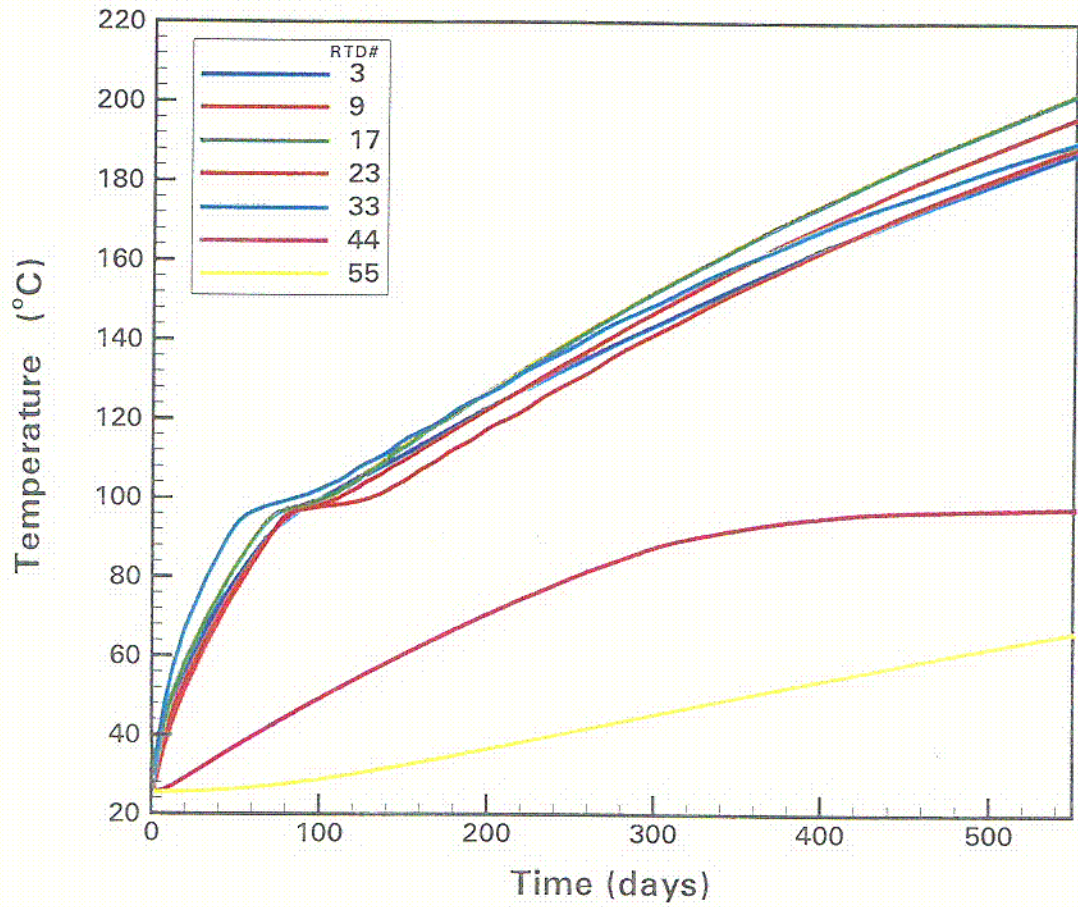


Figure 84. TOUGH2 Simulated Temperature Histories of Selected DST Sensor Locations in RTD Borehole 160 (Horizontal Near the Wing Heaters) for DKM-TT99 Properties

C63

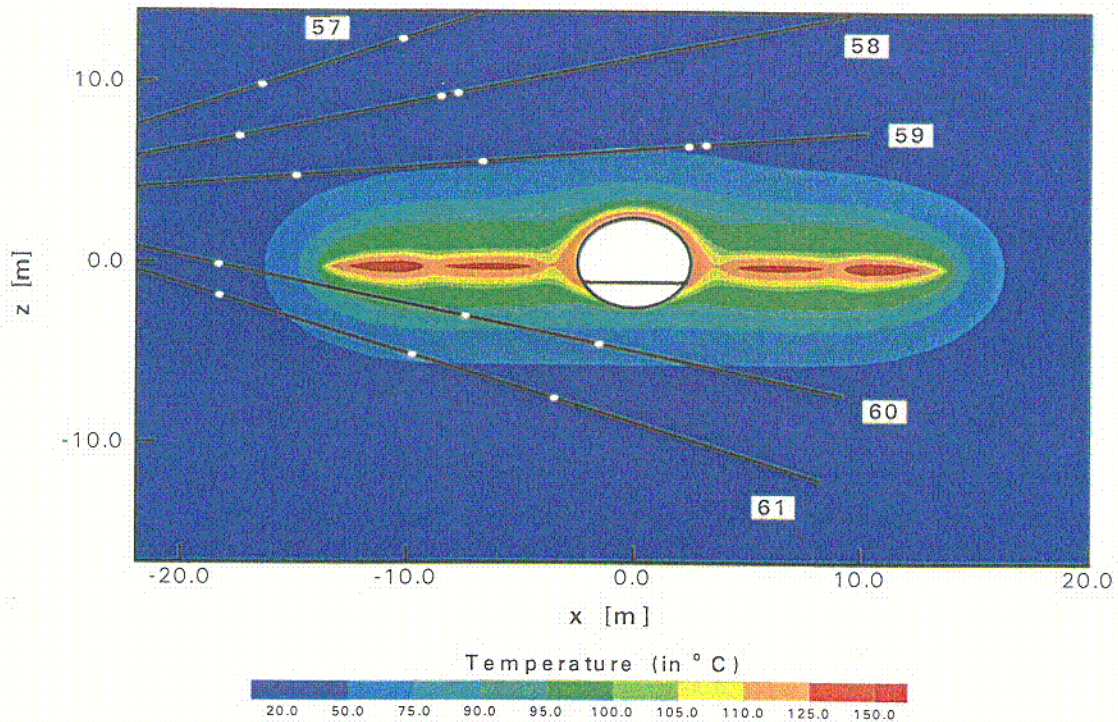
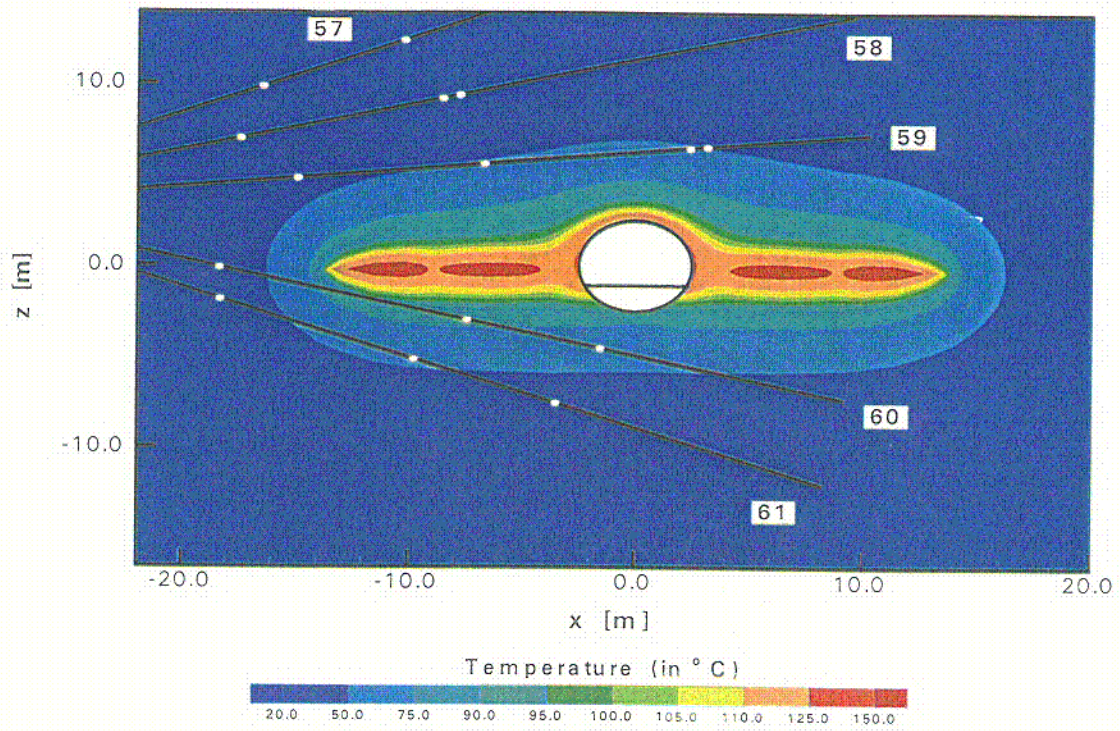


Figure 85. Contours of TOUGH2 Simulated Temperatures in the Plane of DST Hydrology Boreholes 57-61 after 6 Months of Heating (top: Case DS/AFM-UZ99; bottom: Case DKM-TT99)

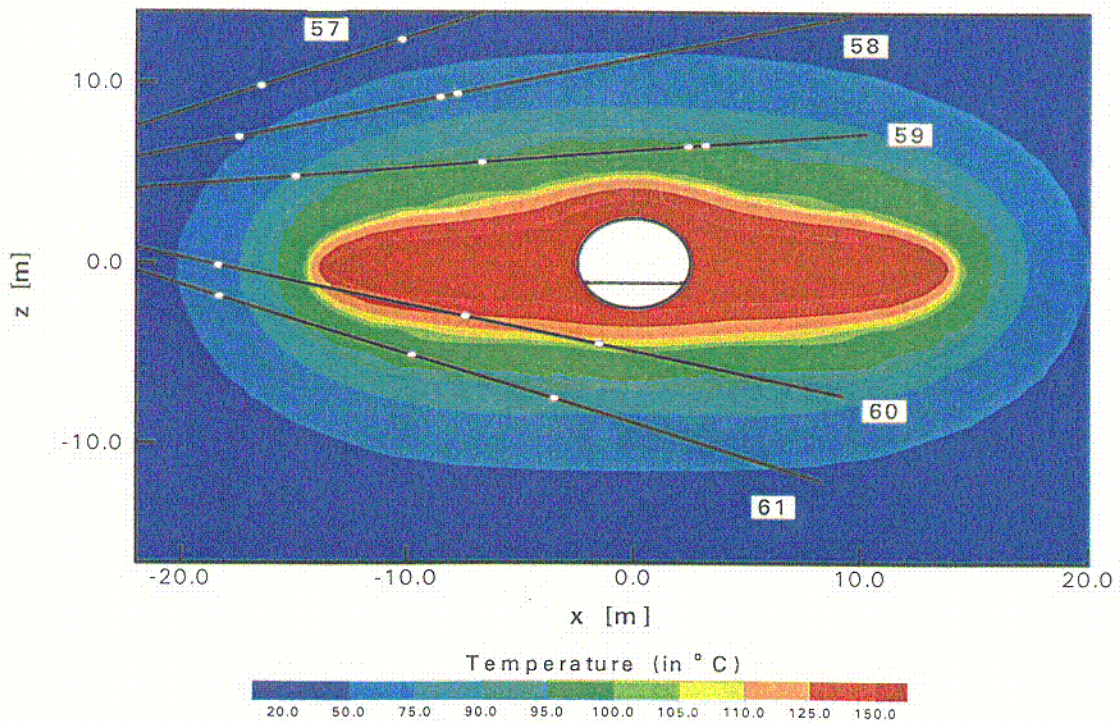
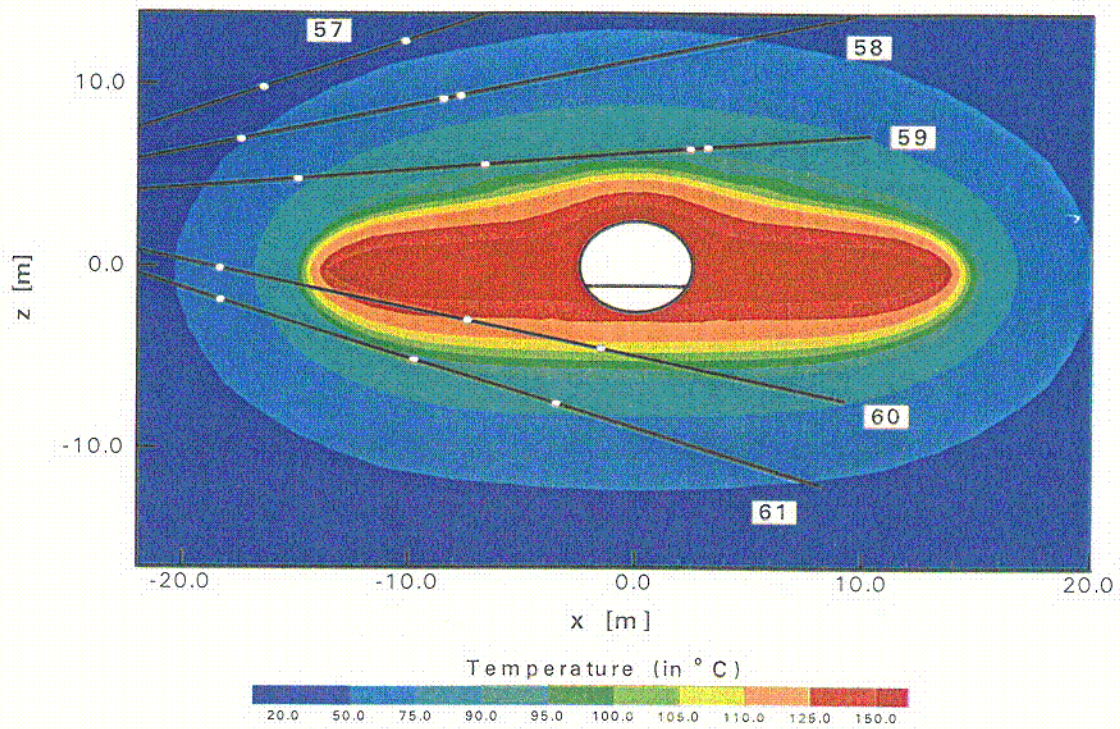
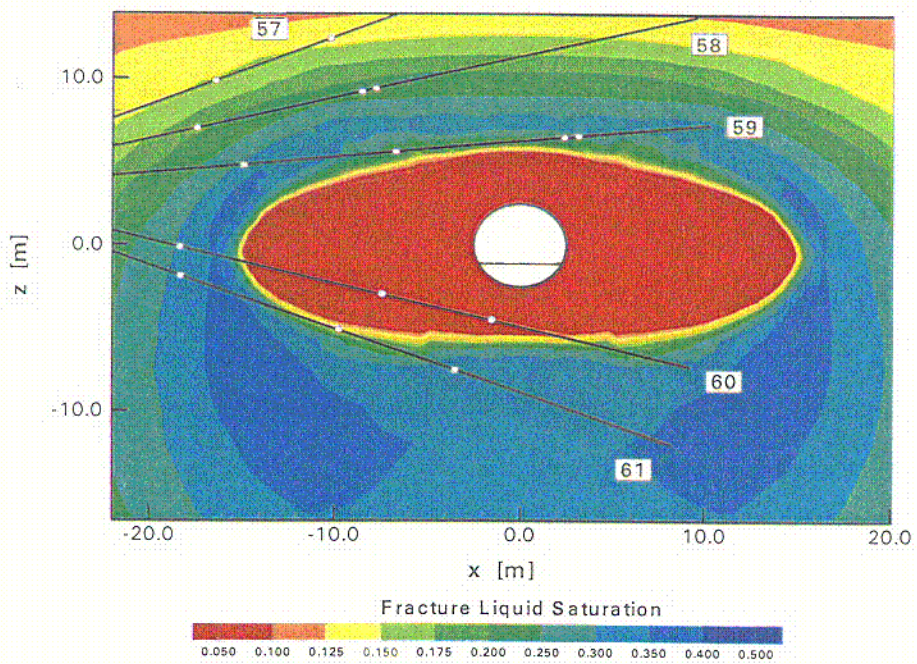
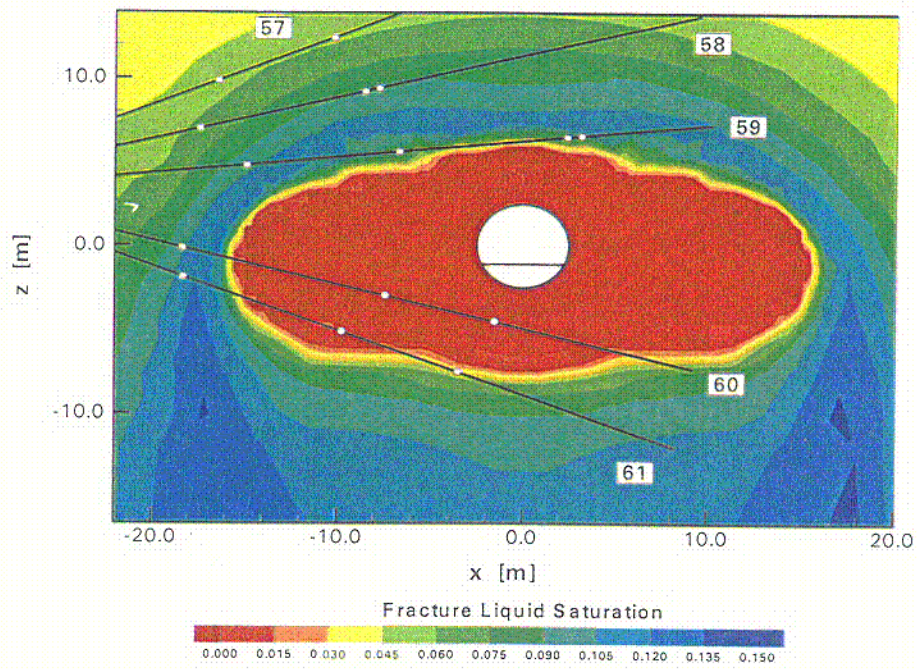


Figure 86. Contours of TOUGH2 Simulated Temperatures in the Plane of DST Hydrology Boreholes 57-61 after 18 Months of Heating (top: Case DS/AFM-UZ99; bottom: Case DKM-TT99)



NOTE: Different saturation scales used in the two contour plots.

Figure 87. Contours of TOUGH2 Simulated Fracture Liquid Saturation after 18 Months of Heating in the Plane of DST Hydrology Boreholes 57-61 (top: Case DS/AFM-UZ99; bottom: Case DKM-TT99)

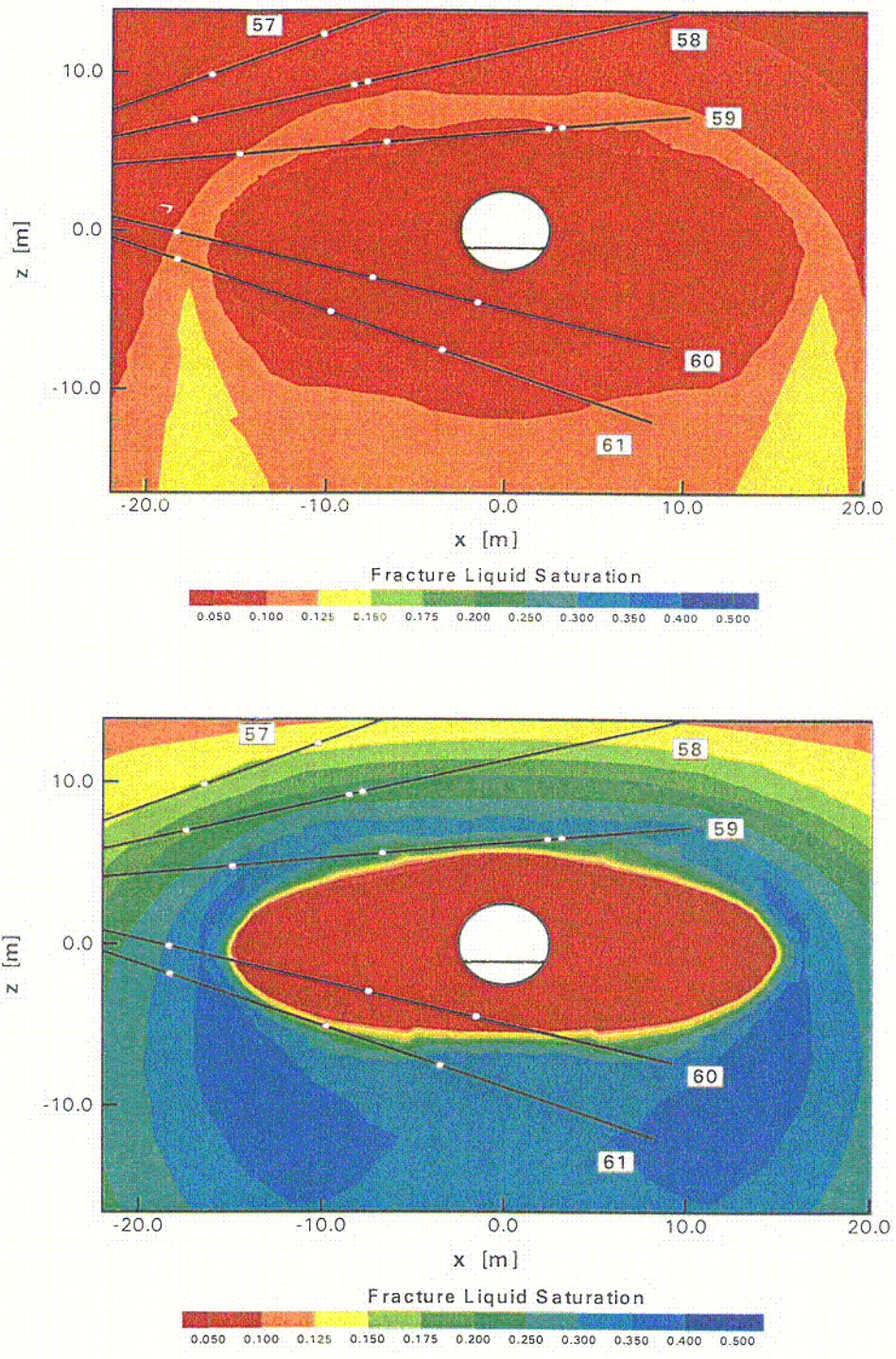


Figure 88. Contours of TOUGH2 Simulated Fracture Liquid Saturation after 18 Months of Heating in the Plane of DST Hydrology Boreholes 57-61 (top: Case DS/AFM-UZ99; bottom: Case DKM-TT99)

C67

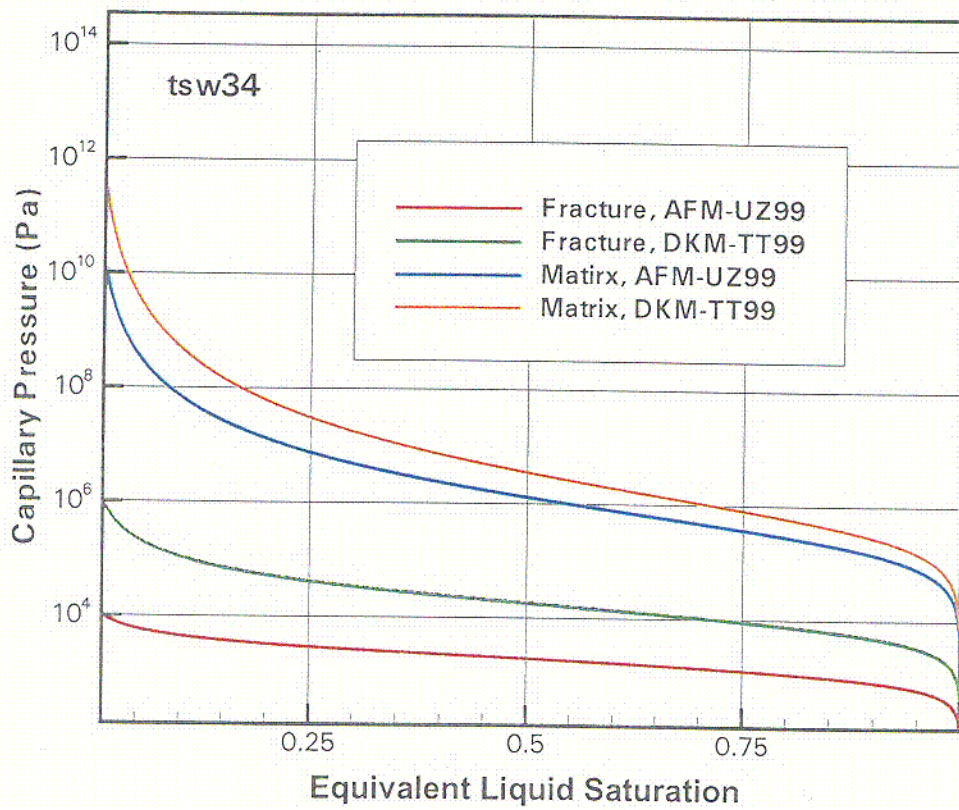


Figure 89. Capillary Pressure Characteristic Curves for Both Fractures and Matrix with the DS/AFM-UZ99 and DKM-TT99 Property Sets

C68

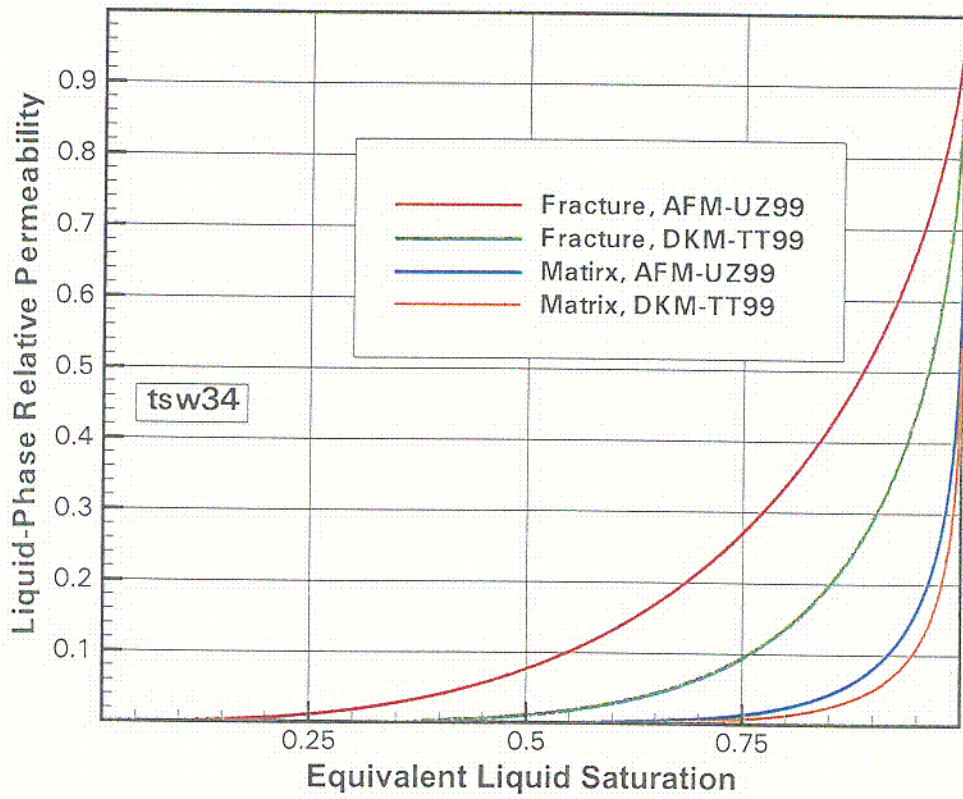


Figure 90. Liquid-Phase Relative Permeability Characteristic Curves for Both Fractures and Matrix with the DS/AFM-UZ99 and DKM-TT99 Property Sets

C69

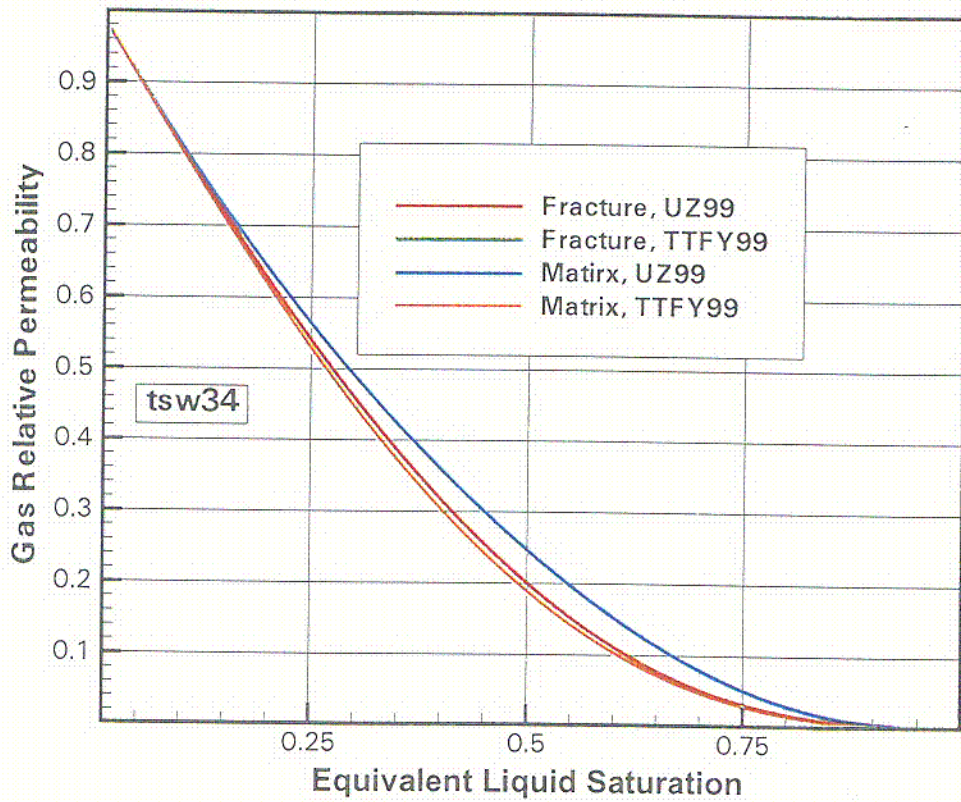


Figure 91. Gas-Phase Relative Permeability Characteristic Curves for Both Fractures and Matrix with the DS/AFM-UZ99 and DKM-TT99 Property Sets

C-70

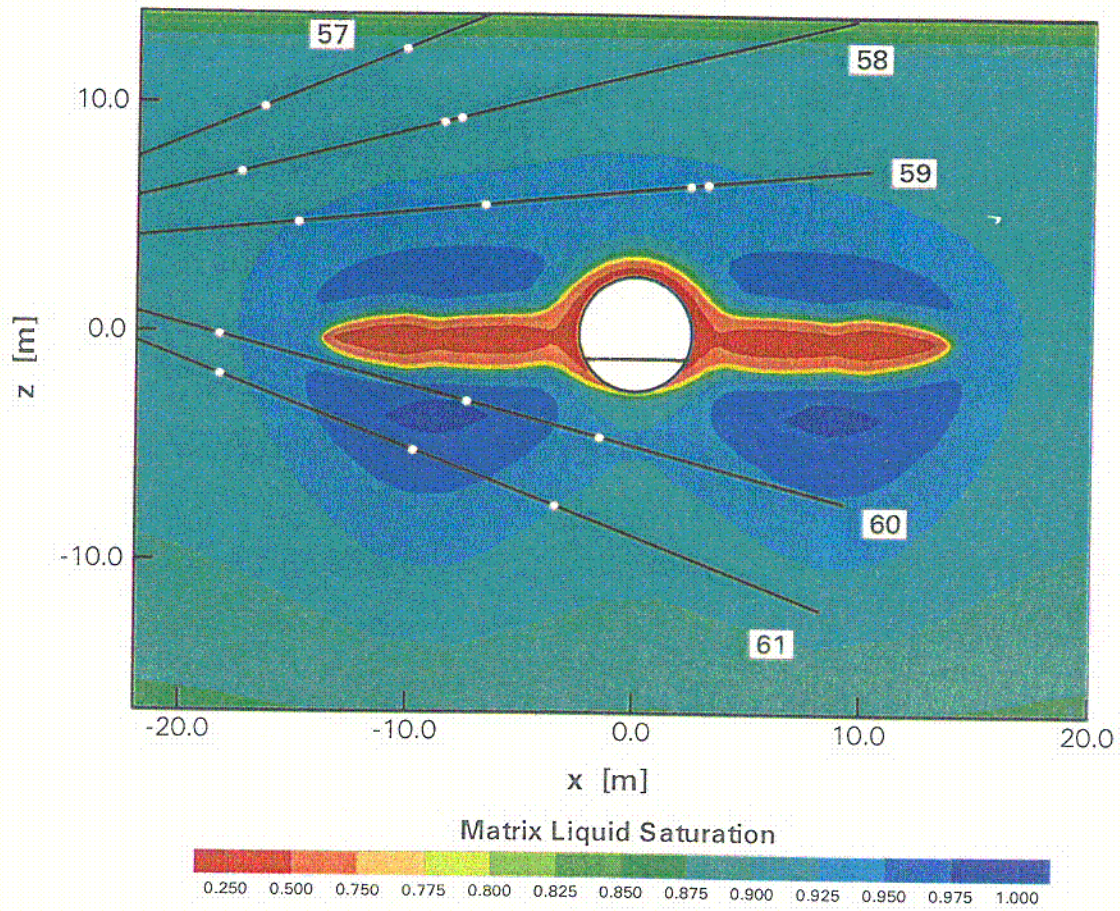


Figure 92. Contours of DST TOUGH2 Simulated Matrix Liquid Saturation in the Plane of Hydrology Boreholes 57-61 after 6 Months of Heating (Case: DKM-TT99)

271

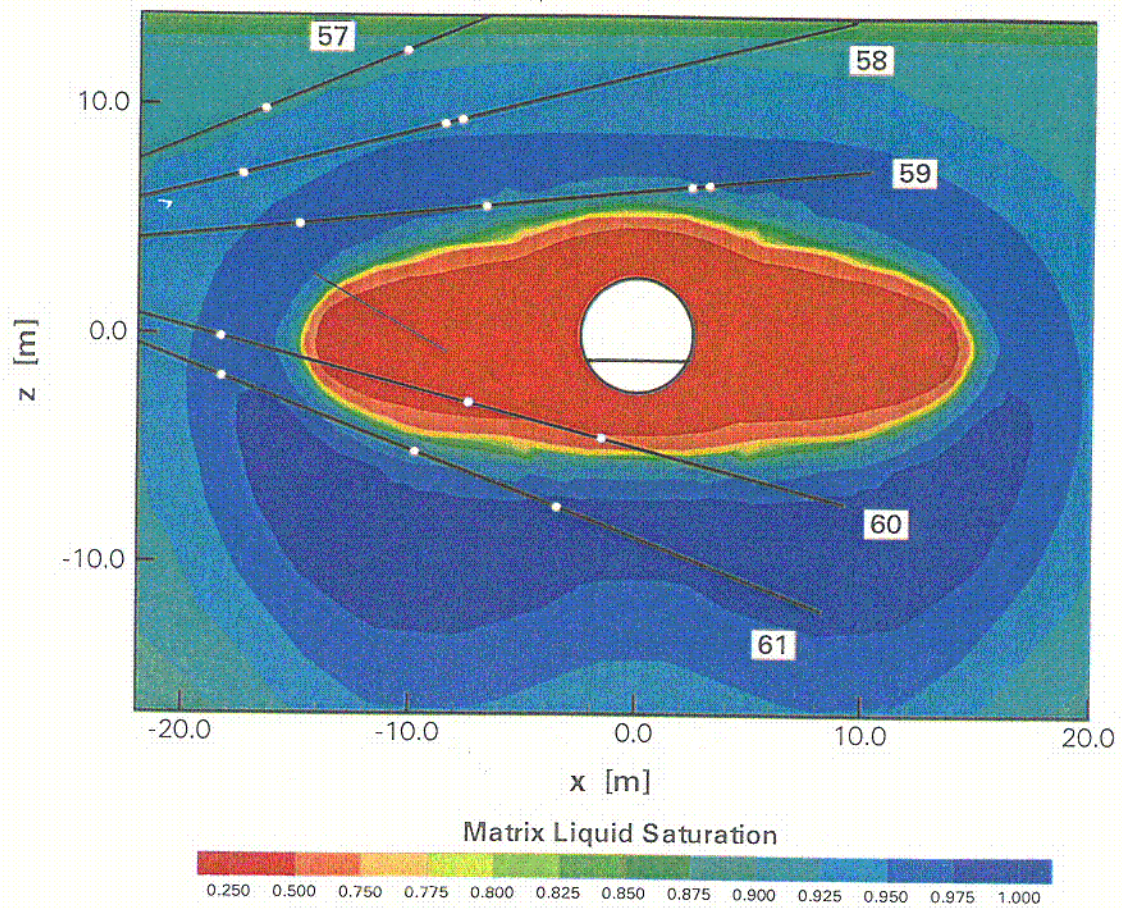


Figure 93. Contours of DST TOUGH2 Simulated Matrix Liquid Saturation in the Plane of DST Hydrology Boreholes 57-61 after 18 Months of Heating (Case: DKM-TT99)

C72

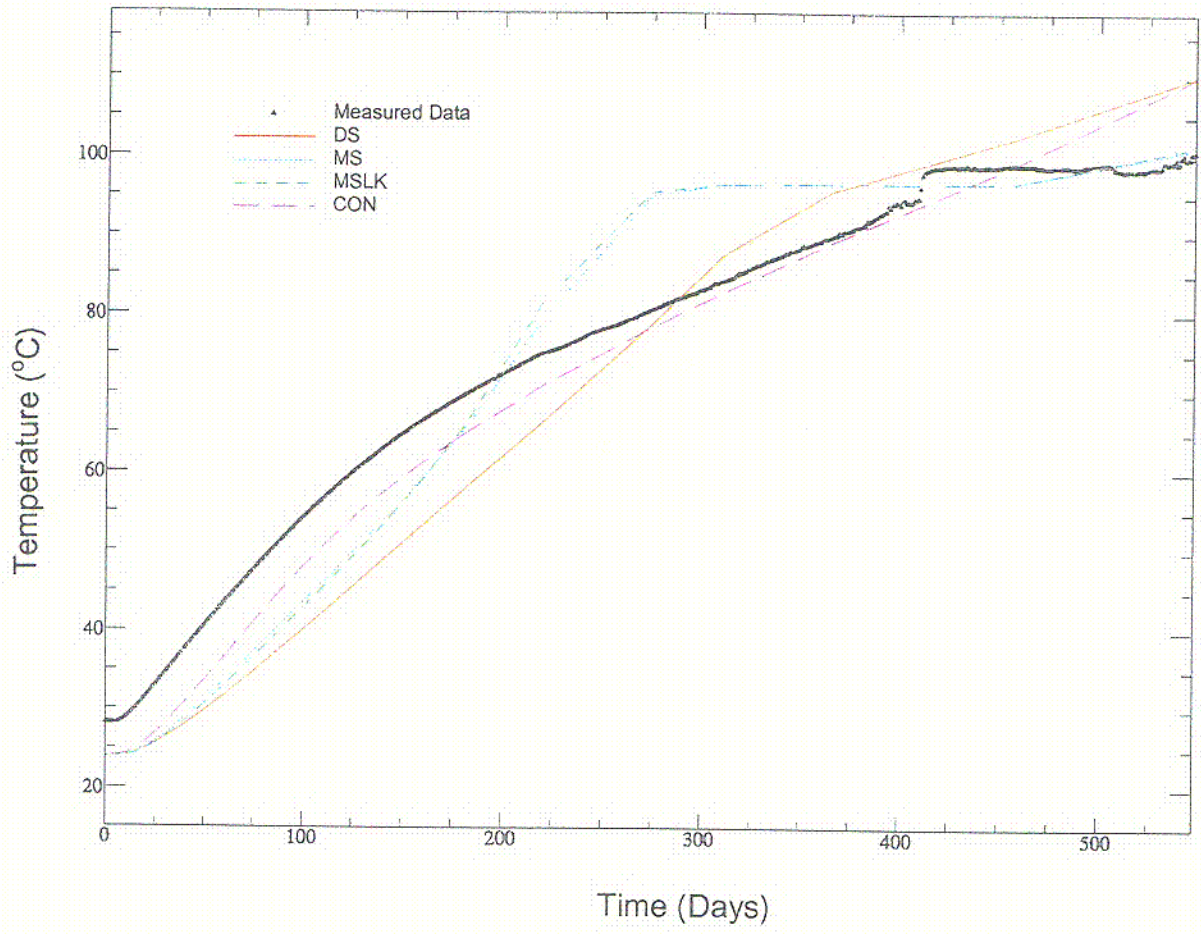


Figure 94. Comparison of Simulated (NUFT) and Measured Temperature Histories for Sensor #10 in Borehole 158 (Vertical Upward) for All Property Sets in the DST

C73

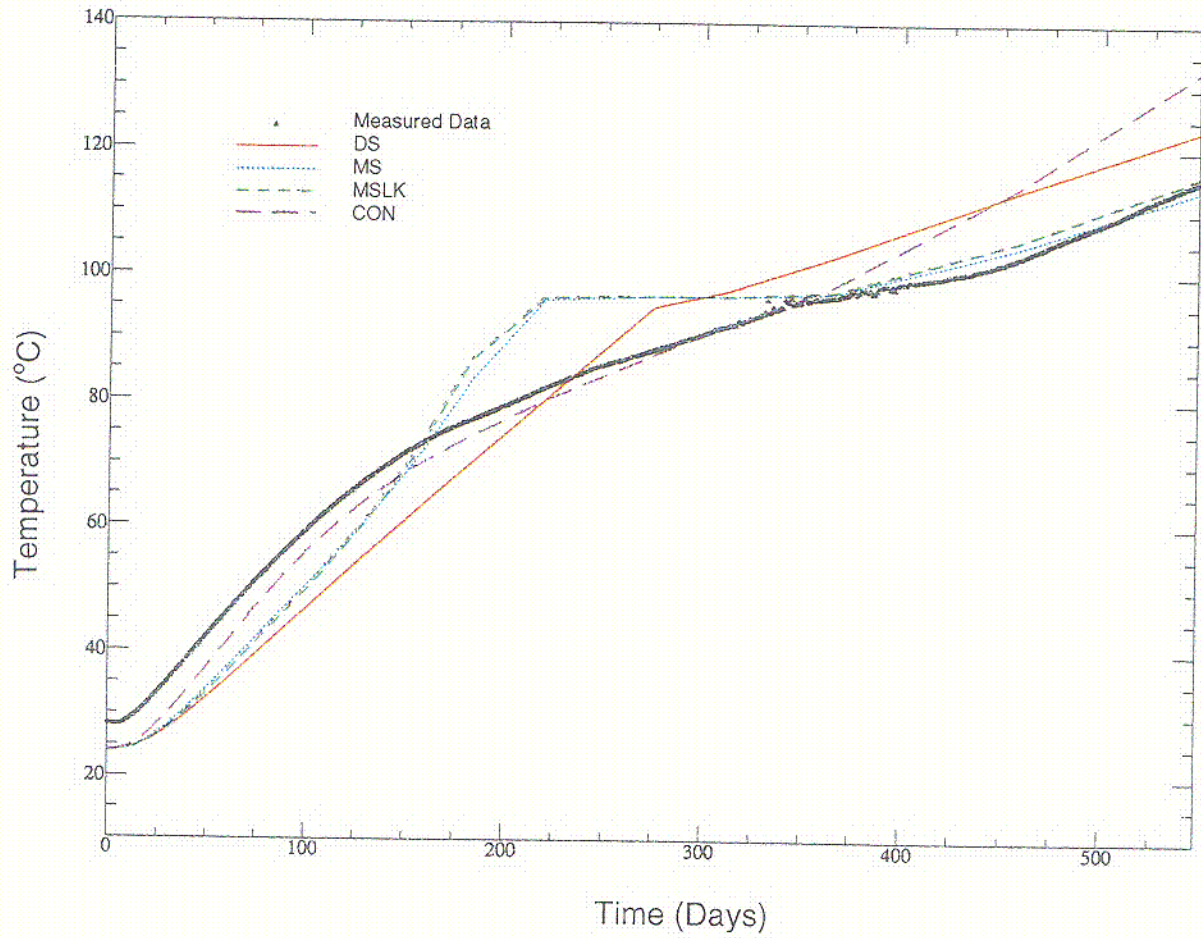


Figure 95. Comparison of Simulated (NUFT) and Measured Temperature Histories for Sensor #10 in Borehole 159 (45° Upward) for All Property Sets in the DST

C74

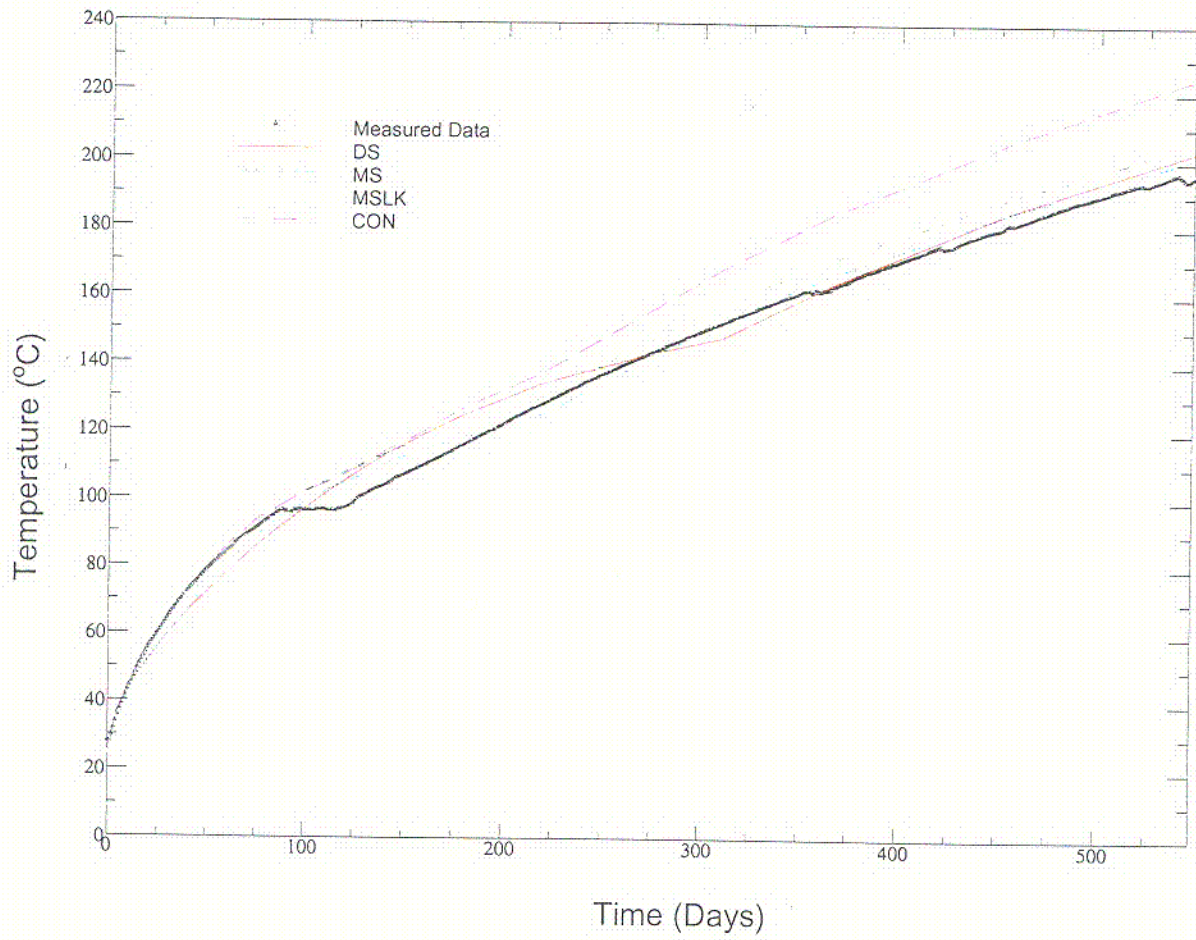


Figure 96. Comparison of Simulated (NUFT) and Measured Temperature Histories for Sensor #10 in Borehole 160 (Horizontal Near the Wing) for All Property Sets in the DST

C75

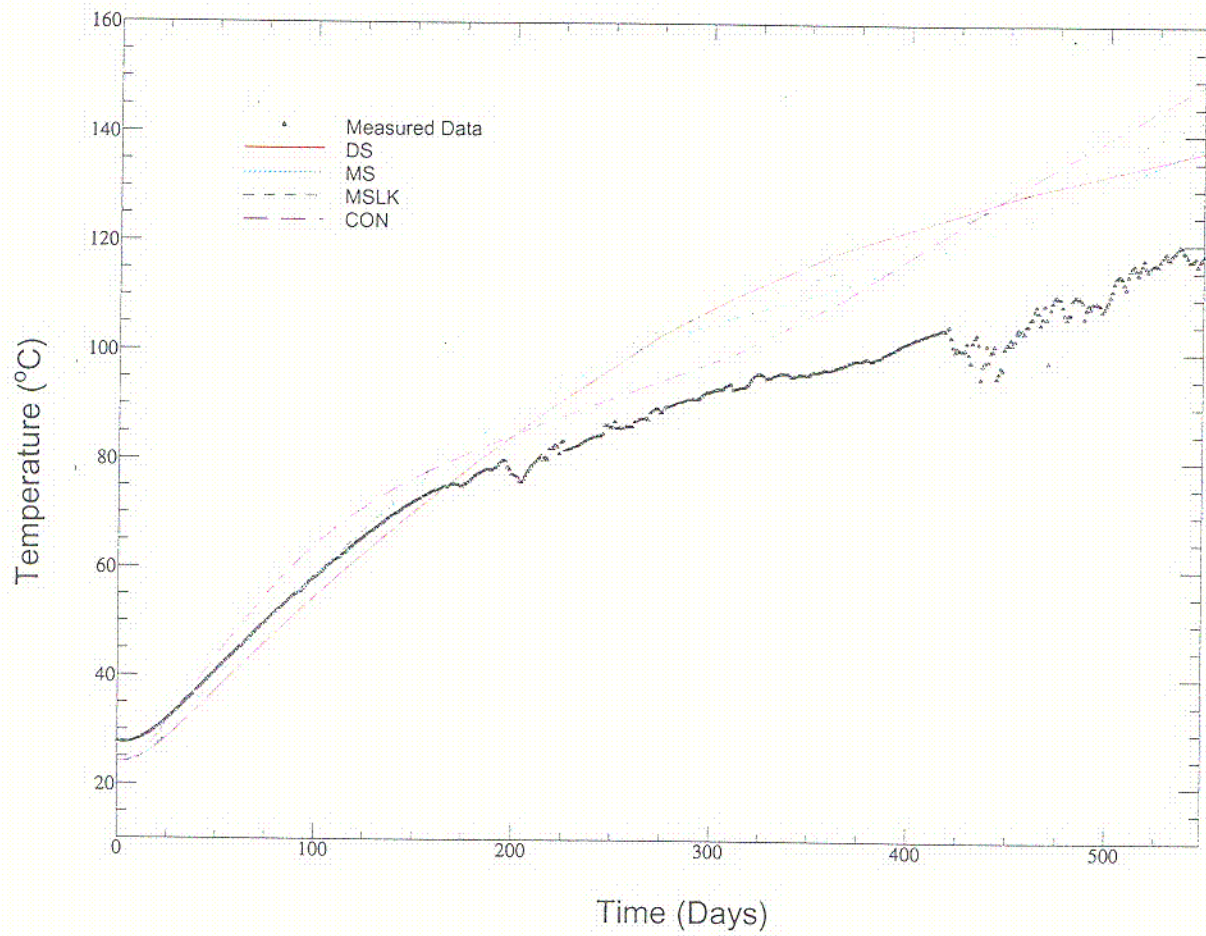


Figure 97. Comparison of Simulated (NUFT) and Measured Temperature Histories for Sensor #10 in Borehole 161 (45° Upward) for All Property Sets in the DST

C-76

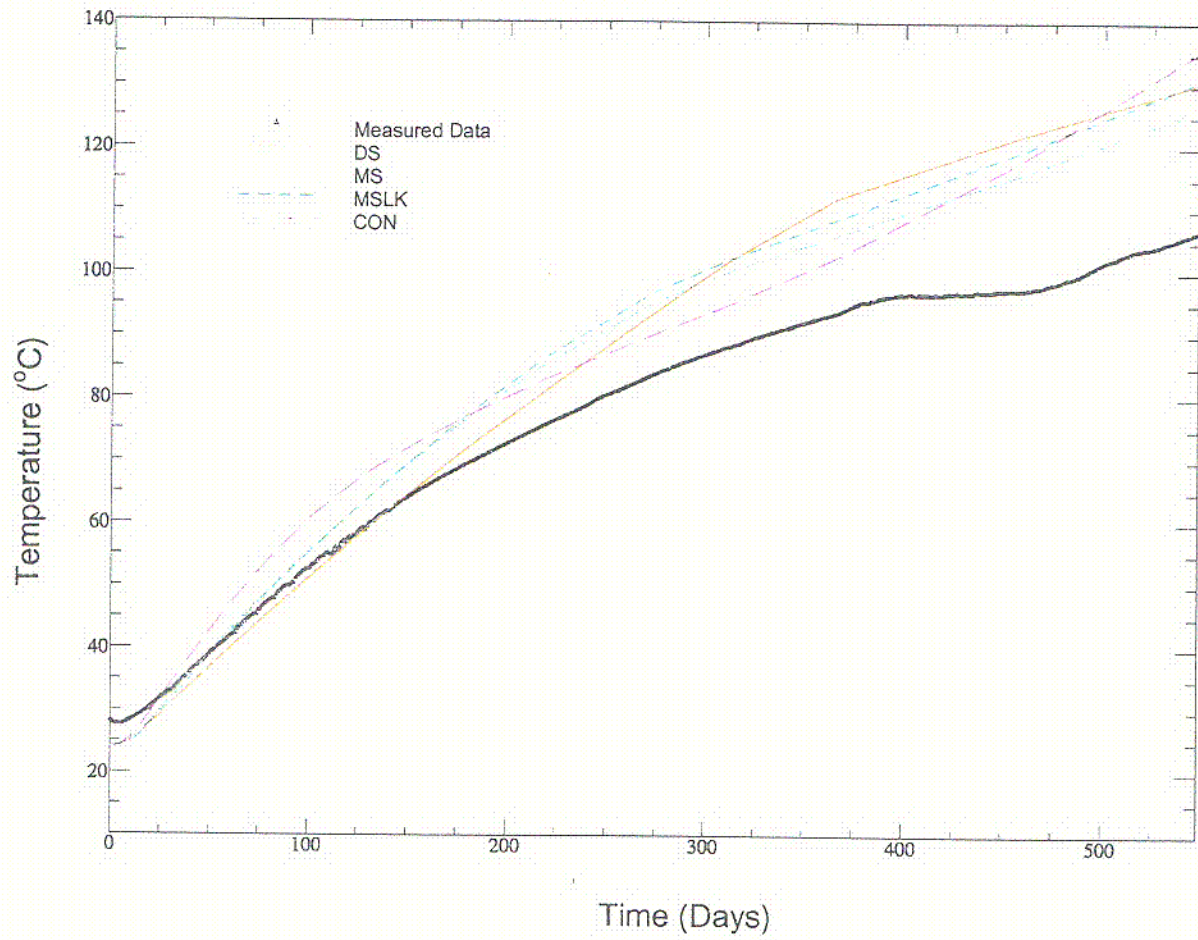


Figure 98. Comparison of Simulated (NUFT) and Measured Temperature Histories for Sensor #10 in Borehole 162 (Vertical Downward) for All Property Sets in the DST

C77

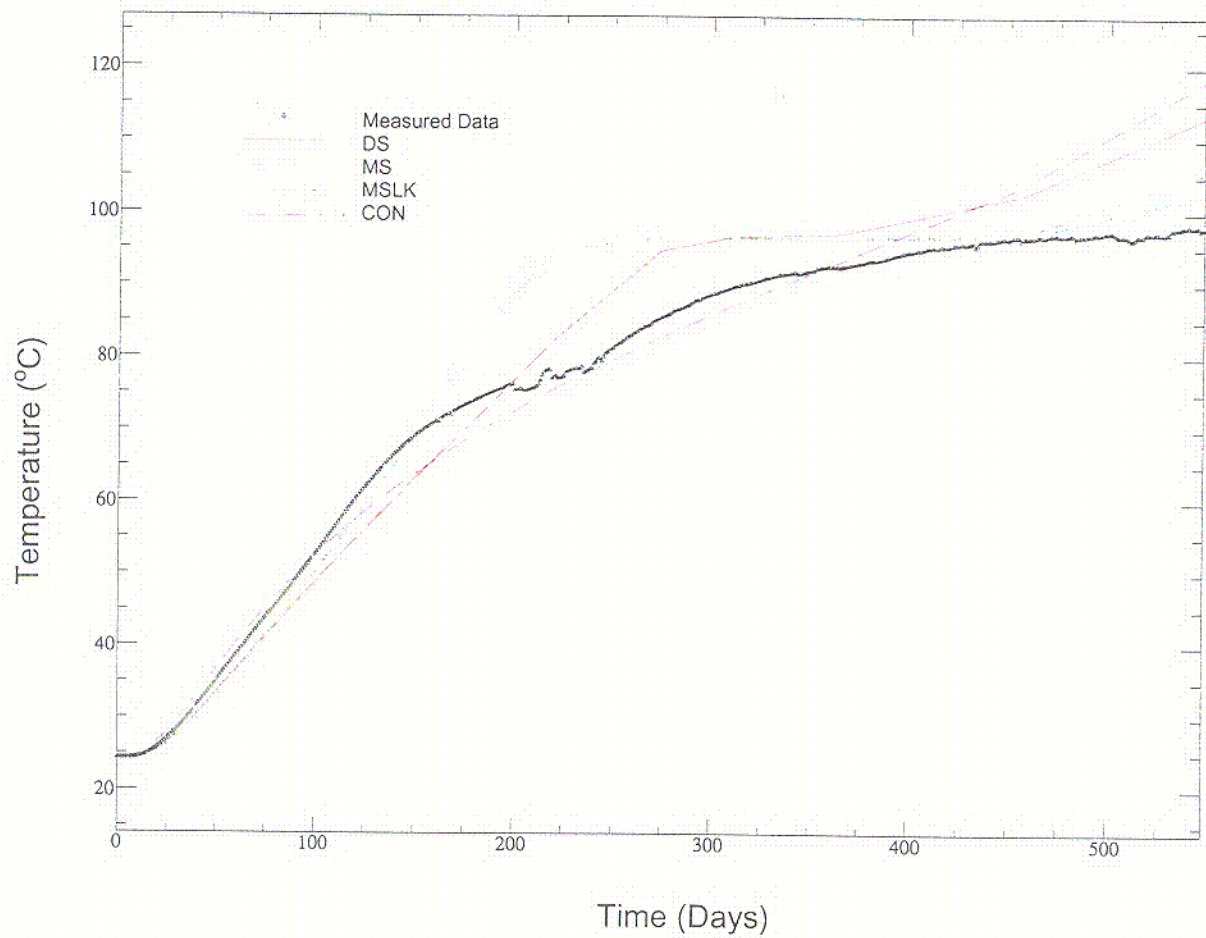


Figure 99. Comparison of Simulated (NUFT) and Measured Temperature Histories for Sensor #30 in Borehole 80 (Parallel to the Drift, Slightly Above and to the Side) for All Property Sets in the DST

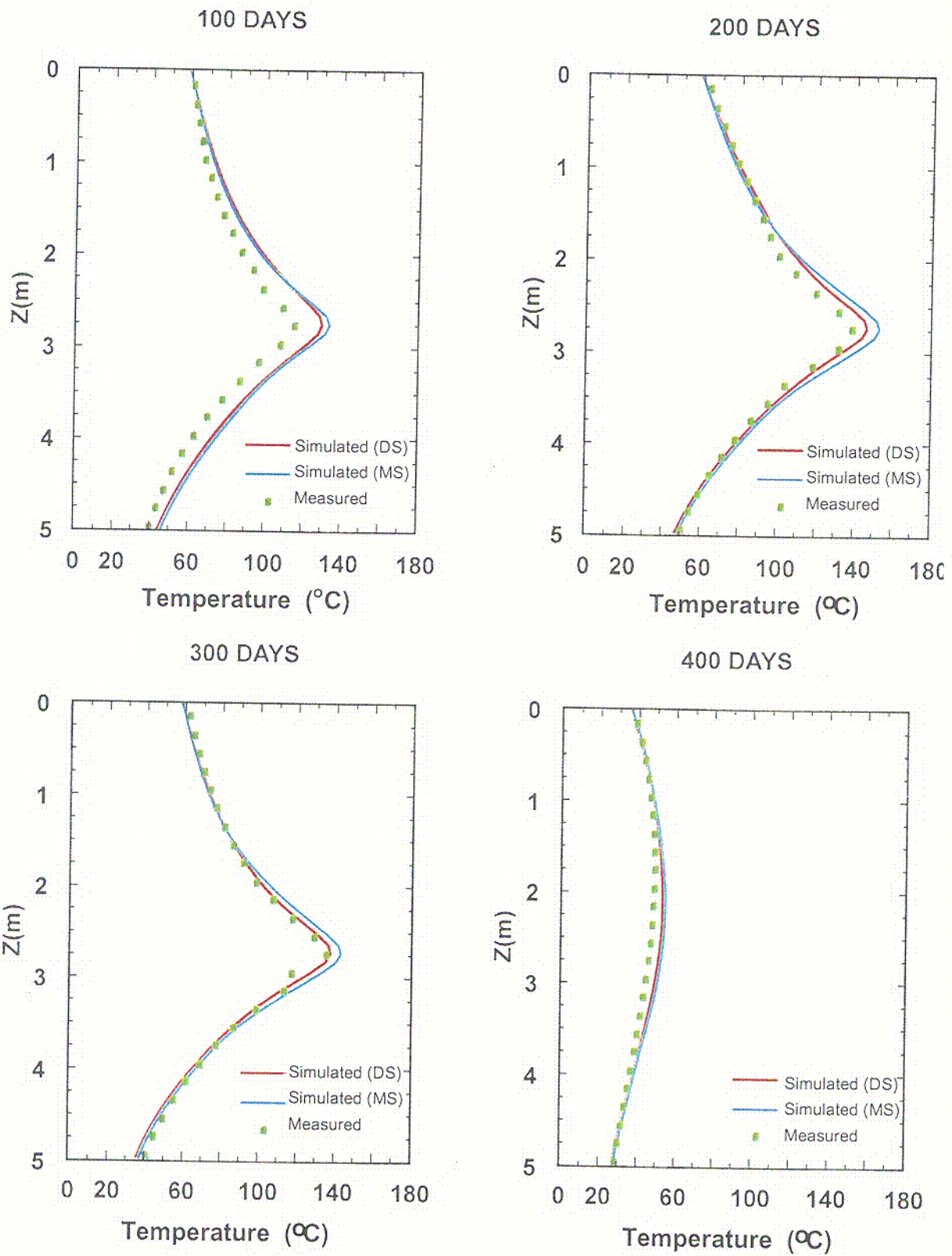


Figure 100. Simulated Temperature Profile Along Borehole TT1 in the LBT Computed Using the DS and MS Rock Property Data Set, Compared to Measured Data

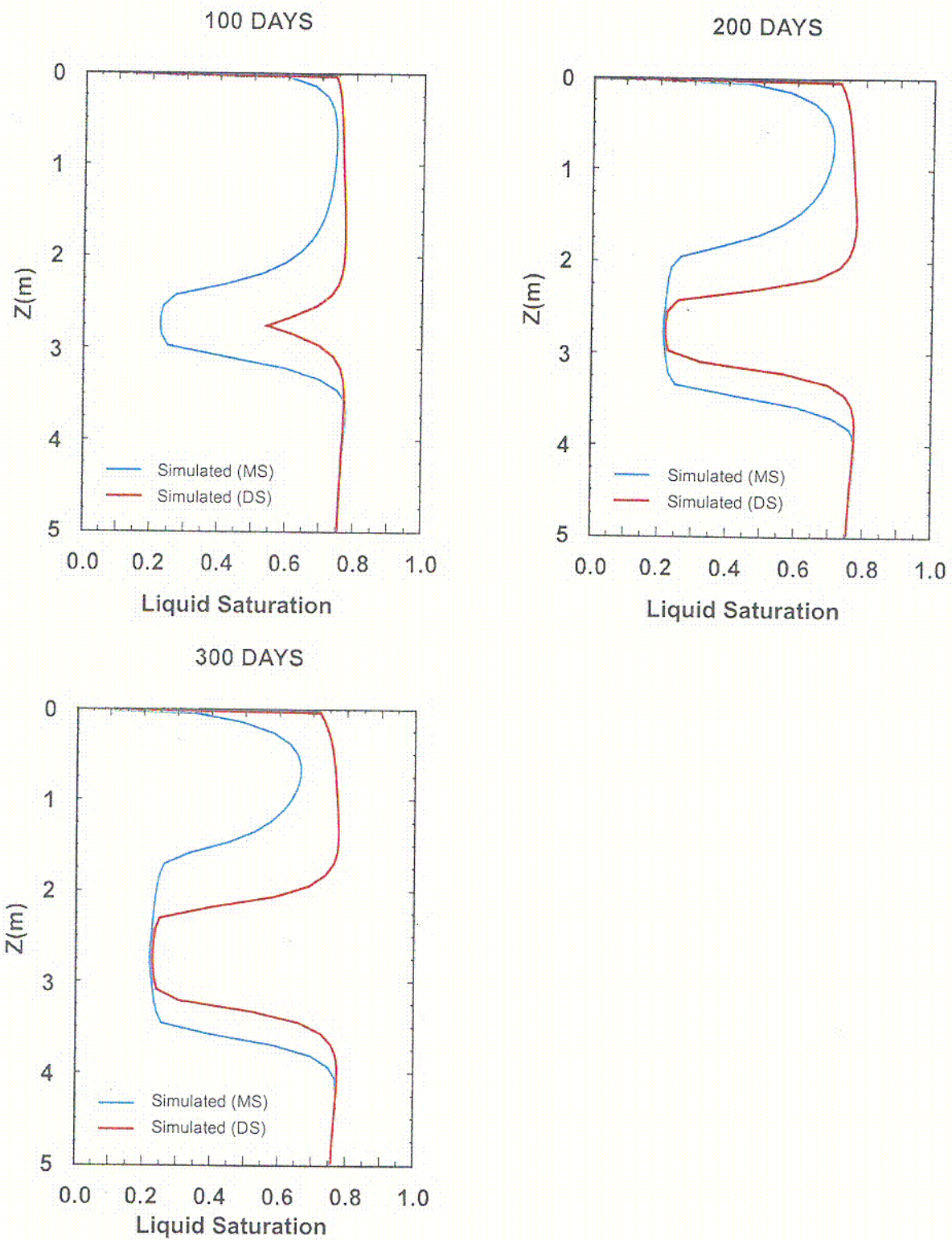


Figure 101. Comparison of the Liquid Saturation Along Borehole TN3 in the LBT for the DS and MS Rock Property Data Set

C80

7. CONCLUSIONS

The applicability of the drift scale property set (DS and DS/AFM-UZ99) from the UZ Flow and Transport Model to thermally perturbed flow and transport in the UZ was examined in this AMR in relation to three thermal tests at Yucca Mountain. These properties have been calibrated by extensive ambient testing, monitoring, and analyses at various locations within and around the repository block. Although this property set was applied to the three thermal tests in this study, it is intended to be used for the entire repository block at ambient conditions. The scales of the three thermal tests are considerably smaller than repository block. These thermal tests have been developed at three locations with the SHT and DST in the subsurface at alcove #5 in the ESF and the LBT on the surface at Fran Ridge. All three thermal tests were conducted in the Tptpmn unit which is within a geologic framework UZ model layer (*tsw34*). This unit is the uppermost of the three potential repository horizon lithologic units. Therefore, the conclusions in this AMR are specific to this particular unit.

Summations for each set of analyses are provided in Sections 6.4.1 through 6.4.4. Comparative analyses between measured and simulated temperatures and saturations for the three thermal tests and the sensitivity studies were discussed in Sections 6.2 and 6.3. DTNs of outputs from the respective simulations are provided in Table 9.

The temperature distributions generated by simulations using the DS/AFM-UZ99 properties in the DKM/AFM model compare well with the overall measured distributions for all three thermal tests. In the sub-boiling regions, the simulated temperatures agree better with the measured temperatures than in the above-boiling regions. Although the percentage deviations are somewhat constant, the temperature differences can be as high as 15 to 20°C, particularly at the higher temperature levels around the wing heaters in the DST. This may in part be explained by localized property interactions, construction-driven property changes at these locations, and coarse grids and smeared sources in the models.

With respect to the heat-driven movement of moisture in the rock, the simulations using the base case DS/AFM-UZ99 properties in the DKM/AFM model do not match the measured moisture movement as well as the measured temperatures. Because of limitations of the moisture measurements in the tests, this outcome is attributed to both moisture measurement uncertainty and model complexity. Nonetheless, the simulations make an adequate representation of the moisture movement, especially the establishment of the dry-out zones. One hydrological parameter that could be improved is associated with the fracture-matrix interaction, namely the active fracture parameter - γ . The effects of this limitation are compounded by stronger gravity drainage allowed by the higher fracture permeability in the base case property set compared to that in the alternate property set, DKM-TT99. Decreasing the active fracture parameter γ will increase the area reduction factor (always < 1) thereby enhancing the fracture-matrix conductance (interactions). This modification will allow for higher matrix saturations below the heated region, as water moving through the fracture continuum will be more readily imbibed into the matrix.

In the case of the NUFT simulations of the DST and the LBT discussed in Section 6.3, the results of the simulations using the DS properties in the DKM/AFM model are compared with those

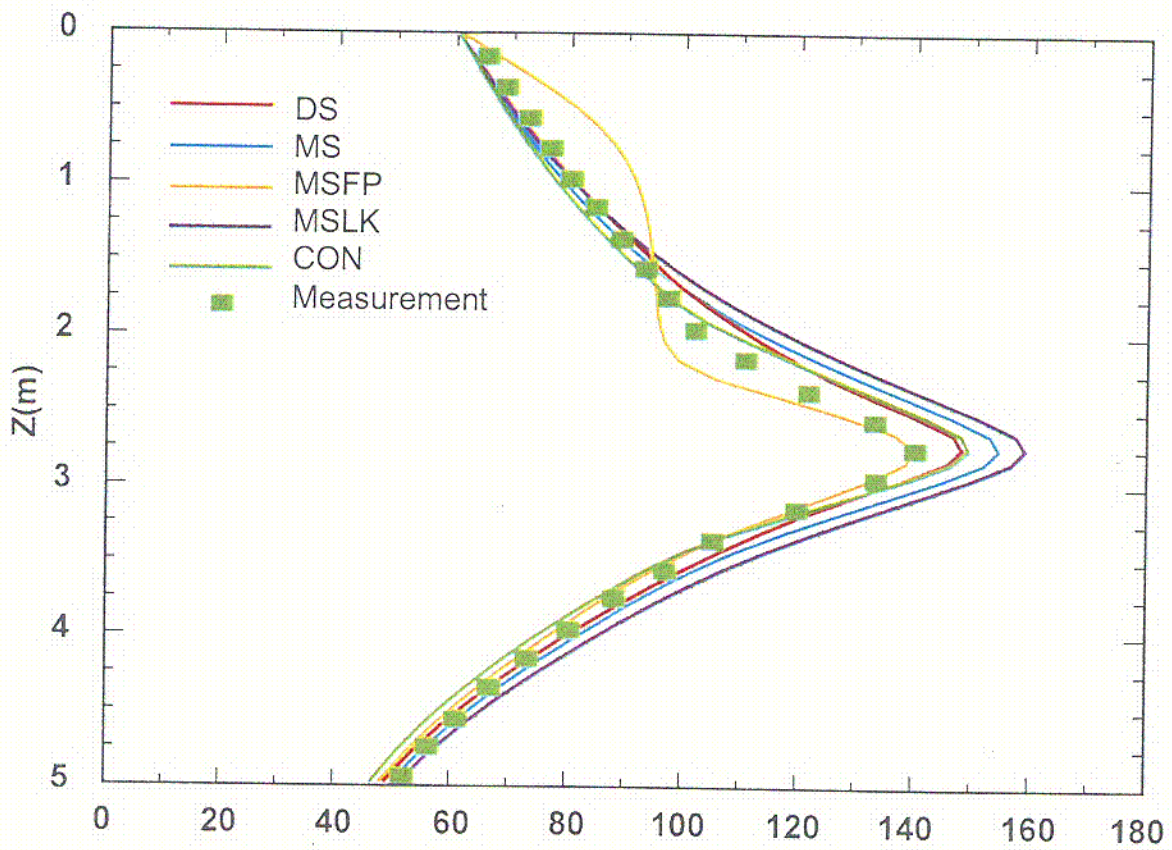


Figure 102. Temperature Profiles along Borehole TT1 in the LBT at 200 Days for Field Measurements and NUFT Simulations

using other property sets. Although all the results were similar, the simulations with the DS properties represent the measured temperatures in the tests better than those by most of the other property sets. The CON properties predict temperatures comparable to those produced with the DS properties, for these limited duration tests. In the case of the TOUGH2 DKM simulations of the DST, the DS/AFM-UZ99 simulation results are compared with those from an earlier simulation using the property set specific to the DST location. The simulation results using the site-specific property set represented the temperature and saturation measurements better than those of the base case.

The base case thermal conductivity values for the Tptpmn (tsw34) stratigraphic unit in the various property sets used in the TH simulations ranged between 1.56 W/m°C for dry conductivity and 2.33 W/m°C for wet conductivity. For the sensitivity cases considered, the dry thermal conductivity ranged from 1.56 to 1.67 W/m°C and the wet thermal conductivity ranged from 2.0 to 2.33 W/m°C. The variations of simulated temperatures resulting from these ranges for both dry and wet thermal conductivities are relatively small when compared to measured temperatures from all three thermal tests.

Overall, the assumptions and constraints discussed in the previous section appear to be appropriate based on generally good agreement between measured and simulated TH behavior for the base case and sensitivity cases considered. The assumptions, uncertainties, restrictions, and constraints used in this analysis do not appear to have a significant impact on the results and conclusion. This observation is based on qualitative and quantitative assessment of the agreement between measured and simulated TH behavior for all cases. TBVs cited in this report are anticipated to have minimal impact on the results and conclusion. This observation is based on past analyses and current understanding of the nature of the TBVs.

Based on the simulations, comparisons with the test measurements, and the sensitivity analyses, the following conclusions were drawn:

- The model validation described in Section 6.5 indicates good overall agreement between measured and simulated temperatures which implies the models considered were sufficiently valid for the purposes of these analyses.
- The DS/AFM-UZ99 property set is suitable for simulating thermally perturbed flow and transport in the UZ. Specifically, this conclusion relates to the uppermost of the three repository horizon lithologic units designated by Tptpmn and tsw34.
- Based on analyses of the SHT, it appears the TSPA-VA property set did not represent TH behavior as well as the DS being used in TSPA SR models.
- In the numerous combinations of property sets and thermal tests considered in the analyses, no one property set is distinctly superior in simulating the thermal response. This outcome is not surprising given the conduction-dominated nature of the thermal tests. It also highlights the need to (1) discern subtle differences in thermal behavior and (2) focus on hydrological behavior which tends to be more complex to simulate as well as measure.

- Property sets other than the DS and MS perform well in the simulations, despite not being as broad-based. This is because they are largely derived from the test block for which they simulate. Alternatively, the DS and MS properties were derived from the repository horizon but used to simulate TH behavior in specific, smaller-scale test blocks. Based on this condition, it is encouraging that the DS property set is reasonably comparable to the site-specific property sets in simulating TH behavior. The DS property set is likely to be generally more suitable when applied across the repository horizon.
- For Tptpmn (tsw34), ranges for dry thermal conductivity (1.56 to 1.67 W/m°C) and wet thermal conductivity (2.00 to 2.33 W/m°C) are considered appropriate for simulating thermal responses from all three thermal tests.
- Based on methods established by this AMR and identified potential improvements to the simulation models, applicability of the DS property set to thermally perturbed flow in the Tptpll can be readily investigated when field test results from that unit are available.
- Refinement of the DS property set should be continued. This can be achieved by adjusting the active fracture gamma parameter and examining decreases in fracture permeability correlated to changes in fracture porosity and the van Genuchten alpha parameter.
- Grids should be re-evaluated for future simulations to ensure optimum refinement is used within the constraints of computing resources and the objectives of the analyses.

NOTE: This document may be affected by technical product input information that requires confirmation. Any changes to the document that may occur as a result of completing the confirmation activities will be reflected in subsequent revisions. The status of the input information quality may be confirmed by review of the DIRS database.

8. INPUTS AND REFERENCES

8.1 DOCUMENTS CITED

Bandurraga, T.M. and Bodvarsson, G.S. 1997. "Calibrating Matrix and Fracture Properties Using Inverse Modeling." Chapter 6 of *The Site-Scale Unsaturated Zone Model of Yucca Mountain, Nevada, for the Viability Assessment*. Bodvarsson, G.S.; Bandurraga, T.M.; and Wu, Y.S., eds. LBNL-40376. Berkeley, California: Lawrence Berkeley National Laboratory. ACC: MOL.19971014.0232.

Bandurraga, T.M. and Bodvarsson, G.S. 1999. "Calibrating Hydrogeologic Parameters for the 3-D Site-Scale Unsaturated Zone Model of Yucca Mountain, Nevada." *Journal of Contaminant Hydrology*, 38, (1-3), 25-46. New York, New York: Elsevier TIC: 244160.

Birkholzer, J.T. and Tsang, Y.W. 1997. *Pretest Analysis of the Thermal-Hydrological Conditions of the ESF Drift Scale Test*. Milestone SP9322M4. Berkeley, California: Lawrence Berkeley National Laboratory. ACC: MOL.19971201.0810.

Blair, S.C.; Buscheck, T.A.; Carlberg, E.; Carlson, R.; Costantino, M.; Daily, W.D.; DeLoach, L.D.; Lee, K.; Lin, W.; Pletcher, R.; Ramirez, A.L.; Roberts, J.; Rosenberg, N.D.; Ruddle, D.; and Wagoner, J. 1998. *Drift-Scale Test Status Report, Satisfying The Deliverables Second-Quarter Drift-Scale Test Report (SP2670M4) and Draft Drift-Scale Test Progress Report (SP2931M4)*. UCRL-ID-131195. Livermore, CA: Lawrence Livermore National Laboratory. ACC: MOL.19980831.0212.

Bowker, A.H. and Lieberman, G.J. 1972. *Engineering Statistics*. 2nd Edition. Englewood Cliffs, New Jersey: Prentice-Hall, Inc. TIC: 240460.

Brooks, R.H. and Corey, A.T. 1966. "Properties of Porous Media Affecting Fluid Flow." *Journal of the American Society of Civil Engineers, Irrigation and Drainage Division*, 92, (IR2), 61-89. New York, New York: American Society of Civil Engineers. TIC: 216867.

Buscheck, T.A. and Nitao, J.J. 1994. *The Impact of Buoyant, Gas-Phase Flow and Heterogeneity on Thermal-Hydrological Behavior at Yucca Mountain*. UCRL-JC-115351. Livermore, California: Lawrence Livermore National Laboratory. ACC: NNA.19940524.0012.

Buscheck, T.A.; Shaffer, R.J.; Lee, K.H.; and Nitao, J.J. 1997. *Analysis of Thermal-Hydrological Behavior During the Heating Phase of the Single-Heater Test at Yucca Mountain*. Supplemental Submission to Deliverable SP9266M4. Livermore, California: Lawrence Livermore National Laboratory. ACC: MOL.19980109.0241.

CRWMS M&O 1997a. *Single Heater Test Status Report*. BAB000000-01717-5700-00002 REV 01. Las Vegas, Nevada: CRWMS M&O. ACC: MOL.19980416.0696.

CRWMS M&O 1997b. *Drift Scale Test Design and Forecast Results*. BAB000000-01717-4600-00007 REV 01. Las Vegas, Nevada: CRWMS M&O. ACC: MOL.19980710.0155.

CRWMS M&O 1997c. *Ambient Characterization of the Drift Scale Test Block*. BADD00000-01717-5705-00001 REV 01. Las Vegas, Nevada: CRWMS M&O. ACC: MOL.19980416.0689.

CRWMS M&O 1998a. *Drift Scale Test As-Built Report*. BAB000000-01717-5700-00003 REV 01. Las Vegas, Nevada: CRWMS M&O. ACC: MOL.19990107.0223.

CRWMS M&O 1998b. *Drift Scale Test Progress Report No. 1*. BAB000000-01717-5700-00004 REV 01. Las Vegas, Nevada: CRWMS M&O. ACC: MOL.19990209.0240.

CRWMS M&O 1998c. "Thermal Hydrology." Chapter 3 of *Total System Performance Assessment-Viability Assessment (TSPA-VA) Analyses Technical Basis Document*. B00000000-01717-4301-00003 REV 01. Las Vegas, Nevada: CRWMS M&O. ACC: MOL.19981008.0003.

CRWMS M&O 1999a. *Thermal Test Thermal-Hydrological Analysis and Models Report, DI # ANL-NBS-TH-000001*. TDP-NBS-TH-000002 Rev. 0 ICN 0. Las Vegas, Nevada: CRWMS M&O. ACC: MOL.20000124.0319.

CRWMS M&O 1999b. *Single Heater Test Final Report*. BAB000000-01717-5700-00005 REV 00 ICN 1. Las Vegas, Nevada: CRWMS M&O. ACC: MOL.20000103.0634.

CRWMS M&O 1999c. *M&O Site Investigations*. Activity Evaluation, September 28, 1999. Las Vegas, Nevada: CRWMS M&O. ACC: MOL.19990928.0224.

CRWMS M&O 2000a. *Repository Safety Strategy: Plan to Prepare the Postclosure Safety Case to Support Yucca Mountain Site Recommendation and Licensing Considerations*. TDR-WIS-RL-000001 REV 03. Las Vegas, Nevada: CRWMS M&O. ACC: MOL.20000119.0189.

CRWMS M&O 2000b. *Unsaturated Zone Flow and Transport Model Process Model Report*. TDR-NBS-HS-000002 REV 00. Las Vegas, Nevada: CRWMS M&O. ACC: MOL.20000320.0400.

CRWMS M&O 2000c. *UZ Flow Models and Submodels*. MDL-NBS-HS-000006. Las Vegas, Nevada: CRWMS M&O. URN-0029.

CRWMS M&O 2000d. *Drift-Scale Coupled Processes (DST and THC Seepage) Models*. MDL-NBS-HS-000001 REV00. Las Vegas, Nevada: CRWMS M&O. URN-0042.

CRWMS M&O 2000e. *Mountain-Scale Coupled Processes (TH) Models*. MDL-NBS-HS-000007. Las Vegas, Nevada: CRWMS M&O. URN-0062.

CRWMS M&O 2000f. *Multiscale Thermohydrologic Model*. ANL-EBS-MD-000049 REV 00. Las Vegas, Nevada: CRWMS M&O. URN-0019.

DOE (U.S. Department of Energy) 1999. *Monitored Geologic Repository Requirements Document*. YMP/CM-0025, Rev. 3, DCN 01. Las Vegas, Nevada: U.S. Department of Energy, Office of Civilian Radioactive Waste Management. ACC: MOL.19990415.0090.

DOE (U.S. Department of Energy) 2000. *Quality Assurance Requirements and Description*. DOE/RW-0333P, Rev. 9. Washington, D.C.: U.S. Department of Energy, Office of Civilian Radioactive Waste Management. ACC: MOL.19991028.0012.

Dyer, J.R. 1999. "Revised Interim Guidance Pending Issuance of New U.S. Nuclear Regulatory Commission (NRC) Regulations (Revision 01, July 22, 1999), for Yucca Mountain, Nevada." Letter from Dr. J.R. Dyer (DOE/YMSCO) to Dr. D.R. Wilkins (CRWMS M&O), September 3, 1999, OL&RC:SB-1714, with enclosure, "Interim Guidance Pending Issuance of New NRC Regulations for Yucca Mountain (Revision 01)." ACC: MOL.19990910.0079.

Francis, N.D.; Sobolik, S.R.; and Ballard, S. 1997. "Thermal-Hydrologic-Mechanical Analyses of the In Situ Single Heater Test, Yucca Mountain, Nevada." *Proceedings of the ASME Fluids Engineering Division, 1997 ASME International Mechanical Engineering Congress and*

Exposition, November 16-21, 1997, Dallas, Texas. Pages 445-456. New York, New York: American Society of Mechanical Engineers. TIC: 240139.

Hardin, E.L. 1998. *Near-Field/Altered-Zone Models Report*. UCRL-ID-129179 DR. Livermore, California: Lawrence Livermore National Laboratory. ACC: MOL.19980504.0577.

Ho, C.K. 1997. "Models of Fracture-Matrix Interactions During Multiphase Heat and Mass Flow in Unsaturated Fractured Porous Media." *ASME International Mechanical Engineering Congress and Exposition, Dallas, Texas, November 16-21, 1997. FED-Vol. 244*, 401-412. New York, New York: American Society of Mechanical Engineers. TIC: 241082.

Liley, P.E.; Reid, R.C.; and Buck, E. 1984. "Physical and Chemical Data." Section 3 of *Perry's Chemical Engineers' Handbook*. 6th Edition. Perry, R.H.; Green, D.W.; and Maloney, J.O., eds. New York, New York: McGraw-Hill. TIC: 246473.

Liu, H.H.; Doughty, C.; and Bodvarsson, G.S. 1998. "An Active Fracture Model for Unsaturated Flow and Transport in Fractured Rocks." *Water Resources Research*, 34, (10), 2633-2646. Washington, D.C.: American Geophysical Union. TIC: 243012.

Morris, C. 1992. *Academic Press Dictionary of Science and Technology*. San Diego, California: Academic Press, Inc. TIC: 206569.

Nitao, J.J. 1993. "The NUFT Code for Modeling Nonisothermal, Multiphase, Multicomponent Flow and Transport in Porous Media." *Eos*, 74, (43), 313. Washington, D.C.: American Geophysical Union. TIC: 226135.

Pruess, K. 1991. *TOUGH2-A General-Purpose Numerical Simulator for Multiphase Fluid and Heat Flow*. LBL-29400. Berkeley, California: Lawrence Berkeley Laboratory. ACC: NNA.19940202.0088.

Swanson Analysis Systems 1995. *ANSYS User's Manual for Revision 5.2. Four volumes*. Houston, Pennsylvania: Swanson Analysis Systems. TIC: 221933.

Tsang, Y.W.; Birkholzer, J.T.; Sonnenthal E.; Spycher N.; Apps, J.; Peterson, J.E., Jr.; and Williams, K.H. 1998. *Drift Scale Test Progress Report Lawrence Berkeley National Laboratory, Version 0.0*. Milestone SP2930M4. Berkeley, California: Lawrence Berkeley National Laboratory. ACC: MOL.19980825.0268.

van Genuchten, M.T. 1980. "A Closed-Form Equation for Predicting the Hydraulic Conductivity of Unsaturated Soils." *Soil Science Society American Journal*, 44, (5), 892-898. Madison, Wisconsin: Soil Science Society of America. TIC: 217327.

Waxman, M.H. and Thomas, E.C. 1974. "Electrical Conductivities in Shaly Sands: I. The Relation between Hydrocarbon Saturation and Resistivity Index; II. The Temperature Coefficient of Electrical Conductivity." *Journal of Petroleum Technology*, 26, 213-225. Dallas, Texas: Society of Petroleum Engineers. TIC: 239699.

Wemheuer, R.F. 1999. "First Issue of FY00 NEPO QAP-2-0 Activity Evaluations." Interoffice correspondence from R.F. Wemheuer (CRWMS M&O) to R.A. Morgan, October 13, 1999, LV.NEPO.RTPS.MAJ.10/99-164, with enclosures. ACC: MOL.19991021.0166.

Wilder, D.G.; Lin, W.; Blair, S.C.; Buscheck, T.; Carlson, R.C.; Lee, K.; Meike, A.; Ramirez, A. L.; Wagoner, J. L.; and Wang, J. 1997. *Large Block Test Status Report*. UCRL-ID-128776. Livermore, California: Lawrence Livermore National Laboratory. ACC: MOL.19980508.0727.

8.2 CODES, STANDARDS, REGULATIONS, AND PROCEDURES

64 FR 46976. 40 CFR 197: Environmental Radiation Protection Standards for Yucca Mountain, Nevada; Proposed Rule. Readily Available

64 FR 8640. Disposal of High Level Radioactive Wastes in a Proposed Geologic Repository at Yucca Mountain. TIC: 242725. Readily Available

QAP-2-0, Rev. 5. *Conduct of Activities*. Las Vegas, Nevada: CRWMS M&O. ACC: MOL.19980826.0209.

AP-3.10Q. Rev.2, ICN 0. *Analyses and Models*. Washington, D. C.: U.S. Department of Energy, Office of Civilian Radioactive Waste Management. ACC: MOL.20000217.0246.

AP-3.15Q. *Managing Technical Product Inputs*. Washington, D.C.: U.S. Department of Energy, Office of Civilian Radioactive Waste Management. ACC: MOL.20000218.0069.

AP-SI.1Q. Rev 2, ICN 4. *Software Management*. Washington, D.C.: U.S. Department of Energy, Office of Civilian Radioactive Waste Management. ACC: MOL.20000223.0508.

8.3 SOURCE DATA (LISTED BY DATA TRACKING NUMBERS)

LB000300123142.001. Thermal-Hydrological Simulations of the Drift Scale Test. AMR N0000, Thermal Tests Thermal Hydrological Analysis/Model Report. Submittal date: 03/24/2000.

LB960500834244.001. Hydrological Characterization of the Single Heater Test Area in ESF. Submittal date: 08/23/1996.

LB971212001254.001. DKM Basecase Parameter Set for UZ Model with Mean Fracture Alpha, Present Day Infiltration, and Estimated Welded, Non-Welded and Zeolitic FMX. Submittal date: 12/12/1997.

LB980120123142.004. Air Injections in Boreholes 57 through 61, 74 through 78, 185 and 186 in the Drift Scale Test Area. Submittal date: 01/20/1998.

LB980120123142.006. Imaging of Dielectric Constants of the Rock. Submittal date: 01/20/1998.

LB980420123142.002. Active Hydrology Testing Data in Boreholes 57-61, 74-78, and 185-186; Air Injection Tests and Gas Tracer Tests. Submittal date: 04/20/1998.

LB980715123142.002. Active Hydrology Testing Data in Boreholes 57-61, 74-78, and 185-186; Air Injection Tests and Gas Tracer Tests in 2ND Quarter TDIF Submission of the Drift Scale Test Heating Phase. Submittal date: 07/15/1998.

LB981016123142.002. Active Hydrology Testing Data (Air Injection) from Boreholes 57-61, 74-78, 185-186 Taken from August 1998 to September 1998 for the Third Quarter TDIF Submission For The Drift Scale Test. Submittal date: 10/16/1998.

LB990501233129.001. Fracture Properties for the UZ Model Grids and Uncalibrated Fracture and Matrix Properties for the UZ Model Layers for AMR U0090, "Analysis of Hydrologic Properties Data". Submittal date: 08/25/1999.

LB990630123142.001. Fourth, Fifth, and Sixth Quarters TDIF Submission for the Drift Scale Test, September 1998 to May 1999. Submittal date: 06/30/1999.

LB990630123142.005. Fourth, Fifth, and Sixth Quarters TDIF Submission for the Drift Scale Test, September 1998 To May 1999. Submittal date: 07/20/1999.

LB990861233129.001. Drift Scale Calibrated 1-D Property Set, FY99. Submittal date: 08/06/1999.

LB997141233129.001. Calibrated Basecase Infiltration 1-D Parameter Set for the UZ Flow and Transport Model, FY99. Submittal date: 07/21/1999.

LL000314304242.094. NUFT Calculation LBT Sensitivity Calcs. Submittal date: 03/28/2000.

LL000314404242.095. NUFT Calculation DST Sensitivity Calcs. Submittal date: 03/28/2000.

LL000321204242.092. NUFT Calculation to Simulate Large Block Environment. Submittal date: 03/24/2000.

LL000321704242.093. NUFT Calculation DST Simulation. Submittal date: 03/24/2000.

LL970803004244.036. Data on Temperature of the Large Block Test (LBT). Submittal date: 08/08/1997.

LL971204304244.047. Neutron Logging Activities at the Large Block Test (LBT). Submittal date: 12/08/1997.

LL980409604244.059. First Quarter Heating Phase Results of the Neutron Logging Report. Submittal date: 04/21/1998.

LL980913304244.072. Data Submission Report For Electrical Resistance Tomography Results Obtained During the Large Block Test FY98. Submittal date: 09/24/1998.

LL980916704244.073. Data Submission Report For Electrical Resistance Tomography Results Obtained During the Large Block Test FY98. Submittal date: 09/25/1998.

LL980918904244.074. Temperature, Relative Humidity and Gas Pressure Results During the Large Block Test FY 98. Submittal date: 09/29/1998.

LL980919304244.075. Neutron Logging Activities at The Large Block Test (LBT). Submittal date: 09/30/1998.

LL990702704244.099. Data for the Drift Scale Test. Submittal date: 07/13/1999.

LL990708904243.033. Compilation of Neutron Logging Data. Submittal date: 07/29/1999.

MO0002ABBLSLDS.000. As-Built Borehole Locations and Sensor Locations for the Drift Scale Test Given in Local (DST) Coordinates. Submittal date: 02/01/2000.

MO9807DSTSET01.000. Drift Scale Test (DST) Temperature, Power, Current, Voltage Data for November 7, 1997 through May 31, 1998. Submittal date: 07/09/1998.

MO9810DSTSET02.000. Drift Scale Test (DST) Temperature, Power, Current, Voltage Data for June 1 through August 31, 1998. Submittal date: 10/09/1998.

MO98METDATA110.000. Validated Meterological Data, October - December, 1997. Submittal date: 01/29/1998.

MO9906DSTSET03.000. Drift Scale Test (DST) Temperature, Power, Current, and Voltage Data for September 1, 1998 through May 31, 1999. Submittal date: 06/08/1999.

MO9912SEPDOIHP.000. Determination of Outer/Inner Heater Power Ratio Using Heater Power Data. Submittal date: 12/16/1999.

SN0003T0872799.010. Single Heater Test (SHT) Model Simulation Sensitivity Study of the SHT Using the Total System Performance Assessment-Viability Assessment (TSPA-VA) Hydrologic Property Set. Submittal date: 03/23/2000.

SN0003T0872799.011. Single Heater Test (SHT) Model Simulation Sensitivity Study of the SHT Using the Median KB Hydrologic Property Set. Submittal date: 03/23/2000.

SN0003T0872799.012. Single Heater Test (SHT) Model Simulation of the SHT Using the Base Case Drift-Scale Hydrologic Property Set. Submittal date: 03/23/2000.

SNF35110695001.008. Evaluation and Comparative Analysis of Single Heater Test, Thermal and Thermomechanical Data: First Quarter FY98 Results (8/26/96 through 11/30/97). Submittal date: 01/06/1998.

SNF35110695001.009. Thermal and Thermomechanical Data for the Single Heater Test Final Report. Submittal date: 08/24/1998.

SNT05071897001.002. Base Case Thermal Property Data for TSPA-VA (Total System Performance Assessment-Viability Assessment). VA Supporting Data. Submittal date: 02/12/1998.

TM000000000001.100. Validated Meteorological Data, January - March 1997. Submittal date: 04/18/1997.

TM000000000001.104. Validated Meteorological Data, April - June 1997. Submittal date: 07/21/1997.

TM000000000001.107. Validated Meteorological Data, July - September 1997. Submittal date: 10/22/1997.

8.4 COMPUTER SOFTWARE AND ROUTINES

Lawrence Berkeley National Laboratory. Software code, TOUGH2, STN:10007-1.4-01. 1999. V1.4.

Lawrence Berkeley National Laboratory. Software code, TOUGH2, STN:10062-1.3MEOS4V1.0-00. 1999. V.1.3, Module EOS4 V1.0.

Lawrence Berkeley National Laboratory. Software routine, 2KGRIDV1.F, STN:10244-1.0-00. 1999. V1.0.

Lawrence Berkeley National Laboratory. Software routine, EXT, STN:10047-1.0-00. 1999. V1.0.

Lawrence Berkeley National Laboratory. Software routine, MK_CAN_POWER.F, STN:10247-1.0-00. 1999. V1.0.

Lawrence Berkeley National Laboratory. Software routine, MK_CLUSTER*.F, STN:10240-1.0-00. 1999. V1.0.

Lawrence Berkeley National Laboratory. Software routine, MK_EVALUATE*.F, STN:10243-1.0-00. 1999. V1.0.

Lawrence Berkeley National Laboratory. Software routine, MK_INCON_3D_DUAL.F, STN:10250-1.0-00. 1999. V1.0.

Lawrence Berkeley National Laboratory. Software routine, MK_MESH_CORRECT.F, STN:10249-1.0-00. 1999. V1.0.

Lawrence Berkeley National Laboratory. Software routine, MK_TEC*.F, STN:10239-1.0-00. 1999. V1.0.

Lawrence Berkeley National Laboratory. Software routine, MK_TEMP3D_ALL.F, STN:10242-1.0-00. 1999. V1.0.

Lawrence Berkeley National Laboratory. Software routine, MK_TIME*.F, STN:10237-1.0-00. 1999. V1.0.

Lawrence Berkeley National Laboratory. Software routine, MK_WING_POWER.F, STN:10248-1.0-00. 1999. V1.0.

Lawrence Berkeley National Laboratory. Software routine, MK_YSW_CONNE.F, STN:10246-1.0-00. 1999. V1.0.

Lawrence Berkeley National Laboratory. Software routine, AMESH, STN:10045-1.0-00. 1999. V1.0.

Lawrence Berkeley National Laboratory. Software routine, MK_3DINTER*.F, STN:10241-1.0-00. 1999. V1.0.

Lawrence Berkeley National Laboratory. Software routine, mk_circ.f, STN:10229-1.0-00. 1999. V1.0.

Lawrence Berkeley National Laboratory. Software routine, MK_GRAV3D.F, STN:10233-1.0-00. 1999. V1.0.

Lawrence Berkeley National Laboratory. Software routine, mk_rect.f, STN:10228-1.0-00. 1999. V1.0.

Lawrence Berkeley National Laboratory. Software routine, merggrid.f, STN: 10230-1.0-00. 1999. V1.0.

Lawrence Berkeley National Laboratory. Software routine. MK_3DSLIZE.F STN:10232-1.0-00. 1999. V1.0.

Lawrence Berkeley National Laboratory. Software routine. MK_DUAL.F, STN:10236-1.0-00. 1999. V1.0.

Lawrence Berkeley National Laboratory. Software routine. MK_GENER.F, STN:10234-1.0-00. 1999. V1.0.

Lawrence Berkeley National Laboratory. Software routine. MK_GRAV2D.F STN:10231-1.0-00. 1999. V1.0.

Lawrence Berkeley National Laboratory. Software routine. MK_OBS3D.F, STN:10238-1.0-00. 1999. V1.0..

Lawrence Berkeley National Laboratory. Software routine. MK_OBSERV.F, STN:10235-1.0-00. 1999. V1.0..

Lawrence Berkeley National Laboratory. Software routine. MK_YSW_ELEME.F, STN:10245-1.0-00. 1999. V1.0.

Lawrence Livermore National Laboratory. Software code, NUFT, STN:10130-3.0.1s-00.
1999. V3.0.1s.

Lawrence Livermore National Laboratory. Software routine, RADPRO, STN:10204-3.22-00.
1999. V3.22.

Lawrence Livermore National Laboratory. Software routine, XTOOL, STN:10208-10.1-00.
1999. V10.1.

Lawrence Livermore National Laboratory. Software routine, YMESH, STN:10172-1.53-00.
1999. V1.53.

Lawrence Livermore National Laboratory. Software routine, LBT_STATS, ANL-NBS-TH-
000001 REV 00. 1999. V1.0.

Lawrence Livermore National Laboratory. Software routine, MULTIDST, ANL-NBS-TH-
000001 REV 00. 1999. V1.0.

Lawrence Livermore National Laboratory. Software macro, Rock_sun.m. ANL-NBS-TH-
000001 REV 00. 1999. V1.0.

Sandia National Laboratories. Software Code, TOUGH2 STN:10146-3.4.3-00. 1999. V3.4.3.

Sandia National Laboratories. Software routine, BDRYINSELEM.F, ANL-NBS-TH-000001
REV 00. 1999. V1.0.

Sandia National Laboratories. Software routine. COMPARE. ANL-NBS-TH-000001 REV 00.
1999. V1.0.

Sandia National Laboratories. Software routine. DKMMESH.F. ANL-NBS-TH-000001 REV
00. 1999. V1.0.

Sandia National Laboratories. Software routine. DKMMESH_MOD.F. ANL-NBS-TH-000001
REV 00. 1999. V2.0.

Sandia National Laboratories. Software routine. TOUGH_EXTRACT_FRAC.F. ANL-NBS-
TH-000001 REV 00. 1999. V1.0.

Sandia National Laboratories. Software routine, tough_extract_mtrx.f, ANS-NBS-TH-000001
REV 00. 1999. V1.0.

Sandia National Laboratories. Software routine. AMB.F. ANL-NBS-TH-000001 REV 00.1999.
V1.0.

Sandia National Laboratories. Software routine. DKMMESHAMB_MOD.F. ANL-NBS-TH-
000001 REV 00.1999. V2.0.

Sandia National Laboratories. Software routine, dkmmeshamb_mod_1D.f, ANL-NBS-TH-
000001 REV 00. 1999. v1.0.

Sandia National Laboratories. Software routine. ICPREDKM.F. ANL-NBS-TH-000001 REV 00. 1999. V1.0.

Sandia National Laboratories. Software routine. READ_TEMP_VS_TIME_MODELS, ANL-NBS-TH-000001 REV 00.1999. V1.0.

Sandia National Laboratories. Software routine. DKMMESHAMB.F. ANL-NBS-TH-000001 REV 00.1999. V1.0.